



# Photoelectrocatalytic CO<sub>2</sub> conversion in ionic liquid/aqueous mixture solution studied by scanning electrochemical microscopy

Lin Zhang

## ► To cite this version:

Lin Zhang. Photoelectrocatalytic CO<sub>2</sub> conversion in ionic liquid/aqueous mixture solution studied by scanning electrochemical microscopy. Theoretical and/or physical chemistry. Sorbonne Université, 2020. English. NNT : 2020SORUS122 . tel-03381506

**HAL Id: tel-03381506**

**<https://theses.hal.science/tel-03381506>**

Submitted on 17 Oct 2021

**HAL** is a multi-disciplinary open access archive for the deposit and dissemination of scientific research documents, whether they are published or not. The documents may come from teaching and research institutions in France or abroad, or from public or private research centers.

L'archive ouverte pluridisciplinaire **HAL**, est destinée au dépôt et à la diffusion de documents scientifiques de niveau recherche, publiés ou non, émanant des établissements d'enseignement et de recherche français ou étrangers, des laboratoires publics ou privés.



Sorbonne Université

École Doctorale 388 – Chimie Physique et Chimie Analytique de  
Paris Centre

*Laboratoire Interfaces et Systèmes Electrochimiques, LISE – UMR 8235*

**Photoelectrocatalytic CO<sub>2</sub> Conversion in Ionic  
Liquid/Aqueous Mixture Solution Studied by  
Scanning Electrochemical Microscopy**

Par **Lin ZHANG**

Thèse de doctorat

Dirigée par Dr. Carlos M. SANCHEZ-SANCHEZ

Présentée et soutenue publiquement le 15 Octobre 2020, à Paris

Devant un jury composé de :

Mme. Conchi ANIA	Directrice de Recherche CNRS - Université d'Orléans	Rapporteuse
M. Enrique HERRERO	Professeur University of Alicante (Spain))	Rapporteur
M. David PORTEHAULT	Chargé de Recherche -HDR CNRS - Sorbonne Université	Examineur
M. Carlos SANCHEZ-SANCHEZ	Chargé de Recherche -HDR CNRS - Sorbonne Université	Directeur de thèse
M. Vincent VIVIER	Directeur de Recherche CNRS - Sorbonne Université	Co-encadrant



# Table of Contents

<b>Abstract .....</b>	<b>v</b>
<b>Résumé .....</b>	<b>vii</b>
<b>English Symbols and Acronyms Used in This Thesis.....</b>	<b>ix</b>
<b>Chapter 1 Introduction.....</b>	<b>1</b>
1.1. The Research on CO <sub>2</sub> Reduction Reaction (CO <sub>2</sub> RR).....	1
1.1.1. Introduction.....	1
1.1.2. Electrochemical CO <sub>2</sub> RR and Photoelectrochemical CO <sub>2</sub> RR.....	2
1.1.3. Relevant Factors and Present limitations on Electrochemical and Photoelectrochemical CO <sub>2</sub> RR.....	6
1.1.3.1. <i>Electrolyte</i> .....	6
1.1.3.2. <i>Electrode materials</i> .....	6
1.1.3.3. <i>Electrolysis Cell Configuration</i> .....	9
1.1.3.4. <i>Other Factors (Pressure, pH and Potential)</i> .....	10
1.2. Scanning Electrochemical Microscopy (SECM) and Scanning Photoelectrochemical Microscopy (SPECM) .....	12
1.2.1. Introduction.....	12
1.2.2. Experimental Device of SECM .....	13
1.2.3. Ultramicroelectrode (UME).....	14
1.2.4. The Operation Modes of SECM .....	17
1.2.4.1. <i>Feedback mode (FB)</i> .....	17
1.2.4.2. <i>Generation/Collection mode (GC)</i> .....	19
1.2.4.3. <i>Redox competition mode (RC)</i> .....	20
1.2.5. Experimental Devices of SPECM.....	21
1.2.6. Applications of SECM in Electrochemistry and Photoelectrochemistry.....	24
1.2.6.1. <i>Applications of SECM in Electrochemistry</i> .....	25
1.2.6.2. <i>Applications of SPECM in Photoelectrochemistry</i> .....	28
1.3. Room Temperature Ionic Liquids (RTILs) .....	29
1.3.1. Introduction of RTILs .....	29
1.3.2. Classification and Properties and of RTILs .....	30
1.3.2.1. <i>Classification and abbreviations</i> .....	30
1.3.2.2. <i>Properties of RTILs</i> .....	32
1.3.3. Applications of RTILs in Electrochemistry and Photoelectrochemistry .....	33



1.3.3.1. Applications of Pure RTILs and RTILs-based Binary and Ternary Solvent Mixtures in Electrochemical CO <sub>2</sub> RR.....	33
1.3.3.2. Mechanisms and Pathways of Imidazolium based RTILs in Electrochemical CO <sub>2</sub> RR.....	37
1.3.3.3. Applications of Imidazolium based RTILs Photocatalytic CO <sub>2</sub> RR.....	42
1.4. Electrochemical and Photoelectrochemical Catalytic Materials .....	45
1.4.1. Applications and Present Limitations of Transition Metal–Nitrogen Doped Carbon (M–N–C) Catalysts in Electrochemical CO <sub>2</sub> RR.....	45
1.4.2. Introduction of p-type Semiconductors for PEC CO <sub>2</sub> RR .....	48
1.4.2.1. The Energy Band Theory and Photoelectrocatalysis of Semiconductors .....	48
1.4.2.2. The Applications of p-type Semiconductor: Oxide-Derived Cu Catalysts for PEC CO <sub>2</sub> RR.....	50
1.5. Summary of Objectives and Outline of the Thesis.....	52
1.6. References .....	54
<b>Chapter 2 Materials and Experimental Methods .....</b>	<b>73</b>
2.1. Reagents and Materials .....	73
2.1.1. Chemical Reagents .....	73
2.1.2. Experimental Materials and Instruments .....	74
2.2. Synthesis of Semiconductors and Preparation of Array Substrate Electrodes .....	77
2.3. Optimization the Picolitor Dispenser Parameters for CuCo <sub>2</sub> O <sub>4</sub> .....	79
2.4. Scanning Photoelectrochemical Microscopy .....	81
2.4.1. Experimental configuration .....	81
2.4.2. SPECM Experimental Procedure.....	83
2.4.2.1. SPECM imaging.....	83
2.4.2.2. Chronoamperometric Photoactivity Quantification by SPECM.....	84
2.4.3. Fabrication of Agar Bridge .....	85
2.5. Fabrication and Characterization of Dual Tip OF-UME.....	86
2.5.1. Introduction of P-2000 Laser-Based Micropipette Puller.....	86
2.5.2. Fabrication Procedure of Dual Tip OF-UME .....	89
2.6. Rotating Disk Electrode (RDE).....	94
2.7. Electrochemical CO <sub>2</sub> RR on Synthesized M–N–Cs.....	96
2.7.1. Synthesis and Characterization of Different M–N–Cs .....	96

2.7.2.	Electrode Preparation and Electrochemical Characterization.....	97
2.7.3.	Evaluation Methods of Electrochemical CO <sub>2</sub> RR Performance on Different M–N–C catalyst by RDE .....	98
2.8.	Bulk Electrolysis under Illumination .....	98
2.9.	Characterization Methods.....	100
2.9.1.	Scanning Electron Microscopy (SEM) .....	100
2.9.2.	Energy-Dispersive X-ray Spectroscopy (EDS) .....	100
2.9.3.	Gas Chromatography (GC) and Ionic Chromatography (IC) .....	100
2.10.	References .....	100
<b>Chapter 3 Photoelectrochemical Activity for CO<sub>2</sub>RR in Different RTILs-based Solvent Media Evaluated by SPECM .....</b>		<b>105</b>
3.1.	Introduction .....	105
3.2.	Screening and Comparison of different p-type Metal Oxide Semiconductors.....	107
3.3.	Results and Discussion .....	113
3.3.1.	SEM and EDS Analysis of p-type Semiconductor CuCo <sub>2</sub> O <sub>4</sub> .....	113
3.3.2.	Effect of the Electrolyte Nature and Composition in CuCo <sub>2</sub> O <sub>4</sub> Photoactivity ..	114
3.3.3.	Photoelectrochemical Activity Evaluation by SPECM on CuCo <sub>2</sub> O <sub>4</sub> in Different Solvent Media .....	117
3.3.4.	Quantification of Photoelectrochemical Activity by SPECM .....	125
3.3.4.1.	<i>Amperometry I-t Curves Analysis</i> .....	125
3.3.4.2.	<i>Photodegradation of CuCo<sub>2</sub>O<sub>4</sub></i> .....	126
3.4.	Conclusions .....	135
3.5.	References .....	136
<b>Chapter 4 Detection and Identification of Photoelectrochemically Generated Products by SPECM and Chromatography.....</b>		<b>141</b>
4.1.	Introduction .....	141
4.2.	Detection of Photoelectrochemically Generated Products by OF-UME.....	142
4.3.	SPECM Imaging by the Dual Tip OF-UME .....	144
4.3.1.	Constant Potential Products Detection by the Dual Tip OF-UME .....	147
4.3.2.	Fast Cyclic Voltammetry Products Detection by the Dual Tip OF-UME .....	148
4.3.3.	Bulk Electrolysis and Products Analysis by Chromatography .....	152
4.4.	Conclusions .....	157
4.5.	References .....	158
<b>Chapter 5 Electrochemical CO<sub>2</sub>RR on Synthesized M–N–Cs Evaluated by RDE .....</b>		<b>163</b>

5.1. Introduction .....	163
5.2. Results and Discussion .....	164
5.2.1. Structure Morphology and Composition of M–N–Cs .....	164
5.2.2. Comparison of M–N–Cs on Electrochemical CO <sub>2</sub> RR Performance .....	167
5.3. Conclusions .....	172
5.4. References .....	172
<b>Chapter 6 General Conclusions and Outlook.....</b>	<b>177</b>
6.1. General Conclusions.....	177
6.2. Outlook .....	179
6.3. References .....	181
<b>Résumé de la Thèse en Français.....</b>	<b>183</b>
<b>List of publications, trainings and conferences.....</b>	<b>199</b>
<b>Acknowledgements .....</b>	<b>201</b>

## Abstract

This thesis studies photoelectrochemical CO<sub>2</sub> reduction reaction (PEC CO<sub>2</sub>RR) on p-type semiconductor CuCo<sub>2</sub>O<sub>4</sub> addressing the cocatalytic role of imidazolium based RTILs by scanning photoelectrochemical microscopy (SPECM). Imidazolium based RTILs strongly absorb photons from ultraviolet (UV) light irradiation.

CuCo<sub>2</sub>O<sub>4</sub> was studied in different solvent supporting electrolyte systems including: aqueous solution (0.1 M KHCO<sub>3</sub> and 0.1 M Na<sub>2</sub>SO<sub>4</sub>), binary mixture solution (25 vol.% [C<sub>2</sub>mim][BF<sub>4</sub>]/H<sub>2</sub>O and 25 vol.% [C<sub>4</sub>mim][BF<sub>4</sub>]/H<sub>2</sub>O) and pure RTILs ([C<sub>2</sub>mim][BF<sub>4</sub>], [C<sub>4</sub>mim][BF<sub>4</sub>], [C<sub>4</sub>mim][NTf<sub>2</sub>] and [C<sub>2</sub>mim][NTf<sub>2</sub>]) to explore by SPECM the role of RTILs in CuCo<sub>2</sub>O<sub>4</sub> semiconductor PEC performance. Significantly enhanced photoreduction current under both UV-vis and visible light illumination is reported in 25 vol.% [C<sub>2</sub>mim][BF<sub>4</sub>]/H<sub>2</sub>O solution. However, no significant difference is observed whether the solution is CO<sub>2</sub> saturated or not, which seems to point out an enhanced performance due to the presence of [C<sub>2</sub>mim][BF<sub>4</sub>] in solution. Only CO generated from PEC CO<sub>2</sub>RR was detected using an in-situ detection method based on a home-made dual tip optical fiber-ultramicroelectrode (OF-UME) and from bulk electrolysis under illumination. The formation of CO at potentials more positive than the thermodynamic value is reported here and it clearly points out that direct CO<sub>2</sub> reduction on the electrode surface is not the mechanism taking place and that CO is underpotential photoelectrochemically produced, which place this approach near artificial photosynthesis. A possible reaction scheme for the PEC CO<sub>2</sub>RR mediated by [C<sub>2</sub>mim]<sup>+</sup> is proposed. Thus, our results have demonstrated for the first time the cocatalytic role of [C<sub>2</sub>mim]<sup>+</sup> for the PEC CO<sub>2</sub>RR.

In addition, electrochemical CO<sub>2</sub>RR has also been studied on various synthesized transition metal–nitrogen–carbon catalysts (M–N–Cs) by rotating disk electrode. 25%Fe25%Co–N–C exhibited the best performance on electrochemical CO<sub>2</sub>RR among the studied M–N–Cs in this thesis. The presence of Co sites in that catalyst provided synergic effect for the generation of distributed Fe-rich microcubes, which act as active sites in electrochemical CO<sub>2</sub>RR.

**Keywords:** photoelectrochemical CO<sub>2</sub> reduction reaction; electrochemical CO<sub>2</sub> reduction reaction; scanning electrochemical microscopy; scanning photoelectrochemical microscopy; imidazolium based room-temperature ionic liquids; transition metal–nitrogen–carbon catalysts

## Résumé

Cette thèse concerne l'étude de la réaction photoélectrochimique de réduction du  $\text{CO}_2$  (PEC  $\text{CO}_2\text{RR}$ ) sur le semi-conducteur de type p  $\text{CuCo}_2\text{O}_4$  en abordant le rôle cocatalytique des RTIL à base d'imidazolium par microscopie photoélectrochimique à balayage (SPECM). Les RTIL à base d'imidazolium absorbent fortement les photons provenant de l'irradiation de la lumière ultraviolette (UV).

Le  $\text{CuCo}_2\text{O}_4$  a été étudié dans différents électrolytes supports, notamment une solution aqueuse (0,1 M  $\text{KHCO}_3$  et 0,1 M  $\text{Na}_2\text{SO}_4$ ), une solution de mélange binaire (25 vol.%  $[\text{C}_2\text{mim}][\text{BF}_4]/\text{H}_2\text{O}$  et 25 vol.%  $[\text{C}_4\text{mim}][\text{BF}_4]/\text{H}_2\text{O}$ ) et des liquides ioniques pur ( $[\text{C}_2\text{mim}][\text{BF}_4]$ ,  $[\text{C}_4\text{mim}][\text{BF}_4]$ ,  $[\text{C}_4\text{mim}][\text{NTf}_2]$  et  $[\text{C}_2\text{mim}][\text{NTf}_2]$ ) pour explorer par SPECM le rôle des RTIL dans les performances des PEC des semi-conducteurs  $\text{CuCo}_2\text{O}_4$ . Un courant de photoréduction significativement amélioré sous l'éclairage UV-vis et visible est obtenu dans une solution à 25 vol.%  $[\text{C}_2\text{mim}][\text{BF}_4]/\text{H}_2\text{O}$ . Cependant, aucune différence significative n'est observée, que la solution soit saturée en  $\text{CO}_2$  ou non, ce qui semble indiquer une amélioration des performances due à la présence de  $[\text{C}_2\text{mim}][\text{BF}_4]$  en solution. Seul le CO généré par la PEC  $\text{CO}_2\text{RR}$  a été détecté à l'aide d'une méthode de détection in situ basée sur une fibre optique à double sonde - ultra-microélectrode (OF-UME) développée au laboratoire et sur une électrolyse en volume sous illumination. La formation de CO à des potentiels plus positifs que la valeur thermodynamique est rapportée ici et il est clairement indiqué que la réduction directe du  $\text{CO}_2$  à la surface de l'électrode n'est pas le mécanisme qui se produit et que le CO est produit photoélectrochimiquement à des potentiels inférieurs, ce qui place cette approche près de la photosynthèse artificielle. Un schéma de réaction possible pour la PEC  $\text{CO}_2\text{RR}$  par l'intermédiaire de  $[\text{C}_2\text{mim}]^+$  est proposé. Ainsi, nos résultats ont démontré pour la première fois le rôle cocatalytique de  $[\text{C}_2\text{mim}]^+$  pour le PEC  $\text{CO}_2\text{RR}$ .

En outre, la  $\text{CO}_2\text{RR}$  électrochimique a également été étudiée sur divers catalyseurs de métaux de transition, d'azote et de carbone (M–N–Cs) par électrode à disque tournant. 25%Fe25%Co–N–C a montré la meilleure performance sur la  $\text{CO}_2\text{RR}$  électrochimique parmi les M–N–Cs étudiés dans cette thèse. La présence de sites Co dans ce catalyseur a fourni un effet synergique pour la génération de microcubes distribués riches en Fe, qui agissent comme des sites actifs dans la  $\text{CO}_2\text{RR}$  électrochimique.

Mots clés : réaction photoélectrochimique de réduction du CO<sub>2</sub> ; réaction électrochimique de réduction du CO<sub>2</sub> ; microscopie électrochimique à balayage ; microscopie photoélectrochimique à balayage ; liquides ioniques à base d'imidazolium ; catalyseurs métal de transition-azote-carbone

## English Symbols and Acronyms Used in This Thesis

Acronyms	Meaning
<b>[C<sub>2</sub>mim]<sup>+</sup></b>	1-Ethyl-3-methylimidazolium cation
<b>[C<sub>n</sub>mim]<sup>+</sup></b>	1,3-dialkyl-imidazolium cation
<b>[EMIM][BF<sub>4</sub>]</b>	1-ethyl-3-methylimidazolium tetrafluoroborate
<b>[EMIM][TFO]</b>	1-ethyl-3-methylimidazolium trifluoromethanesulfonate
<b>[EtMeim<sup>+</sup>][BF<sub>4</sub>]</b>	1-ethyl-3-methylimidazolium tetrafluoroborate
<b>[EtNH<sub>3</sub>]-[NO<sub>3</sub>]</b>	Ethylammonium nitrate
<b>[HMIM]Cl</b>	1-hexyl-3-methylimidazolium chloride
<b>[OMIM][DS]</b>	1-octyl-3-methylimidazolium dodecylsulphate
<b>[TBA][PF<sub>6</sub>]</b>	Tetrabutylammonium hexafluorophosphate
<b>AFM</b>	Atomic force microscope
<b>AN</b>	Acetonitrile
<b>C<sub>2</sub><sup>+</sup></b>	Multicarbon
<b>CB</b>	Conduction band
<b>CCS</b>	Carbon capture and storage
<b>CCU</b>	Carbon capture and utilization
<b>CE</b>	Counter electrode
<b>CIBH</b>	Catalyst ionomer bulk heterojunction
<b>CIPH</b>	Catalyst ionomer planer heterojunction
<b>CNFs</b>	Carbon nanofiber catalysts
<b>CO<sub>2</sub>RR</b>	CO <sub>2</sub> reduction reaction
<b>CV</b>	Cyclic voltammetry
<b>DMF</b>	Dimethyl formamide
<b>DMSO</b>	Dimethyl sulfoxide
<b>E<sub>F</sub></b>	Fermi level
<b>E<sub>R</sub></b>	Redox potential
<b>FAOR</b>	Formic acid oxidation reaction
<b>FB</b>	Feedback mode
<b>FE</b>	Faradaic efficiency



<b>FTO</b>	Fluorine-doped tin oxide
<b>GC</b>	Generation/Collection mode
<b>GC</b>	Gas chromatography
<b>GDE</b>	Gas diffusion electrodes
<b>HER</b>	Hydrogen evolution reaction
<b>HOMO</b>	Highest occupied molecular orbital
<b>IC</b>	Ionic chromatography
<b>ILs</b>	Ionic liquids
<b>IR</b>	Ohmic drop
<b>ITO</b>	Indium tin oxide
<b>LUMO</b>	Lowest unoccupied molecular orbital
<b>MD-SC</b>	Micropipet delivery-substrate collection mode
<b>MEA</b>	Monoethanolamine
<b>M–N–Cs</b>	Metal–nitrogen–doped carbon catalysts
<b>NHE</b>	Normal hydrogen electrode
<b>NPs</b>	Nanoparticles
<b>NTf<sub>2</sub><sup>−</sup></b>	N(SO <sub>2</sub> CF <sub>3</sub> ) <sub>2</sub> <sup>−</sup>
<b>OCP</b>	Open circuit potential
<b>OD-Cu</b>	Oxide derived copper
<b>OF</b>	Optical fiber
<b>OF-UME</b>	Optical fiber- ultramicroelectrode
<b>ORR</b>	Oxygen reduction reaction
<b>OTf<sup>−</sup></b>	CF <sub>3</sub> SO <sub>3</sub> <sup>−</sup>
<b>OTs<sup>−</sup></b>	C <sub>6</sub> H <sub>5</sub> SO <sub>3</sub> <sup>−</sup>
<b>PEC</b>	Photoelectrochemical
<b>PFSA</b>	Perfluorinated sulfonic acid
<b>PTFE</b>	Polytetrafluoroethylene
<b>RC</b>	Time constant
<b>RC</b>	Redox competition
<b>RDE</b>	Rotating disk electrode
<b>RDS</b>	Rate determining step

<b>RE</b>	Reference electrode
<b>RHE</b>	Reversible hydrogen electrode
<b>RTILs</b>	Room temperature ionic liquids
<b>SCs</b>	Semiconductors
<b>SECM</b>	Scanning electrochemical microscopy
<b>SG-TC</b>	Substrate generation-tip collection
<b>SICM</b>	Scanning ion conductance microscope
<b>SPECM</b>	Scanning photoelectrochemical microscopy
<b>STM</b>	Scanning tunneling microscopy
<b>TG-SC</b>	Tip generation-substrate collection
<b>TEAP</b>	Tetraethylammonium perchlorate
<b>TEOA</b>	Triethanolamine
<b>TON</b>	Turnover number
<b>UME</b>	Ultramicroelectrode
<b>VB</b>	Valence band
<b>WE</b>	Working electrode



Chapter

**1**

Introduction

---



## Chapter 1 Introduction

### 1.1. The Research on CO<sub>2</sub> Reduction Reaction (CO<sub>2</sub>RR)

#### 1.1.1. Introduction

To satisfy the energy demand of the global development, the consumption of fossil fuels has been on an unprecedented scale up, leading to a sustainable increasing concentration of the greenhouse carbon dioxide (CO<sub>2</sub>) gas, which reached a monthly average value of 413 ppm [1]. This anthropogenic CO<sub>2</sub> emission breaks the global balance of carbon cycle as shown in Figure 1.1a, as well as causes environmental problems and energy crisis [2]. Therefore, carbon capture and storage (CCS) and carbon capture and utilization (CCU) strategies are necessary to mitigate CO<sub>2</sub>. CCU is preferred than CCS because CO<sub>2</sub> can be converted to useful feedstocks. Among all the CO<sub>2</sub> conversion approaches including thermal, chemical, biological, electrochemical, photochemical and photoelectrochemical methods, electrochemical and photoelectrochemical CO<sub>2</sub> reduction reaction (CO<sub>2</sub>RR) powered by electricity from renewable sources such as solar energy or wind have become attractive because they possess advantages and can produce useful chemicals and fuels [3–9]. Figure 1.1b shows this artificial carbon recycling. This kind of reaction can occur under ambient conditions and can be turned by the surface free energy through the control of the electrode potential.

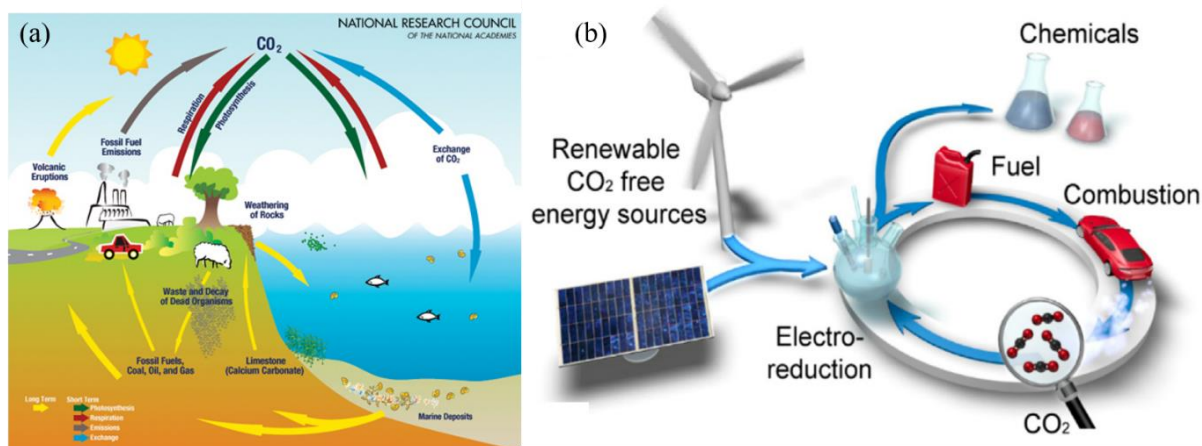
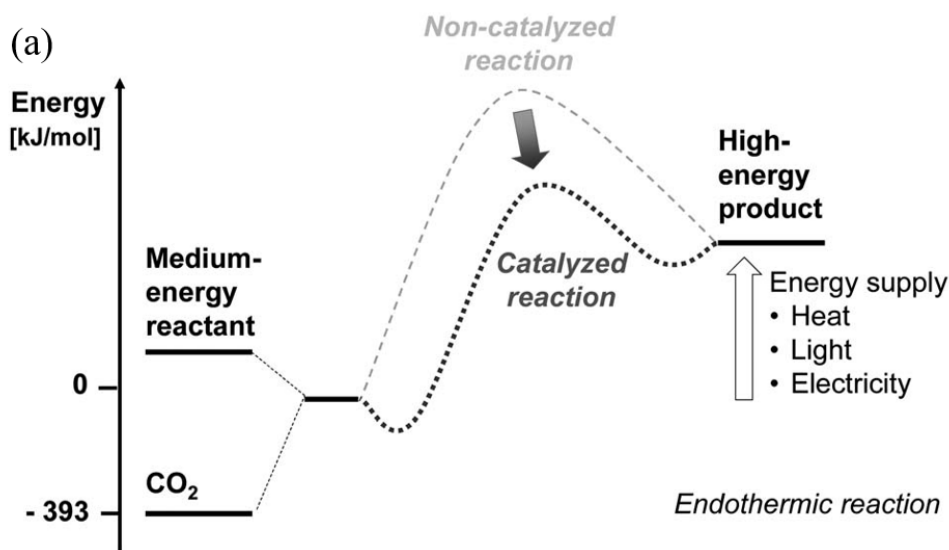


Figure 1.1 Illustrations of the (a) carbon cycle [2] and (b) carbon recycling by artificial way powered by renewable electricity sources of wind and solar [10].

In this chapter, the challenges and the advanced researches of electrochemical and photoelectrochemical CO<sub>2</sub>RR are introduced, as well as the mechanisms and pathways for the generation of different products. In addition, different elements constituted in the reaction system, which can affect the CO<sub>2</sub>RR performance, are explained and discussed, aiming to provide an exhaustive reversion and background in CO<sub>2</sub>RR.

### 1.1.2. Electrochemical CO<sub>2</sub>RR and Photoelectrochemical CO<sub>2</sub>RR

CO<sub>2</sub> is a non-polar, linear, thermodynamically stable molecule, which requires some energy input (heat, light or electricity) to overcome the barrier for endothermic chemical transformation. A catalyst is desired to lower the free energy needed so that increasing the reaction rate and promoting products selectivity as shown in Figure 1.2a [11]. Moreover, CO<sub>2</sub> is also kinetically difficult to convert. Figure 1.2b shows thermodynamic potentials for numerous reactions of various products, these potentials represent the minimum required potentials for each reaction to take place following a direct mechanism in aqueous solution [12]. Normally, the initial one electron transfer reaction requires high energy and happens at -1.9 V vs. NHE (E1) because of the reorganization of the linear molecule and the formation of radical anion species (CO<sub>2</sub><sup>•-</sup>). However, proton-coupled multi-electrons transfer reaction to form other products require much lower energy since the generated products are more thermodynamically stable molecules [13].



(b)

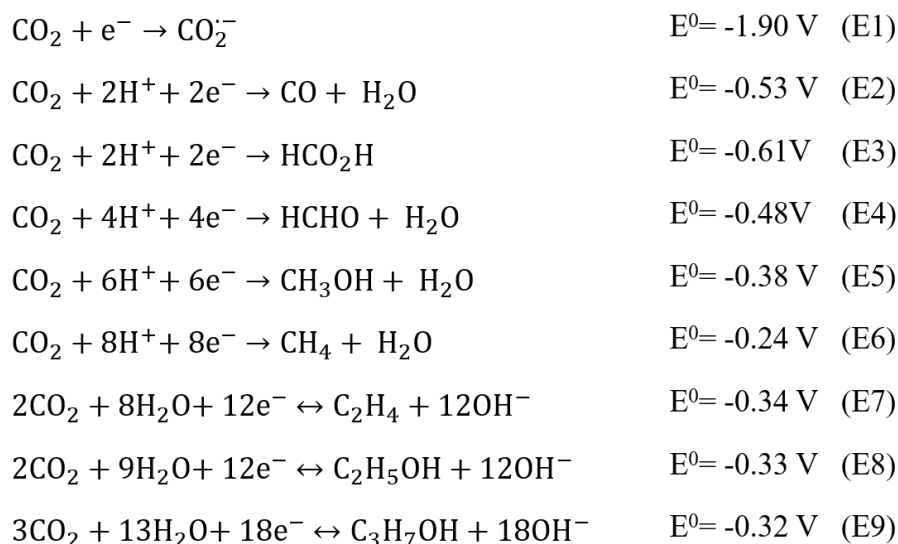


Figure 1.2 (a) Energy balance for CO<sub>2</sub>RR with medium-energy reactants to high-energy products in endothermic process powered by extra energy [11]. (b) The electrode potentials for numerous electrochemical CO<sub>2</sub>RR half-reactions (E1 ~ E6, pH 7 in aqueous solution versus NHE, 25 °C, 1 atmosphere gas pressure, and 1 M for the other solutes [13]; E7 ~ E9 were in aqueous media at pH 7, atmospheric pressure and 25 °C [6].

Powered by renewable electricity and using water as proton source, electrochemical CO<sub>2</sub>RR is capable to yield various value-added products such as carbon monoxide (CO) [14,15], formic acid (HCOOH) [16–18], methane (CH<sub>4</sub>) [19,20], methanol (CH<sub>3</sub>OH) [21,22], ethanol (CH<sub>3</sub>CH<sub>2</sub>OH) [23,24], ethylene (C<sub>2</sub>H<sub>4</sub>) [25], acetone ((CH<sub>3</sub>)<sub>2</sub>CO) [26], etc. [5]. So far,



electrochemical CO<sub>2</sub>RR still faces several relevant challenges due to necessity of a large amount of electricity because of the high overpotential, unclear reaction mechanism, instability of catalysts and competing hydrogen evolution reaction (HER), which affects the overall current efficiency reached.

Alternatively, solar or ultraviolet (UV) energy powered catalytic materials such as semiconductor materials photo-generate charge carriers to drive reduction reactions under light illumination. Therefore, light irradiation has been introduced to electrochemical CO<sub>2</sub>RR to facilitate catalyzing reduction reactions, leading to the concept of photoelectrochemical (PEC) CO<sub>2</sub>RR. PEC CO<sub>2</sub>RR combines the photocatalysis and electrochemical catalysis hence compensates the drawbacks present on both and possesses outstanding advantages: lowering the overpotential thus save electricity; promoting the separation of photogenerated electrons and positive holes thus suppressing their recombination; increasing the low efficiency of visible light absorption and quantum efficiency [3,27–29]. In 1972, Fujishima and Honda proposed for the first time the electrochemical photolysis of water on n-type semiconductor materials TiO<sub>2</sub> [30], and after that, Halman *et al.* firstly reported photoelectrochemical CO<sub>2</sub>RR on p-type GaP in buffer solution to yield HCOOH, HCHO, CH<sub>3</sub>OH [31]. Since then, photoelectrochemical CO<sub>2</sub>RR has been expanded by trying to improve solar light absorption and producing fuel molecules.

PEC cells require the semiconductor electrode to be connected to a counter electrode in an external circuit. Conventional, PEC CO<sub>2</sub>RR system is shown in Figure 1.3 [32] presents two-chambers separated by a conducting membrane where anode and an illuminated photocathode are connected. For instance, Figure 1.4a shows a PEC CO<sub>2</sub>RR system which adopted a p-type semiconductor material such as Co<sub>3</sub>O<sub>4</sub> nanotubes decorated with Cu nanoparticles as photocathode to reduce CO<sub>2</sub> and generate formate with high yield and selectivity of nearly 100% [33]. The photogenerated electrons of the semiconductor can reduce CO<sub>2</sub> at the interface between the electrolyte and the semiconductor surface [29]. Figure 1.4b shows an alternative PEC system where both electrodes are semiconductors.

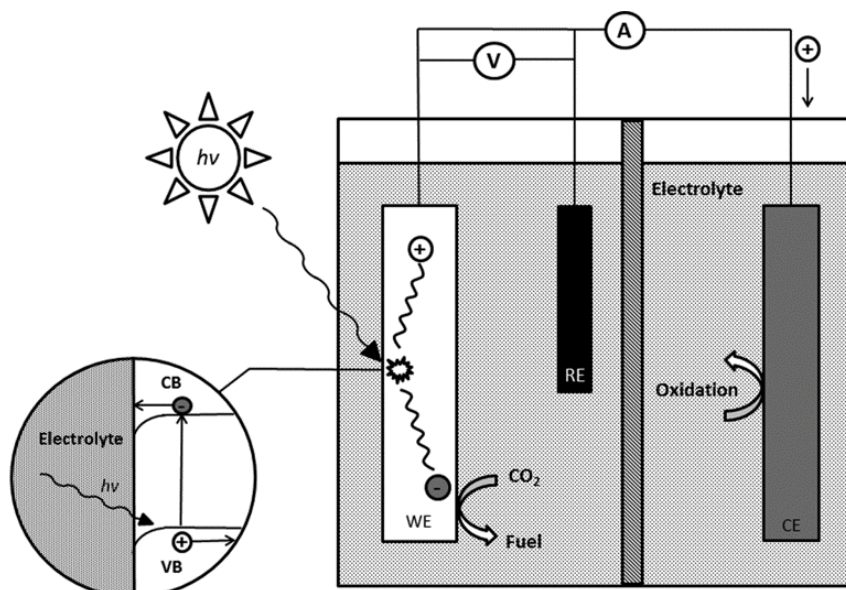


Figure 1.3 Photoelectrochemical cell under illumination, with a p-type SC working electrode immersed in an electrolyte containing  $\text{CO}_2$ . (Inset) Bent SC bands at the electrolyte interface and the separation of the photogenerated electron and hole [32].

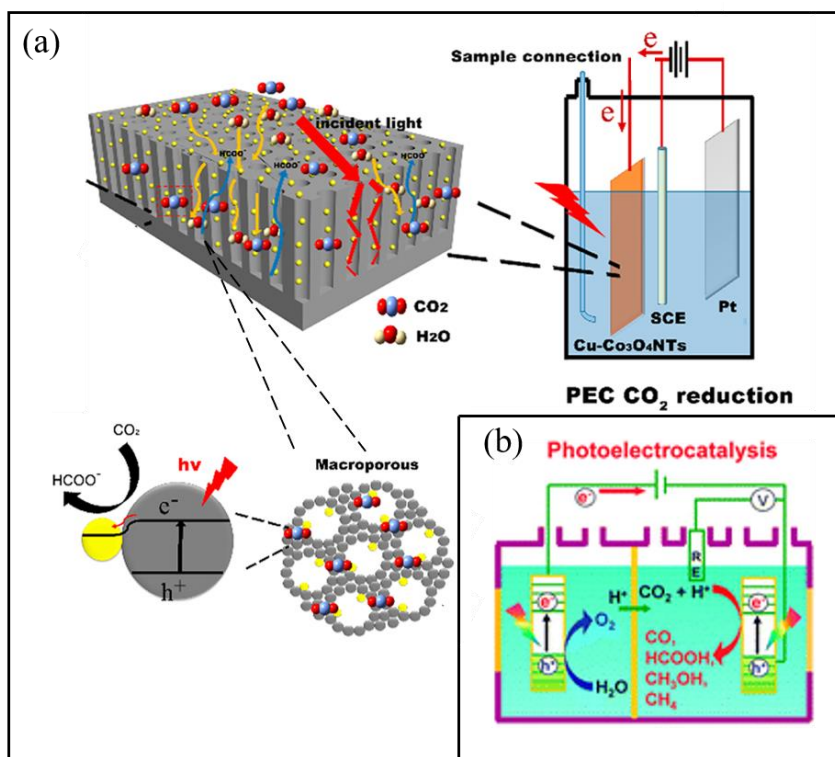


Figure 1.4 Schematic illustrations of (a) mechanism of PEC  $\text{CO}_2\text{RR}$  on photocathodes  $\text{Cu-Co}_3\text{O}_4$  nanotubes. Adapted from ref [33] and (b) two-compartment PEC  $\text{CO}_2\text{RR}$  cells separated by proton-exchange membrane using semiconductors as both photocathode and photoanode [29].

### 1.1.3. Relevant Factors and Present limitations on Electrochemical and Photoelectrochemical CO<sub>2</sub>RR

Activity and/or the products selectivity of electrochemical and (photo)electrochemical CO<sub>2</sub>RR are controlled by experimental parameters such as the electrolyte composition, the nature of the catalytic and cocatalytic materials, the electrolysis cell configuration, the local pH, the applied potential, the CO<sub>2</sub> solubility, the pressure and the temperature, etc. Either the impact of one element or their combination deserves deep investigation and understanding, although many systematic work has already put some effort on this [28,34–36].

#### 1.1.3.1. *Electrolyte*

For instance, the protonation of the absorbed CO intermediate to form absorbed CHO is the key step in the generation of hydrocarbons (CH<sub>4</sub> and C<sub>2</sub>H<sub>4</sub>) [37]. Hence, aqueous solution or water-containing solution are attractive electrolytes to generate hydrocarbons by providing a proton source. Typically, electrochemical CO<sub>2</sub>RR mainly takes place in neutral or moderately acid or basic solutions such as Na<sub>2</sub>SO<sub>4</sub>, NaHCO<sub>3</sub>/KHCO<sub>3</sub> or phosphate buffers. Moreover, 0.1 ~ 0.5 M bicarbonate solution is the most common electrolyte, which forms a buffer solution after saturation with CO<sub>2</sub> (pH ≈ 7). In addition to this, bicarbonate is cheap and environmentally friendly, making it the electrolyte of choice in most electrochemical CO<sub>2</sub>RR studies [34].

However, the HER occurs at the similar thermodynamic potentials than CO<sub>2</sub>RR in aqueous solution, which provokes the competition between both reactions. In addition, CO<sub>2</sub> mass transfer is limited in aqueous solutions by the CO<sub>2</sub> solubility (33 mM at 25 °C). For this reason, nonaqueous solvents such as acetonitrile (AN), dimethyl sulfoxide (DMSO), dimethyl formamide (DMF) and room temperature ionic liquids (RTILs) obtained popularity because of their high CO<sub>2</sub> solubility, products selectivity, HER suppression and even lowering the reaction overpotential [38]. The utilization of RTILs will be introduced in detail in chapter 1.3.

#### 1.1.3.2. *Electrode materials*

The key and core element controlling CO<sub>2</sub> reduction performance is the electrochemical catalytic material, which defines the overall activity, efficiency and the selectivity of CO<sub>2</sub>RR. Thus, the exploration and investigation of practical (photo)electrochemical CO<sub>2</sub>RR catalytic materials are urgent. Several criteria for evaluating the performance of an electrochemical catalysts have been already defined in the literature, they include following figures of merit [3]:

(1) Faradaic efficiency (FE): Equation 1-1

$$\mathcal{E}_{Faradaic} = \frac{z \cdot n \cdot F}{Q} \quad 1-1$$

Where  $z$  is the number of electrons exchanged,  $n$  is the number of moles of a particular product,  $F$  is Faraday constant ( $F = 96485 \text{ C/mol}$ ) and  $Q$  is the charge circulated (C) [7].

(2) Overpotential = (applied potential at a given current density) – (thermodynamic potential of the reaction).

(3) catalytic selectivity = moles of intended products / (moles  $\text{H}_2$  + moles other products).

(4) Turnover number (TON) = moles of intended products/moles of catalyst.

(5) Turnover frequency = catalytic turnovers per unit time.

The catalytic materials should be stable, highly catalytic, capable of absorbing light, etc.. So far, numerous efficient catalysts have been reported and developed for (photo)electrochemical  $\text{CO}_2\text{RR}$  [34,39].

As Figure 1.5 shown, the majority of the catalysts are classified in 3 groups: metallic, non-metallic and molecular catalysts [34]. Firstly, polycrystalline monometallic catalysts have been widely studied because of their high catalytic activity and simple structure. Cu is most likely the unique metal for the generation of multicarbon products including hydrocarbons and alcohols [40,41]; Au, Ag, Zn mainly selective to CO [42–44], and Pb In Sn Bi to formate or formic acid [45–47]. Besides monometallic catalysts, ion-modified metallic and bimetallic catalysts such as oxide-derived metallic catalysts are popular because they present better long-term stability and keep less-changeable selectivity [48]. Nanostructured (nanopores, nanoparticles and nanotubes) metallic catalysts possess the advantages of high catalytic surface area and numerous edges or low-coordinated sites, which can dramatically enhance the catalytic performance. Non-metallic and molecular catalysts and some semiconductor materials such as  $\text{TiO}_2$ ,  $\text{ZnO}$ ,  $\text{CaS}$ ,  $\text{GaP}$ ,  $\text{SiC}$  and  $\text{WO}_3$  [49] have also been widely investigated and shown promising and potential in the (photo)electrochemical  $\text{CO}_2\text{RR}$ . In this thesis, transition metal–N doped–carbon and metal oxide semiconductor materials will be introduced in chapter 1.4. Overall, despite the development of a large amount of different catalysts, it is far from satisfying the industrial demand or specific task. Ideal electrochemical catalysts with

high efficiency and selectivity, low overpotential, high stability and cost-effective abundance are the final goal of electrochemical CO<sub>2</sub>RR and it is still an open challenge.

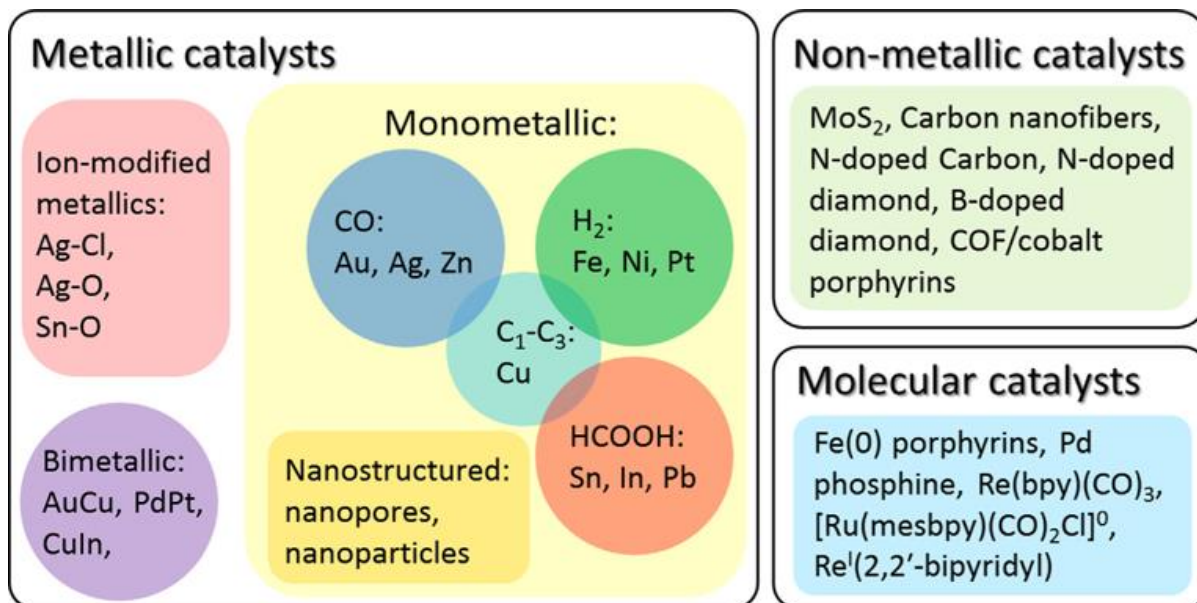


Figure 1.5 An outline of three major categories of electrocatalysts for CO<sub>2</sub> reduction [34].

The cocatalysts in PEC systems can be classified into two main categories: *i*) nanoparticles of metals or oxides deposited on the surface of semiconductor photoelectrodes and *ii*) dissolved species present in the electrolyte [32]. The modification of semiconductor surfaces with molecular catalysts or metals has long been a technique employed to increase catalytic activity and stability. For this reason, an original study about the role of imidazolium based RTILs as dissolved cocatalytic species in solution for CO<sub>2</sub>RR is presented in this thesis.

The concept of artificial photosynthesis is employed when the PEC system converts light energy to stored chemical energy. But if the potential applied in PEC systems is more negative than the thermodynamic CO<sub>2</sub> reduction potential, the system does not convert light energy to stored chemical energy. Thus, in some cases, light energy can be used in such a way as to allow the reduction of CO<sub>2</sub> to proceed at applied electric potentials more positive than the formal redox potential. One of the few examples of underpotential CO<sub>2</sub> reduction has been reported using p-GaP photoelectrodes [50]. In this case, the Faradaic efficiency is almost 100% for producing methanol at underpotentials as high as 320 mV thanks to the presence of a small concentration of pyridine in solution. In particular, it is a PEC system containing a soluble pyridinium (10 mM) component in 0.5 M KCl aqueous solution, pH = 5.2. The authors proved

that the photocurrent drop off drastically in the absence of pyridinium. The mechanistic study proposed an amine mediated catalytic reduction of  $\text{CO}_2$  pathway, where  $\text{CO}_2$  in solution reacts to reversibly form an electroactive carbamate by coupling  $\text{CO}_2$  and pyridinium, which undergoes further reduction and produces  $\text{CO}_2$  reduction products at lower potential than the thermodynamic potential for  $\text{CO}_2\text{RR}$  on the electrode surface.

### 1.1.3.3. Electrolysis Cell Configuration

The design of the (photo)electrochemical reduction cell configuration governs the mass transfer regime thus requires to consider many factors such as the morphology and geometry of electrode materials, the mixing and mass transport of the electrolyte, solubility of  $\text{CO}_2$ , light source power, heat exchange and products detection, etc. [22,36].

As mentioned above, two-compartment configuration can avoid the reoxidation of the reduced products and convenient to operate hence popular in the experimental design. Figure 1.6a exhibits a typical H-type PEC configuration of  $\text{CO}_2\text{RR}$  [36]. The anode and the cathode are separated by ion exchange membrane (such as proton exchange membrane or anion exchange membrane). At the anode, water splitting takes place to form  $\text{O}_2$  whereas photoelectrochemical  $\text{CO}_2\text{RR}$  happens at the cathode with the photogenerated electrons. In this configuration,  $\text{CO}_2$  is dissolved in the electrolyte and transports to the catalysts surface subsequently reduced, yet the drawbacks are the limited  $\text{CO}_2$  solubility and the mobility.

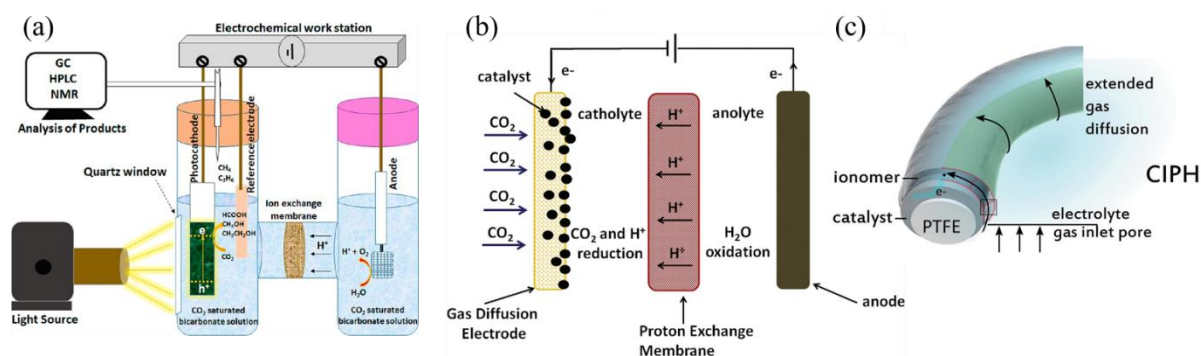


Figure 1.6 (a) Schematic representation of an H-type PEC  $\text{CO}_2\text{RR}$  into value-added products [36]; (b) Electrochemical  $\text{CO}_2\text{RR}$  system with gas diffusion electrode under flow conditions for electrochemical  $\text{CO}_2\text{RR}$  [28]; (c) Schematic representation of metal catalyst deposited onto a polytetrafluoroethylene (PTFE) hydrophobic fiber support. A flat ionomer layer conformally coats the metal [51].

Alternatively, gas diffusion electrodes (GDE) configuration together with membrane electrode assembly have been used to speed the CO<sub>2</sub> transport rate and lowering ohmic drop in the electrolyte [28]. Figure 1.6b shows a setup adopted GDE for electrochemical CO<sub>2</sub>RR. The GDE consisted of catalysts deposited on a porous structure support. Instead of dissolving in the electrolyte, CO<sub>2</sub> was provided through the GDE then transports to the GDE/catalyst/electrolyte triple phase interface and reduced, dramatically improved the reactant feeding rate because of the gas-phase transportation.

Recently, an interesting catalyst was reported to electrochemical reduce CO<sub>2</sub> to ethylene with an industrial current density of 1.3 A cm<sup>-2</sup>, which is called ionomer bulk heterojunction (CIBH, and also ionomer planer heterojunction, CIPH) and can decouples gas, ion and electron transportation [51]. As shown in Figure 1.6c, the perfluorinated sulfonic acid (PFSA) ionomers possess hydrophobic and hydrophilic groups hence can separate the species transportation pathways: gas transport through the hydrophobic groups and water and ions transport through hydrophilic domains. This creative function enabled the gas transport increasing to micrometer scale meanwhile maintaining the high electrocatalysis efficiency and current density, lighting up the direction for CO<sub>2</sub>RR from experimental scale to industrial application.

### ***1.1.3.4. Other Factors (Pressure, pH and Potential)***

The solubility of CO<sub>2</sub> in aqueous solution is very low, reaching 0.033 M at ambient temperature and pressure, which limits electrochemical CO<sub>2</sub> conversion because of the poor reactant feeding [52]. However, as the pressure increases, the CO<sub>2</sub> solubility will be increased according to Henry's Law [53]. Based on that, Kas *et al.* [54] studied the influence of CO<sub>2</sub> pressure on the products selectivity on Cu catalyst in 0.5 M KHCO<sub>3</sub>. Figure 1.7a shown the relationship of generated hydrocarbons with the CO<sub>2</sub> pressure, as the pressure increasing, the overall FE was raised and the same to the FE to ethylene (44%), while the generated methane decreased to 2%. The reason existed in that the formation of ethylene relied on CO dimerization, the increasing of CO<sub>2</sub> pressure leading to an increase of local CO concentration and surface coverage, which in turn promoted the ethylene selectivity.



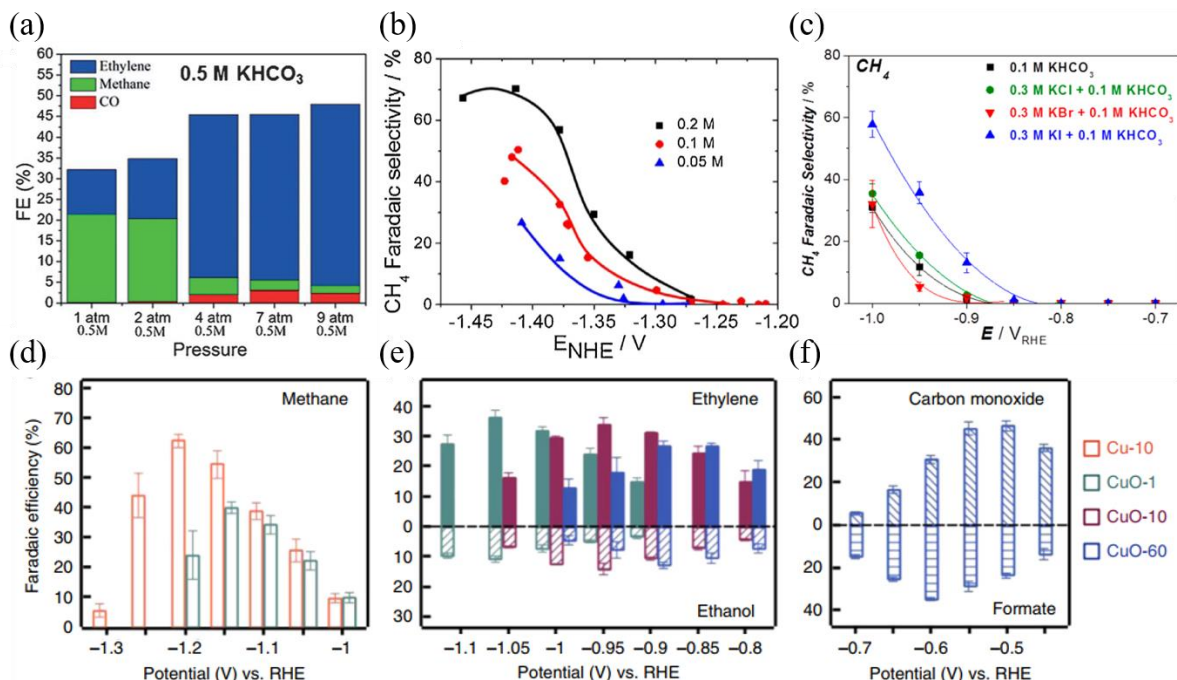


Figure 1.7 (a) Products distributions as a function of  $\text{CO}_2$  pressure [54]; (b) Absolute product formation rates of  $\text{CH}_4$  as a function of applied electrode potentials in  $\text{CO}_2$  saturated 0.05 M  $\text{KHCO}_3$  (blue), 0.1 M  $\text{KHCO}_3$  (red) 0.2 M  $\text{KHCO}_3$  (black) [55]; (c) Stationary Faradaic selectivity of  $\text{CH}_4$  of the  $\text{CO}_2\text{RR}$  as a function of electrode potentials after 10 min of bulk  $\text{CO}_2$  electrolysis at a constant potential, in  $\text{CO}_2$  saturated 0.1 M  $\text{KHCO}_3$  (black) and 0.3 M  $\text{KX}$  ( $\text{X}$  means halides) [56]; (d)(e)(f) Faradaic efficiency of methane, ethylene and ethanol, carbon monoxide and formate on different catalysts at different potentials, respectively. Different catalysts Cu-10, CuO-1, CuO-10, and CuO-60 are Cu-based catalysts electrodeposited for 1 min, 10 min, and 60 min, respectively, which are shown in color of orange, green, red and blue, respectively. Error bars in (d)-(f) represent the standard deviations of three independent measurements [35].

In addition, different local pH can have an effect on controlling the products selectivity of electrochemical  $\text{CO}_2\text{RR}$  [55]. Figure 1.7b exhibited  $\text{CH}_4$  Faradaic selectivity differed along with the different concentration of the  $\text{KHCO}_3$  buffer solution, which was caused by the local interfacial pH changing. The concentrated  $\text{KHCO}_3$  possessed high buffer capacity thus suppressed local pH changing, which is favor of  $\text{CH}_4$  formation since it relied on coupled electron/proton transfer. In contrast, diluted  $\text{KHCO}_3$  with low buffer capacity decreased  $\text{CH}_4$  formation owing to a low proton concentration.

Furthermore, the addition of halides can tune the activity and selectivity in electrochemical  $\text{CO}_2\text{RR}$  on Cu. It is demonstrated that  $\text{Cl}^-$  and  $\text{Br}^-$  increased CO and  $\text{I}^-$  promoted methane



formation (Figure 1.7c) because the adsorption of halides led to negative charge on the reaction surface [56].

Besides, the control of the applied potential is crucial to tailor the selectivity of CO<sub>2</sub>RR. Figure 1.7d, e and f shown that as the potential changing from -0.45 V to -1.3 V vs. RHE, the products selectivity successively tuned towards CO and formate, ethylene and ethanol and finally methane. The different products are related to the different energy barriers in the CO<sub>2</sub>RR process. For instance, a slightly rough metallic Cu surface (Cu-10) produces preferentially CH<sub>4</sub>, whereas OD-Cu surfaces (CuO-1, CuO-10 and CuO-60) produce more C<sub>2</sub>H<sub>4</sub> and C<sub>2</sub>H<sub>5</sub>OH [35].

In addition to this, light source, catalysts properties and surface structure, electrolyte effects (buffer strength, ion effects) and mass transport conditions were also studied by their influence on the performance of electrochemical CO<sub>2</sub>RR [57].

Although electrochemical and PEC CO<sub>2</sub>RR catalysts have been extensively explored and evaluated, the present limitations are large indeed because many vital processes are not very clear and desire more efforts. Every factor involved in the catalysis needs to be considered and optimized for synergetic working on converting CO<sub>2</sub> to value-added chemicals or fuel products. Take the metallic catalysts as example, the most challengeable thermodynamic step is CO<sub>2</sub> binding to the metal center whereas the kinetic step belongs to C–O bond breaking in the metal–CO<sub>2</sub> complex [3]. Finding abundant, cheap metals which can meantime satisfy these thermodynamic and kinetic determining steps is indispensable. In addition to this, catalysts capable of lowering the overpotential and improving the current density and maintaining the long-term stability to scale up in the industrial application is imperative. Besides, for the PEC CO<sub>2</sub>RR system, increasing the light harvesting efficiency and the separation of photogenerated electron-hole pairs should be paid more attention [29].

## **1.2. Scanning Electrochemical Microscopy (SECM) and Scanning Photoelectrochemical Microscopy (SPECM)**

### **1.2.1. Introduction**

Scanning Electrochemical Microscopy (SECM, the same abbreviation name for the instrument) is an electroanalytical scanning probe technique which was first introduced and developed by the Bard [58] and Engstrom [59] groups in 1980s. Bard developed the SECM based on the use of the tip and the piezoelectric element for positioning the tip in scanning

tunneling microscopy (STM) but enlarged the measurements spacings to implement in-situ electrochemical detection of the interest surface, including its topography and electrochemical information [58,60]. So far, thousands of papers related to SECM on the research of its instruments and methodology have been published for the application in variety of fields including chemistry, energy, kinetics, biology, corrosion [61–63].

The basic principle of SECM is that it employs an ultramicroelectrode (UME, “tip”) to scan in the vicinity of the surface of the substrate which immersed in the solution and to probe and collect the information from the tip and the substrate. The unique advantage of SECM of its ability to probe the diffusion layer of the substrate surface with high special resolution makes it powerful and useful in many applications.

Moreover, SECM has been combined with other techniques or energy to extend and complement its applications. For example, the combination of SECM to atomic force microscope (AFM) can benefit from ① the AFM tip for a high-resolution topographical imaging and the controlling of the desired tip-substrate distance, ② the SECM tip to investigate and obtain electrochemical activities [64,65]. Furthermore, Shear-force positioning SECM fulfills the simultaneous electrochemical-topographical imaging by a laterally vibrated probe [66]; Scanning ion conductance microscope (SICM) and SECM coupling can improve the sensitivity of the measured current to the tip-surface separation via nanopipette [65,67].

In addition, the integration of the SECM and illumination system such as a Xenon lamp generated the concept of scanning photoelectrochemical microscopy (SPECM) available for the study of photocatalysts. Bard *et al.* firstly employed SECM and replace the UME with an optical fiber connected to Xenon lamp for rapid screening bimetallic and trimetallic photocatalyst [68,69]. So far, SPECM has been booming in many applications [70].

This chapter introduces the techniques, instruments, operation modes and methodologies of SECM and SPECM, and summarizes their recent and advanced applications in electrochemistry.

### 1.2.2. Experimental Device of SECM

Figure 1.8 shows (a) the picture and (b) the schematic representation of a commercial SECM instrument. It consists of five components: ① An UME tip (or probe) with a micrometer or nanometer surface can induce or collect the reactions in the solution, it also

scans and probes the interest substrate surface. Here the substrate can be a solid surface (glass, metal, polymer) or a liquid surface (mercury immiscible oil) [60]. ② A bipotentiostat is used to independently apply and collect the currents and potentials on the tip and/or the substrate in the 4-electrode system (or 3-electrode system). ③ A 3-dimensional position controller controls the tip to move in X-Y-Z directions and to scan the substrate in the X-Y plane, this position controller system includes a stepper motor and a piezo motor for coarse and fine movement, respectively. ④ The electrochemical cell shown in Figure 1.8c contains 4 electrodes: working electrode 1 (WE1, tip); working electrode 2 (WE2, substrate, sometimes not biased), which is fixed in the bottom of the cell and immersed in the solution; reference electrode (RE) to provide a stable potential to regulate the WE; counter (or auxiliary) electrode (CE) to complete the circuit and allow a current flow. ⑤ A data acquisition is adapted to coordinate each part and also to collect, analyze and process the information to data. Some applications may demand other component addition base on conventional SECM such as an optical microscope for biological observation and a light power for photoelectrochemical catalysis.

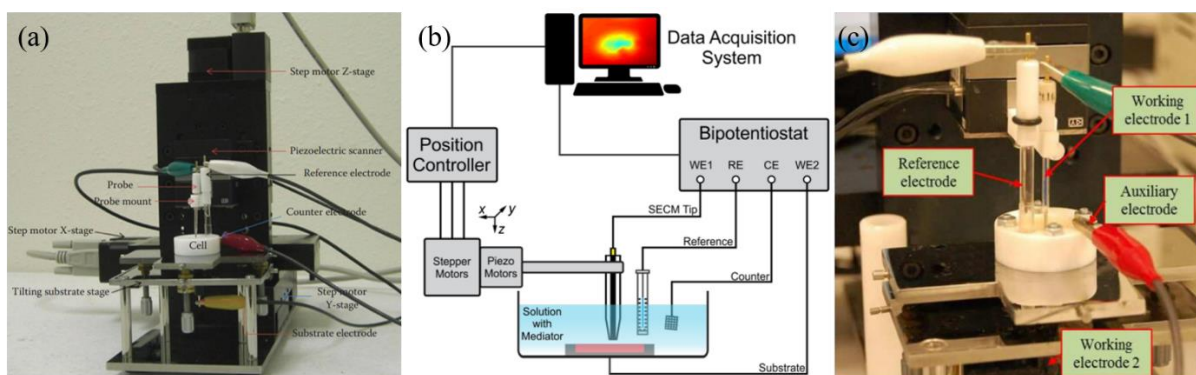


Figure 1.8 (a) Illustration of the commercial CH Instruments model 920C [60]; (b) Schematic representation of a SECM instrument [61]; (c) Picture of the overview of the whole electrochemical cell of CH Instruments 920D [71].

### 1.2.3. Ultramicroelectrode (UME)

The most important part in the SECM equipment is the ultramicroelectrode, with the dimension from a few nanometers to 25  $\mu\text{m}$  (radius). Its size and shape define the lateral spatial resolution of the SECM experiment together with the resolution of the position controller and/or the tip-to-substrate distance [60,62]. There are various shapes and dimensions of UME

specific to different applications such as microdisk UME [73], conical UME [74], ring/ring-disk UME [75], spherical/hemispherical UME [76] and some others [77,78]. One of the most common used UMEs in SECM is the microdisk UME, which is the only focus and introduced in detail in this chapter.

Figure 1.9 shows a typical disk UME composed by the metal wire in the middle and the surrounding insulating sheath. The preparation procedures of a disk UME have been reported in detail [60,62,79] and will be introduced concisely here. Firstly, a Pt/Au wire (of  $\mu\text{m}$ ) is put in the end of a capillary glass with one end sealed and the other connected to a vacuum pump, the capillary is fixed perpendicularly inside the helix Ni-Cr coil whose temperature is increased for melting the capillary until the wire is sealed. Secondly, a Cu wire is inserted and electrically connect with the metal wire by silver paint in the capillary, the open end is sealed with epoxy for strain relief of the wire. Finally, the sealed end is polished by sandpaper to expose the cross section of the metal wire, which is then polished by ( $0.3 \sim 0.05 \mu\text{m}$ ) alumina slurry for a mirror surface. (Figure 1.9a) for a reliable and reproducible data in the experiment. The glass sheath around is sharpened to a conical shape (Figure 1.9b) until the radius of the metal ( $a$ ) is 10 times less than that of the disk ( $r_g$ ) ( $RG = r_g/a \leq 10$ ). The prepared disk UME can be used for approaching curve and SECM imaging. Unlike the current in the STM which origins from the electron tunneling in a tunneling distance (less than 1 nm) of the tip and the conductive substrate, the current in SECM comes from the electrochemical reactions of the sample and flows by the dissolved active species between the UME and the sample, making the possibility of a larger tip-to-substrate distance (up to several  $\mu\text{m}$ ) so that expanding the applications of SECM [80].

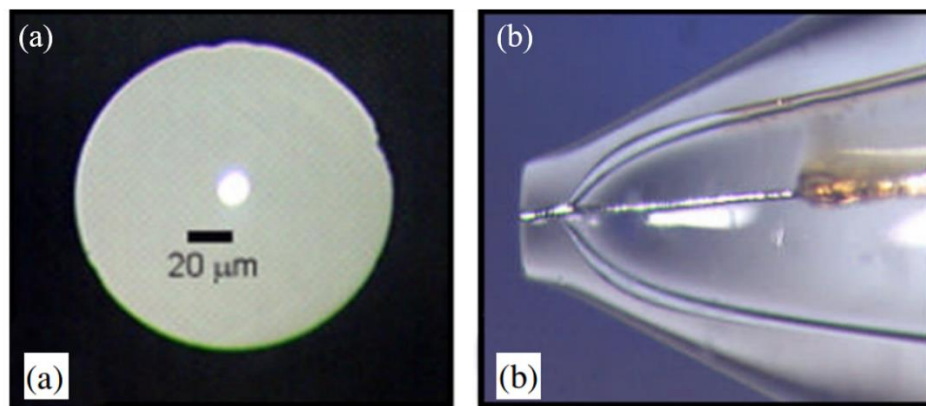


Figure 1.9 Optical microscope images of a normal disc UME: (a) top view, (b) side view [72].

Moreover, the mass transfer within the diffusion layer (the electrolyte region in the vicinity of WE in which the redox species diffuse) occurs by semi-infinite linear diffusion at a normal macroelectrode (Figure 1.10a, inset). The type of the diffusion changes as the electrode size and shape changes. In UME, as the size decreased, mass transfer happens by hemispherical diffusion including axial and radial diffusion (Figure 1.10b, inset), which increases the rate of mass transport and reaches the steady-state fast [60,81]. Furthermore, the steady-state diffusion limiting current density is much larger than that in a macroelectrode if under the convection so that the tip movement has negligible contribute to the Faradaic current (the current generated by the reduction or oxidation of some chemical substance at an electrode) [80]. The different behavior between the UME and macroelectrode are shown on the cyclic voltammograms (CV): the rapid depletion of the reactive species in the macroelectrode surface causes a peak-shaped CV response (Figure 1.10a), whereas with an UME, the rate of mass transfer is high to compensate to a certain extend the depletion of the species reacted on the surface, the current is finally controlled by the mass transfer and reaching a steady-state current response in a short time, shown S-shape plot in CV (Figure 1.10b). The steady-state diffusion current of disk UME tip ( $i_{T,\infty}$ ) is given by (Equation 1-2):

$$i_{T,\infty} = 4nFDca \quad 1-2$$

In the equation,  $n$  is the electron number transferred in the redox reactions;  $F$  is the Faraday constant (96485 C/mol);  $D$  is the diffusion coefficient of the mediator ( $\text{cm}^2/\text{s}$ ),  $c$  is the bulk concentration of the reactant ( $\text{mol}/\text{cm}^3$ ),  $a$  is the radius of the active part of the UME (cm).

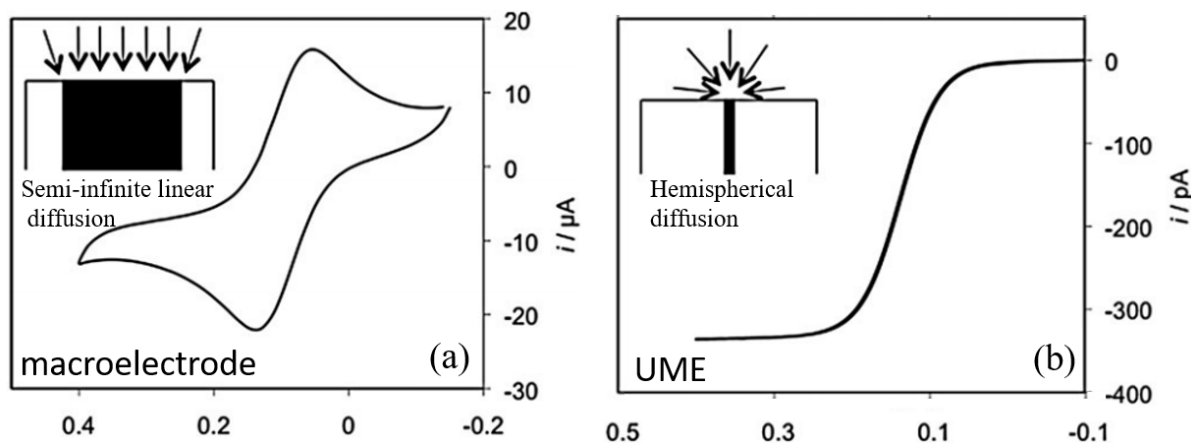


Figure 1.10 Typical cyclic voltammograms of (a) macroelectrode (Pt disk, 2 mm diameter) and (b) UME (Pt disk, 1.3 mm diameter) in 1 mM ferrocenemethanol + 0.1 M KCl. RE: Ag/AgCl and CE: Pt were used in each case and the scan rates were (a) 100 mV/s and (b) 5 mV/s. The insets in each figure

*show the predominant mode of mass transfer to the electrode surface: (a) Semi-infinite linear diffusion to a macroelectrode; (b) Hemispherical diffusion to an UME. Adapted from ref [81].*

Overall, given the properties and the principles of disk UME previously mentioned, it shows several advantages. Because of the small size, the current obtained is small (pA to nA), which lowers the Ohmic drop ( $IR$ ) in the solution so that it can be used in solutions with low supporting electrolyte concentration (or no supporting electrolyte); moreover, with the high spatial resolution, it can probe the information in small volumes; the rapid charging current decreases the time constant ( $RC$ ) for the possibility of studying transient electrochemistry. As the popularity of UME, it has been developed and improved by miniaturization and combination with other instruments for widespread applications [82]. So far, the size of the UME reaches a few nanometers [83,84], and multiple and functional UMEs such as Au ring optical fiber electrode [85], and dual optical fiber-UME [86], cavity-microelectrode [87], shear force-SECM nano-disk [88] have been used making the UME and SECM more and more important in many fields.

### 1.2.4. The Operation Modes of SECM

SECM has been developed many operation modes for desired applications, including *feedback mode, generation/collection mode, redox competition mode, direct mode, potentiometric mode, penetration mode, equilibrium perturbation mode, ion transfer feedback mode, constant high mode etc.* The instruction is restricted to the most common used operation modes in electrochemistry: Feedback mode (FB), generation/collection mode (Tip Generation-Substrate Collection mode (TG/SC) and Substrate Generation-Tip Collection mode (SG/TC)), redox competition mode and constant high mode. To illustrate the principle of each mode, “ $R$ ” is adopted to represent the reduced form of the initially added redox mediator (electroactive species) in the solution.

#### 1.2.4.1. Feedback mode (FB)

Feedback mode is the most common mode because of its versatility, it has been widely used in the research of electron transfer kinetics [89,90]. The principle is shown in Figure 1.11.  $R$  is reduced to  $O$  (the oxidized form of the mediator) according to the reaction (Equation 1-3) on the biased tip which is far from the substrate ( $\geq 5$  tip diameters), the mass transfer belongs to hemispherical diffusion and the measured current is  $i_{T,\infty}$  (Figure 1.11a).

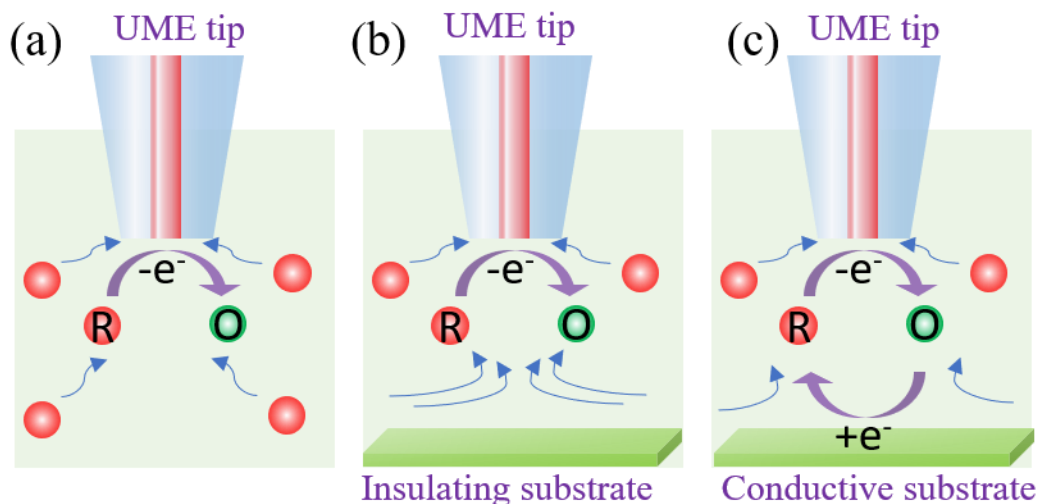


Figure 1.11 Schematic representation of SECM operational modes: (a) Steady-state diffusion when the tip is far from the substrate in bulk solution, (b) negative feedback over an insulating substrate, (c) positive feedback over a conductive substrate.

As the tip approaches near to an insulating substrate (glass or plastic), the diffusion of R is hindered by the substrate resulting decreased concentration and  $i_T$  ( $i_T < i_{T,\infty}$ ), the closer the tip to substrate, the smaller of  $i_T$  until zero, which is called *negative feedback mode* as shown in Figure 1.11b.



In contrast, if the tip probes a conductive substrate (Fluorine-doped tin oxide (FTO), Indium tin oxide (ITO), and metal surface), although the blockage still exists, O diffused to the substrate and is reduced to R in turn causing an increased flux of R and a contribution to  $i_T$  ( $i_T > i_{T,\infty}$ ). This is referred to *positive feedback mode* (Figure 1.11c). The value of  $i_T$  will be very large as the tip to substrate distance ( $d$ ) decreased. The plot of  $i_T$  vs.  $d$  is called *approach curve* [60]. Figure 1.12 shows the approach curve of positive feedback (a) and negative feedback (b). Thereinto, the dimensionless  $I_T = i_T/i_{T,\infty}$  and  $L = d/a$  are normalized to eliminate the effect of concentration and diffusion coefficient. The recording of the approach curve helps to study the real tip-substrate distance and the property of the substrate [60]. Feedback mode provides possibilities to study kinetics on various substrate.

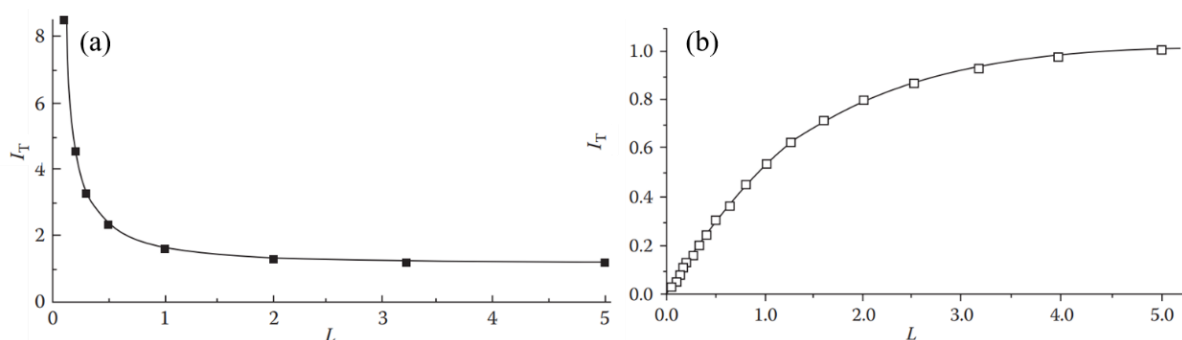


Figure 1.12 Steady-state diffusion tip current as a function of tip-substrate distance: (a) positive feedback mode, (b) negative feedback mode [60].

#### 1.2.4.2. Generation/Collection mode (GC)

Generation/collection mode is another favorable SECM operation mode [60]. The tip is biased at a suitable potential at which R can be reduced to O which will be oxidized back to R or other products on the biased substrate (collected), this is the *Tip Generation-Substrate Collection mode* (Figure 1.13a). While the origin of the reduction reaction starts on the substrate where R transfers to O (Equation 1-3) whereas the O diffuses to the tip and forms R at suitable potential, which is called *Substrate Generation-Tip Collection mode* (Figure 1.13b). In the GC mode, the currents and potentials are measured both on the tip and the substrate. Compared to FB mode, the biggest difference of GC mode is that it doesn't need an original concentration of the reactants and the products instead it produces the mediator on the tip or substrate for further reactions. Moreover, it needs a good controlling of the tip-substrate distance, that's why it always firstly combines FB mode to position the tip and control  $d$  with another mediator (like ferrocenemethanol) different with that of the GC mode.

In the TG-SC mode, the tip current is controlled as a constant flux of reactants [62]. The collection efficiency is defined by  $i_S/i_T$  ( $i_S$  is the substrate current), as the products O generated on the tip and diffused to the substrate reaching a high collection efficiency (CE,  $> 0.99$ ) when  $d$  is small ( $L \leq 2$ ) [91]. TG/SC is widely used as a high throughput methodology in the research of rapid screening electrocatalysts and quantify reaction intermediators such as the oxygen reduction reaction (ORR) [92] and formic acid oxidation [93].

SG-TC mode is more applicable than TG-SC mode because it is not confined in a thin diffusion layer between the tip and substrate rather than a thicker diffusion layer the because of the big size of the substrate. The collection efficiency ( $i_T/i_S$ ) is related to  $a$ ,  $d$ , and  $r_s$ , which



can be quantified and calibrated by a simulation method [94]. It can be applicable in the detection of ORR at various electrodes [95,96] and electrochemical CO<sub>2</sub>RR [97]. The drawbacks of SG-TC mode, the background current is relatively big because of the large substrate, making the difficulty of O to be collected by the tip and the low CE.

However, some neural species cannot be generated electrochemically on the tip by TG-SC mode such as formic acid and methanol. Then a suitable modification of the TG-SC tip to a micropipet for delivering these species to the substrate has been invented and developed to study the ion / electron transfer across liquid/liquid interfaces, which is called *Micropipet Delivery-Substrate Collection mode* (MD-SC) [98–100]. The pipet is full of immiscible solvent with outside containing the interest species, which can be used for electron/ion transfer across liquid/liquid surface, on the other side, it can be also filled with the same solvent inside and outside for the application of SICM.

### 1.2.4.3. *Redox competition mode (RC)*

The *redox competition mode (RC)* was first introduced by Schuhmann's group to study the catalytic activities of the metal catalysts on the substrate for ORR simultaneously decreasing the big background current from the large substrate [101]. The principle is shown in Figure 1.13c: both the tip and the substrate are applied a potential at which R can be reduced. Once R is reduced at the tip, its following diffusion to the substrate with an inactive part will be blocked (like the negative feedback mode). On the contrary, if R diffuses to an active catalysts spot on the biased substrate where it can be reduced, the concentration of R in the tip-substrate gap will decrease and induces a diminished tip current. Hence, the information of the catalysts on substrate can be visualized by the changes of the  $i_T$ , making the system independent of the size of the substrate. RC mode has been used to study the local degradation of the coated-metal [102], the bio-electrocatalytic activity in biofuel cell cathodes [103] and the reduction of H<sub>2</sub>O<sub>2</sub> by microstructure film [104] etc.

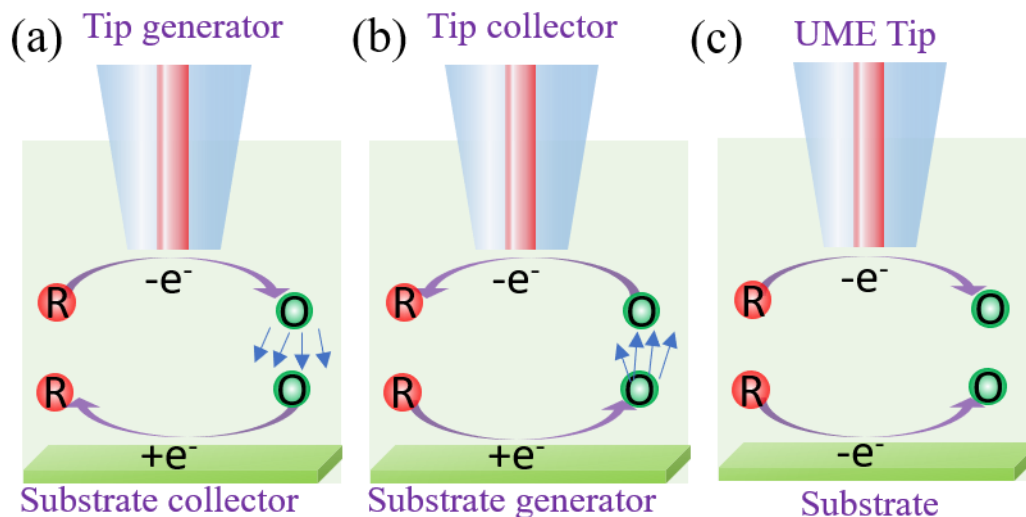


Figure 1.13 Schematic representation of the SECM operation modes: (a) Tip Generation-Substrate Collection (TG/SC) mode, (b) Substrate Generation-Tip collection (SG/TC) mode, (c) Redox competition mode.

Although SECM has many operation modes, in the practical, more than one mode is usually adopted and even other techniques are combined as mentioned previously for studying complicated systems.

### 1.2.5. Experimental Devices of SPECM

Since the combinatorial techniques was firstly reported by Maier's group for high-throughput screening photocatalysts (*i.e.* semiconducting oxide) under irradiation of visible light in 2001 [105], various researches have been implemented to develop advanced combinatorial equipment for high throughput screening efficiency photocatalytic materials. Among that, Lee *et al.* firstly combined SECM with optical fiber (OF) to locally illuminate and scan the photocatalytic activities of various metal oxides spots by measuring their photocurrent. This locally illumination overcomes the drawbacks of the mixed photocurrent and photodegradation because of the global illumination on the entire sample surface [106,107]. After that, SECM has been widely applied for photoelectrochemical catalysis in the abbreviation of SPECM [86,108–112]. In this part, various SPECM experimental configurations are introduced.

Figure 1.14a shows a schematic representation of SPECM instrument developed by Mullins *et al.* Each composition is resembled with SECM (Figure 1.8) except for the tip. In SPECM, the UME tip in the SECM is replaced with an optical fiber connected to a Xenon

lamp for introducing light to locally irradiate the biased substrate (WE). The OF can be controlled for movement and scan the various catalysts along X-Y plane on the WE. In Figure 1.14b, the SPECM tip involving an UME and an OF together acts as the WE, which can electrochemically probe the substrate information simultaneously providing locally illumination for photocatalysis during scans.

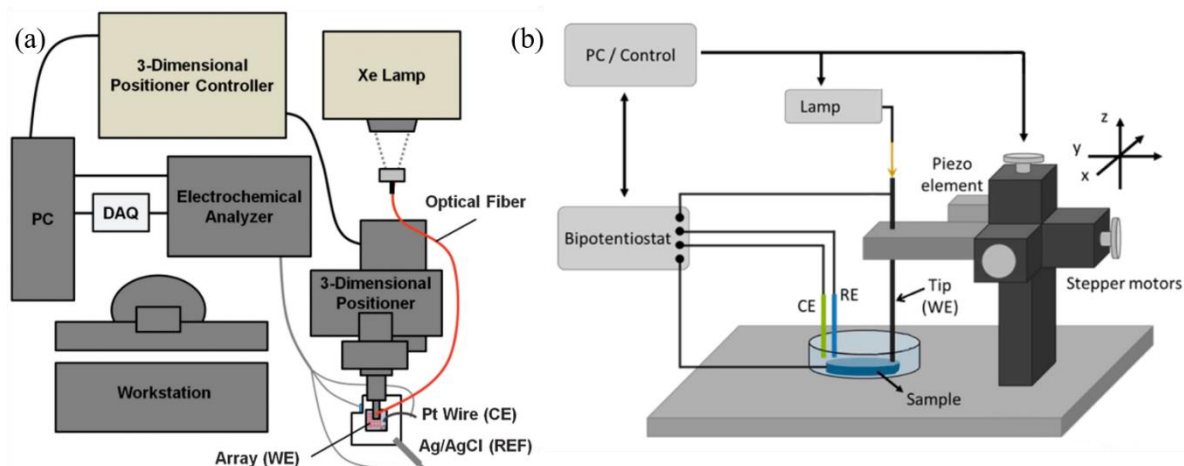


Figure 1.14 Schematic representation of SPECM instrument: (a) An optical fiber works as the tip [109]. (b) The tip is a combination of UME and optical fiber. Adapted from ref [108].

In the configuration of the electrochemical cell, the light introduction ways are of vital importance in the photoelectrochemical catalysis. Figure 1.15 shows a summary of four different illumination means illustrated by the mechanic of HER [113] following a corresponding reported application example in Figure 1.16. Figure 1.15a depicts a vertical UME combined with an incident light irradiate the entire substrate surface. This orientation benefits from the simple implementation and available of abundant protons yet confined by the shadow of the UME and the supersaturated products gas in the solution. The shadow problem can be solved by the back-illumination on a thin photocatalysts (Figure 1.15b) The representation of this configuration is shown in Figure 1.16a, the photocatalysts  $\text{TiO}_2$  is coated on the end face of a quartz fiber, its backside is illuminated and the front side photocatalyzes the  $\text{O}_2$  reduction reaction (SECM redox competition mode) [106]. However, the photo-generated carriers by backside illumination can recombine during the diffusion to the front surface which lowers the transformation efficiency. Alternatively, the arrangement of acute-angled combination of the UME and the light was developed. The light can be provided by a laser-beam (Figure 1.15c) [114] or a Xenon lamp (Figure 1.16b) [107]. This reduced the

shadowing affect and bring down the high background current from nearby irradiated area. The disadvantages are the concentrated carrier-injection and the numerous bubbles generated on the substrate. In addition, the conjunction of the UME and OF can form a powerful SPECM tip consisting an OF core coated with metal layer (ring UME) for photoelectrochemical catalysis (Figure 1.15d). An Au ring coated OF sealed in a glass sheath is employed for the water splitting reaction as shown in Figure 1.16c [85]. Similarly, one can also couple the OF at the end of the UME in a glass sheath which can guide the light to locally illuminate the samples (Figure 1.16d) [108]. Finally, Zigah *et al.* created a parallel oriented dual OF-UME to photoelectrochemically scan the surface firstly and subsequently detect the photoelectrochemically generated  $O_2$  (Figure 1.16e) [86]. This configuration will be illustrated and adopted in the work of chapter 4 of this thesis.

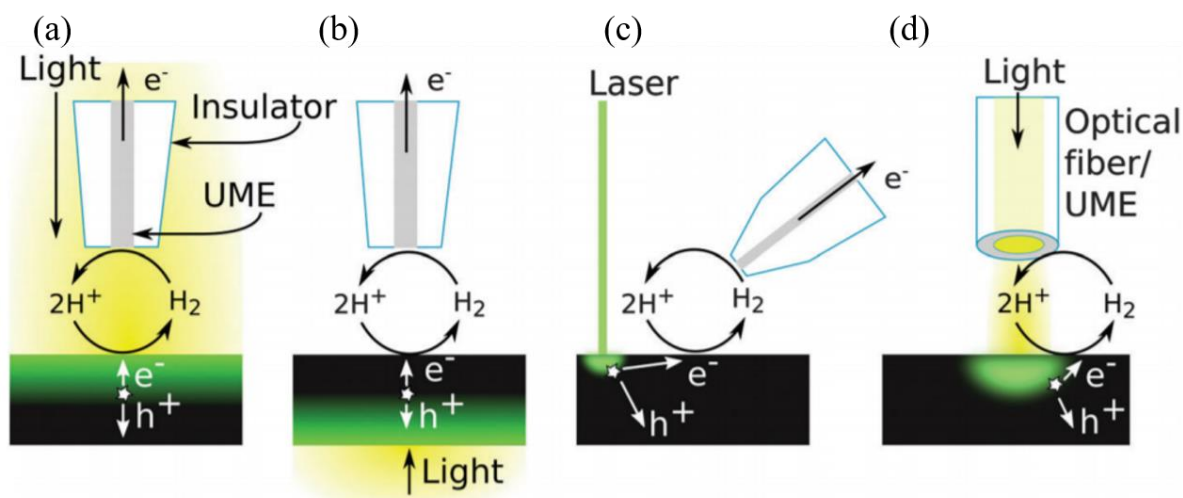


Figure 1.15 Schematic side-views of several SPECM configurations for investigating photoelectrode surfaces. The light green regions represent the photon absorption/charge carrier generation volume in the semiconducting photoelectrode [113].

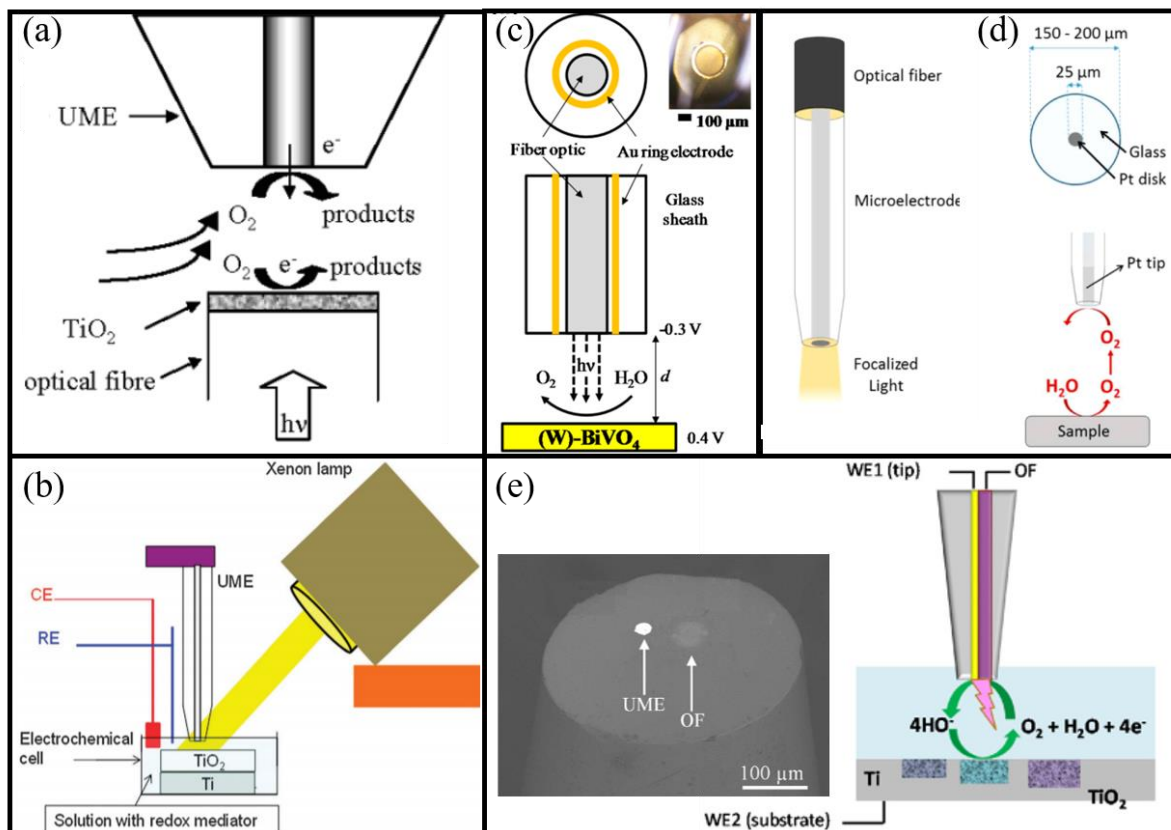


Figure 1.16 Schematic representation of the SECM configurations adopted in literature: (a) The light is incident from the back side of the photocatalysts [106]; (b) The light beam is introduced to the entire surface and orientated with the UME in acute-angle [107]; (c) The tip is an OF core coated with Au ring UME sealed in the glass sheath [85]; (d) The tip is an UME coupled with an OF at the end to provide light through a glass sheath [108]; (e) The parallel combination of dual OF and UME in a capillary [86].

### 1.2.6. Applications of SECM in Electrochemistry and Photoelectrochemistry

The SECM is capable to locally induce and detect electrochemical activities in a micro/nanoscale regime and able to qualitatively and quantitatively analyze the reaction kinetics and the properties of the sample, with the advantages of small  $IR$  drop, high mass transfer rate, low time constant, high signal to noise ratio and current density, making it unique among other scanning probe technique and employed in many applications. It has been used to analyze the electrocatalytic activities of different electrochemical catalysts in electrochemistry [70], and adapted to monitor the structures and process in the nanoscale such as the nanoparticles [71]. It can also analyze the biological process in the studies of enzymes,

DNA, proteins, and living cells [115]. In this part, the content is restricted to the applications related to electrochemistry.

### *1.2.6.1. Applications of SECM in Electrochemistry*

The SECM has been intensively utilized in many aspects of electrochemical with different operation mode: it can image the morphology of the substrate such as the circuit board by feedback mode [116]; it can investigate corrosion mechanism and mitigation methods [117]; it can detect the  $O_2$  evolution reaction in the water splitting [118], formic acid oxidation [93] etc.. Here the ORR and  $CO_2RR$  applications with various operation modes are especially illustrated as examples.

The energy conversion is a hot topic and numerous researches have been carried out to find efficiency catalysts. Various SECM operation modes have been widely adopted in ORR for the development of the fuel cells. Bard's group studied ORR with SECM feedback mode in which the  $O_2$  was produced at a gold tip by oxidation of  $OH^-$  and reduced at a Pt substrate in alkaline medium [119]. Moreover, they also adopted TG/SC mode to expand the pH range to acidic environment on Pt/Ru electrodes, as shown in Figure 1.17a. The  $O_2$  generated on the tip diffused and was reduced back to  $H_2O$  on the biased substrate, by comparing the current in the imaging of the Pt and Ru spots loaded on the glass carbon substrate, the materials with good catalytic performance can be fast screened by SECM [120]. Meanwhile, with TG/SC mode, Sánchez-Sánchez *et.al* investigated the catalytic activities of shape-controlled Pt nanoparticles (Pt NPs) for ORR and found that hexagonal Pt NPs shown the highest catalysis than tetrahedral-octahedral, spherical and cubic one. (Figure 1.17b) [96] Alternatively, they also tried SG/TC mode and Comsol simulation to quantify intermediators ORR generated at small substrate [94]. The experimental and simulation results are coincident. Figure 1.17c shows the simulation results on half of an axial 2D symmetric tip of the concentration profile of active species.

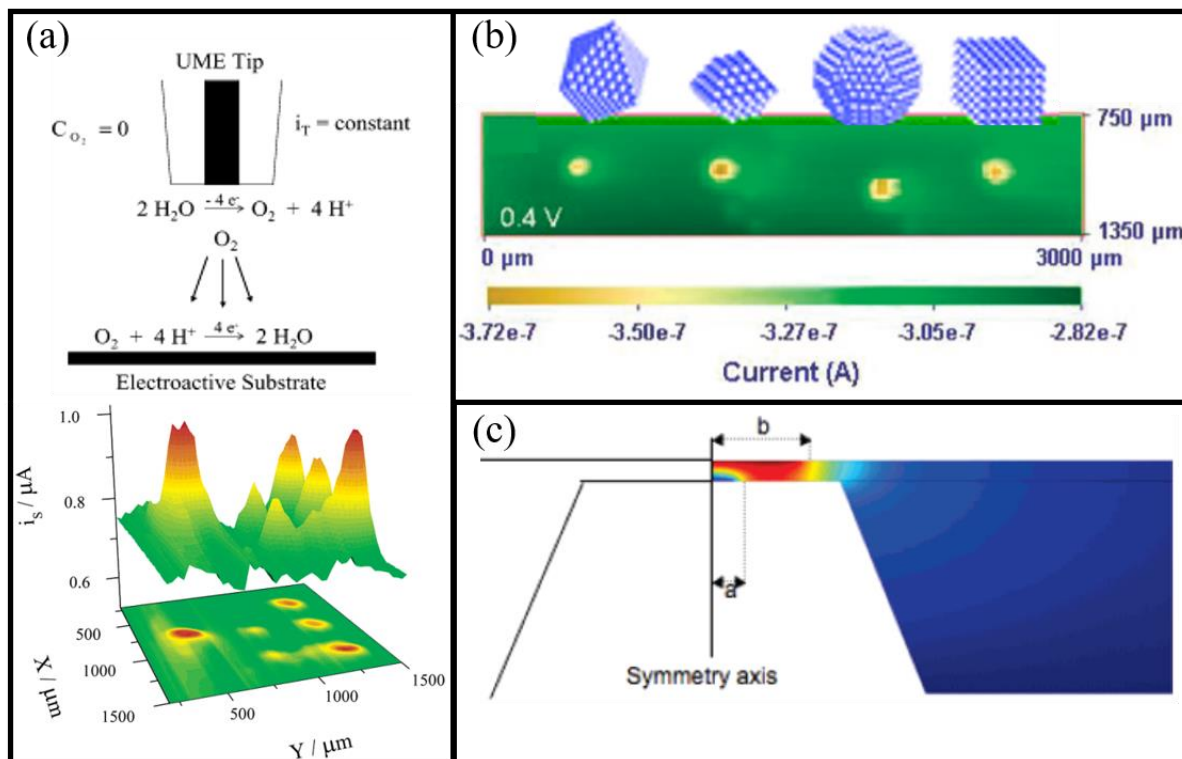


Figure 1.17 (a) Scheme of the modified TG-SC mode (up), and the SECM image of an array of Pt (left spot and right row) and Ru (middle row) spots supported on glassy carbon (down) for ORR in acidic medium [120]. (b) SECM TG/SC images displaying the reduction current collected for ORR tetrahedral-octahedral, hexagonal, spherical and cubic Pt NPs array. The color represents the measured photocurrent shown in the scale bar of the SECM image [96]. (c) Schematic representation of the nonsimulated portion (left-half tip) and the simulation (right-half tip) result for the concentration profile of species O near the surface of an axial 2D symmetry model of a SECM tip [94].

As mentioned previously,  $CO_2$  conversion is of vital importance for the environment and the energy crisis. Excepted for ORR, various SECM operation modes also serve for  $CO_2$ RR. Phani *et al.* raised a new insight of the selective reduction in electrochemical  $CO_2$ RR on Au substrate in  $KHCO_3$  solution saturated with  $CO_2$ . As shown in Figure 1.18a, SG/TC mode was used to sense the products generated from the reduction  $CO_2/HCO_3^-$  on the Au substrate by a Pt UME tip. They showed that the formate originates only from the reduction of bicarbonate rather CO comes from the reduction of  $CO_2$  (under low pH and high overpotential), which directs a way for the  $CO_2$ RR products selectivity [121]. Numerous researches revealed that the vital intermediate of radical anion  $CO_2^{\cdot-}$  formed at the first step in the  $CO_2$ RR then converted



to other products. Nevertheless, its lifetime is short because of the easy dimerization with protons leading to the difficult detection.

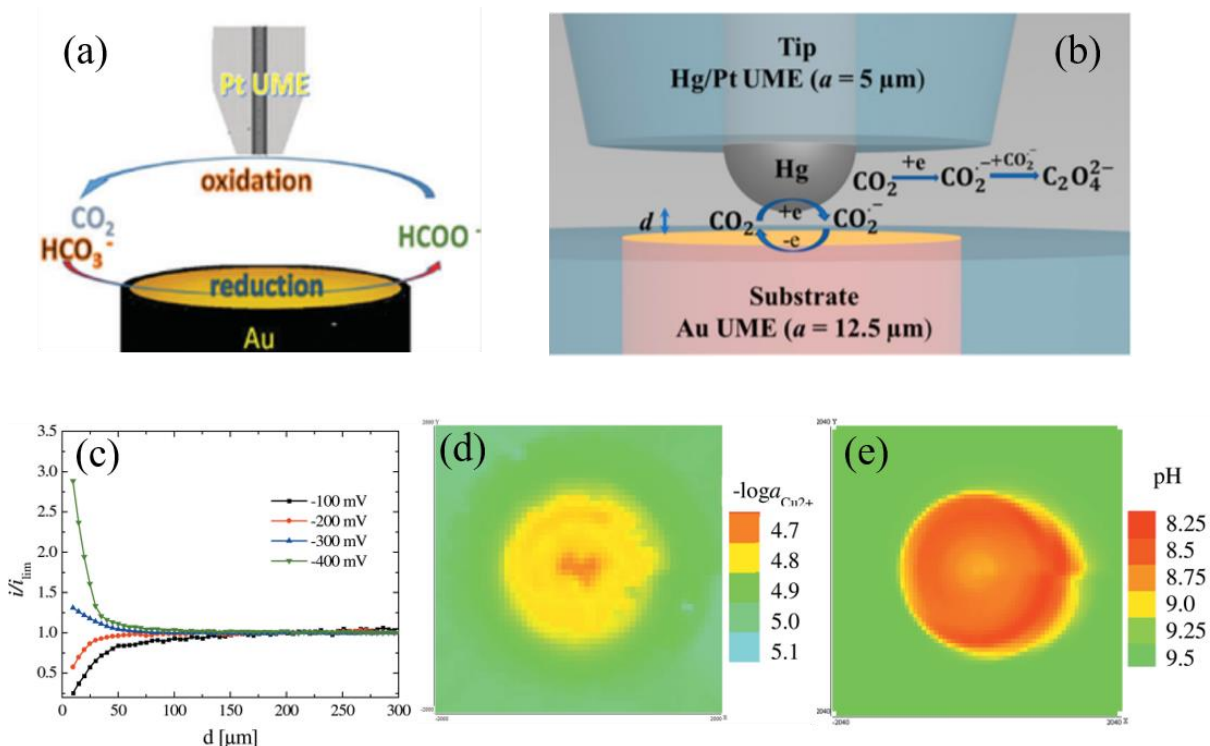


Figure 1.18 (a) Schematic representation of the SG-TC mode for bicarbonate reduction-formate oxidation [121]; (b) Schematic representation of the collection of the  $\text{CO}_2^{\bullet-}$  radical in TG/SC mode of SECM [122]; (c) Z approach curves in towards copper electrode. the electrolyte was 30% monoethanolamine with 0.1 M KCl and 1.25 mM ferrocene-methanol. The applied potential to the tip (Pt disc:  $25 \mu\text{m}$  diameter) was 600 mV; (d) Distribution of  $\text{Cu}^{2+}$  and (e) pH above the copper electrode after 30 min exposure to 30% monoethanolamine solution [123].

Recently, TG/SC mode of SECM has been implemented to successfully generate and detect this radical. (Figure 1.18b) A hemisphere-shaped Hg/Pt UME works to reduce  $\text{CO}_2$  to generate  $\text{CO}_2^{\bullet-}$ , which will diffuse to and oxidized at the Au substrate back to  $\text{CO}_2$  then feed back to the tip, accompanied by their dimerization during the diffusion in the nanogap [123].

Nagy *et al.* explored the electrode passivation in 30% monoethanolamine (MEA) solution during catalyzing  $\text{CO}_2\text{RR}$  with SECM. Firstly, the approach curve in feedback mode is used to study the surface change on the Cu electrode, which was negatively polarized to reduce the oxide films on its surface. As the oxide film was reduced, the negative feedback characterization changed to positive feedback, providing a suitable potential range where the  $\text{CO}_2\text{RR}$  can be fulfilled (Figure 1.18c). The following is the employment of ion-selective



microelectrodes of SECM for the local investigation of the  $\text{Cu}^{2+}$  concentration (Figure 1.18d) and the pH changes profile in the surrounding electrolyte of the Cu electrode by the SECM imaging (Figure 1.18e), giving a deep understanding in the local change of the reactive interfaces.

### 1.2.6.2. Applications of SPECM in Photoelectrochemistry

The development of photoelectrochemical catalysts has grasped tons of attention recently because of their high efficiency on converting sustainable energy (like solar energy) to useful products. The SPECM takes a place in the research of photoelectrochemistry among other techniques.

The SPECM provides an efficient high throughput screening method for fast screening photoelectrochemistry catalysts. Bard *et al.* employed SG/TC mode for screening photoelectrochemical catalysts on HER and ORR. Among the Pb-Bi-Mo trimetal oxide catalysts, different atomic ratio of the 3 elements shown different photoelectrochemical current, which implies the property of the photoelectrochemical catalysts. The highest current originated from the ration of  $\text{Pb:Bi:Mo} = 1:1:1$  ( $p\text{-PbMoO}_4/n\text{-Bi}_2\text{O}_3$ ), illustrating its best photoelectrochemical catalysis (Figure 1.19a and b) [111] They also conducted SPECM for probing photoelectrochemical performance under the visible light which is more common and easier to harvest in nature than Ultraviolet-visible light on different combination of Pb-Cr oxides [110]. Similar study was carried by Mullines' group [109].

The SPECM has been popular in accelerating electrolysis process. As shown in Figure 1.16a, the redox competition mode was used for ORR on the n-type photocatalysts  $\text{TiO}_2$  [106]. The PEC and photocatalytic water splitting are hot topics for the renewable  $\text{H}_2$  energy. Pan *et al.* adopted SPECM for fast detecting coupled p- and n-type heterojunction photoelectrodes Cobalt doped  $\text{BiVO}_4$  (Figure 1.19c), the 3D data shows the best doping concentration of Co is 6% because of an enhancement in the water oxidation kinetics by the surface formed  $\text{Co}_3\text{O}_4$  [124]. In addition, Bard's group studied the  $\text{Bi}_2\text{WO}_6$  catalyst for improved photocatalytic water oxidation [125].

Perovskites possess excellent properties for photovoltaic cell. Different ratios of  $\text{PbI}_2$  were doped to methylammonium lead iodide ( $\text{MAPbI}_3$ ) and rapidly screened by SPECM to find optimal ratio. Figure 1.19d shown the ratio of 2.5%  $\text{PbI}_2/\text{MAPbI}_3$  exhibited the highest photoelectrochemical current which means the best PEC catalysis [126].

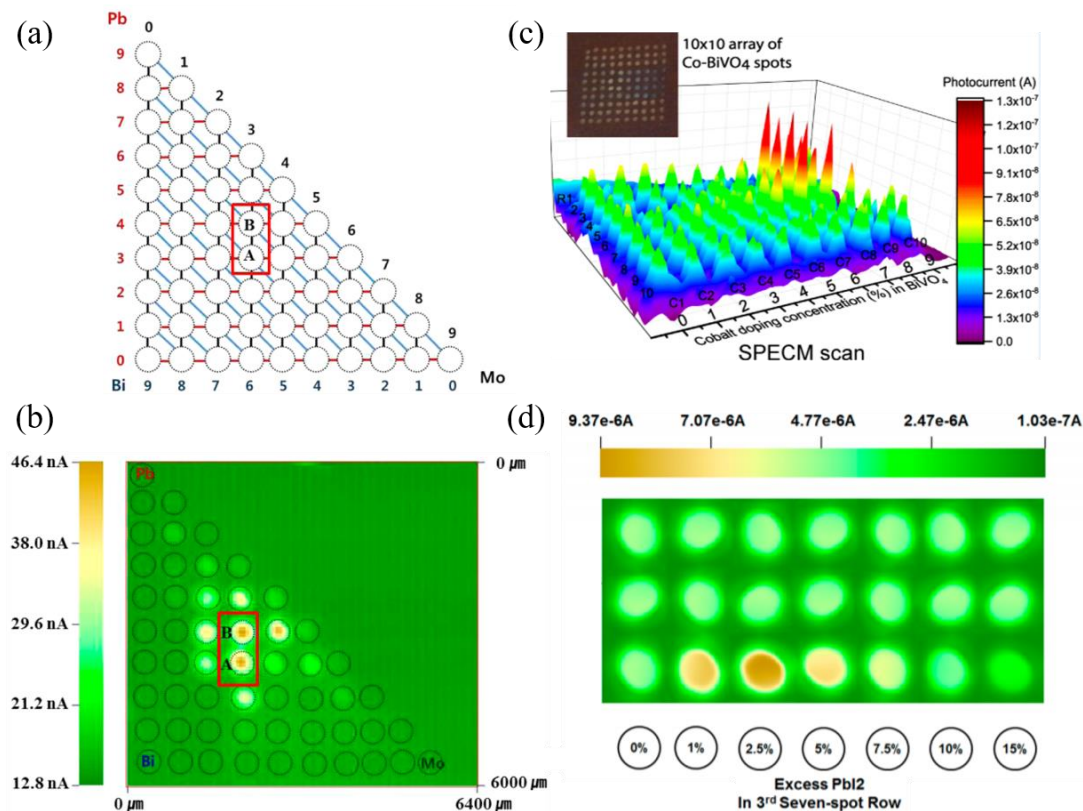


Figure 1.19 (a) Dispensed pattern of photocatalyst arrays with three components. The top corner is pure Pb, the bottom left corner is Bi, and the bottom right corner is Mo. Spots A and B represent Pb-Bi-Mo at 3:3:3 and 4:2:3 atomic ratios, respectively; (b) SECM image of a Pb-Bi-Mo oxide photocatalyst at an applied potential of 0 V vs. Ag/AgCl in 0.1 M Na<sub>2</sub>SO<sub>4</sub> with 0.2 M phosphate buffer solution (pH = 7) [111]; (c) 3D presentation of SPECM data obtained at 0.1 V vs Ag/AgCl along with a photo of the Co-BiVO<sub>4</sub> spots array prepared on Ti substrate. The highest photocurrent is from BiVO<sub>4</sub> spot doped with 6% Co. The inset is the photo of 10×10 array of Co-BiVO<sub>4</sub> spots [124]; (d) SECM images for a typical photocurrent response of PbI<sub>2</sub>/MAPbI<sub>3</sub> composites under irradiation. The first and second seven-spot rows are pure MAPbI<sub>3</sub> perovskites. The third seven-spot row represents the amount of excess PbI<sub>2</sub> in each spot in the array electrode [126].

### 1.3. Room Temperature Ionic Liquids (RTILs)

#### 1.3.1. Introduction of RTILs

CO<sub>2</sub>RR in aqueous solution such as KHCO<sub>3</sub> solution is accompanied with a competitive HER which happens in the similar thermodynamic potentials with CO<sub>2</sub>RR leading to a low conversion efficiency [127]. Moreover, the solubility of CO<sub>2</sub> is low in aqueous solution which unfavors the its availability on catalyst surface during the reduction reaction. Given that, conventional nonaqueous solvents such as acetonitrile (AN), dimethyl formamide (DMF) and

dimethyl sulfoxide (DMSO) have been adopted for their HER suppression and higher CO<sub>2</sub> solubility. Yet the high toxicity, volatility, flammability and non-recyclability restrained their popularization. However, a series of non-aqueous solvents as promising candidates in electrochemistry have been widely applied called ionic liquids (ILs), which is composed entirely of cations and anions. Normally, the strong ionic bond in ionic compounds (such as NaCl) confined the vibration of cations and anions leading to a high melting point, so liquid state of the ionic compounds is possible under high temperature. However, if the cation and anion are asymmetric and with high molecular weight, the interaction between the ions is weakened and the lattice energy decreases by steric hindrance, and following the decreased melting points. The ILs which melt at or below 100 °C are called room temperature ionic liquids (RTILs). They are formed totally by organic cations and organic / inorganic anions.

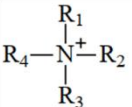
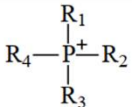
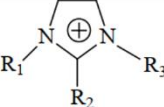
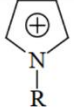
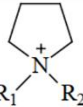
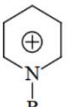
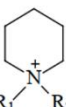
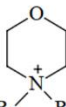
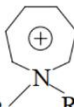
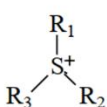
The first RTIL — ethylammonium nitrate ([EtNH<sub>3</sub>]<sup>+</sup>·[NO<sub>3</sub>]<sup>-</sup>) with a melting point of 12 °C — was first synthesized in 1914 [128] yet failed to provoke attention. Until 1992, Wilkes' group firstly reported 1-ethyl-3-methylimidazolium tetrafluoroborate ([EtMeim<sup>+</sup>][BF<sub>4</sub>]<sup>-</sup>) stable in air and water with low melting point [129], RTILs started to cascade in various fields, in particular in electrochemistry.

### 1.3.2. Classification and Properties and of RTILs

#### 1.3.2.1. Classification and abbreviations

There are a huge amount of combinations of cations and anions in RTILs (> 10<sup>6</sup>) [130]. Classifications are various according to different criteria. Normally, RTILs can divide into two branches depending on the availability of proton in the cation: protic ionic liquids [131] and aprotic ionic liquids [132]. In terms of the water solubility, they are classified to water-miscible and water-immiscible ionic liquids. On the basis of the category of cations, there are imidazolium, pyridinium, pyrrolinium, phosphonium pyrrolidinium cations based RTILs and so on; regarding to the category of anions, there are inorganic anions such as Br<sup>-</sup>, Cl<sup>-</sup>, BF<sub>4</sub><sup>-</sup>, PF<sub>6</sub><sup>-</sup>, AuCl<sub>4</sub><sup>-</sup> etc., and organic anions including CH<sub>3</sub>COO<sup>-</sup>, C<sub>6</sub>H<sub>5</sub>SO<sub>3</sub><sup>-</sup> (= OTs<sup>-</sup>), C(CF<sub>3</sub>SO<sub>2</sub>)<sub>3</sub><sup>-</sup>, CF<sub>3</sub>SO<sub>3</sub><sup>-</sup> (= OTf<sup>-</sup>), N(SO<sub>2</sub>CF<sub>3</sub>)<sub>2</sub><sup>-</sup> (= NTf<sub>2</sub><sup>-</sup>) etc. Table 1.1 shows some cations and anions of commonly used RTILs.

Table 1.1 Cations and anions of some common RTILs.

Cations					
	Ammonium	Phosphonium	Imidazolium	Pyrrolinium	Pyrrolidinium
Cations					
	Pyridinium	Piperidinium	Morpholinium	Azepanium	Sulfonium
Inorganic anions	$\text{F}^-, \text{Cl}^-, \text{Br}^-, \text{I}^-, \text{BF}_4^-, \text{PF}_6^-, \text{NO}_3^-, \text{SO}_4^-, \text{HSO}_4^-, \text{ClO}_4^-, \text{CuCl}_2^-, \text{AuCl}_4^-, \text{ZnCl}_3^-, \text{SnCl}_3^-$				
Organic anions	$\text{CH}_3\text{COO}^-, \text{C}_6\text{H}_5\text{SO}_3^-(=\text{OTs}^-), \text{C}(\text{CF}_3\text{SO}_2)_3^-, \text{CF}_3\text{SO}_3^-(=\text{OTf}^-), \text{N}(\text{SO}_2\text{CF}_3)_2^-(=\text{NTf}_2^-), \text{R}_3\text{BOH}^-$				

As for the complicated structure of RTILs, disunity of the abbreviations of the same RTIL can be find in research. Take the imidazolium cation based RTILs as example, Sánchez-Sánchez summarized the abbreviations of 4 kinds of imidazolium cation based RTILs as shown in Table 1.2, 1-Ethyl-3-methylimidazolium can be abbreviated as  $[\text{C}_2\text{mim}]^+$ ,  $[\text{EMIm}]^+ / [\text{Emim}]^+$  and  $[\text{C}_2\text{C}_1\text{Im}]^+$ . In this thesis, all the used RTILs are abbreviated by  $[\text{C}_2\text{mim}]^+$ . Here, in 1-Ethyl-3-methylimidazolium, “Ethyl” and “methyl” represent the alkyl chains joint to the “N” of the imidazolium ring at position “1” and “3”, respectively. (Figure 1.20).

Table 1.2 Nomenclature for imidazolium based cations [52].

RTIL cation IUPAC name	Abbreviation system 1	Abbreviation system 2	Abbreviation system 3
1-Ethyl-3-methylimidazolium	$[\text{C}_2\text{mim}]^+$	$[\text{EMIm}]^+ / [\text{Emim}]^+$	$[\text{C}_2\text{C}_1\text{Im}]^+$
1-Butyl-3-methylimidazolium	$[\text{C}_4\text{mim}]^+$	$[\text{BMIm}]^+ / [\text{Bmim}]^+$	$[\text{C}_4\text{C}_1\text{Im}]^+$
1-Ethyl-2,3-dimethyl-imidazolium	$[\text{C}_2\text{m}_2\text{im}]^+$	$[\text{EMMIm}]^+ / [\text{Emmim}]^+$	$[\text{C}_2\text{C}_1\text{C}_1\text{Im}]^+$
1-Butyl-2,3-dimethyl-imidazolium	$[\text{C}_4\text{m}_2\text{im}]^+$	$[\text{BMMIm}]^+ / [\text{Bmmim}]^+$	$[\text{C}_4\text{C}_1\text{C}_1\text{Im}]^+$

The synthesis methods of RTILs divide to two kinds: “one-step” and “two-step”. The one-step method can transfer the imidazole to imidazolium cation by protonation via acid-base neutralization reaction or quaternization to form alkyl chain on the N atom of the imidazolium ring, which can lead directly to the desired imidazolium cations efficiently and with high yield.

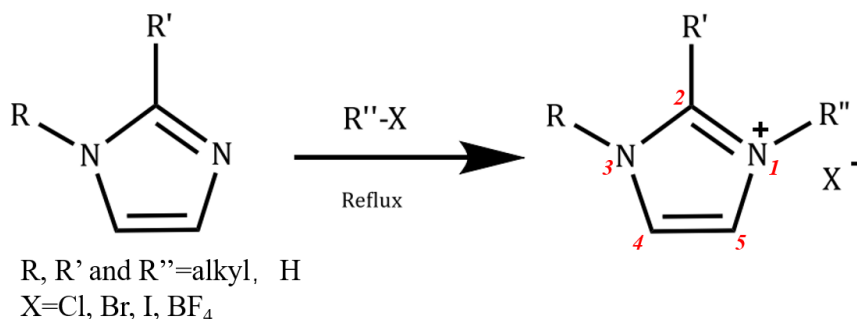


Figure 1.20 Quaternization reaction of the imidazole nucleus. Adapted from ref [133]

Nevertheless, some of the complicate cations are not available by the direct “one-step” synthesis but need “two-step” method which means a metathesis after the “one-step” process [134].

### 1.3.2.2. Properties of RTILs

Composed only by cations and anions in a liquid state, RTILs possess special properties compared to other solvents [132,135]. The optional anions and designable alkyl chains of the cations providing tunable physicochemical properties of RTILs.

1. High thermal and chemical stability. These allow RTILs work in a wide temperature range ( $-40^{\circ}\text{C} \sim 300^{\circ}\text{C}$ ), one remains liquid even down to  $-96^{\circ}\text{C}$  [136].
2. High conductivity and wide electrochemical window (4 ~ 6 V). The oxidation of the anions and the reduction of the cations in the RTILs confined the potential limits of the electrochemical window [132]. Figure 1.21a and b show the electrochemical window of [EMIM][BF<sub>4</sub>] under dry and with a bit of water respectively, which indicated the effect of the impurity on the properties [137]. The high conductivity guarantees the role of solvent as well as a supporting electrolyte [138].
3. Outstanding electrocatalysis. Imidazolium based RTILs have been widely used as cocatalyst for promoting CO<sub>2</sub>RR via different catalytic mechanisms [139,140].
4. High dissolving capacity. They can dissolve many organics and inorganics (including H<sub>2</sub>, O<sub>2</sub>, CO<sub>2</sub>, *etc.*) and even high molecular polymer. For example, the CO<sub>2</sub> solubility in [C<sub>4</sub>mim][BF<sub>4</sub>] is 3 times than that in 0.5 M H<sub>2</sub>SO<sub>4</sub> [52].
5. Low melting point and volatility, because the vapor pressure is almost undetectable [141]. So, they can be used in the high vacuum systems and decreasing the environment pollution caused by the solvent volatilization.

6. high heat capacity and cohesive energy density.
7. Low toxicity and non-flammability.
8. High viscosity. This can be a drawback in the application of electrochemistry because of the inhibition on the mass transfer rate.

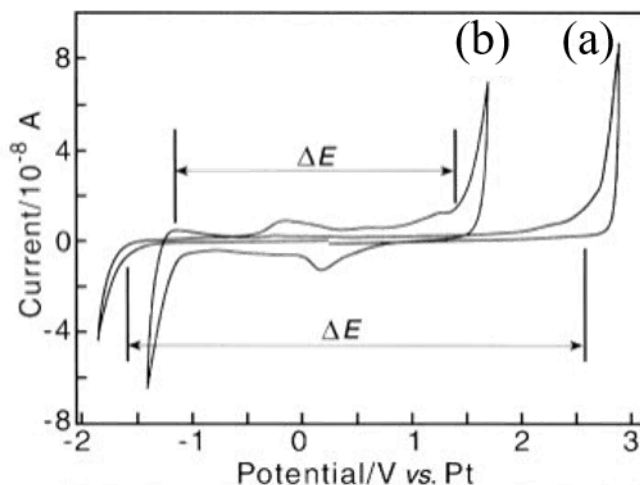


Figure 1.21 Cyclic voltammograms recorded in neat  $[BMIM^+][BF_4^-]$  at a  $50\ \mu\text{m}$  Pt disc electrode, (a) under “dry” conditions and (b) with a water content of approximately 3 wt.% in the ionic liquid (scan rate 100 mV/s).

### 1.3.3. Applications of RTILs in Electrochemistry and Photoelectrochemistry

Possessing various excellent properties, RTILs have shown promising capability as novel green solvent and catalysis in numerous fields such as energy, materials, medicine, gas captures, analytical chemistry [142–146], especially in electrochemistry such as electrocatalysis, electrodeposition, electrochemical sensors, electrosynthesis, fuel cells, solar cells and so on [147–152].

#### 1.3.3.1. Applications of Pure RTILs and RTILs-based Binary and Ternary Solvent Mixtures in Electrochemical $\text{CO}_2\text{RR}$

Since RTILs can work as solvent [153] and electrolyte [138] simultaneously, they are popular in the electrocatalysis and electrosynthesis. The capability of RTILs exists in either  $\text{CO}_2$  capture from the post-combustion gases emission or  $\text{CO}_2$  conversion to value-added products. The most mature methods in the sequestering of  $\text{CO}_2$  is the application of cyclic chemical absorption/desorption by aqueous solution such as monoethanolamine, which, however, is confined by the corrosive and volatile properties of amines. Given that RTILs are

developed to be a substitution and more effective CO<sub>2</sub> capture solvents because of the outstanding nature mentioned previously [154,155]. On the other hand, RTILs play a vital role in the electrochemical CO<sub>2</sub>RR to generate value-added products. Benefited from the chemisorption of the CO<sub>2</sub> on the electrode surface, RTILs possess remarkable CO<sub>2</sub> solubility as an electrolyte to meet the reactant transport demand [156,157]. Normally, the CO<sub>2</sub> solubility is greatly relied on the nature of the anions because of its strong affinity with CO<sub>2</sub> [158]. In addition, the formation of complex with CO<sub>2</sub> and RTILs cations enhances the solubility. Among all the common RTILs, 1,3-dialkyl-imidazolium (C<sub>n</sub>mim<sup>+</sup>) based RTILs such as [C<sub>2</sub>mim][BF<sub>4</sub>] (or [EMIM][BF<sub>4</sub>]) [157,159–163] and [C<sub>4</sub>mim][BF<sub>4</sub>] (or [BMIM][BF<sub>4</sub>]) [153,156,164] have been the most researched class and gained tons of attentions in the electrochemical CO<sub>2</sub>RR thanks to its high conductivity and the ability for CO<sub>2</sub> capture. Moreover, most researches on the CO<sub>2</sub> reduction encounter the first and rate-determining step of forming an anion radical (CO<sub>2</sub><sup>•-</sup>) intermediate which demand extremely high energy. Rosen *et al.* reported the positive effect of 18 mol% 1-ethyl-3-methylimidazolium tetrafluoroborate ([EMIM][BF<sub>4</sub>]) in H<sub>2</sub>O on lowering the reduction overpotential of CO<sub>2</sub> to CO on the silver electrode at a small overpotential (< 0.2 V). They declared that the formation of a complex (EMIM-CO<sub>2</sub>) by which the energy barrier of CO<sub>2</sub><sup>•-</sup> can be lowered (Figure 1.22a) [159]. This discovery demonstrated the cocatalytic role of the RTILs simultaneously as supporting electrolyte, provides promising future for widespread use of imidazolium based RTILs on CO<sub>2</sub>RR. Numerous groups studied the mechanisms and principles of electrochemical CO<sub>2</sub>RR combined with RTILs which will be introduced in the following section.

Direct electrochemical CO<sub>2</sub>RR in pure imidazolium based RTILs have been studied. Kumar's group reported the decreased overpotential of CO<sub>2</sub>RR on metal-free carbon nanofiber catalysts (CNFs) in pure [EMIM][BF<sub>4</sub>] [153], together with the study of the dependency of CO<sub>2</sub> reduction efficiency on the [MIM<sup>+</sup>] alkyl chain [165], illustrated the feasibility of the role of supporting electrolyte and cocatalyst of imidazolium based RTILs. However, the high viscosity of pure RTILs inhibits the mass transportation rate and also the current density, moreover, the hygroscopicity of some imidazolium based RTILs (containing Cl<sup>-</sup>) are sensitive to the impurities such as water, which may trigger changes in the properties and catalytic behavior via proton-coupled electron-transfer pathways [140]. Given this, some researches mixed the RTILs with molecular solvents like AN or water to affect the viscosity and

conductivity and the pH of the solvent system. These binary mixtures of RTIL/AN, RTIL/H<sub>2</sub>O and even ternary mixture of RTIL/AN/H<sub>2</sub>O have been investigated to facilitate efficient electrochemical CO<sub>2</sub>RR [52]. Binary mixture of 1-ethyl-3-methylimidazolium trifluoromethanesulfonate ([EMIM][TFO]) and water were used as electrolyte to convert CO<sub>2</sub> to CO at lower overpotential and inhibit competing HER by modifying the concentration of [EMIM][TFO] [161]. Likewise, Kumar *et al.* analyzed the relationship of the water mole fraction and the current density in [EMIM][BF<sub>4</sub>]. The highest current density was obtained for a ratio of 25 mol% EMIMBF<sub>4</sub> and 75 mol% H<sub>2</sub>O as shown in Figure 1.22b [153]. Nevertheless, there is controversy about the optimum water content. The best operation condition for [EMIM][TFO] to catalyze CO<sub>2</sub> reduction by forming EMIM–CO<sub>2</sub> complex on the CNFs is 50 mol%/H<sub>2</sub>O [161] rather 80 wt.% of [BMIM]Cl to convert CO<sub>2</sub> to CO on Ag electrode with a selectivity and efficiency of ~99% [166].

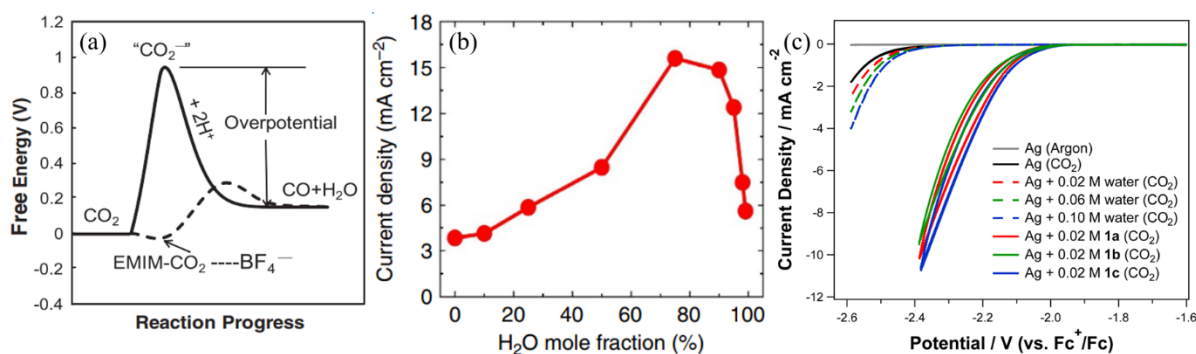


Figure 1.22 (a) Schematic of how the free energy of the system changes during the reaction  $\text{CO}_2 + 2\text{H}^+ + 2\text{e}^- \rightarrow \text{CO} + \text{H}_2\text{O}$  in water or acetonitrile (solid line) or [EMIM][BF<sub>4</sub>] (dashed line). The label CO<sub>2</sub><sup>-</sup> refers to the intermediate that forms when the first electron is transferred during the reaction [159]; (b) Current density (at the highest CO<sub>2</sub> reduction potential) for carbon nanofiber catalyst with respect to water mole fraction (%) in [EMIM][BF<sub>4</sub>] [153]; (c) Cyclic voltammograms recorded for effect of different anions and water concentrations in 0.1 M [TBA][PF<sub>6</sub>] AN solution on the electrochemical reduction of CO<sub>2</sub> 1a, 1b, 1c stand for [EMIM][BF<sub>4</sub>], [EMIM][TFSI] and [EMIM][OTf] [140].

Many studies adopted AN solvent containing imidazolium cations as supporting electrolyte and/or cocatalyst (RTIL/AN), some of them also introducing tetrabutylammonium hexafluorophosphate ([TBA][PF<sub>6</sub>]) as the extra supporting electrolyte of for electrochemical CO<sub>2</sub>RR [160,164,165]. Lau *et al.* evaluated series of imidazolium based RTILs as cocatalysts in AN containing 0.1M [TBA][PF<sub>6</sub>] for electrochemical CO<sub>2</sub>RR on Ag electrode. By comparing the performance of the addition of a small quantity of water or imidazolium salts,



they found that the dramatically increase of the current density should not be credited to the presence of water but to the imidazolium cations, thus proving the cocatalyst role of imidazolium cations and by contrast the anions didn't affect a lot on the  $\text{CO}_2\text{RR}$  (Figure 1.22c) [140]. Figure 1.23 shows that the addition of  $[\text{EMIM}][\text{Tf}_2\text{N}]$  shifts the reaction course from oxalate to CO and carboxylate in 0.1M tetraethylammonium perchlorate/acetonitrile (TEAP/AN) [160]. Zhu *et al.* [164] evaluated  $[\text{BMIM}][\text{PF}_6]/\text{AN}/\text{H}_2\text{O}$  ternary mixture and found that the addition of small amount water can greatly enhance the efficiency of  $\text{CO}_2$  to  $\text{HCOOH}$  compared to binary mixture  $[\text{BMIM}][\text{PF}_6]/\text{AN}$  and pure  $[\text{BMIM}][\text{PF}_6]$ , indicated by the highest current density as shown in Figure 1.24a. Furthermore, the best operational RTIL content was identified to 30 wt.% in the ternary mixture since it shown the maximum FE to the  $\text{HCOOH}$  and current density of  $\text{CO}_2\text{RR}$  (Figure 1.24b).

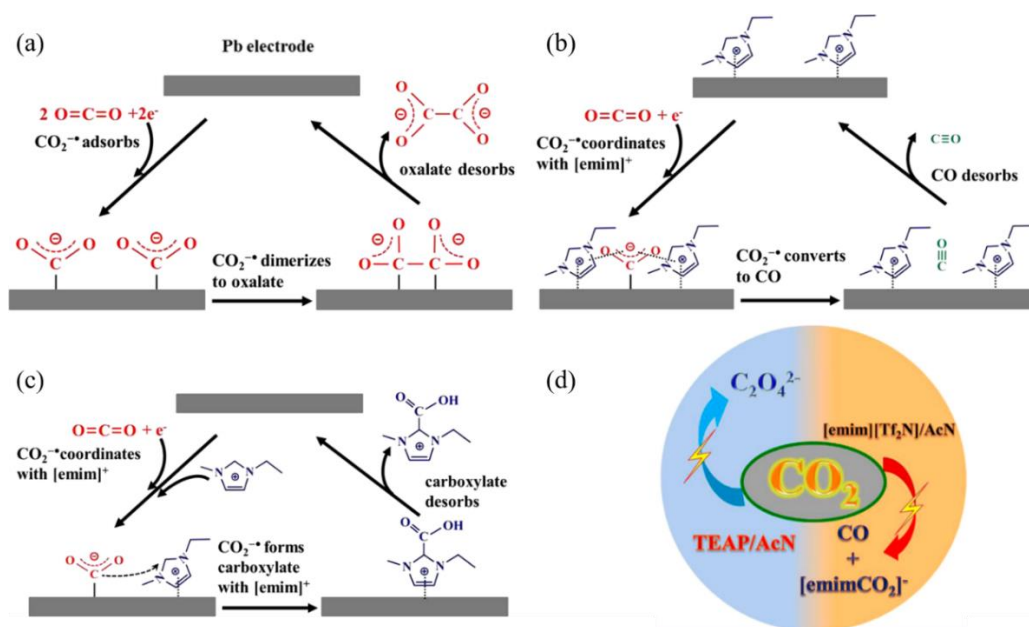


Figure 1.23 Reaction pathways for the  $\text{CO}_2\text{RR}$  in the (a) absence  $[\text{EMIM}][\text{Tf}_2\text{N}]$  to oxalate and presence of  $[\text{EMIM}][\text{Tf}_2\text{N}]$  to (b) CO and (c) carboxylate at a Pb electrode in AN; (d) General picture of the reaction course [160].

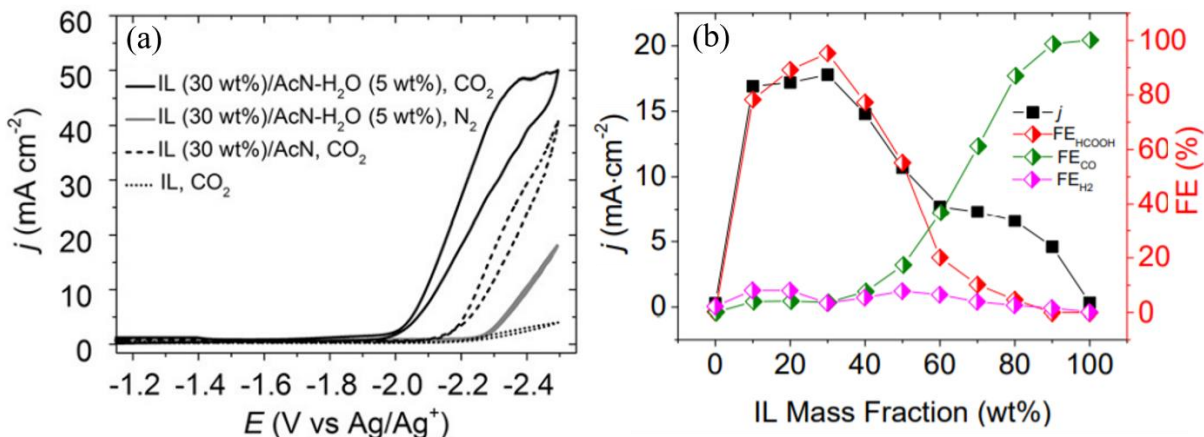


Figure 1.24 (a) CV of in various electrolytes containing  $[\text{BMIM}][\text{PF}_6]$  saturated with  $\text{CO}_2$  or  $\text{N}_2$  at Pb electrode in various electrolytes; (b) Effect of  $[\text{BMIM}][\text{PF}_6]$  content as a part of the ternary  $[\text{BMIM}][\text{PF}_6]/\text{AN}/\text{H}_2\text{O}$  (5 wt.%) mixture on the current density and products Faradaic efficiency in  $\text{CO}_2$  electrolysis at -2.2 V vs.  $\text{Ag}/\text{Ag}^+$  at Pb electrode [164].

### 1.3.3.2. Mechanisms and Pathways of Imidazolium based RTILs in Electrochemical $\text{CO}_2\text{RR}$

Imidazolium based RTILs contribute to enhance the  $\text{CO}_2$  reduction process either as a supporting electrolyte or as cocatalyst. However, the mechanism and the pathways on how they play a role are attractive and researchers have controversial perspectives. This section concentrates on some most popular theories about the reaction mechanisms related to imidazolium cations on electrochemically catalyze  $\text{CO}_2$  reduction to various value-added products in literature, trying to depict a clear and macroscopic outline for the research background of this thesis.

It is well known that the one electron transfer process of the first step in  $\text{CO}_2$  electrochemical conversion to the radical anion  $\text{CO}_2^{\cdot-}$  (Equation 1-4, M represents metal electrocatalyst [18]) represents high energy barrier and requires very negative equilibrium potential. Rosen's theory mentioned above proved the cocatalyst role of imidazolium cation on lowering the overpotential and the free energy needed to form  $\text{CO}_2^{\cdot-}$  by the formation of  $\text{EMIM}-\text{CO}_2$  complex. Numerous studies endorsed this cocatalyst role yet proposed different rational mechanism regarding the combination of imidazolium cation with  $\text{CO}_2$  based on the detection of the intermediates and products. Here some mainstream mechanisms are introduced and discussed for the imidazolium cation cocatalyst.



A significant research was reported on various RTILs about their ability to promote electrochemical CO<sub>2</sub>RR at Ag electrode [167]. Among 20 different RTILs, many have catalytic activity on CO<sub>2</sub>RR indicating that the cocatalyst role is not restricted to imidazolium cations. However, their catalytic mechanisms were different with imidazolium cations. As shown in Figure 1.25a, only the imidazolium cations worked as cocatalyst by forming complex by imidazolium radical and CO<sub>2</sub>, others made impact by modifying the double layer. As for the imidazolium cations, it was first reported to combine directly with CO<sub>2</sub><sup>•-</sup> to lower the free energy of the following the Scheme 1-5 [157]. Akin to this scheme is the study of Kumar in the electrocatalysis of metal-free CNFs (Figure 1.25b) [153]. The EMIM–CO<sub>2</sub> complex was absorbed on the reduced C atom and electrochemically catalyze CO<sub>2</sub> to CO.

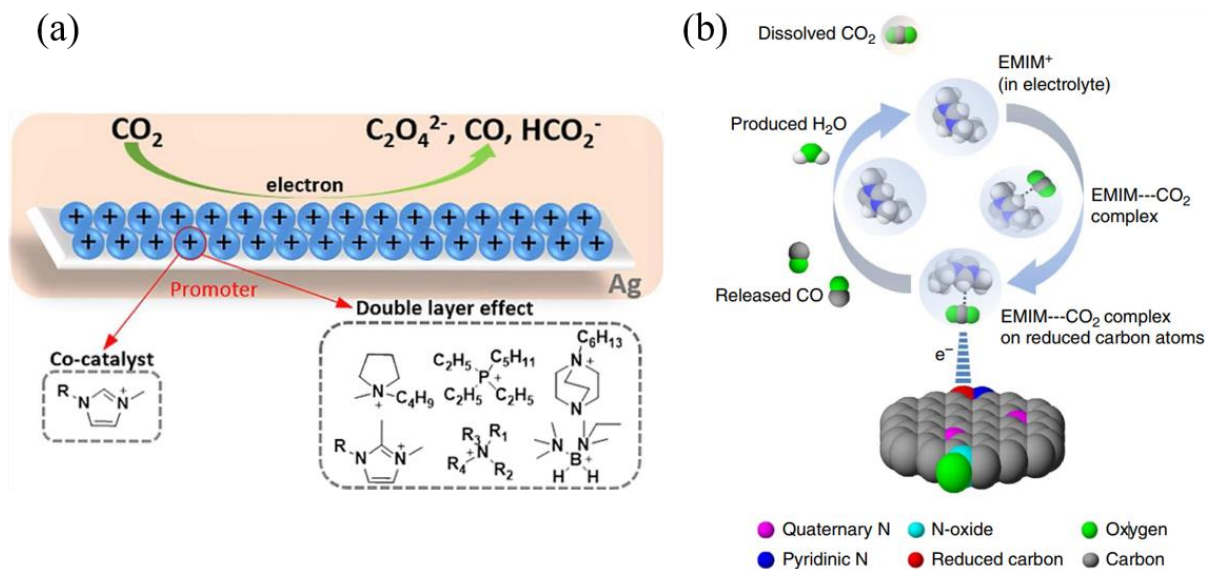
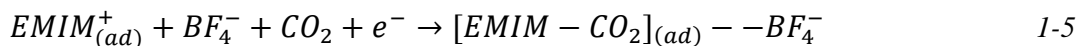


Figure 1.25 (a) Schematic diagram of different RTILs additives used as potential promoters for the electrochemical CO<sub>2</sub>RR to various products at Ag electrode [167]; (b) Schematic diagram of CO<sub>2</sub> reduction mechanism. The CO<sub>2</sub> reduction reaction takes place in three steps: (1) an intermediate (EMIM–CO<sub>2</sub> complex) formation, (2) adsorption of EMIM–CO<sub>2</sub> complex on the reduced carbon atoms and (3) CO formation [153].



In general, the C2 between two N atoms is the most electron deficient atom in the 1,3-dialkyl-imidazolium ring hence the reduction site [168]. [EMIM<sup>+</sup>] accepted one electron and transferred to two different intermediates depending on the reactive conditions such as the applied potentials [162]. At -1.3 V to 1.0 V (vs Pt wire) at Pt (111) electrode, [EMIM<sup>+</sup>] was reduced to radical [EMIM<sup>•</sup>], which is quasi-reversible and can be oxidized back to [EMIM<sup>+</sup>];

subsequently, [EMIM<sup>•</sup>] may either combine with CO<sub>2</sub><sup>•-</sup> to form [EMIMH-CO<sub>2</sub><sup>-</sup>] (Figure 1.26a) [162] or with CO<sub>2</sub> for [EMIMH-CO<sub>2</sub><sup>-</sup>] generation (Figure 1.26b) [169]. The former adduct is electroactive and identified by an oxidation peak on Pt (100) and Pt (110) surface, yet the latter is detected by Raman spectroscopy plus DFT calculation as energetically feasible intermediate. However, as the reduction potential was very negative, the intermediate of 1-butyl-3-methylimidazole-2-ylidene (N-heterocyclic carbene, NHC) and ½ H<sub>2</sub> or H<sub>(ad)</sub> were generated, followed by the combination with CO<sub>2</sub> to imidazolium-2-carboxylate ([EMIM<sup>+</sup>-CO<sub>2</sub><sup>-</sup>]) (Figure 1.26c) [160,170]. Nevertheless, this NHC catalysis was ruled out by the researches of Wang *et al.* [163] and Zhao *et al.* [167]. The calculated acidity constant (pK<sub>a</sub>) indicating the difficulty of deprotonation of C2 to form imidazolium carboxylate because the intermediate is too large. Instead, the proton at C2 is important to attach CO<sub>2</sub> to form the intermediate [EMIM-COOH]<sup>-</sup>, as also proved by Niu *et al.* who showed that the H at C2 can stabilize the CO<sub>2</sub><sup>•-</sup> via hydrogen bond [171]. Furthermore, the carbene did appear after CO decomposition in the overall catalytic reduction pathway shown in Figure 1.26d.

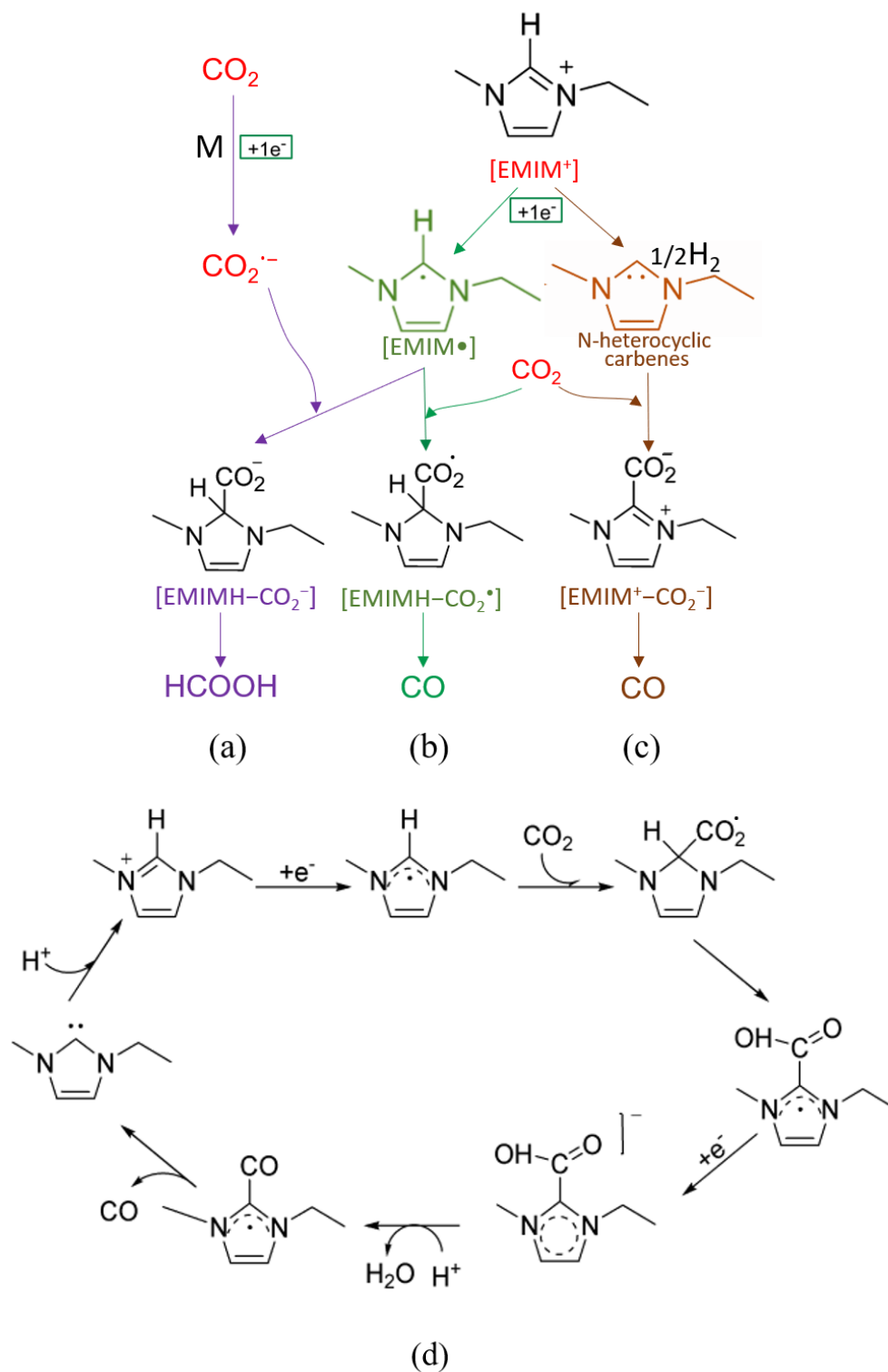


Figure 1.26 Reaction mechanisms and pathways associated with [EMIM]<sup>+</sup> cocatalysis of the CO<sub>2</sub>RR to value-added products in literature.

Despite the intermediate formation have been studied by numbers of researches, the relationship of electrochemical interfaces between the RTILs and the electrode is under deeply exploring.

Mao *et al.* [172] studied the electrochemical interfaces of imidazolium based RTILs on Au single crystal electrode by shell-isolated nanoparticle enhanced Raman spectroscopy. Results illustrated that the interfacial structure of the imidazolium cation and Au were potential dependent. As shown in Figure 1.27a: (1) at potentials positive to potential of zero charge (PZC,  $E > \text{PZC}$ ), anions absorbed to the Au surface by electrostatic forces while cations were near to the anions in the bulk electrolyte side. (2)  $E \approx \text{PZC}$ , neither cations nor anions adsorb at the surface significantly. (3)  $E < \text{PZC}$ , imidazolium cation started to adsorb on the Au surface with a flat-lying structure, as the potentials became more and more negative, the cations tend to up-leaning and finally vertical-standing on the Au surface by HC4C5H side. This theory provides a rational explanation on the various pathways of electrochemical  $\text{CO}_2\text{RR}$  enhanced by imidazolium cations.

Lau *et al.* also evaluated various imidazolium salts and found that catalytic activity was related to the structures of cations, demonstrating that the C4 and C5 protons on the imidazolium ring play a vital role on stabilizing the  $\text{CO}_2^{\bullet-}$  on the Ag surface by hydrogen bonds. They proposed a possible bonding mode of 1-ethyl-2,3-dimethylimidazolium cation with  $\text{CO}_2^{\bullet-}$  on Ag surface as shown in Figure 1.27b [140].

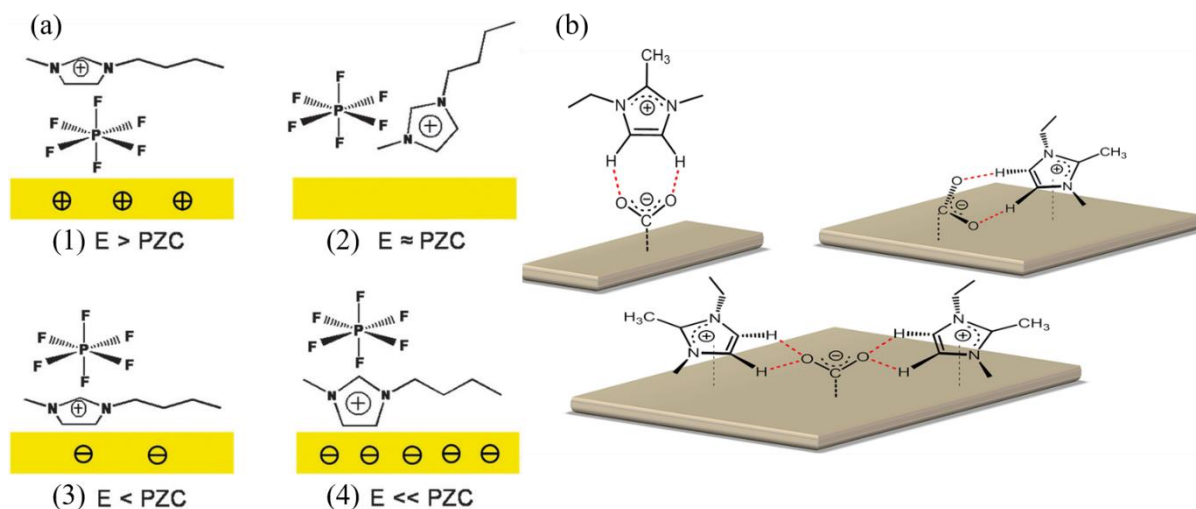


Figure 1.27 (a) Proposed interfacial structure of Au single crystal electrode/imidazolium based ionic liquid at different potential regions: (1) positive of the PZC, (2) near the PZC, (3) negative of the PZC

*and (4) more negative of the PZC. PZC represents potential of zero charge [172]. (b) Possible binding modes of 1-ethyl-2,3-dimethylimidazolium cation with  $\text{CO}_2^{*}$  on Ag surface. Red dashed line represents hydrogen bonds [140].*

Overall, the benefit of imidazolium based RTILs on promoting  $\text{CO}_2$  conversion to various products lie in 4 aspects: (1) lowering the overpotential for the  $\text{CO}_2\text{RR}$ ; (2) cocatalytic role on  $\text{CO}_2\text{RR}$  either by forming intermediate or absorption in the reaction system; (3) suppressing the competitive HER and (4) increasing the selectivity of products such as CO formation.

### ***1.3.3.3. Applications of Imidazolium based RTILs Photocatalytic $\text{CO}_2\text{RR}$***

Based on the advantage of imidazolium cation as cocatalyst on lowering free energy of electrochemical  $\text{CO}_2\text{RR}$ , photocatalytic  $\text{CO}_2\text{RR}$  can be fulfilled in imidazolium based RTIL/ $\text{H}_2\text{O}$  combined with photocatalytic system ( $[\text{Ru}(\text{bpy})_3]\text{Cl}_2$  ( $\text{bpy} = 2,2'$ -bipyridine) and  $\text{CoCl}_2 \cdot 6\text{H}_2\text{O}$ , and triethanolamine (TEOA) as a light sensitizer, an electron mediator, and an electron donor, respectively) [139]. They proved the essential cocatalyst role of  $[\text{EMIM}^+][\text{BF}_4^-]$  because no products generated when it is replaced by  $\text{HBF}_4$ . Furthermore, the absorption spectrum was obtained to explore the relationship of incident light wavelength on the gas evolution rate of photogenerated CO and  $\text{H}_2$  in  $[\text{EMIM}][\text{BF}_4]/\text{H}_2\text{O}$  (Figure 1.28a) The results shown that the CO generation performance was coincident to the optical absorption spectrum, indicating that  $\text{CO}_2\text{RR}$  depended on the charge photogeneration, separation and the subsequent electron transfer in the mixture. In addition, after comparing the different photocatalytic reduction performance in various imidazolium based RTILs with different alkyl chain or anions, it is clear that the photocatalytic  $\text{CO}_2\text{RR}$  relied deeply on the chemical properties of anions and the organic functional groups on the imidazolium cation.



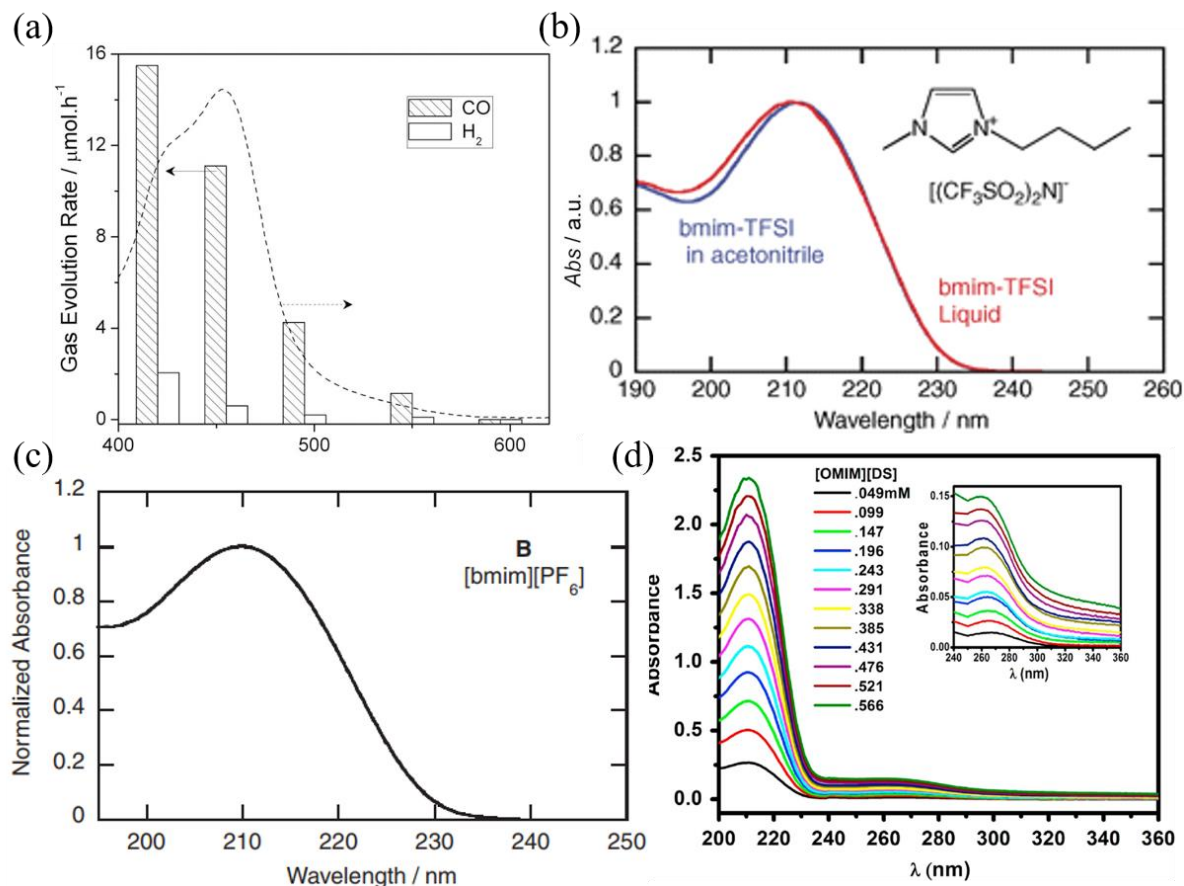


Figure 1.28 UV-vis absorption spectra of (a) The dependence of the wavelength of incident light on the gas evolution rate of CO and  $\text{H}_2$  from the  $\text{CO}_2$  photoreduction system in  $[\text{EMIM}][\text{BF}_4]/\text{H}_2\text{O}$  [139]; (b)  $[\text{BMIM}][\text{TFSI}]$  and (c)  $[\text{BMIM}][\text{PF}_6]$  in the liquid phase in a thin optical cell [173]; (d) changing concentrations of 1-octyl-3-methylimidazolium dodecylsulphate ( $[\text{OMIM}][\text{DS}]$ ) in water. The inset shows magnified version of the spectra in the wavelength range 24 ~ 360 nm [174].

In fact, imidazolium cations are expected to have strong absorption peak about 200-400 nm wavelength because of the aromatic carbons in the imidazolium ring [173]. Katoh measured the absorption spectra of  $[\text{BMIM}][\text{TFSI}]$  in liquid state and in AN, as well as  $[\text{BMIM}][\text{PF}_6]$  and found that those spectra were similar, indicating a weak electronic intermolecular interaction of imidazolium cation with others in the RTILs. The strong peaks for pure  $[\text{BMIM}][\text{TFSI}]$  and  $[\text{BMIM}][\text{PF}_6]$  were at 210.5 nm and 210 nm, respectively and were assigned to  $\pi-\pi^*$  transition that originates from the  $\text{C}=\text{C}$  bond of the imidazolium cation because the  $[\text{TFSI}]$  anion had negligible absorption in this range. (Figure 1.28b and c) In addition, Boutiti *et al.* [175] and Rather *et al.* [174] also obtained a maximum absorption peak at 210 nm in 1-hexyl-3-methylimidazolium chloride ( $[\text{HMIM}]\text{Cl}/\text{H}_2\text{O}$ ) and of 1-octyl-3-



methylimidazolium dodecylsulphate ([OMIM][DS]/H<sub>2</sub>O) respectively. The relationship between the absorption and the concentration of [OMIM][DS] is linearly and in accordance with Lambert-Beer's law. However, the wavelength of the strongest absorption peak in the absorption spectrum can be affected by the impurities present in the RTILs such as water or other species left after the synthesis process [176]. Thus, researchers need to purify the RTILs regarding to the specific task.

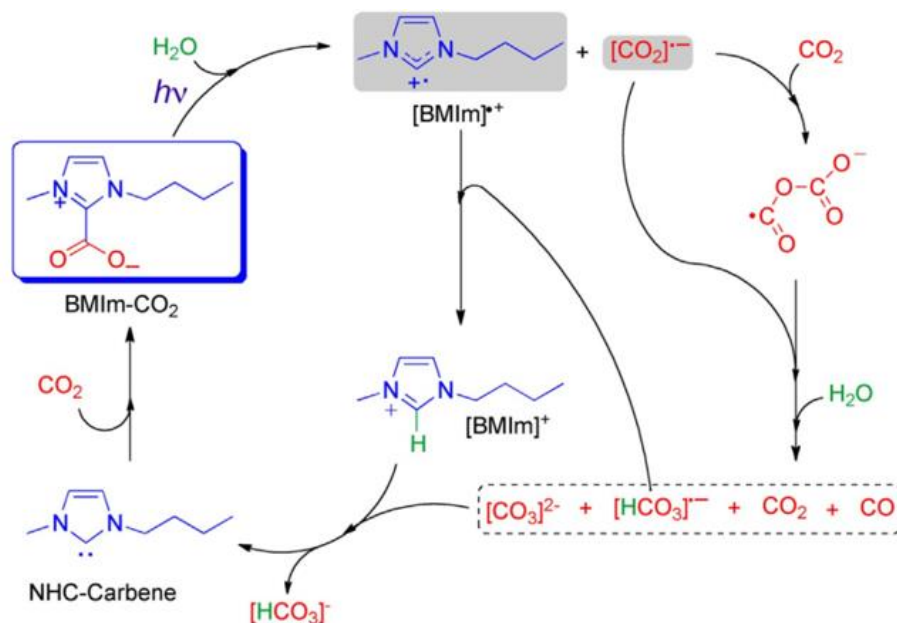


Figure 1.29 Possible species involved in the CO<sub>2</sub> photoreduction driven by RTILs [177].

The light-absorption ability of imidazolium based RTILs can facilitate to create valuable species combined with catalysts during the photocatalytic or photoelectrochemical CO<sub>2</sub>RR process yet the mechanisms and principle research are still in the infant stage and desired study thoroughly. Here one example is shown to illustrate how the imidazolium cation functionate in the photoreduction of CO<sub>2</sub>. Qadir *et al.* reported an efficient method to photoconvert CO<sub>2</sub> to CO without the presence of the photosensitizers or sacrificial agents, rather only adopt RTILs to promote CO<sub>2</sub>•<sup>-</sup> generation by “homolytic C–C cleavage” in the cation–CO<sub>2</sub> complex [177]. As shown in Figure 1.29, First of all, a zwitterionic RTIL 1-n-butyl-3-methylimidazolium-2-carboxylate [BMIm.CO<sub>2</sub>] absorbed light and photolysis happened to form [BMIm]<sup>+</sup> and CO<sub>2</sub>•<sup>-</sup>, combined with CO<sub>2</sub> to generate CO<sub>2</sub>-dimer radical anion [C<sub>2</sub>O<sub>4</sub>]•<sup>-</sup>, which interact with the addition of another CO<sub>2</sub>•<sup>-</sup> to form CO and carbonate. The [BMIm]<sup>+</sup> can be regenerated from [BMIm]<sup>+</sup> and [HCO<sub>3</sub>]•<sup>-</sup>, the generated [CO<sub>3</sub>]<sup>2-</sup> and [HCO<sub>3</sub>]<sup>-</sup> can deprotonate [BMIm]<sup>+</sup> to form

NHC, which can combine with CO<sub>2</sub> to regenerate [BMim.CO<sub>2</sub>]. This promising discovery provided an efficient method for harvest solar energy and the ability of imidazolium based RTILs for photocatalytic CO<sub>2</sub>RR.

Overall, RTILs, especially imidazolium based RTILs have been extensively investigated for promoting electrochemical or photocatalytic CO<sub>2</sub>RR because of their outstanding physicochemical properties. No matter in pure RTILs or the RTILs-based mixture solvents, they all shown promising contribution either as supporting electrolyte or cocatalyst in the CO<sub>2</sub>RR systems. Great effort has been made to figure out why and how the RTILs play a role as one key step in the reduction process yet far from enough. Not only the electrolyte has effects on the performance of electrochemical CO<sub>2</sub>RR, but also the catalyst/electrode materials have impact and controlling on that. Seek and develop efficient and cost-effective catalysts possess the top priority in the electrocatalysis field.

### 1.4. Electrochemical and Photoelectrochemical Catalytic Materials

Among a large amount of electrochemical and PEC CO<sub>2</sub>RR catalysts, the cost-effective oxide-derived copper catalysts for the generation of multicarbon (C<sub>2+</sub>) products (hydrocarbons and alcohols) from electrochemical CO<sub>2</sub>RR and transition metal–nitrogen–doped carbon electrocatalytic materials for C<sub>1</sub> compounds (CO) production from PEC CO<sub>2</sub>RR have been widely studied and proved promising, paved a way for the future design and development of electrocatalysts for electrochemical and photoelectrochemical CO<sub>2</sub>RR.

#### 1.4.1. Applications and Present Limitations of Transition Metal–Nitrogen Doped Carbon (M–N–C) Catalysts in Electrochemical CO<sub>2</sub>RR

The CO<sub>2</sub>RR conversion to CO can carry out at the surface of noble metals (Ag and Au) which are expensive and scarce. Alternatively, the cost-effective pyrolyzed catalysts of transition metal–nitrogen–doped carbon (M–N–C) materials have been extensively studied for electrochemical CO<sub>2</sub>RR to form C<sub>1</sub> products [178], HER [179] and oxygen reduction reaction [180] because of their high selectivity, stability and activity, huge catalytic surface area and low-cost. Varela *et al.* reported the use of Fe/Mn–N–C for the first time on CO<sub>2</sub>RR to CO with a FE of 80% in 2015 [181] since then there have been several attempts to explore different metals in M–N–C to catalyze CO<sub>2</sub>RR such as Fe, Co, Ni, Mn, Cu, Cr, etc. [179,182–184].

In general, M–N–C catalysts are prepared by heat treatment of the mixture of metal salts, high surface area carbon precursors (citric acid, chitosan, *etc.*) and nitrogen precursors ( $\text{N}_2$ ,  $\text{NH}_3$ , urea and phenanthroline). The synthesis process and the structure were shown in Figure 1.30a [178]. The N atom located in the high surface carbon structure forming 3 kinds of chemical functionalities: pyrrolic, graphitic and pyridinic N. The metal atom combined with the surrounding N atoms to form  $\text{M–N}_x$  moieties as active sites which were influenced by the adjacent C atoms [178,185]. Figure 1.30b shown the electrochemical  $\text{CO}_2\text{RR}$  to CO on the huge surface with numerous active sites of M–N–C.

Each component in M–N–C catalysts for electrochemical  $\text{CO}_2\text{RR}$  may have a particular impact on the overall activity performance and for this reason different types of carbon, nitrogen source, and metallic center have been explored [186–189]. But the most important element is the metallic centers and the related active sites. M–N–C exhibits superior electrocatalysis either by lowering the overpotential (such as Fe–N–C) [182] or improving CO selectivity (like Ni–N–C) [190].

The judgment of the performance of M–N–C on electrochemical  $\text{CO}_2\text{RR}$  can use the Faradaic efficiency, the overpotential and the current density. Different M–N–C were evaluated by the comparison of CO FEs as a function of the applied potential (Figure 1.30c) [182]. The highest CO production efficiency is exhibited by Ni–N–C, but the lowest overpotential is achieved by Fe–N–C catalyst. In addition, to prove the indispensable catalytic role of the metal center, rotating disk electrode (RDE) was used to carry out linear sweep voltammetry (LSV) analyses to measure the electrochemical response in the presence or absence of Fe center (Figure 1.30d). In this regard, the presence of Fe center notably enhances the catalytic performance by decreasing the overpotential and increasing the current density despite nitrogen moieties are already catalytically active for  $\text{CO}_2\text{RR}$ . This leads to the conclusion that the Fe atom plays a vital role in the active sites of the electrocatalytic material for an efficient  $\text{CO}_2\text{RR}$  [191].

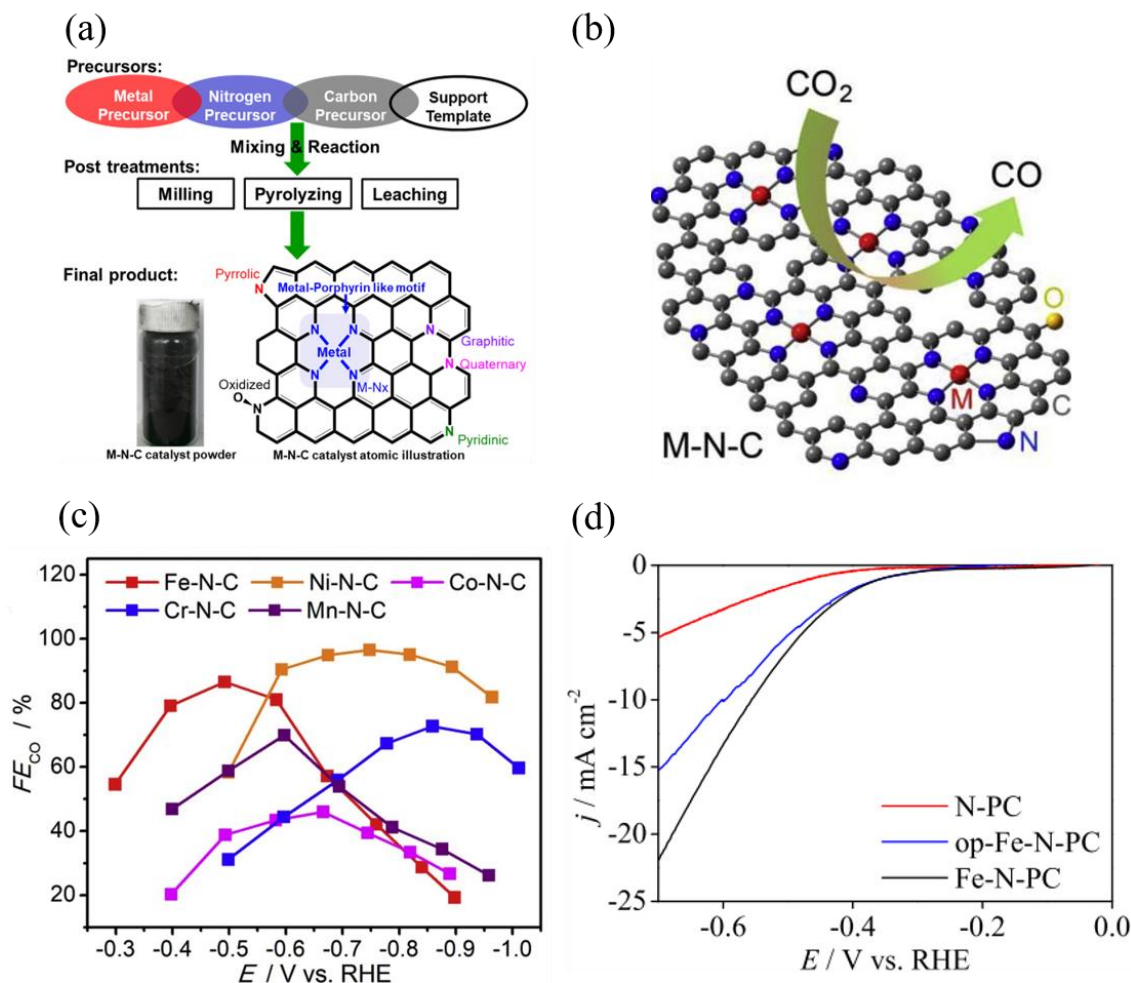


Figure 1.30 (a) General synthesis strategy of M-N-C catalysts and their obtained structure [178]; (b) CO<sub>2</sub>RR to CO on the surface of M-N-C catalysts, the balls in grey, red and blue are C, metal and N atoms, respectively; (c) CO Faradaic efficiencies at different metal-N-C catalysts [182]; (d) Linear sweep voltammetry curves of Fe-N-PC, op-Fe-N-PC and N-PC in CO<sub>2</sub>-saturated 0.5 mol L<sup>-1</sup> KHCO<sub>3</sub> solution (scan rate = 10 mV/s) PC is porous carbon nanosphere. Op-Fe-N-PC is the samples without the addition of NH<sub>3</sub>·H<sub>2</sub>O and tetraethylorthosilicate to form the SiO<sub>2</sub> shell [191].

The M-N-C possess extraordinary product selectivity simultaneously with high FE. It is stated that Fe-N-C materials derived from Fe(SCN)<sub>3</sub> (denoted as SMFeSCN) are responsible for an improved FE to CO up to 99% at a moderate overpotential of 0.44 V [192]. Likely, sulfur (S) incorporation in the micropoles containing Fe-N-C can promote CO generation with FE of 98% because the combination of S with Fe-N<sub>4</sub> changed the Fermi level and charge density [193].

Although M-N-C catalysts have exhibited inspiring FEs to electrochemically convert CO<sub>2</sub> into CO at low overpotentials, the real mechanisms of catalysis still remain controversial. So

far, generation of  $C_{2+}$  products from  $CO_2RR$  is not possible on M–N–C catalysts because those are considered single active site catalysts and do not allow carbon–carbon coupling. Furthermore, the long-term stability of M–N–C materials is still an issue because relevant leaching of the metal center is produced under reaction conditions during  $CO_2RR$  [189]. To conclude, the exploration of M–N–C needs more efforts and attention to meet the updated demands.

### 1.4.2. Introduction of p-type Semiconductors for PEC $CO_2RR$

Semiconductors (SCs) have displayed extraordinary role for photoelectrochemical reduction since Fujishima firstly reported the photoelectrocatalysis ability of semiconductor  $TiO_2$  powder on water splitting to  $H_2$  and  $O_2$  [49]. SCs are capable to absorb light and produce photovoltage to facilitate electrochemical  $CO_2RR$  to lower the overpotential. The mechanism of SCs catalyze  $CO_2RR$  is complicate and different from metals as photocathodes, usually explained by energy band theory in literature. In this section, the band theory and mechanism of SCs on how they function are introduced.

#### 1.4.2.1. *The Energy Band Theory and Photoelectrocatalysis of Semiconductors*

Semiconductors are materials with a conductivity between conductors and insulators, including inorganic SCs and organic SCs. Unlike the conductors with continuum energy states where electrons can move among delocalized empty orbitals with small energy, SCs possess discontinuous energy states thus different bands: valence band (VB,  $E_V$ ) is a low-energy band filled with electrons and are composed with the highest occupied molecular orbital (HOMO), as well as conduction band (CB,  $E_C$ ) represents higher energy band where almost absent with electrons but can jump up into from the VB and composed by lowest unoccupied molecular orbital (LUMO). Between the VB and the CB is the Band gap ( $E_g$ ) where no energy states exist. Absorbing the light ( $h\nu \geq E_g$ ) electrons are activated from VB and excited to CB, leaving photogenerated positive charged holes in the VB and freely moving electrons in the CB. These electron-hole ( $h^+$ ) pairs then separate and move to the catalyst/electrolyte interface as charge carriers and subsequently participate in the redox reaction [194,195]. Fermi level ( $E_F$ ) is the energy level at which the probability of an electron exist in a continuum of electronic state is  $\frac{1}{2}$  at 0 K, it usually lies between the VB and the CB [32]. Intrinsic SCs has the equal number of electrons and holes, doping impurities can change their conductivity because of the charge

carrier change. Introducing acceptor impurities to form p-type SCs because the positive holes are more than the electrons and work as the main charge carrier. In contrast, n-type SCs are available by doping donor impurities since more electrons are brought in [194,196]. The Fermi level lies near the VB in p-type SCs rather near to the CB in n-type SCs.

Electron transfer occurs at the interface of SC/electrolyte to eliminate the difference between  $E_F$  and  $E_R$  (the redox potential of the electrolyte) when SC is immersed in the electrolyte.  $E_F$  changes accompanied by the VB and the CB bending at the interface until realizing an equal  $E_F$  both sides at the equilibrium state. Figure 1.31a and b shown the band bending diagram of p-type SCs immersed in electrolyte before and at equilibrium. The  $E_F$  moves upward and so do the VB and the CB. Typically, p-type SCs are widely used in the photoelectrochemical reduction because the increase of  $E_F$  can move the excited electrons in the CB to the SC/electrolyte interface and captured by the following reduction reaction [197].

However, the electron-hole recombination is a dramatically fast process and common in the SCs, suppressing the electron transfer at the interface and, subsequently, the reduction current density. The application of electricity power can promote the separation of electron-hole pairs thus increase the light harvesting efficiency [195]. The typical configuration of PEC CO<sub>2</sub>RR used p-type SC is shown in Figure 1.3. The SC photocathode under illumination photogenerated electron-hole charge carriers, the separated electrons moves to SC/electrolyte interface for the CO<sub>2</sub>RR half reaction whereas water oxidation occurred at the counter electrode. The detail mechanism in the SC was shown in Figure 1.31c [197]. The biased photocathode SC under illumination was immersed in the electrolyte, the Fermi level as well as the VB and CB upward bended leading to a band-bending gradient, the photogenerated electrons and holes hence were separated also along with the external electric field, the electrons transferred to the interface and reduced CO<sub>2</sub>. This combination of electrochemical and photocatalysis can surprisingly lower the overpotential and increasing the light harvesting efficiency in PEC CO<sub>2</sub>RR. The final goal is that utilize SCs to harvest the solar (visible light) and applied a small overpotential to drive the PEC CO<sub>2</sub>RR meantime maintain a high catalytic activity [28].

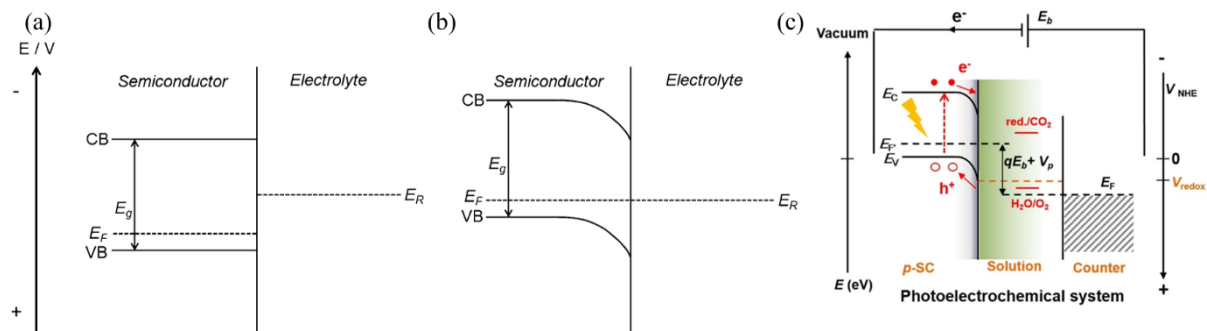


Figure 1.31 Energy band diagrams of the interface between p-SC and electrolyte with redox potential  $E_R$  (a) before equilibrium and (b) at equilibrium; (c) Energy band diagram of a p-type SC photocathode and electron transfer pathways in PEC  $\text{CO}_2\text{RR}$  system. Semiconductor (SC); NHE (normal hydrogen electrode) [197].

#### 1.4.2.2. The Applications of p-type Semiconductor: Oxide-Derived Cu Catalysts for PEC $\text{CO}_2\text{RR}$

Photoelectrochemical  $\text{CO}_2\text{RR}$  based on semiconductors represents an inspiring method to mitigate  $\text{CO}_2$  unbalance and harvests sunlight. Especially, some of the oxide-derived Cu (OD-Cu) catalysts belongs to p-type semiconductors and possess the commonly photoelectrolytic properties of p-type semiconductors, hence popular in the PEC field [198]. In general, Cu-based electrocatalysts represents a promising ability to generate  $\text{C}_{2+}$  products (hydrocarbons and alcohols) with high energy density from  $\text{CO}_2\text{RR}$ . Nevertheless, Cu atoms mobility is common and provokes surface restructuring, which affects the electrode activity and product selectivity. For this reason, (OD-Cu) electrocatalytic materials have been widely studied because OD-Cu electrodes provide better long-term stability and keep similar product selectivity under reaction conditions.

Copper (I)-based p-type transition metal oxides were studied for photoelectrochemical and photovoltaic solar energy conversion. The incorporation of filled  $d^{10}$  configurations of Cu(I) can semiconducting modify the transition-metal oxides thus extending the absorption of visible light from UV absorption only [199]. Semiconductor  $\text{Cu}_2\text{O}$  has been widely evaluated for PEC studies [32]. Thin films of electrodeposited  $\text{Cu}_2\text{O}$  on Cu electrode allowed to photoelectrochemically convert  $\text{CO}_2$  to  $\text{CH}_4$  and  $\text{C}_2\text{H}_4$  under visible light illumination. The comparison of p-type  $\text{Cu}_2\text{O}$  had better performance than n-type  $\text{Cu}_2\text{O}$  under the same morphology with a 33% current efficiency to  $\text{C}_2\text{H}_4$ , yet required high overpotential ( $-2.0$  V vs Ag/AgCl) [200].

In addition, the spinel ternary transition metal oxides (such as  $\text{CuCo}_2\text{O}_4$ ,  $\text{BiCo}_2\text{O}_4$ ,  $\text{FeCo}_2\text{O}_4$  and  $\text{MgCo}_2\text{O}_4$ ) isomorphic to  $\text{Co}_3\text{O}_4$  crystal structure are promising for photoelectrochemical  $\text{CO}_2\text{RR}$  because they possess stable crystal structure, multi redox state and hierarchical structure helping electron-hole pair separation [24]. In fact, copper cobaltite  $\text{CuCo}_2\text{O}_4$  has been attractive in various applications such as catalysts, capacitor, humidity sensors, anodes in lithium battery [201,202]. Trari *et al.* [203] studied the photocatalytic ability of spinel  $\text{CuM}_2\text{O}_4$  and identified  $\text{CuCo}_2\text{O}_4$  as a promising p-type semiconductor material for HER, proved that cobalt enhanced the electron affinity. Interestingly, the addition of  $\text{S}_n^{2-}$  and  $\text{S}_2\text{O}_6^{2-}$  competed for photoelectrons which indicated that  $\text{CuCo}_2\text{O}_4$  was also applicable in PEC  $\text{CO}_2\text{RR}$ . Ding *et al.* reported the cocatalyst role of  $\text{CuCo}_2\text{O}_4$  for the photochemical  $\text{CO}_2\text{RR}$  together with homogeneous photosensitizer ( $\text{Ru}(\text{bpy})_3^{2+}$ ) and heterogeneous semiconductor ( $\text{CdS}$ ) by harvesting visible light [204]. These nanoplate microstructure  $\text{CuCo}_2\text{O}_4$  with mesopores were synthesized by calcination. (Figure 1.32a) The combination of  $\text{CuCo}_2\text{O}_4$  with  $\text{Ru}(\text{bpy})_3^{2+}$  greatly promoted photocatalyze  $\text{CO}_2$  to  $\text{CO}$  with good current density and inhibited the proton reduction reaction. In addition, Figure 1.32b exhibited the relationship of absorption wavelength of incident light and the products activity, the trend of products yields matches well with the absorption spectrum of  $\text{Ru}(\text{bpy})_3^{2+}$ . All phenomena mentioned above indicated that the catalysis started by the “visible-light-triggered excitation” of the ruthenium dye and then activated the cocatalysis of  $\text{CuCo}_2\text{O}_4$ . In addition, the crystallinity and the specific surface can be modified by calcination temperature hence induced different catalytic performance as shown in Figure 1.32c.

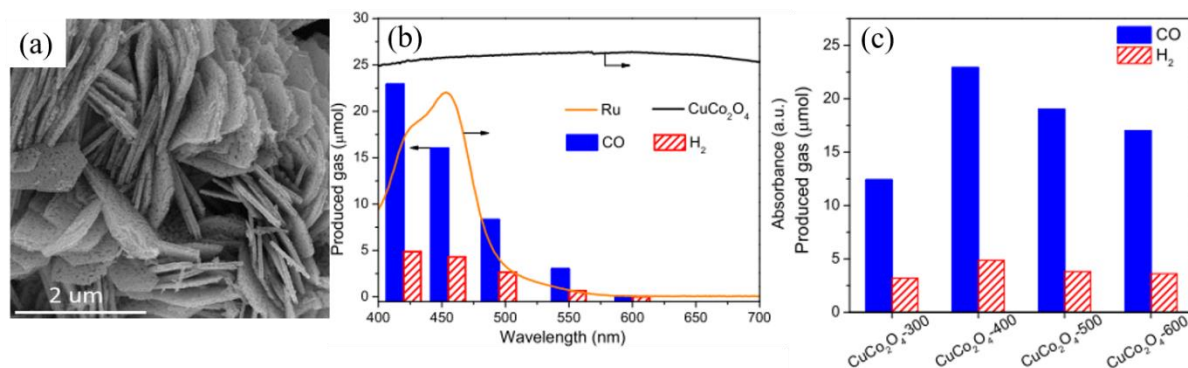


Figure 1.32 (a) SEM image of  $\text{CuCo}_2\text{O}_4$  structure; (b) Comparison of the performance of  $\text{CO}_2\text{RR}$  of the  $\text{CuCo}_2\text{O}_4$  synthesized at different calcination temperatures; (c) Productions of  $\text{CO}/\text{H}_2$  from the photochemical  $\text{CO}_2\text{RR}$  under irradiation light with different wavelengths. The lines are the



*absorption spectrum of  $\text{Ru}(\text{bpy})_3^{2+}$  and  $\text{CuCo}_2\text{O}_4$ . The wavelength of the incident light was adjusted by suitable long-pass cutoff filters [204].*

Overall, efficient (photo)electrocatalytic materials with high electrocatalysis, strong stability and high product selectivity must be explored with the purpose of lowering the high overpotential of electrochemical or PEC  $\text{CO}_2\text{RR}$ .

### 1.5. Summary of Objectives and Outline of the Thesis

The electrochemical and photoelectrochemical  $\text{CO}_2\text{RR}$  to value-added products provides an effective and promising approach to mitigate the high  $\text{CO}_2$  concentration in the atmosphere and promote energy storage. Although electrochemical and photoelectrochemical  $\text{CO}_2\text{RR}$  catalysts have been extensively explored and evaluated, the present limitations are large because many vital processes are not very clear and desire more efforts. Every participated factor during the catalysis needs to be considered and optimized for synergetic working on converting  $\text{CO}_2$ , hereinto, finding cost-effective and abundant catalysts with high catalysis, long-term stability, high products selectivity is the most imperative element.

Compared to aqueous solution, imidazolium based RTILs possess various physicochemical properties and can dissolve more  $\text{CO}_2$  and inhibit competitive hydrogen evolution reaction, as well as work as cocatalyst of imidazolium cation for  $\text{CO}_2\text{RR}$ , given that, they are promising to play a role as either a supporting electrolyte or cocatalyst in electrochemical and photoelectrochemical  $\text{CO}_2\text{RR}$ . However, due to the high viscosity and the low mass transfer rate, pure RTILs are limited for their applications, hence, binary and ternary mixture of RTILs with molecular solvent (water or acetonitrile) has been intriguing and earned a tremendous attention for the electrochemical and photoelectrochemical  $\text{CO}_2\text{RR}$ .

SECM employs an ultramicroelectrode tip to apply a suitable potential and collect the corresponding electrochemical signal response as a current, which allows to explore the electrocatalytic properties of different materials. Then, scanning photoelectrochemical microscopy has been developed by replacing the UME tip by an optical fiber, which is connected to a Xenon light source and provides UV-visible or visible light to locally illuminate the candidate catalysts for PEC  $\text{CO}_2\text{RR}$  activity evaluation.

The objectives of this thesis are thus:

(1) Synthesize different p-type metal oxide semiconductors, screen and choose model p-type semiconductor with high catalytic efficiency for photoelectrochemical CO<sub>2</sub>RR by SPECM.

(2) Investigate photoelectrochemical CO<sub>2</sub> reduction reaction on model p-type CuCo<sub>2</sub>O<sub>4</sub> in aqueous solution/pure imidazolium based RTILs/binary mixture solution of imidazolium based RTILs and H<sub>2</sub>O by SPECM.

(3) In situ detect the photoelectrochemical CO<sub>2</sub>RR products with dual tip of optical fiber-ultramicroelectrode, and analyze those products after bulk electrolysis by GC and IC.

(4) Synthesize and screen transition metal–nitrogen–carbon materials for electrochemical CO<sub>2</sub>RR.

The outline of the thesis is as following:

In Chapter 2, all the chemical reagents and materials and instruments involved will be introduced. Besides, some synthesis processes and general operations will be described. Furthermore, the characterization methods and techniques used will be introduced, including instrument type and configuration.

In Chapter 3, several transition metals adopted and combined to form different p-type metal oxide semiconductors as catalysts for photoelectrochemical CO<sub>2</sub>RR will be introduced. SPECM will be applied to locally illuminate these p-type semiconductor materials immersed in different electrolytes solutions for evaluating their performance for PEC CO<sub>2</sub>RR, CuCo<sub>2</sub>O<sub>4</sub> will be appointed as model catalysts for its high photoactivity performance. It will quantify and compare the photoelectrochemical activity of CuCo<sub>2</sub>O<sub>4</sub> by SPECM in different media including aqueous solutions (0.1 M KHCO<sub>3</sub>, 0.1 M Na<sub>2</sub>SO<sub>4</sub>), binary mixture solution (25 vol.% [C<sub>2</sub>mim][BF<sub>4</sub>]/H<sub>2</sub>O and 25 vol.% and 50 vol.% [C<sub>4</sub>mim][BF<sub>4</sub>]/H<sub>2</sub>O) and pure RTILs either under UV-visible or visible illumination in this work. In addition, the cocatalyst role of imidazolium based RTILs with an incomparable performance in enhancing the photoelectrochemical CO<sub>2</sub> reduction reaction will be explored.

In the Chapter 4, a home-made dual tip OF-UME fabricated for in situ detecting the products from PEC CO<sub>2</sub>RR will be introduced. The OF allows the light to locally illuminate p-type semiconductor CuCo<sub>2</sub>O<sub>4</sub> which is biased. The OF is scanned in the X-Y direction and introduces UV-vis light locally on CuCo<sub>2</sub>O<sub>4</sub> spot, which might convert CO<sub>2</sub> into CO or HCOOH or other products. Simultaneously, the biased Pt UME can detect the generated

products by electrochemical oxidation reactions. In addition, the photoelectrochemical catalysis products will be analyzed through bulk electrolysis by the GC and IC.

In Chapter 5, it will introduce different M–N–Cs including 50%Cu–N–C, 50%Co–N–C, 50%Fe–N–C, and bimetal doped 25%Fe25%Co–N–C, 25%Co25%Mn–N–C, 25%Fe25%Cu–N–C, 25%Cu25%Co–N–C and metal free–N–C, which were synthesized by pyrolysis with transition metal (Fe, Co, Cu, Mn) and chitosan. Their performance on electrochemical CO<sub>2</sub>RR will be evaluated by RDE through comparison of the onset potential and reduction current. Furthermore, sodium thiocyanate (NaSCN) will be explored as a probe agent to understand the role of Fe moieties for identifying the active sites of 25%Fe25%Co–N–C for CO<sub>2</sub>RR.

In Chapter 6, general conclusions and outlook will be discussed. Although CuCo<sub>2</sub>O<sub>4</sub> exhibited promising PEC catalysis ability, its degradation under the super high light power inhibited its large-scale application. Thus, developing synergetic methods to enhance the long-term stability is imperative. Alternatively, CuBi<sub>2</sub>O<sub>4</sub> will be evaluated and compared with other spinel ternary transition metal oxides, which shown better stability under the UV-visible light, deserving a deep investigation in the application of PEC CO<sub>2</sub>RR.

## 1.6. References

- [1] Earth System Research Laboratory, Global greenhouse gas reference network: trends in atmospheric carbon dioxide, Global Greenhouse Gas Reference Network. (2020). <https://www.esrl.noaa.gov/gmd/ccgg/trends/global.html> (accessed May 26, 2020).
- [2] P.M. Cox, R.A. Betts, C.D. Jones, S.A. Spall, I.J. Totterdell, Acceleration of global warming due to carbon-cycle feedbacks in a coupled climate model, *Nature*. 408 (2000) 184–187. <https://doi.org/10.1038/35041539>.
- [3] B. Kumar, M. Llorente, J. Froehlich, T. Dang, A. Sathrum, C.P. Kubiak, Photochemical and photoelectrochemical reduction of CO<sub>2</sub>, *Annual Review of Physical Chemistry*. 63 (2012) 541–569. <https://doi.org/10.1146/annurev-physchem-032511-143759>.
- [4] N.S. Spinner, J.A. Vega, W.E. Mustain, Recent progress in the electrochemical conversion and utilization of CO<sub>2</sub>, *Catal. Sci. Technol.* 2 (2011) 19–28. <https://doi.org/10.1039/C1CY00314C>.
- [5] G. Centi, E.A. Quadrelli, S. Perathoner, Catalysis for CO<sub>2</sub> conversion: a key technology for rapid introduction of renewable energy in the value chain of chemical industries, *Energy Environ. Sci.* 6 (2013) 1711–1731. <https://doi.org/10.1039/C3EE00056G>.
- [6] R.J. Lim, M. Xie, M.A. Sk, J.M. Lee, A. Fisher, X. Wang, K.H. Lim, A review on the electrochemical reduction of CO<sub>2</sub> in fuel cells, metal electrodes and molecular catalysts, *Catalysis Today*. 233 (2014) 169–180. <https://doi.org/10.1016/j.cattod.2013.11.037>.
- [7] H.-R. “Molly” Jhong, S. Ma, P.J. Kenis, Electrochemical conversion of CO<sub>2</sub> to useful chemicals: current status, remaining challenges, and future opportunities, *Current Opinion in Chemical Engineering*. 2 (2013) 191–199. <https://doi.org/10.1016/j.coche.2013.03.005>.

- [8] W. Tu, Y. Zhou, Z. Zou, Photocatalytic conversion of CO<sub>2</sub> into renewable hydrocarbon fuels: state-of-the-art accomplishment, challenges, and prospects, *Advanced Materials*. 26 (2014) 4607–4626. <https://doi.org/10.1002/adma.201400087>.
- [9] M. Tahir, N.S. Amin, Recycling of carbon dioxide to renewable fuels by photocatalysis: prospects and challenges, *Renewable and Sustainable Energy Reviews*. 25 (2013) 560–579. <https://doi.org/10.1016/j.rser.2013.05.027>.
- [10] Z.-L. Wang, C. Li, Y. Yamauchi, Nanostructured nonprecious metal catalysts for electrochemical reduction of carbon dioxide, *Nano Today*. 11 (2016) 373–391. <https://doi.org/10.1016/j.nantod.2016.05.007>.
- [11] P. Markewitz, W. Kuckshinrichs, W. Leitner, J. Linssen, P. Zapp, R. Bongartz, A. Schreiber, T.E. Müller, Worldwide innovations in the development of carbon capture technologies and the utilization of CO<sub>2</sub>, *Energy Environ. Sci.* 5 (2012) 7281–7305. <https://doi.org/10.1039/C2EE03403D>.
- [12] B. Kumar, J.P. Brian, V. Atla, S. Kumari, K.A. Bertram, R.T. White, J.M. Spurgeon, New trends in the development of heterogeneous catalysts for electrochemical CO<sub>2</sub> reduction, *Catalysis Today*. 270 (2016) 19–30. <https://doi.org/10.1016/j.cattod.2016.02.006>.
- [13] E.E. Benson, C.P. Kubiak, A.J. Sathrum, J.M. Smieja, Electrocatalytic and homogeneous approaches to conversion of CO<sub>2</sub> to liquid fuels, *Chemical Society Reviews*. 38 (2009) 89–99. <https://doi.org/10.1039/b804323j>.
- [14] B. Qin, Y. Li, H. Wang, G. Yang, Y. Cao, H. Yu, Q. Zhang, H. Liang, F. Peng, Efficient electrochemical reduction of CO<sub>2</sub> into CO promoted by sulfur vacancies, *Nano Energy*. 60 (2019) 43–51. <https://doi.org/10.1016/j.nanoen.2019.03.024>.
- [15] L. Wei, H. Li, J. Chen, Z. Yuan, Q. Huang, X. Liao, G. Henkelman, Y. Chen, Thiocyanate-modified silver nanofoam for efficient CO<sub>2</sub> reduction to CO, *ACS Catal.* 10 (2020) 1444–1453. <https://doi.org/10.1021/acscatal.9b04633>.
- [16] G. Piao, S.H. Yoon, D.S. Han, H. Park, Ion-enhanced conversion of CO<sub>2</sub> into formate on porous dendritic bismuth electrodes with high efficiency and durability, *ChemSusChem*. 13 (2020) 698–706. <https://doi.org/10.1002/cssc.201902581>.
- [17] G. Díaz-Sainz, M. Alvarez-Guerra, J. Solla-Gullón, L. García-Cruz, V. Montiel, A. Irabien, CO<sub>2</sub> electroreduction to formate: Continuous single-pass operation in a filter-press reactor at high current densities using Bi gas diffusion electrodes, *Journal of CO<sub>2</sub> Utilization*. 34 (2019) 12–19. <https://doi.org/10.1016/j.jcou.2019.05.035>.
- [18] R.P.S. Chaplin, A.A. Wragg, Effects of process conditions and electrode material on reaction pathways for carbon dioxide electroreduction with particular reference to formate formation, *Journal of Applied Electrochemistry*. 33 (2003) 1107–1123. <https://doi.org/10.1023/B:JACH.00000004018.57792.b8>.
- [19] A. Guan, Z. Chen, Y. Quan, C. Peng, Z. Wang, T.-K. Sham, C. Yang, Y. Ji, L. Qian, X. Xu, G. Zheng, Boosting CO<sub>2</sub> electroreduction to CH<sub>4</sub> via tuning neighboring single-copper sites, *ACS Energy Lett.* (2020) 1044–1053. <https://doi.org/10.1021/acsenenergylett.0c00018>.
- [20] T. Zhang, S. Verma, S. Kim, T.T. Fister, P.J.A. Kenis, A.A. Gewirth, Highly dispersed, single-site copper catalysts for the electroreduction of CO<sub>2</sub> to methane, *Journal of Electroanalytical Chemistry*. (2020) 113862. <https://doi.org/10.1016/j.jelechem.2020.113862>.

- [21] J. Hazarika, M.S. Manna, Electrochemical reduction of CO<sub>2</sub> to methanol with synthesized Cu<sub>2</sub>O nanocatalyst: Study of the selectivity, *Electrochimica Acta*. 328 (2019) 135053. <https://doi.org/10.1016/j.electacta.2019.135053>.
- [22] J. Albo, G. Beobide, P. Castaño, A. Irabien, Methanol electrosynthesis from CO<sub>2</sub> at Cu<sub>2</sub>O/ZnO prompted by pyridine-based aqueous solutions, *Journal of CO<sub>2</sub> Utilization*. 18 (2017) 164–172. <https://doi.org/10.1016/j.jcou.2017.02.003>.
- [23] J. Yuan, M.-P. Yang, W.-Y. Zhi, H. Wang, H. Wang, J.-X. Lu, Efficient electrochemical reduction of CO<sub>2</sub> to ethanol on Cu nanoparticles decorated on N-doped graphene oxide catalysts, *Journal of CO<sub>2</sub> Utilization*. 33 (2019) 452–460. <https://doi.org/10.1016/j.jcou.2019.07.014>.
- [24] X. Su, Y. Sun, L. Jin, L. Zhang, Y. Yang, P. Kerns, B. Liu, S. Li, J. He, Hierarchically porous Cu/Zn bimetallic catalysts for highly selective CO<sub>2</sub> electroreduction to liquid C<sub>2</sub> products, *Applied Catalysis B: Environmental*. 269 (2020) 118800. <https://doi.org/10.1016/j.apcatb.2020.118800>.
- [25] Y. Gao, Q. Wu, X. Liang, Z. Wang, Z. Zheng, P. Wang, Y. Liu, Y. Dai, M.-H. Whangbo, B. Huang, Cu<sub>2</sub>O nanoparticles with both {100} and {111} facets for enhancing the selectivity and activity of CO<sub>2</sub> electroreduction to ethylene, *Advanced Science*. 7 (2020) 1902820. <https://doi.org/10.1002/advs.201902820>.
- [26] K. Zhao, X. Nie, H. Wang, S. Chen, X. Quan, H. Yu, W. Choi, G. Zhang, B. Kim, J.G. Chen, Selective electroreduction of CO<sub>2</sub> to acetone by single copper atoms anchored on N-doped porous carbon, *Nature Communications*. 11 (2020) 2455. <https://doi.org/10.1038/s41467-020-16381-8>.
- [27] G. Centi, S. Perathoner, Towards solar fuels from water and CO<sub>2</sub>, *ChemSusChem*. 3 (2010) 195–208. <https://doi.org/10.1002/cssc.200900289>.
- [28] P.J. Kulesza, I.A. Rutkowska, A. Wadas, Electrocatalytic and photoelectrochemical reduction of carbon dioxide in aqueous media: toward generation of fuels and utility chemicals, Elsevier, 2017. <https://doi.org/10.1016/B978-0-12-409547-2.14132-0>.
- [29] S. Xie, Q. Zhang, G. Liu, Y. Wang, Photocatalytic and photoelectrocatalytic reduction of CO<sub>2</sub> using heterogeneous catalysts with controlled nanostructures, *Chem. Commun*. 52 (2015) 35–59. <https://doi.org/10.1039/C5CC07613G>.
- [30] A. Fujishima, K. Honda, Electrochemical photolysis of water at a semiconductor electrode, *Nature*. 238 (1972) 37–38. <https://doi.org/10.1038/238037a0>.
- [31] M. Halmann, Photoelectrochemical reduction of aqueous carbon dioxide on p-type gallium phosphide in liquid junction solar cells, *Nature*. 275 (1978) 115–116. <https://doi.org/10.1038/275115a0>.
- [32] J.L. White, M.F. Baruch, J.E. Pander, Y. Hu, I.C. Fortmeyer, J.E. Park, T. Zhang, K. Liao, J. Gu, Y. Yan, T.W. Shaw, E. Abelev, A.B. Bocarsly, Light-driven heterogeneous reduction of carbon dioxide: photocatalysts and photoelectrodes, *Chem. Rev*. 115 (2015) 12888–12935. <https://doi.org/10.1021/acs.chemrev.5b00370>.
- [33] Q. Shen, Z. Chen, X. Huang, M. Liu, G. Zhao, High-yield and selective photoelectrocatalytic reduction of CO<sub>2</sub> to formate by metallic copper decorated Co<sub>3</sub>O<sub>4</sub> nanotube arrays, *Environ. Sci. Technol*. 49 (2015) 5828–5835. <https://doi.org/10.1021/acs.est.5b00066>.
- [34] Q. Lu, F. Jiao, Electrochemical CO<sub>2</sub> reduction: Electrocatalyst, reaction mechanism, and process engineering, *Nano Energy*. 29 (2016) 439–456. <https://doi.org/10.1016/j.nanoen.2016.04.009>.

- [35] D. Ren, J. Fong, B.S. Yeo, The effects of currents and potentials on the selectivities of copper toward carbon dioxide electroreduction, *Nature Communications*. 9 (2018) 925 doi:10.1038/s41467-018-03286-w. <https://doi.org/10.1038/s41467-018-03286-w>.
- [36] V. Kumaravel, J. Bartlett, S.C. Pillai, Photoelectrochemical conversion of carbon dioxide (CO<sub>2</sub>) into fuels and value-added products, *ACS Energy Lett.* 5 (2020) 486–519. <https://doi.org/10.1021/acsenenergylett.9b02585>.
- [37] A.A. Peterson, F. Abild-Pedersen, F. Studt, J. Rossmeisl, J.K. Nørskov, How copper catalyzes the electroreduction of carbon dioxide into hydrocarbon fuels, *Energy Environ. Sci.* 3 (2010) 1311–1315. <https://doi.org/10.1039/C0EE00071J>.
- [38] C.M. Sánchez-Sánchez, V. Montiel, D.A. Tryk, A. Aldaz, A. Fujishima, Electrochemical approaches to alleviation of the problem of carbon dioxide accumulation, *Pure and Applied Chemistry*. 73 (2001) 1917–1927. <https://doi.org/10.1351/pac200173121917>.
- [39] J. Qiao, Y. Liu, F. Hong, J. Zhang, A review of catalysts for the electroreduction of carbon dioxide to produce low-carbon fuels, *Chem. Soc. Rev.* 43 (2014) 631–675. <https://doi.org/10.1039/C3CS60323G>.
- [40] J. Albo, D. Vallejo, G. Beobide, O. Castillo, P. Castaño, A. Irabien, Copper-based metal–organic porous materials for CO<sub>2</sub> electrocatalytic reduction to alcohols, *ChemSusChem*. 10 (2017) 1100–1109. <https://doi.org/10.1002/cssc.201600693>.
- [41] Y. Huo, X. Peng, X. Liu, H. Li, J. Luo, High selectivity toward C<sub>2</sub>H<sub>4</sub> production over Cu particles supported by butterfly-wing-derived carbon frameworks, *ACS Applied Materials & Interfaces*. 10 (2018) 12618–12625. <https://doi.org/10.1021/acsami.7b19423>.
- [42] F. Zhang, A.C. Co, Direct evidence of local pH change and the role of alkali cation during CO<sub>2</sub> electroreduction in aqueous media, *Angewandte Chemie International Edition*. (2019). <https://doi.org/10.1002/anie.201912637>.
- [43] S.Y. Chae, S.Y. Lee, O.-S. Joo, Directly synthesized silver nanoparticles on gas diffusion layers by electrospray pyrolysis for electrochemical CO<sub>2</sub> reduction, *Electrochimica Acta*. 303 (2019) 118–124. <https://doi.org/10.1016/j.electacta.2019.02.046>.
- [44] W. Luo, J. Zhang, M. Li, A. Züttel, Boosting CO production in electrocatalytic CO<sub>2</sub> reduction on highly porous Zn catalysts, *ACS Catal.* 9 (2019) 3783–3791. <https://doi.org/10.1021/acscatal.8b05109>.
- [45] J.E. Pander, J.W.J. Lum, B.S. Yeo, The importance of morphology on the activity of lead cathodes for the reduction of carbon dioxide to formate, *J. Mater. Chem. A*. 7 (2019) 4093–4101. <https://doi.org/10.1039/C8TA10752A>.
- [46] B. Bohlen, D. Wastl, J. Radomski, V. Sieber, L. Vieira, Electrochemical CO<sub>2</sub> reduction to formate on indium catalysts prepared by electrodeposition in deep eutectic solvents, *Electrochemistry Communications*. 110 (2020) 106597. <https://doi.org/10.1016/j.elecom.2019.106597>.
- [47] Q. Lai, W. Yuan, W. Huang, G. Yuan, Sn/SnO<sub>x</sub> electrode catalyst with mesoporous structure for efficient electroreduction of CO<sub>2</sub> to formate, *Applied Surface Science*. 508 (2020) 145221. <https://doi.org/10.1016/j.apsusc.2019.145221>.
- [48] Y. Lum, B. Yue, P. Lobaccaro, A.T. Bell, J.W. Ager, Optimizing C-C coupling on oxide-derived copper catalysts for electrochemical CO<sub>2</sub> reduction, *J. Phys. Chem. C*. 121 (2017) 14191–14203. <https://doi.org/10.1021/acs.jpcc.7b03673>.

- [49] T. Inoue, A. Fujishima, S. Konishi, K. Honda, Photoelectrocatalytic reduction of carbon dioxide in aqueous suspensions of semiconductor powders, *Nature*. 277 (1979) 637–638. <https://doi.org/10.1038/277637a0>.
- [50] E.E. Barton, D.M. Rampulla, A.B. Bocarsly, Selective solar-driven reduction of CO<sub>2</sub> to methanol using a catalyzed p-GaP based photoelectrochemical cell, *J. Am. Chem. Soc.* 130 (2008) 6342–6344. <https://doi.org/10.1021/ja0776327>.
- [51] F.P. García de Arquer, C.-T. Dinh, A. Ozden, J. Wicks, C. McCallum, A.R. Kirmani, D.-H. Nam, C. Gabardo, A. Seifitokaldani, X. Wang, Y.C. Li, F. Li, J. Edwards, L.J. Richter, S.J. Thorpe, D. Sinton, E.H. Sargent, CO<sub>2</sub> electrolysis to multicarbon products at activities greater than 1 A cm<sup>-2</sup>, *Science*. 367 (2020) 661–666. <https://doi.org/10.1126/science.aay4217>.
- [52] C.M. Sánchez-Sánchez, Electrocatalytic reduction of CO<sub>2</sub> in imidazolium based ionic liquids, In: Wandelt, K., (Ed.) *Encyclopedia of Interfacial Chemistry: Surface Science and Electrochemistry*. 5 (2018) 539–551.
- [53] S. Supasitmongkol, P. Styring, High CO<sub>2</sub> solubility in ionic liquids and a tetraalkylammonium-based poly(ionic liquid), *Energy Environ. Sci.* 3 (2010) 1961–1972. <https://doi.org/10.1039/C0EE00293C>.
- [54] R. Kas, R. Kortlever, H. Yılmaz, M.T.M. Koper, G. Mul, Manipulating the hydrocarbon selectivity of copper nanoparticles in CO<sub>2</sub> electroreduction by process conditions, *ChemElectroChem*. 2 (2015) 354–358. <https://doi.org/10.1002/celec.201402373>.
- [55] A.S. Varela, M. Kroschel, T. Reier, P. Strasser, Controlling the selectivity of CO<sub>2</sub> electroreduction on copper: The effect of the electrolyte concentration and the importance of the local pH, *Catalysis Today*. 260 (2016) 8–13. <https://doi.org/10.1016/j.cattod.2015.06.009>.
- [56] A.S. Varela, W. Ju, T. Reier, P. Strasser, Tuning the catalytic activity and selectivity of Cu for CO<sub>2</sub> electroreduction in the presence of halides, *ACS Catalysis*. 6 (2016) 2136–2144. <https://doi.org/10.1021/acscatal.5b02550>.
- [57] Y.Y. Birdja, E. Pérez-Gallent, M.C. Figueiredo, A.J. Göttele, F. Calle-Vallejo, M.T.M. Koper, Advances and challenges in understanding the electrocatalytic conversion of carbon dioxide to fuels, *Nat Energy*. 4 (2019) 732–745. <https://doi.org/10.1038/s41560-019-0450-y>.
- [58] A.J. Bard, F.R.F. Fan, Juhyoun. Kwak, Ovadia. Lev, Scanning electrochemical microscopy. Introduction and principles, *Anal. Chem.* 61 (1989) 132–138. <https://doi.org/10.1021/ac00177a011>.
- [59] R.C. Engstrom, C.M. Pharr, Scanning electrochemical microscopy, *Anal. Chem.* 61 (1989) 1099A – 1104. <https://doi.org/10.1021/ac00194a735>.
- [60] A.J. Bard, M.V. Mirkin, Scanning electrochemical microscopy, CRC Press, 2012.
- [61] D. Polcari, P. Dauphin-Ducharme, J. Mauzeroll, Scanning electrochemical microscopy: a comprehensive review of experimental parameters from 1989 to 2015, *Chem. Rev.* 116 (2016) 13234–13278. <https://doi.org/10.1021/acs.chemrev.6b00067>.
- [62] S. Amemiya, A.J. Bard, F.-R.F. Fan, M.V. Mirkin, P.R. Unwin, Scanning electrochemical microscopy, *Annual Rev. Anal. Chem.* 1 (2008) 95–131. <https://doi.org/10.1146/annurev.anchem.1.031207.112938>.
- [63] P. Bertoncello, Advances on scanning electrochemical microscopy (SECM) for energy, *Energy Environ. Sci.* 3 (2010) 1620–1633. <https://doi.org/10.1039/C0EE00046A>.

- [64] J.V. Macpherson, P.R. Unwin, Combined scanning electrochemical-atomic force microscopy, *Anal. Chem.* 72 (2000) 276–285. <https://doi.org/10.1021/ac990921w>.
- [65] M.A. O’Connell, Combined electrochemical-topographical imaging: a critical review, *Analytical Methods*. (2015) 17.
- [66] I. Beaulieu, S. Kuss, J. Mauzeroll, M. Geissler, Biological scanning electrochemical microscopy and its application to live cell studies, *Anal. Chem.* 83 (2011) 1485–1492. <https://doi.org/10.1021/ac101906a>.
- [67] Y. Takahashi, A.I. Shevchuk, P. Novak, Y. Murakami, H. Shiku, Y.E. Korchev, T. Matsue, Simultaneous noncontact topography and electrochemical imaging by SECM/SICM featuring ion current feedback regulation, *J. Am. Chem. Soc.* 132 (2010) 10118–10126. <https://doi.org/10.1021/ja1029478>.
- [68] Y. Lee, Z. Ding, A.J. Bard, Combined scanning electrochemical/optical microscopy with shear force and current feedback, *Anal. Chem.* 74 (2002) 3634–3643. <https://doi.org/10.1021/ac015713u>.
- [69] J. Lee, H. Ye, S. Pan, A.J. Bard, Screening of photocatalysts by scanning electrochemical microscopy, *Analytical Chemistry*. 80 (2008) 7445–7450. <https://doi.org/10.1021/ac801142g>.
- [70] A.J. Wain, Scanning electrochemical microscopy for combinatorial screening applications: A mini-review, *Electrochemistry Communications*. 46 (2014) 9–12. <https://doi.org/10.1016/j.elecom.2014.05.028>.
- [71] D. Hynek, M. Zurek, P. Babula, V. Adam, R. Kizek, Monitoring of the surface modification of nanoparticles by electrochemical measurements using scanning electrochemical microscope, in: M. Aliofkhazraei (Ed.), *Modern Electrochemical Methods in Nano, Surface and Corrosion Science*, InTech, 2014. <https://doi.org/10.5772/57203>.
- [72] M.A. Edwards, S. Martin, A.L. Whitworth, J.V. Macpherson, P.R. Unwin, Scanning electrochemical microscopy: principles and applications to biophysical systems, *Physiol. Meas.* 27 (2006) R63–R108. <https://doi.org/10.1088/0967-3334/27/12/R01>.
- [73] L. Danis, D. Polcari, A. Kwan, S.M. Gateman, J. Mauzeroll, Fabrication of carbon, gold, platinum, silver, and mercury ultramicroelectrodes with controlled geometry, *Anal. Chem.* 87 (2015) 2565–2569. <https://doi.org/10.1021/ac503767n>.
- [74] F.-R.F. Fan, A.J. Bard, R. Guckenberger, M. Heim, STM on wet insulators: electrochemistry or tunneling?, *Science*. 270 (1995) 1849–1852.
- [75] Y. Lee, S. Amemiya, A.J. Bard, Scanning electrochemical microscopy. 41. theory and characterization of ring electrodes, *Anal. Chem.* 73 (2001) 2261–2267. <https://doi.org/10.1021/ac0014764>.
- [76] J. Mauzeroll, E.A. Hueske, A.J. Bard, Scanning electrochemical microscopy. 48. Hg/Pt hemispherical ultramicroelectrodes: fabrication and characterization, *Anal. Chem.* 75 (2003) 3880–3889. <https://doi.org/10.1021/ac034088l>.
- [77] M.V. Mirkin, F.-R.F. Fan, A.J. Bard, Scanning electrochemical microscopy part 13. Evaluation of the tip shapes of nanometer size microelectrodes, *Journal of Electroanalytical Chemistry*. 328 (1992) 47–62. [https://doi.org/10.1016/0022-0728\(92\)80169-5](https://doi.org/10.1016/0022-0728(92)80169-5).
- [78] C.G. Zoski, Ultramicroelectrodes: design, fabrication, and characterization, *Electroanalysis*. 14 (2002) 1041–1051. [https://doi.org/10.1002/1521-4109\(200208\)14:15/16<1041::AID-ELAN1041>3.0.CO;2-8](https://doi.org/10.1002/1521-4109(200208)14:15/16<1041::AID-ELAN1041>3.0.CO;2-8).



- [79] C.G. Zoski, ed., Handbook of electrochemistry, 1st ed, Elsevier, Amsterdam ; Boston, 2007.
- [80] G. Wittstock, M. Burchardt, S.E. Pust, Y. Shen, C. Zhao, Scanning electrochemical microscopy for direct imaging of reaction rates, *Angewandte Chemie International Edition*. 46 (2007) 1584–1617. <https://doi.org/10.1002/anie.200602750>.
- [81] D.A. Walsh, K.R.J. Lovelock, P. Licence, Ultramicroelectrode voltammetry and scanning electrochemical microscopy in room-temperature ionic liquid electrolytes, *Chem. Soc. Rev.* 39 (2010) 4185. <https://doi.org/10.1039/b822846a>.
- [82] C. Kranz, Recent advancements in nanoelectrodes and nanopipettes used in combined scanning electrochemical microscopy techniques, *Analyst*. 139 (2013) 336–352. <https://doi.org/10.1039/C3AN01651J>.
- [83] C.G. Zoski, M. Wijesinghe, Electrochemistry at ultramicroelectrode arrays and nanoelectrode ensembles of macro- and ultramicroelectrode dimensions, *Israel Journal of Chemistry*. 50 (2010) 347–359. <https://doi.org/10.1002/ijch.201000025>.
- [84] B.B. Katemann, W. Schuhmann, Fabrication and characterization of needle-type Pt-disk nanoelectrodes, *Electroanalysis*. 14 (2002) 22–28. [https://doi.org/10.1002/1521-4109\(200201\)14:1<22::AID-ELAN22>3.0.CO;2-F](https://doi.org/10.1002/1521-4109(200201)14:1<22::AID-ELAN22>3.0.CO;2-F).
- [85] S.K. Cho, H.S. Park, H.C. Lee, K.M. Nam, A.J. Bard, Metal doping of BiVO<sub>4</sub> by composite electrodeposition with improved photoelectrochemical water oxidation, *J. Phys. Chem. C*. 117 (2013) 23048–23056. <https://doi.org/10.1021/jp408619u>.
- [86] V. Badets, G. Loget, P. Garrigue, N. Sojic, D. Zigah, Combined local anodization of titanium and scanning photoelectrochemical mapping of TiO<sub>2</sub> spot arrays, *Electrochimica Acta*. 222 (2016) 84–91. <https://doi.org/10.1016/j.electacta.2016.10.151>.
- [87] S. Morandi, A. Minguzzi, The cavity-microelectrode as a tip for scanning electrochemical microscopy, *Electrochemistry Communications*. 59 (2015) 100–103. <https://doi.org/10.1016/j.elecom.2015.07.010>.
- [88] L. Danis, M.E. Snowden, U.M. Tefashe, C.N. Heinemann, J. Mauzeroll, Development of nano-disc electrodes for application as shear force sensitive electrochemical probes, *Electrochimica Acta*. 136 (2014) 121–129. <https://doi.org/10.1016/j.electacta.2014.05.047>.
- [89] B. Liu, A.J. Bard, M.V. Mirkin, S.E. Creager, Electron transfer at self-assembled monolayers measured by scanning electrochemical microscopy, *J. Am. Chem. Soc.* 126 (2004) 1485–1492. <https://doi.org/10.1021/ja038611p>.
- [90] C. Lefrou, R. Cornut, Analytical expressions for quantitative scanning electrochemical microscopy (SECM), *ChemPhysChem*. 11 (2010) 547–556. <https://doi.org/10.1002/cphc.200900600>.
- [91] F. Zhou, P.R. Unwin, A.J. Bard, Scanning electrochemical microscopy. 16. study of second-order homogeneous chemical reactions via the feedback and generation/collection modes, *J. Phys. Chem.* 96 (1992) 4917–4924. <https://doi.org/10.1021/j100191a036>.
- [92] C.M. Sánchez-Sánchez, F.J. Vidal-Iglesias, J. Solla-Gullón, V. Montiel, A. Aldaz, J.M. Feliu, E. Herrero, Scanning electrochemical microscopy for studying electrocatalysis on shape-controlled gold nanoparticles and nanorods, *Electrochimica Acta*. 55 (2010) 8252–8257. <https://doi.org/10.1016/j.electacta.2010.04.010>.
- [93] C. Jung, C.M. Sánchez-Sánchez, C.-L. Lin, J. Rodríguez-López, A.J. Bard, Electrocatalytic activity of Pd–Co bimetallic mixtures for formic acid oxidation studied by scanning electrochemical microscopy, *Anal. Chem.* 81 (2009) 7003–7008. <https://doi.org/10.1021/ac901096h>.

- [94] C.M. Sánchez-Sánchez, J. Rodríguez-López, A.J. Bard, Scanning electrochemical microscopy. 60. quantitative calibration of the SECM substrate generation/tip collection mode and its use for the study of the oxygen reduction mechanism, *Anal. Chem.* 80 (2008) 3254–3260. <https://doi.org/10.1021/ac702453n>.
- [95] Y. Shen, M. Träuble, G. Wittstock, Detection of hydrogen peroxide produced during electrochemical oxygen reduction using scanning electrochemical microscopy, *Anal. Chem.* 80 (2008) 750–759. <https://doi.org/10.1021/ac0711889>.
- [96] C.M. Sánchez-Sánchez, J. Solla-Gullón, F.J. Vidal-Iglesias, A. Aldaz, V. Montiel, E. Herrero, Imaging structure sensitive catalysis on different shape-controlled platinum nanoparticles, *Journal of the American Chemical Society.* 132 (2010) 5622–5624. <https://doi.org/10.1021/ja100922h>.
- [97] S. Narayanaru, J. Chinnaiyah, K.L. Phani, F. Scholz, pH dependent CO adsorption and roughness-induced selectivity of CO<sub>2</sub> electroreduction on gold surfaces, *Electrochimica Acta.* 264 (2018) 269–274. <https://doi.org/10.1016/j.electacta.2018.01.106>.
- [98] D.A. Walsh, J.L. Fernández, J. Mauzeroll, A.J. Bard, Scanning electrochemical microscopy. 55. fabrication and characterization of micropipet probes, *Anal. Chem.* 77 (2005) 5182–5188. <https://doi.org/10.1021/ac0505122>.
- [99] D. Zhan, X. Li, W. Zhan, F.-R.F. Fan, A.J. Bard, Scanning electrochemical microscopy. 58. application of a micropipet-supported ITIES tip to detect Ag<sup>+</sup> and study its effect on fibroblast cells, *Anal. Chem.* 79 (2007) 5225–5231. <https://doi.org/10.1021/ac070318a>.
- [100] C.-L. Lin, J. Rodríguez-López, A.J. Bard, Micropipet delivery–substrate collection mode of scanning electrochemical microscopy for the imaging of electrochemical reactions and the screening of methanol oxidation electrocatalysts, *Anal. Chem.* 81 (2009) 8868–8877. <https://doi.org/10.1021/ac901434a>.
- [101] K. Eckhard, X. Chen, F. Turcu, W. Schuhmann, Redox competition mode of scanning electrochemical microscopy (RC-SECM) for visualisation of local catalytic activity, *Phys. Chem. Chem. Phys.* 8 (2006) 5359–5365. <https://doi.org/10.1039/B609511A>.
- [102] J.J. Santana, J. González-Guzmán, L. Fernández-Mérida, S. González, R.M. Souto, Visualization of local degradation processes in coated metals by means of scanning electrochemical microscopy in the redox competition mode, *Electrochimica Acta.* 55 (2010) 4488–4494. <https://doi.org/10.1016/j.electacta.2010.02.091>.
- [103] K. Karnicka, K. Eckhard, D.A. Guschin, L. Stoica, P.J. Kulesza, W. Schuhmann, Visualisation of the local bio-electrocatalytic activity in biofuel cell cathodes by means of redox competition scanning electrochemical microscopy (RC-SECM), *Electrochemistry Communications.* 9 (2007) 1998–2002. <https://doi.org/10.1016/j.elecom.2007.05.015>.
- [104] L. Guadagnini, A. Maljusch, X. Chen, S. Neugebauer, D. Tonelli, W. Schuhmann, Visualization of electrocatalytic activity of microstructured metal hexacyanoferrates by means of redox competition mode of scanning electrochemical microscopy (RC-SECM), *Electrochimica Acta.* 54 (2009) 3753–3758. <https://doi.org/10.1016/j.electacta.2009.01.076>.
- [105] C. Lettmann, H. Hinrichs, W.F. Maier, Combinatorial discovery of new photocatalysts for water purification with visible light, *Angewandte Chemie International Edition.* 40 (2001) 3160–3164. [https://doi.org/10.1002/1521-3773\(20010903\)40:17<3160::AID-ANIE3160>3.0.CO;2-Z](https://doi.org/10.1002/1521-3773(20010903)40:17<3160::AID-ANIE3160>3.0.CO;2-Z).
- [106] S.M. Fonseca, A.L. Barker, S. Ahmed, T.J. Kemp, P.R. Unwin, Direct observation of oxygen depletion and product formation during photocatalysis at a TiO<sub>2</sub> surface using

- p scanning electrochemical microscopy, Chem. Commun. (2003) 1002–1003.
- <https://doi.org/10.1039/B212222G>
- .
- [107] D. Zigah, J. Rodríguez-López, A.J. Bard, Quantification of photoelectrogenerated hydroxyl radical on TiO<sub>2</sub> by surface interrogation scanning electrochemical microscopy, Phys. Chem. Chem. Phys. 14 (2012) 12764–12772. <https://doi.org/10.1039/C2CP40907K>.
- [108] F. Conzuelo, K. Sliozberg, R. Gutkowski, S. Grütze, M. Nebel, W. Schuhmann, High-resolution analysis of photoanodes for water splitting by means of scanning photoelectrochemical microscopy, Analytical Chemistry. 89 (2017) 1222–1228. <https://doi.org/10.1021/acs.analchem.6b03706>.
- [109] S.P. Berglund, H.C. Lee, P.D. Núñez, A.J. Bard, C.B. Mullins, Screening of transition and post-transition metals to incorporate into copper oxide and copper bismuth oxide for photoelectrochemical hydrogen evolution, Physical Chemistry Chemical Physics. 15 (2013) 4554–4565.
- [110] H.C. Lee, S.K. Cho, H.S. Park, K.M. Nam, A.J. Bard, Visible light photoelectrochemical properties of PbCrO<sub>4</sub>, Pb<sub>2</sub>CrO<sub>5</sub>, and Pb<sub>5</sub>CrO<sub>8</sub>, Journal of Physical Chemistry C. 121 (2017) 17561–17568. <https://doi.org/10.1021/acs.jpcc.7b03230>.
- [111] K.M. Nam, H.S. Park, H.C. Lee, B.H. Meekins, K.C. Leonard, A.J. Bard, Compositional screening of the Pb-Bi-Mo-O system. Spontaneous formation of a composite of *p*-PbMoO<sub>4</sub> and *n*-Bi<sub>2</sub>O<sub>3</sub> with improved photoelectrochemical efficiency and stability, Journal of Physical Chemistry Letters. 4 (2013) 2707–2710. <https://doi.org/10.1021/jz401334k>.
- [112] H.S. Park, K.E. Kweon, H. Ye, E. Paek, G.S. Hwang, A.J. Bard, Factors in the metal doping of BiVO<sub>4</sub> for improved photoelectrocatalytic activity as studied by scanning electrochemical microscopy and first-principles density-functional calculation, J. Phys. Chem. C. 115 (2011) 17870–17879. <https://doi.org/10.1021/jp204492r>.
- [113] D.V. Esposito, J.B. Baxter, J. John, N.S. Lewis, T.P. Moffat, T. Ogitsu, G.D. O’Neil, T.A. Pham, A.A. Talin, J.M. Velazquez, B.C. Wood, Methods of photoelectrode characterization with high spatial and temporal resolution, Energy Environ. Sci. 8 (2015) 2863–2885. <https://doi.org/10.1039/C5EE00835B>.
- [114] D.V. Esposito, I. Levin, T.P. Moffat, A.A. Talin, H<sub>2</sub> evolution at Si-based metal–insulator–semiconductor photoelectrodes enhanced by inversion channel charge collection and H spillover, Nature Mater. 12 (2013) 562–568. <https://doi.org/10.1038/nmat3626>.
- [115] L. Huang, Z. Li, Y. Lou, F. Cao, D. Zhang, X. Li, Recent advances in scanning electrochemical microscopy for biological applications, Materials. 11 (2018) 1389. <https://doi.org/10.3390/ma11081389>.
- [116] L. Han, Y. Yuan, J. Zhang, X. Zhao, Y. Cao, Z. Hu, Y. Yan, S. Dong, Z.-Q. Tian, Z.-W. Tian, D. Zhan, A leveling method based on current feedback mode of scanning electrochemical microscopy, Anal. Chem. 85 (2013) 1322–1326. <https://doi.org/10.1021/ac303122v>.
- [117] L. Niu, Y. Yin, W. Guo, M. Lu, R. Qin, S. Chen, Application of scanning electrochemical microscope in the study of corrosion of metals, J Mater Sci. 44 (2009) 4511–4521. <https://doi.org/10.1007/s10853-009-3654-x>.
- [118] A. Minguzzi, M.A. Alpuche-Aviles, J.R. López, S. Rondinini, A.J. Bard, Screening of oxygen evolution electrocatalysts by scanning electrochemical microscopy using a shielded tip approach, (2008). <https://doi.org/10.1021/ac8001287>.

- [119] B. Liu, A.J. Bard, Scanning electrochemical microscopy. 45. study of the kinetics of oxygen reduction on platinum with potential programming of the tip, *J. Phys. Chem. B.* 106 (2002) 12801–12806. <https://doi.org/10.1021/jp026824f>.
- [120] J.L. Fernández, A.J. Bard, Scanning electrochemical microscopy. 47. imaging electrocatalytic activity for oxygen reduction in an acidic medium by the tip generation-substrate collection mode, *Anal. Chem.* 75 (2003) 2967–2974. <https://doi.org/10.1021/ac0340354>.
- [121] N. Sreekanth, K.L. Phani, Selective reduction of CO<sub>2</sub> to formate through bicarbonate reduction on metal electrodes: new insights gained from SG/TC mode of SECM, *Chem. Commun.* 50 (2014) 11143–11146. <https://doi.org/10.1039/C4CC03099K>.
- [122] D. Filotás, T. Nagy, L. Nagy, P. Mizsey, G. Nagy, Extended investigation of electrochemical CO<sub>2</sub> reduction in ethanolamine solutions by SECM, *Electroanalysis.* 30 (2018) 690–697. <https://doi.org/10.1002/elan.201700693>.
- [123] T. Kai, M. Zhou, Z. Duan, G.A. Henkelman, A.J. Bard, Detection of CO<sub>2</sub><sup>•-</sup> in the electrochemical reduction of carbon dioxide in *N,N*-Dimethylformamide by scanning electrochemical microscopy, *J. Am. Chem. Soc.* 139 (2017) 18552–18557. <https://doi.org/10.1021/jacs.7b08702>.
- [124] P.S. Shinde, X. Peng, J. Wang, Y. Ma, L.E. McNamara, N.I. Hammer, A. Gupta, S. Pan, Rapid screening of photoanode materials using scanning photoelectrochemical microscopy technique and formation of Z-scheme solar water splitting system by coupling p- and n-type heterojunction photoelectrodes, *ACS Appl. Energy Mater.* 1 (2018) 2283–2294. <https://doi.org/10.1021/acsaem.8b00381>.
- [125] C. Bhattacharya, H.C. Lee, A.J. Bard, Rapid screening by scanning electrochemical microscopy (SECM) of dopants for Bi<sub>2</sub>WO<sub>6</sub> improved photocatalytic water oxidation with Zn doping, *J. Phys. Chem. C.* 117 (2013) 9633–9640. <https://doi.org/10.1021/jp308629q>.
- [126] H.-Y. Hsu, L. Ji, M. Du, J. Zhao, E.T. Yu, A.J. Bard, Optimization of PbI<sub>2</sub>/MAPbI<sub>3</sub> perovskite composites by scanning electrochemical microscopy, *J. Phys. Chem. C.* 120 (2016) 19890–19895. <https://doi.org/10.1021/acs.jpcc.6b07850>.
- [127] M. Gattrell, N. Gupta, A. Co, A review of the aqueous electrochemical reduction of CO<sub>2</sub> to hydrocarbons at copper, *Journal of Electroanalytical Chemistry.* 594 (2006) 1–19. <https://doi.org/10.1016/j.jelechem.2006.05.013>.
- [128] P. WALDEN, Molecular weights and electrical conductivity of several fused salts, *Bull. Acad. Imper. Sci. (St. Petersburg).* 1800 (1914). <https://ci.nii.ac.jp/naid/10025720020/> (accessed May 13, 2020).
- [129] J.S. Wilkes, M.J. Zaworotko, Air and water stable 1-ethyl-3-methylimidazolium based ionic liquids, *J. Chem. Soc., Chem. Commun.* (1992) 965–967. <https://doi.org/10.1039/C39920000965>.
- [130] N.V. Plechkova, K.R. Seddon, Applications of ionic liquids in the chemical industry, *Chem. Soc. Rev.* 37 (2008) 123–150. <https://doi.org/10.1039/B006677J>.
- [131] T.L. Greaves, C.J. Drummond, Protic ionic liquids: properties and applications, *Chemical Reviews.* 108 (2008) 206–237.
- [132] P. Hapiot, C. Lagrost, Electrochemical reactivity in room-temperature ionic liquids electrochemical reactivity in room-temperature Ionic liquids, *Chem. Rev.* 108 (2008) 2238–2264. <https://doi.org/10.1021/cr0680686>.
- [133] R. Khalil, Electrodéposition de ZnO en milieux liquides ioniques: études physico-chimiques des différentes étapes, (2018).

- [134] T. Gutel, Les liquides ioniques, leur utilisation et leur role comme solvants de réaction catalytique, phdthesis, Université Claude Bernard-Lyon I, 2007. <https://tel.archives-ouvertes.fr/tel-00182860> (accessed May 14, 2020).
- [135] T. Mu, B. Han, Structures and thermodynamic properties of ionic liquids, in: S. Zhang, J. Wang, X. Lu, Q. Zhou (Eds.), Structures and Interactions of Ionic Liquids, Springer, Berlin, Heidelberg, 2014: pp. 107–139. [https://doi.org/10.1007/978-3-642-38619-0\\_4](https://doi.org/10.1007/978-3-642-38619-0_4).
- [136] K.R. Seddon, A. Stark, M.-J. Torres, Influence of chloride, water, and organic solvents on the physical properties of ionic liquids, *Pure and Applied Chemistry*. 72 (2000) 2275–2287. <https://doi.org/10.1351/pac200072122275>.
- [137] U. Schröder, J.D. Wadhawan, R.G. Compton, F. Marken, P.A.Z. Suarez, C.S. Consorti, R.F. de Souza, J. Dupont, Water-induced accelerated ion diffusion: voltammetric studies in 1-methyl-3-[2,6-(S)-dimethylocten-2-yl]imidazolium tetrafluoroborate, 1-butyl-3-methylimidazolium tetrafluoroborate and hexafluorophosphate ionic liquids, *New J. Chem.* 24 (2000) 1009–1015. <https://doi.org/10.1039/b007172m>.
- [138] M. Galiński, A. Lewandowski, I. Stepniak, Ionic liquids as electrolytes, *Electrochimica Acta*. 51 (2006) 5567–5580. <https://doi.org/10.1016/j.electacta.2006.03.016>.
- [139] J. Lin, Z. Ding, Y. Hou, X. Wang, Ionic liquid co-catalyzed artificial photosynthesis of CO, *Sci Rep.* 3 (2013) 1056. <https://doi.org/10.1038/srep01056>.
- [140] G.P.S. Lau, M. Schreier, D. Vasilyev, R. Scopelliti, M. Grätzel, P.J. Dyson, New insights into the role of imidazolium based promoters for the electroreduction of CO<sub>2</sub> on a silver electrode, *Journal of the American Chemical Society*. 138 (2016) 7820–7823. <https://doi.org/10.1021/jacs.6b03366>.
- [141] R.D. Rogers, CHEMISTRY: Ionic liquids-Solvents of the future?, *Science*. 302 (2003) 792–793. <https://doi.org/10.1126/science.1090313>.
- [142] P. Wang, S.M. Zakeeruddin, J.-E. Moser, M. Grätzel, A new ionic liquid electrolyte enhances the conversion efficiency of dye-sensitized solar cells, *J. Phys. Chem. B*. 107 (2003) 13280–13285. <https://doi.org/10.1021/jp0355399>.
- [143] M. Smiglak, J. M. Pringle, X. Lu, L. Han, S. Zhang, H. Gao, D. R. MacFarlane, R. D. Rogers, Ionic liquids for energy, materials, and medicine, *Chemical Communications*. 50 (2014) 9228–9250. <https://doi.org/10.1039/C4CC02021A>.
- [144] B. Gurkan, B.F. Goodrich, E.M. Mindrup, L.E. Ficke, M. Massel, S. Seo, T.P. Senftle, H. Wu, M.F. Glaser, J.K. Shah, E.J. Maginn, J.F. Brennecke, W.F. Schneider, Molecular design of high capacity, low viscosity, chemically tunable ionic liquids for CO<sub>2</sub> capture, *J. Phys. Chem. Lett.* 1 (2010) 3494–3499. <https://doi.org/10.1021/jz101533k>.
- [145] P. Sun, D.W. Armstrong, Ionic liquids in analytical chemistry, *Analytica Chimica Acta*. 661 (2010) 1–16. <https://doi.org/10.1016/j.aca.2009.12.007>.
- [146] E.D. Bates, R.D. Mayton, I. Ntai, J.H. Davis, CO<sub>2</sub> capture by a task-specific ionic liquid, *J. Am. Chem. Soc.* 124 (2002) 926–927. <https://doi.org/10.1021/ja017593d>.
- [147] M. Armand, F. Endres, D.R. MacFarlane, H. Ohno, B. Scrosati, Ionic-liquid materials for the electrochemical challenges of the future, *Nature Materials*. 8 (2009) 621–629. <https://doi.org/10.1038/nmat2448>.
- [148] M.C. Buzzeo, R.G. Evans, R.G. Compton, Non-haloaluminate room-temperature ionic liquids in electrochemistry-A review, *ChemPhysChem*. 5 (2004) 1106–1120. <https://doi.org/10.1002/cphc.200301017>.

- [149] D.S. Silvester, R.G. Compton, Electrochemistry in room temperature ionic liquids: a review and some possible applications, *Zeitschrift Für Physikalische Chemie*. 220 (2006) 1247–1274. <https://doi.org/10.1524/zpch.2006.220.10.1247>.
- [150] M. Díaz, A. Ortiz, I. Ortiz, Progress in the use of ionic liquids as electrolyte membranes in fuel cells, *Journal of Membrane Science*. 469 (2014) 379–396. <https://doi.org/10.1016/j.memsci.2014.06.033>.
- [151] D. Wei, A. Ivaska, Applications of ionic liquids in electrochemical sensors, *Analytica Chimica Acta*. 607 (2008) 126–135. <https://doi.org/10.1016/j.aca.2007.12.011>.
- [152] G.-R. Zhang, B.J.M. Etzold, Ionic liquids in electrocatalysis, *Journal of Energy Chemistry*. 25 (2016) 199–207. <https://doi.org/10.1016/j.jechem.2016.01.007>.
- [153] B. Kumar, M. Asadi, D. Pisasale, S. Sinha-Ray, B.A. Rosen, R. Haasch, J. Abiade, A.L. Yarin, A. Salehi-Khojin, Renewable and metal-free carbon nanofibre catalysts for carbon dioxide reduction, *Nature Communications*. 4 (2013) 1–8. <https://doi.org/10.1038/ncomms3819>.
- [154] S.D. Kenarsari, D. Yang, G. Jiang, S. Zhang, J. Wang, A.G. Russell, Q. Wei, M. Fan, Review of recent advances in carbon dioxide separation and capture, *RSC Adv*. 3 (2013) 22739–22773. <https://doi.org/10.1039/C3RA43965H>.
- [155] D.R. MacFarlane, N. Tachikawa, M. Forsyth, J.M. Pringle, P.C. Howlett, G.D. Elliott, J.H. Davis, M. Watanabe, P. Simon, C.A. Angell, Energy applications of ionic liquids, *Energy Environ. Sci*. 7 (2013) 232–250. <https://doi.org/10.1039/C3EE42099J>.
- [156] S.S. Neubauer, B. Schmid, C. Reller, D.M. Guldi, G. Schmid, Alkalinity initiated decomposition of mediating imidazolium ions in high current density CO<sub>2</sub> electrolysis, *ChemElectroChem*. 4 (2017) 160–167. <https://doi.org/10.1002/celec.201600461>.
- [157] B.A. Rosen, J.L. Haan, P. Mukherjee, B. Braunschweig, W. Zhu, A. Salehi-Khojin, D.D. Dlott, R.I. Masel, In situ spectroscopic examination of a low overpotential pathway for carbon dioxide conversion to carbon monoxide, *J. Phys. Chem. C*. 116 (2012) 15307–15312. <https://doi.org/10.1021/jp210542v>.
- [158] C. Cadena, J.L. Anthony, J.K. Shah, T.I. Morrow, J.F. Brennecke, E.J. Maginn, Why is CO<sub>2</sub> so soluble in imidazolium based ionic liquids?, *J. Am. Chem. Soc*. 126 (2004) 5300–5308. <https://doi.org/10.1021/ja039615x>.
- [159] B.A. Rosen, A. Salehi-Khojin, M.R. Thorson, W. Zhu, D.T. Whipple, P.J.A. Kenis, R.I. Masel, Ionic liquid-mediated selective conversion of CO<sub>2</sub> to CO at low overpotentials, *Science*. 334 (2011) 643–644. <https://doi.org/10.1126/science.1209786>.
- [160] L. Sun, G.K. Ramesha, P.V. Kamat, J.F. Brennecke, Switching the reaction course of electrochemical CO<sub>2</sub> reduction with ionic liquids, *Langmuir*. 30 (2014) 6302–6308. <https://doi.org/10.1021/la5009076>.
- [161] S.S. Neubauer, R.K. Krause, B. Schmid, D.M. Guldi, G. Schmid, Overpotentials and faraday efficiencies in CO<sub>2</sub> electrocatalysis—the impact of 1-ethyl-3-methylimidazolium trifluoromethanesulfonate, *Advanced Energy Materials*. 6 (2016) 1502231. <https://doi.org/10.1002/aenm.201502231>.
- [162] F.A. Hanc-Scherer, M.A. Montiel, V. Montiel, E. Herrero, C.M. Sánchez-Sánchez, Surface structured platinum electrodes for the electrochemical reduction of carbon dioxide in imidazolium based ionic liquids, *Physical Chemistry Chemical Physics*. 17 (2015) 23909–23916. <https://doi.org/10.1039/c5cp02361k>.

- [163] Y. Wang, M. Hatakeyama, K. Ogata, M. Wakabayashi, F. Jin, S. Nakamura, Activation of CO<sub>2</sub> by ionic liquid EMIM-BF<sub>4</sub> in the electrochemical system: a theoretical study, *Phys. Chem. Chem. Phys.* 17 (2015) 23521–23531. <https://doi.org/10.1039/C5CP02008E>.
- [164] Q. Zhu, J. Ma, X. Kang, X. Sun, H. Liu, J. Hu, Z. Liu, B. Han, Efficient reduction of CO<sub>2</sub> into formic acid on a lead or tin electrode using an ionic liquid catholyte mixture, *Angewandte Chemie International Edition*. 55 (2016) 9012–9016. <https://doi.org/10.1002/anie.201601974>.
- [165] Q. Wang, C. Chen, J. Zhong, B. Zhang, Z. Cheng, Effect of alkyl chain length of imidazolium cation on the electroreduction of CO<sub>2</sub> to CO on Ag electrode in acetonitrile, *Aust. J. Chem.* 70 (2017) 293–300. <https://doi.org/10.1071/CH16138>.
- [166] F. Zhou, S. Liu, B. Yang, P. Wang, A.S. Alshammari, Y. Deng, Highly selective electrocatalytic reduction of carbon dioxide to carbon monoxide on silver electrode with aqueous ionic liquids, *Electrochemistry Communications*. 46 (2014) 103–106. <https://doi.org/10.1016/j.elecom.2014.06.023>.
- [167] S.-F. Zhao, M. Horne, A.M. Bond, J. Zhang, Is the imidazolium cation a unique promoter for electrocatalytic reduction of carbon dioxide?, *J. Phys. Chem. C*. 120 (2016) 23989–24001. <https://doi.org/10.1021/acs.jpcc.6b08182>.
- [168] G.H. Lane, Electrochemical reduction mechanisms and stabilities of some cation types used in ionic liquids and other organic salts, *Electrochimica Acta*. 83 (2012) 513–528. <https://doi.org/10.1016/j.electacta.2012.08.046>.
- [169] Y. Wang, T. Hayashi, D. He, Y. Li, F. Jin, R. Nakamura, A reduced imidazolium cation layer serves as the active site for electrochemical carbon dioxide reduction, *Applied Catalysis B: Environmental*. 264 (2020) 118495. <https://doi.org/10.1016/j.apcatb.2019.118495>.
- [170] M. Feroci, I. Chiarotto, G. Forte, A. Inesi, An electrochemical methodology for the cyclic CO<sub>2</sub> “catch and release”. The role of the electrogenerated N-heterocyclic carbene in BMIm-BF<sub>4</sub>, *Journal of CO<sub>2</sub> Utilization*. 2 (2013) 29–34. <https://doi.org/10.1016/j.jcou.2013.07.002>.
- [171] D. Niu, H. Wang, H. Li, Z. Wu, X. Zhang, Roles of ion pairing on electroreduction of carbon dioxide based on imidazolium based salts, *Electrochimica Acta*. 158 (2015) 138–142. <https://doi.org/10.1016/j.electacta.2015.01.096>.
- [172] M. Zhang, L.-J. Yu, Y.-F. Huang, J.-W. Yan, G.-K. Liu, D.-Y. Wu, Z.-Q. Tian, B.-W. Mao, Extending the shell-isolated nanoparticle-enhanced Raman spectroscopy approach to interfacial ionic liquids at single crystal electrode surfaces, *Chem. Commun.* 50 (2014) 14740–14743. <https://doi.org/10.1039/C4CC06269H>.
- [173] R. Katoh, Absorption spectra of imidazolium ionic liquids, *Chem. Lett.* 36 (2007) 1256–1257. <https://doi.org/10.1246/cl.2007.1256>.
- [174] M.A. Rather, G.M. Rather, S.A. Pandit, S.A. Bhat, M.A. Bhat, Determination of *cmc* of imidazolium based surface active ionic liquids through probe-less UV–vis spectrophotometry, *Talanta*. 131 (2015) 55–58. <https://doi.org/10.1016/j.talanta.2014.07.046>.
- [175] A. Boutiti, R. Zouaghi, S.E. Bendjabeur, S. Guittonneau, T. Sehili, Photodegradation of 1-hexyl-3-methylimidazolium by UV/H<sub>2</sub>O<sub>2</sub> and UV/TiO<sub>2</sub>: Influence of pH and chloride, *Journal of Photochemistry and Photobiology A: Chemistry*. 336 (2017) 164–169. <https://doi.org/10.1016/j.jphotochem.2016.12.030>.

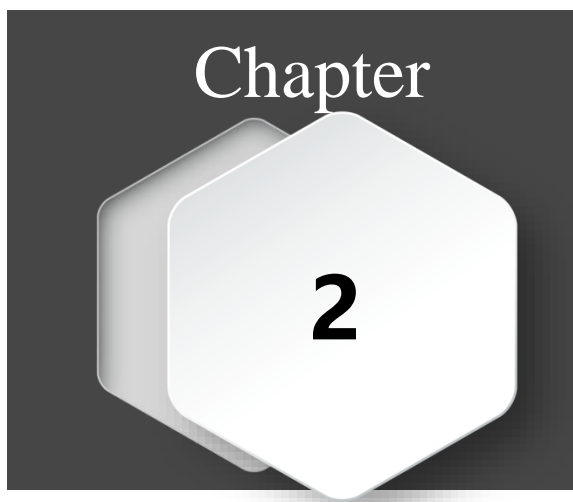
- [176] N. Gutowska, A. Maciejewski, HPLC coupled with a spectrophotometer as a reliable setup for the study of absorption properties of imidazolium ionic liquids using bmimBF<sub>4</sub> as an example, *RSC Adv.* 4 (2014) 31775–31781. <https://doi.org/10.1039/C4RA03868A>.
- [177] M.I. Qadir, M. Zanatta, E.S. Gil, H.K. Stassen, P. Gonçalves, B.A.D. Neto, P.E.N. de Souza, J. Dupont, Photocatalytic reverse semi-combustion driven by ionic liquids, *ChemSusChem*. 12 (2019) 1011–1016. <https://doi.org/10.1002/cssc.201802974>.
- [178] A.S. Varela, W. Ju, A. Bagger, P. Franco, J. Rossmeisl, P. Strasser, Electrochemical reduction of CO<sub>2</sub> on metal-nitrogen-doped carbon catalysts, *ACS Catalysis*. 9 (2019) 7270–7284. <https://doi.org/10.1021/acscatal.9b01405>.
- [179] A. Roy, D. Hursán, K. Artyushkova, P. Atanassov, C. Janáky, A. Serov, Nanostructured metal-N-C electrocatalysts for CO<sub>2</sub> reduction and hydrogen evolution reactions, *Applied Catalysis B: Environmental*. 232 (2018) 512–520. <https://doi.org/10.1016/j.apcatb.2018.03.093>.
- [180] C. Zúñiga, C. Candia-Onfray, R. Venegas, K. Muñoz, J. Urrea, M. Sánchez-Arenillas, J.F. Marco, J.H. Zagal, F.J. Recio, Elucidating the mechanism of the oxygen reduction reaction for pyrolyzed Fe-N-C catalysts in basic media, *Electrochemistry Communications*. 102 (2019) 78–82. <https://doi.org/10.1016/j.elecom.2019.04.005>.
- [181] A.S. Varela, N. Ranjbar Sahraie, J. Steinberg, W. Ju, H.-S. Oh, P. Strasser, Metal-doped nitrogenated carbon as an efficient catalyst for direct CO<sub>2</sub> electroreduction to CO and hydrocarbons, *Angewandte Chemie International Edition*. 54 (2015) 10758–10762. <https://doi.org/10.1002/anie.201502099>.
- [182] F. Pan, W. Deng, C. Justiniano, Y. Li, Identification of champion transition metals centers in metal and nitrogen-codoped carbon catalysts for CO<sub>2</sub> reduction, *Applied Catalysis B: Environmental*. 226 (2018) 463–472. <https://doi.org/10.1016/j.apcatb.2018.01.001>.
- [183] J. Li, P. Pršlja, T. Shinagawa, A.J. Martín Fernández, F. Krumeich, K. Artyushkova, P. Atanassov, A. Zitolo, Y. Zhou, R. García-Muelas, N. López, J. Pérez-Ramírez, F. Jaouen, Volcano trend in electrocatalytic CO<sub>2</sub> reduction activity over atomically dispersed metal sites on nitrogen-doped carbon, *ACS Catal.* 9 (2019) 10426–10439. <https://doi.org/10.1021/acscatal.9b02594>.
- [184] Y. He, S. Liu, C. Priest, Q. Shi, G. Wu, Atomically dispersed metal–nitrogen–carbon catalysts for fuel cells: advances in catalyst design, electrode performance, and durability improvement, *Chem. Soc. Rev.* (2020). <https://doi.org/10.1039/C9CS00903E>.
- [185] F. Pan, H. Zhang, Z. Liu, D. Cullen, K. Liu, K. More, G. Wu, G. Wang, Y. Li, Atomic-level active sites of efficient imidazolate framework-derived nickel catalysts for CO<sub>2</sub> reduction, *J. Mater. Chem. A*. 7 (2019) 26231–26237. <https://doi.org/10.1039/C9TA08862H>.
- [186] A.S. Varela, M. Kroschel, N.D. Leonard, W. Ju, J. Steinberg, A. Bagger, J. Rossmeisl, P. Strasser, pH effects on the selectivity of the electrocatalytic CO<sub>2</sub> reduction on graphene-embedded Fe–N–C motifs: bridging concepts between molecular homogeneous and solid-state heterogeneous catalysis, *ACS Energy Lett.* 3 (2018) 812–817. <https://doi.org/10.1021/acsenenergylett.8b00273>.
- [187] K. Jiang, S. Siahrostami, T. Zheng, Y. Hu, S. Hwang, E. Stavitski, Y. Peng, J. Dynes, M. Gangisetty, D. Su, K. Attenkofer, H. Wang, Isolated Ni single atoms in graphene nanosheets for high-performance CO<sub>2</sub> reduction, *Energy & Environmental Science*. 11 (2018) 893–903. <https://doi.org/10.1039/C7EE03245E>.



- [188] N. Daems, B.D. Mot, D. Choukroun, K.V. Daele, C. Li, A. Hubin, S. Bals, J. Hereijgers, T. Breugelmans, Nickel-containing N-doped carbon as effective electrocatalysts for the reduction of CO<sub>2</sub> to CO in a continuous-flow electrolyzer, *Sustainable Energy Fuels*. (2019). <https://doi.org/10.1039/C9SE00814D>.
- [189] L. Zhang, I. Merino-Garcia, J. Albo, C.M. Sánchez-Sánchez, Electrochemical CO<sub>2</sub> reduction reaction on cost-effective oxide-derived copper and transition metal–nitrogen–carbon catalysts, *Current Opinion in Electrochemistry*. 23 (2020) 65–73. <https://doi.org/10.1016/j.coelec.2020.04.005>.
- [190] X.-M. Hu, H.H. Hval, E.T. Bjerglund, K.J. Dalgaard, M.R. Madsen, M.-M. Pohl, E. Welter, P. Lamagni, K.B. Buhl, M. Bremholm, M. Beller, S.U. Pedersen, T. Skrydstrup, K. Daasbjerg, Selective CO<sub>2</sub> reduction to CO in water using earth-abundant metal and nitrogen-doped carbon electrocatalysts, *ACS Catal.* 8 (2018) 6255–6264. <https://doi.org/10.1021/acscatal.8b01022>.
- [191] Y. Chen, L. Zou, H. Liu, C. Chen, Q. Wang, M. Gu, B. Yang, Z. Zou, J. Fang, H. Yang, Fe and N co-doped porous carbon nanospheres with high density of active sites for efficient CO<sub>2</sub> electroreduction, *J. Phys. Chem. C*. 123 (2019) 16651–16659. <https://doi.org/10.1021/acs.jpcc.9b02195>.
- [192] H.-J. Yang, X. Zhang, Y.-H. Hong, H.M.K. Sari, Z.-Y. Zhou, S.-G. Sun, X.-F. Li, Superior selectivity and tolerance towards metal-ion impurities of a Fe/N/C catalyst for CO<sub>2</sub> reduction, *ChemSusChem*. 12 (2019) 3988–3995. <https://doi.org/10.1002/cssc.201901330>.
- [193] F. Pan, B. Li, E. Sarnello, S. Hwang, Y. Gang, X. Feng, X. Xiang, N.M. Adli, T. Li, D. Su, G. Wu, G. Wang, Y. Li, Boosting CO<sub>2</sub> reduction on Fe-N-C with sulfur incorporation: synergistic electronic and structural engineering, *Nano Energy*. 68 (2020) 104384. <https://doi.org/10.1016/j.nanoen.2019.104384>.
- [194] K. Rajeshwar, J.G. Ibanez, *Environmental electrochemistry: fundamentals and applications in pollution sensors and abatement*, Elsevier, 1997.
- [195] S.M. Sze, K.K. Ng, *Physics of semiconductor devices*, John Wiley & Sons, 2006.
- [196] D.A. Neamen, *Semiconductor physics and devices: basic principles*, 4th ed, McGraw-Hill, New York, NY, 2012.
- [197] H. Pang, T. Masuda, J. Ye, Semiconductor-based photoelectrochemical conversion of carbon dioxide: stepping towards artificial photosynthesis, *Chemistry – An Asian Journal*. 13 (2018) 127–142. <https://doi.org/10.1002/asia.201701596>.
- [198] K. Rajeshwar, M.K. Hossain, R.T. Macaluso, C. Janáky, A. Varga, P.J. Kulesza, Review-copper oxide-based ternary and quaternary oxides: where solid-state chemistry meets photoelectrochemistry, *J. Electrochem. Soc.* 165 (2018) H3192–H3206. <https://doi.org/10.1149/2.0271804jes>.
- [199] U.A. Joshi, A. Palasyuk, D. Arney, P.A. Maggard, Semiconducting oxides to facilitate the conversion of solar energy to chemical fuels, *J. Phys. Chem. Lett.* 1 (2010) 2719–2726. <https://doi.org/10.1021/jz100961d>.
- [200] X. Ba, L.-L. Yan, S. Huang, J. Yu, X.-J. Xia, Y. Yu, New way for CO<sub>2</sub> reduction under visible light by a combination of a Cu electrode and semiconductor thin film: Cu<sub>2</sub>O conduction type and morphology effect, *J. Phys. Chem. C*. 118 (2014) 24467–24478. <https://doi.org/10.1021/jp5063397>.
- [201] R. Rahmatolahzadeh, M. Mousavi-Kamazani, S.A. Shobeiri, Facile co-precipitation-calcination synthesis of CuCo<sub>2</sub>O<sub>4</sub> nanostructures using novel precursors for degradation of

- azo dyes, *J Inorg Organomet Polym.* 27 (2017) 313–322. <https://doi.org/10.1007/s10904-016-0473-9>.
- [202] S.M.N. Jeghan, J.Y. Do, M. Kang, Fabrication of flower-like copper cobaltite/graphitic-carbon nitride ( $\text{CuCo}_2\text{O}_4/\text{g-C}_3\text{N}_4$ ) composite with superior photocatalytic activity, *Journal of Industrial and Engineering Chemistry.* 57 (2018) 405–415. <https://doi.org/10.1016/j.jiec.2017.08.049>.
- [203] S. Saadi, A. Bouguelia, M. Trari, Photoassisted hydrogen evolution over spinel  $\text{CuM}_2\text{O}_4$  (M=Al, Cr, Mn, Fe and Co), *Renewable Energy.* 31 (2006) 2245–2256. <https://doi.org/10.1016/j.renene.2005.10.014>.
- [204] M. Jiang, Y. Gao, Z. Wang, Z. Ding, Photocatalytic  $\text{CO}_2$  reduction promoted by a  $\text{CuCo}_2\text{O}_4$  cocatalyst with homogeneous and heterogeneous light harvesters, *Applied Catalysis B: Environmental.* 198 (2016) 180–188. <https://doi.org/10.1016/j.apcatb.2016.05.055>.





## Materials and Experimental Methods

---



## Chapter 2 Materials and Experimental Methods

This chapter presents all the chemical reagents, materials and instruments used in the thesis. In addition to this, experimental procedures and synthesis processes are described in detail. Finally, the characterization methods and techniques used are introduced including their instruments type and configuration.

### 2.1. Reagents and Materials

#### 2.1.1. Chemical Reagents

All chemical reagents used for synthesis or analysis are analytical grade and were used without any further treatment. Water used in all experiments is ultrapure with a resistivity  $> 18 \text{ M}\Omega\cdot\text{cm}$ . Table 2.1 shows all the chemical reagents used in experiments.

*Table 2.1 Chemical reagents used in experiments*

Reagent Name	Reagent formula	Reagent Grade	Brand
Copper nitrate trihydrate	$\text{Cu}(\text{NO}_3)_2 \cdot 3\text{H}_2\text{O}$	99.5%	Merck
Cobalt nitrate hexahydrate <sup>1</sup>	$\text{Co}(\text{NO}_3)_2 \cdot 6\text{H}_2\text{O}$	99%	Acros Organics
Cobalt nitrate hexahydrate <sup>2</sup>	$\text{Co}(\text{NO}_3)_2 \cdot 6\text{H}_2\text{O}$	99.5%	Merck
Iron nitrate nonahydrate	$\text{Fe}(\text{NO}_3)_3 \cdot 9\text{H}_2\text{O}$	98%	Sigma-Aldrich
Bismuth nitrate pentahydrate	$\text{Bi}(\text{NO}_3)_3 \cdot 5\text{H}_2\text{O}$	98%	Sigma-Aldrich
Manganese nitrate hydrate	$\text{Mn}(\text{NO}_3)_2$	98%	Merck
Manganese chloride	$\text{MnCl}_2$	99%	Merck
Nickel sulfate hexahydrate	$\text{NiSO}_4 \cdot 6\text{H}_2\text{O}$	98%	Sigma-Aldrich
Iron sulfate heptahydrate	$\text{FeSO}_4 \cdot 7\text{H}_2\text{O}$	99%	Sigma-Aldrich
Silver nitrate	$\text{AgNO}_3$	99%	Sigma-Aldrich
Sulfuric acid	$\text{H}_2\text{SO}_4$	95%	Fluka Analytical
Potassium hydroxide	$\text{KOH}$	85%	VWR
Potassium bicarbonate	$\text{KHCO}_3$	99.5%	PROLABO

<sup>1</sup> Used in the synthesis of p-type semiconductor  $\text{CuCo}_2\text{O}_4$ .

<sup>2</sup> Used in the synthesis of M–N–Cs.

Sodium sulfate anhydrous	Na <sub>2</sub> SO <sub>4</sub>	99.9%	PROLABO
Acetone	CH <sub>3</sub> COCH <sub>3</sub>	99%	VWR
Ethanol	CH <sub>3</sub> CH <sub>2</sub> OH	96%	VWR
Agar	(C <sub>12</sub> H <sub>18</sub> O <sub>9</sub> ) <sub>n</sub>	Cat 1056	CONDA
Ethylene glycol	HOCH <sub>2</sub> CH <sub>2</sub> OH	99%	Alfa Aesar
Ferrocene	FeC <sub>10</sub> H <sub>10</sub>	98%	Sigma-Aldrich
Ferrocene methanol	FeC <sub>11</sub> H <sub>12</sub> O	97%	Acros Organics
1-Butyl-3-methylimidazolium tetrafluoroborate	[C <sub>4</sub> mim][BF <sub>4</sub> ]	99% Water < 250 ppm	IoLiTec
1-Ethyl-3-methylimidazolium tetrafluoroborate	[C <sub>2</sub> mim][BF <sub>4</sub> ]	98% Water < 1000 ppm	IoLiTec
1-Butyl-3-methylimidazolium bis(trifluoromethylsulfonyl)imide	[C <sub>4</sub> mim][NTf <sub>2</sub> ]	99% Water < 100 ppm	IoLiTec
1-Ethyl -3-methylimidazolium bis(trifluoromethylsulfonyl)imide	[C <sub>2</sub> mim][NTf <sub>2</sub> ]	99% Water < 100 ppm	IoLiTec
Chitosan	n.a.	low molecular weight	Sigma-Aldrich
Nafion perfluorinated resin solution	n.a	5 wt. % in lower aliphatic alcohols and water, contains 15-20% water	Sigma-Aldrich
N,N-Dimethylformamide	HCON(CH <sub>3</sub> ) <sub>2</sub>	99.8%	VWR
Carbon dioxide gas	CO <sub>2</sub>	99.998%	Alphagaz
Argon gas	Ar	99.9999%	Alphagaz

### 2.1.2. Experimental Materials and Instruments

- (1) Optical fiber (OF) was purchased from IDIL. There are two kinds of optical fibers used in the SPECM experiment namely UV-visible (COCOM01384) and Visible (COCOM01936). Both of them have a pure silica core (diameter of 50 μm) with a fluorine-doped silica cladding (diameter 125 μm).
- (2) Two kinds of Fluorine-doped tin oxide (FTO) -coated glass were used in the thesis as a current collector:

- FTO (A), Sigma-Aldrich,  $L \times W \times \text{thickness}$  100 mm  $\times$  100 mm  $\times$  2.3 mm, which was cut to small piece of 18 mm  $\times$  18 mm  $\times$  2.3 mm, surface resistivity  $\sim 7 \Omega/\text{sq}$ .
- FTO (B), Solems,  $L \times W \times \text{thickness}$  18 mm  $\times$  18 mm  $\times$  3 mm each piece. The conductive layer thickness and the surface resistivity of FTO thin-film are 600 nm and  $6 \sim 8 \Omega/\text{sq}$ , respectively. The total transmission is  $70 \sim 80\%$  (400  $\sim$  800 nm).

The FTO glass was cleaned with ultrapure water for 1 min and dried under a stream of air before used. FTO was used for the preparation of spot array substrate electrode in the SPECM experiment.

- (3) In the fabrication of the dual tip OF-UME, 25  $\mu\text{m}$  Pt wire (MaTeck, 99.99%) or 25  $\mu\text{m}$  Au wire (GoodFellow, 99.99%) were used as the ultramicroelectrode (UME); copper tinned wire (TCW 35 301802) was purchased from Rowan cable products Ltd.
- (4) Silver paint (G302) was purchased from Agar Scientific. A very fine flake of silver suspended in 4-methylpentan-2-one which has high conductivity and stickiness. It was used for the electrical connection of Pt/Au wire with Copper Tinned wire in the fabrication of the dual tip OF-UME.
- (5) Epoxy glue (Quick set epoxy adhesive, RS) was use for sealing the end of the OF-UME.
- (6) Borosilicate glass capillary (1B100-4) was purchased for World Precision Instruments, Ltd., which has an outer diameter of 1 mm and an inner diameter of 0.58 mm and 100 mm length. It was used for fabrication of the dual tip OF-UME.
- (7) Bipotentiostat (920D) for the SPECM configuration was from CH Instruments.
- (8) Solution Dispenser (Model 1550A workstation) was purchased from CH Instruments (Figure 2.2a). It is composed by a high-resolution three-dimensional (3D) positioner, a piezoelectric jetting device, and a sample platform.



- (9) Xenon lamp (HPX-2000-HP-DUV, 75 W) from Ocean Optics was used for providing the 185 – 2000 nm spectrum light with a typical output power > 150 mW for fibers  $d = 600\ \mu\text{m}$ . This lamp was used for providing a local illumination with high power on the catalyst spots.
- (10) HPX-2000-HP-DUV light controller (homemade) was designed and used for the chronoamperometry in SPECM.
- (11) LI-A 250 Light Meter from LI-COR companied by Quantum Sensor Q40474 (PAR, in  $\mu\text{mol of photons m}^{-2}\text{ s}^{-1}$ ) was used to measure the light power from the end of the visible light OF.
- (12) Laser-Based Micropipette Puller-2000 from Sutter Instrument Co. was used for processing the borosilicate capillary in the fabrication of OF-UME.
- (13) Tube furnace (type 301) was purchased from Carbolite and used for the annealing in air of the FTO array substrate electrode to synthesized metal oxides materials on FTO.
- (14) Conductivity meter (CM 230) from Radiometer analytical. It was used to measure the conductivity of 5 different solutions: 0.1 M  $\text{Na}_2\text{SO}_4$ , 0.1 M  $\text{KHCO}_3$ , 25 vol.%  $[\text{C}_2\text{mim}][\text{BF}_4]$  in  $\text{H}_2\text{O}$ , 25 vol.%  $[\text{C}_4\text{mim}][\text{BF}_4]$  in  $\text{H}_2\text{O}$ , 50 vol.%  $[\text{C}_4\text{mim}][\text{BF}_4]$  in  $\text{H}_2\text{O}$ .
- (15) pH meter (Five Easy) from Mettler Toledo.
- (16) The potentiostat SP 300 used in bulk electrolysis was from Bio-Logic Science.
- (17) Rotating disk electrode (WaveVortex 10) was purchased from Pine research. The connected Bipotentiostat Workstation is 760E from CH Instruments.
- (18) Photoelectrochemical bulk electrolysis were performed using a 280 W lamp (Newport Instruments), high pressure Xe arc lamp (lamp power:  $10\text{ mW/cm}^2$ ). The beam was passed through a water infrared filter and a collimating lens (Asahi Spectra).
- (19) Three kinds of electrolyte solutions were used in the thesis: aqueous solution, binary RTIL/ $\text{H}_2\text{O}$  and pure RTILs as shown in Table 2.2, the structure of RTILs is shown in Figure 2.1.

Table 2.2 Concentrations of different electrolyte solutions used in this thesis and the comparison with some selected examples from the literature.

	Electrolyte solutions	Electrolyte volume fraction (vol.%)	Electrolyte molarity (M)	Electrolyte mass fraction (wt.%)	Electrolyte mole fraction (mol %)
Aqueous solutions	KHCO <sub>3</sub>	-	0.1	1.0	-
	Na <sub>2</sub> SO <sub>4</sub>	-	0.1	1.4	-
Pure RTILs	100% [C <sub>2</sub> mim][BF <sub>4</sub> ]	-	-	-	-
	100% [C <sub>4</sub> mim][BF <sub>4</sub> ]	-	-	-	-
	100% [C <sub>2</sub> mim][NTf <sub>2</sub> ]	Immiscible in water		-	-
	100% [C <sub>4</sub> mim][NTf <sub>2</sub> ]	Immiscible in water		-	-
Binary RTIL/H <sub>2</sub> O mixtures	[C <sub>2</sub> mim][BF <sub>4</sub> ]/H <sub>2</sub> O	25	1.6	29.9	3.7
	[C <sub>4</sub> mim][BF <sub>4</sub> ]/H <sub>2</sub> O	25	1.4	30.2	3.3
	[C <sub>4</sub> mim][BF <sub>4</sub> ]/H <sub>2</sub> O	50	2.9	56.5	9.4
Ref. [1]	[C <sub>2</sub> mim][BF <sub>4</sub> ]/H <sub>2</sub> O	65.4	4.2	70.7	18.0
Ref. [2]	[C <sub>2</sub> mim][BF <sub>4</sub> ]/H <sub>2</sub> O	79.7	5.2	83.4	31.3

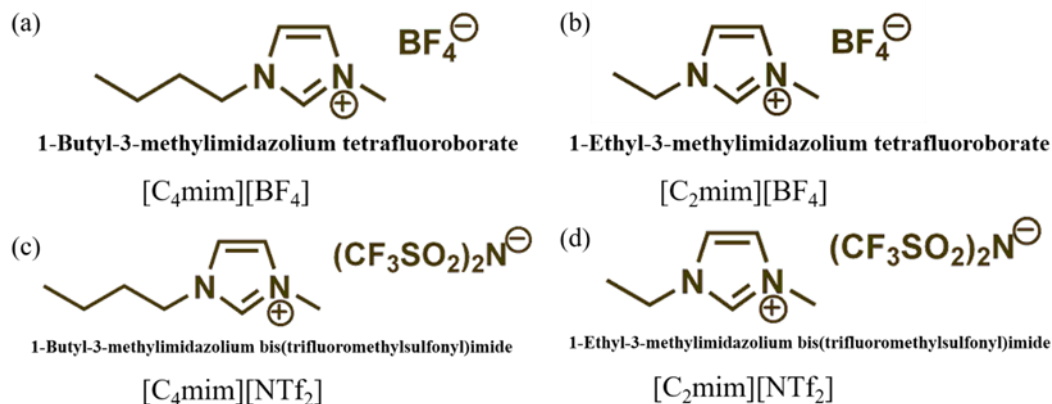


Figure 2.1 Chemical structure, name and the corresponding abbreviation of room-temperature ionic liquids used in this work.

## 2.2. Synthesis of Semiconductors and Preparation of Array Substrate Electrodes

For this study, the array substrate electrode was prepared using a similar and simplified methodology previously reported by the Bard's group [3,4] and Lewis' group [5]. Figure 2.2a shows the commercially available solution dispenser (CHI 1550A) used for dispensing the

metallic precursor solutions on FTO. The 3D-positioner controls the movement of the jet device in XYZ directions according to a preset pattern. The jet device has a nozzle size of 60  $\mu\text{m}$ , which can produce individual drops ranging from 100 to 200 picoliters, depending on the applied parameters and the properties of solvent used in the precursor solutions. Both the positioner and the jet device are connected to a controller in the workstation.

To prepare the spot array on FTO, a series of independent metal precursor solutions were firstly prepared by dissolving metal nitrates in anhydrous ethylene glycol (vapor pressure: 0.12 mmHg at 20  $^{\circ}\text{C}$ , viscosity: 21 cP at 20  $^{\circ}\text{C}$ ). These metal nitrates included  $\text{Cu}(\text{NO}_3)_2 \cdot 3\text{H}_2\text{O}$ ,  $\text{Co}(\text{NO}_3)_2 \cdot 6\text{H}_2\text{O}$ ,  $\text{Fe}(\text{NO}_3)_3 \cdot 9\text{H}_2\text{O}$ ,  $\text{Bi}(\text{NO}_3)_3 \cdot 5\text{H}_2\text{O}$ ,  $\text{AgNO}_3$  and  $\text{NiSO}_4 \cdot 6\text{H}_2\text{O}$ . The procedure of synthesizing spot array of  $\text{CuCo}_2\text{O}_4$  is shown in Figure 2.2b. The array substrate was obtained by preparing independent solution of 0.3 M  $\text{Cu}(\text{NO}_3)_2$  and 0.3 M  $\text{Co}(\text{NO}_3)_2$  in ethylene glycol. Then, by mixing both metal ion solutions ( $\text{Cu}^{2+}$ :  $\text{Co}^{2+}$ ) in a volume ratio (1:2) and stirring the new solution well to blend. This mixed solution is used as the precursor solution, which is locally dispensed on FTO glass using the jet device of the solution dispenser. The common parameters used at dispenser are a pulse amplitude of 100 V, pulse duration of 60  $\mu\text{s}$ , pulse period of 10 ms, 30 drops per spot, and a spot spacing of 800  $\mu\text{m}$  from center to center. Then, the FTO glass with the spots array was annealed in the furnace at 500  $^{\circ}\text{C}$  for 1 hour in air atmosphere with a heating rate of 10  $^{\circ}\text{C}/\text{min}$  after which the array followed a natural cooling down staying at the furnace resulting in flattened and adhered spots of  $\text{CuCo}_2\text{O}_4$ .

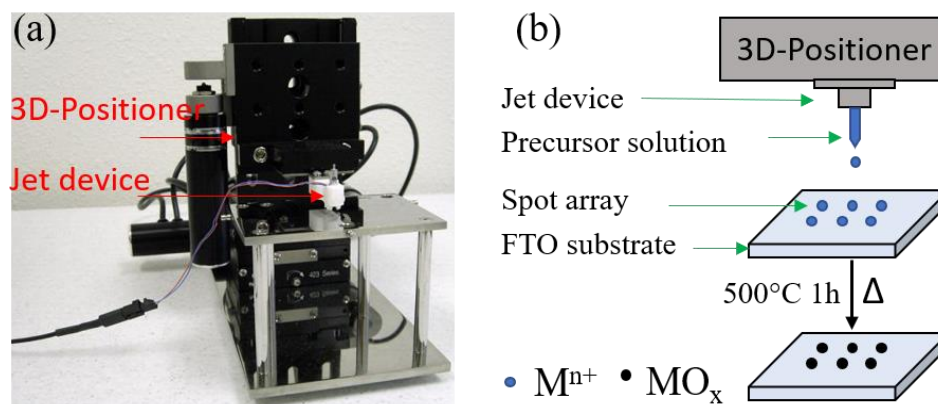


Figure 2.2 (a) Solution Dispenser. (b) Schematic representation of preparation of array substrate electrode synthesis.

In the thesis, 9 kinds of metal/mixed-metal oxides were synthesized by this methodology which will be compared and discussed in detailed for their performance on

photoelectrochemical CO<sub>2</sub>RR in chapter 3. Dispensing and annealing parameters in in-situ synthesis of these different metal oxide semiconductors are shown in Table 2.3. Optimal conditions are highlighted in yellow.

*Table 2.3 Dispensing and annealing parameters in in-situ synthesis of different metal oxide semiconductors*

Metal oxide semiconductors	Dispensing parameters				Annealing parameters		
	Pulse amplitude (V)	Pulse duration (μs)	Pulse period (ms)	Drops	Temp. (°C)	Ramp (°C/min)	Duration (h)
CuO <sub>x</sub>	100	60	10	30	500	1	4.5
NiO <sub>x</sub>	80	25	10	30	500	1	4.5
CuNi <sub>x</sub> O <sub>y</sub>	100	60	10	30	500	1	3
FeO <sub>x</sub>	100	60	10	30	500	1	3
CuFe <sub>2</sub> O <sub>x</sub>	100	60	10	30	500	1	3
CoO <sub>x</sub>	100	60	10	30	500	1	3
CuCo <sub>2</sub> O <sub>x</sub> <sup>a</sup>	100	60	10	30	500	1	3
CuCo <sub>2</sub> O <sub>4</sub> <sup>b</sup>	100	60	10	30	500	10	1
CuBi <sub>2</sub> O <sub>x</sub>	100	60	10	30	500	10	1
AgCoO <sub>x</sub>	100	60	10	30	500	10	1

<sup>a</sup> CuCo<sub>2</sub>O<sub>x</sub> only reported in Figure 3.5.

<sup>b</sup> CuCo<sub>2</sub>O<sub>4</sub> used as model p-type semiconductor in chapter 3 and chapter 4.

### 2.3. Optimization the Picolitor Dispenser Parameters for CuCo<sub>2</sub>O<sub>4</sub>

Using this dispensing system, different p-type semiconductors array substrates were prepared and compared for their catalytic activity and stability. Given the comparison results of different metallic combinations, the CuCo<sub>2</sub>O<sub>4</sub> exhibited the best performance in the PEC CO<sub>2</sub>RR system, making it a model catalyst to study the role of different electrolytes in PEC reactions by SPECM.

In this thesis, all the earlier synthesis of different p-type semiconductors were done on the FTO A (Aldrich). For the reproducibility and the configuration requirements of the experiment, FTO B (Solems) was chosen to prepare the model catalyst CuCo<sub>2</sub>O<sub>4</sub> array substrate. However,

the dispenser parameters and the annealing parameters needed to be changed and optimized for the new FTO in order to obtain nice catalyst spots with reproducible size and morphology.

The solvent of the precursor solution is ethylene glycol, which is necessary owing to its high viscosity and low volatility to ensure reproducible spots and also prevent the precursor solution drying before the annealing process.

After comparing different combination of dispensing and annealing parameters for FTO (B), the final set of parameters are: pulse amplitude of 100 V, pulse duration of 60  $\mu$ s, pulse period of 10 ms, 30 drops per spot, and a spot spacing of 800  $\mu$ m from center to center. Then, the FTO glass with the spots array is annealed in the furnace at 500  $^{\circ}$ C for 1 hour in air atmosphere with a ramp of 10  $^{\circ}$ C/min, after which the array follows a natural furnace cooling down step resulting in flattened and adhered spots of  $\text{CuCo}_2\text{O}_4$  on the FTO glass surface.

Figure 2.3a shows the  $\text{CuCo}_2\text{O}_4$  array substrate on FTO (A) with an annealing process of 500  $^{\circ}$ C for 1 hour in air atmosphere with a ramp of 10  $^{\circ}$ C/min and Figure 2.3b shows the array on the FTO (B) with an annealing process of 500  $^{\circ}$ C for 3 hours in air atmosphere with a ramp of 1  $^{\circ}$ C/min. Good reproducibility and very little variations between spots in an individual array substrate were found. Each spot of the array was generally of the order of *ca.* 475  $\mu$ m in diameter. In general, the coexistence of Co and Cu in the oxide favors the formation of  $\text{CuCo}_2\text{O}_4$  microparticles [6,7].

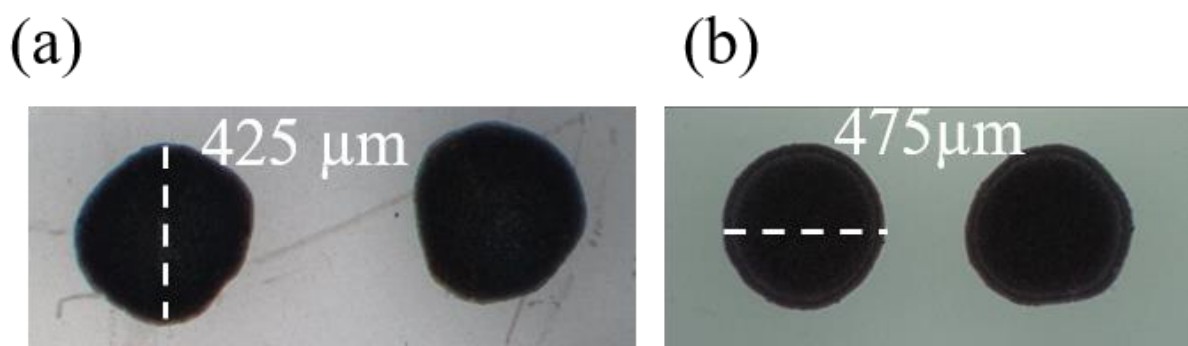


Figure 2.3 the  $\text{CuCo}_2\text{O}_4$  array substrate on (a) FTO (A) with an annealing process of 500  $^{\circ}$ C for 1 hour in air atmosphere with a ramp of 10  $^{\circ}$ C/min and (b) FTO (B) with an annealing process of 500  $^{\circ}$ C for 3 hours in air atmosphere with a ramp of 1  $^{\circ}$ C/min.

## 2.4. Scanning Photoelectrochemical Microscopy

### 2.4.1. Experimental configuration

The SPECM configuration shown in Figure 2.4a, (adapted from the image of ref [8]) was the mainly used equipment for photoelectrochemical measurements in this work. The configuration consisted in four parts: (1) a data acquisition system controlling each component to carry out the experiment, (2) a 3D-positioner with stepper and piezoelectric motors to control the movement of SPECM tip/optical fiber along XYZ directions in order to scan the substrate, (3) a bipotentiostat (CHI 920D) operated by the data acquisition system, which can apply and measure the currents and potentials at both the SPECM tip and the substrate, (4) a conventional 4-electrode electrochemical cell built in Teflon with the array substrate in the bottom acting as the working electrode (WE). At one corner of the substrate, a copper tape was used for ensuring the electrical connection between the WE and the bipotentiostat.

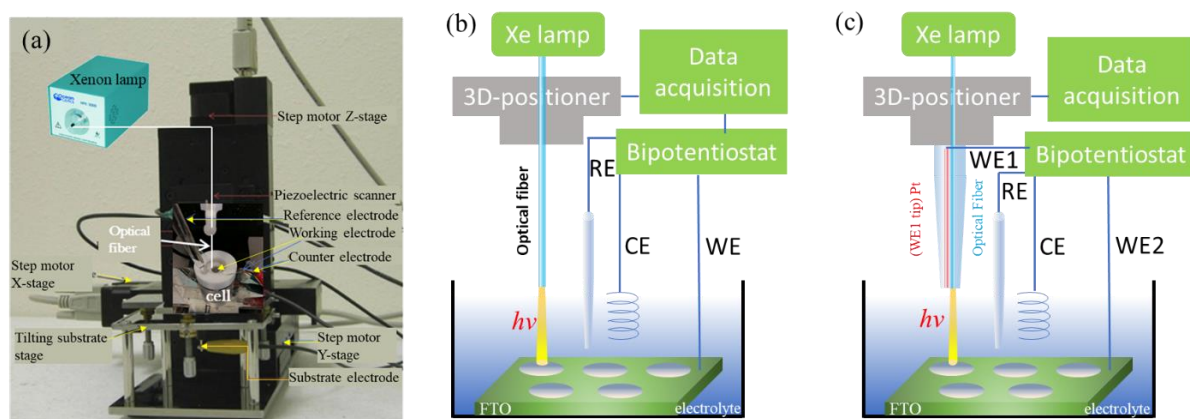


Figure 2.4 (a) Picture of the SPECM instrument. (b) Sketch of the SPECM for PEC activity evaluation (c) Sketch of the SPECM for PEC experiment with the simultaneous detection of generated products.

The electrochemical cell limits the working electrode area in contact with the solution by an O-ring ( $d = 0.7$  mm). A 0.5 mm Pt wire was used as a counter electrode in the electrochemical cell. The reference electrode employed in different electrolyte solutions is shown in Table 2.4. Ag/AgCl (3 M KCl) was connected to the cell through an agar bridge containing agar saturated with 0.5 M  $\text{KHCO}_3$  when purely aqueous solutions or binary RTIL/ $\text{H}_2\text{O}$  mixtures were used. However, building a solvent independent reference scale in

nonaqueous electrolyte is necessary to maintain a stable and electrochemically defined system. Ferrocene/ferricenium ( $\text{Fc}/\text{Fc}^+$ ) potential scale is a well-accepted redox potential reference scale in RTILs. Therefore, unlike the aqueous and the binary RTIL/ $\text{H}_2\text{O}$  mixtures, a 0.5 mm in diameter Pt wire directly immersed in solution (quasi-reference electrode) was used when electrochemical measurements were performed in pure RTILs. Then, a small amount of Fc was added in solution at the end to calibrate the  $\text{Fc}/\text{Fc}^+$  potential scale. Potentials measured in pure RTILs have been converted to the ferrocene/ferrocenium ( $\text{Fc}/\text{Fc}^+$ ) potential scale, as shown in Figure 2.5,  $E_{(\text{Fc}/\text{Fc}^+)}$  was obtained from the formal potential  $\frac{1}{2} (E_{\text{pa}} + E_{\text{pc}})$ , being  $E_{(\text{Fc}/\text{Fc}^+)} = 0.45$  V vs. Pt wire in pure  $[\text{C}_2\text{mim}][\text{BF}_4]$ .

Table 2.4 Reference electrode used in different electrolyte solutions.

	Electrolyte solutions	Reference electrode
Aqueous solutions	0.1 M $\text{KHCO}_3$	Ag/AgCl (3 M)
	0.1M $\text{Na}_2\text{SO}_4$	Ag/AgCl (3 M)
Pure RTILs	100% $[\text{C}_2\text{mim}][\text{BF}_4]$	Pt (vs. $\text{Fc}/\text{Fc}^+$ )
	100% $[\text{C}_4\text{mim}][\text{BF}_4]$	Pt (vs. $\text{Fc}/\text{Fc}^+$ )
	100% $[\text{C}_2\text{mim}][\text{NTf}_2]$	Pt (vs. $\text{Fc}/\text{Fc}^+$ )
	100% $[\text{C}_4\text{mim}][\text{NTf}_2]$	Pt (vs. $\text{Fc}/\text{Fc}^+$ )
Binary RTIL/ $\text{H}_2\text{O}$ mixtures	25 vol.% $[\text{C}_2\text{mim}][\text{BF}_4]/\text{H}_2\text{O}$	Ag/AgCl (3 M)
	25 vol.% $[\text{C}_4\text{mim}][\text{BF}_4]/\text{H}_2\text{O}$	Ag/AgCl (3 M)
	50 vol.% $[\text{C}_4\text{mim}][\text{BF}_4]/\text{H}_2\text{O}$	Ag/AgCl (3 M)

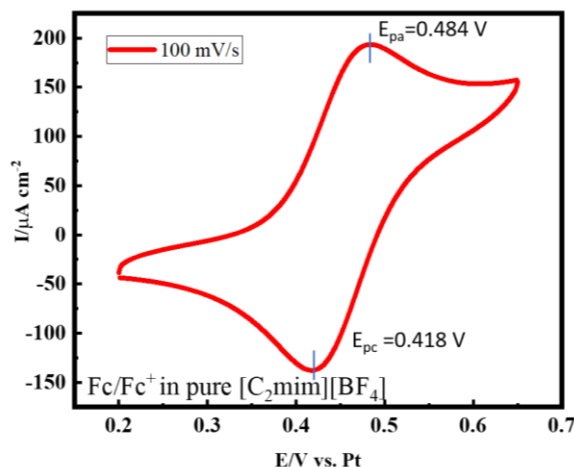


Figure 2.5 Cyclic voltammetry of ferrocene/ferricenium in pure  $[C_2mim][BF_4]$  on Pt electrode at scan rate of 100 mV/s. WE: Pt disc (2 mm diameter); CE and RE: Pt wire (500  $\mu m$  diameter).

## 2.4.2. SPECM Experimental Procedure

### 2.4.2.1. SPECM imaging

In Figure 2.4b, an optical fiber (silica core of 50  $\mu m$  in diameter) was adopted and set up perpendicularly to the substrate electrode for introducing UV-visible or visible light provided by the Xenon lamp (75 W). The optical fiber provided local illumination of the substrate and was scanned in the X-Y plane meanwhile the array substrate electrode was held at a constant potential where  $CO_2RR$  may take place. The distance between the optical fiber and the substrate (distance  $OF_{-}subs$ ) was 150  $\mu m$ . Electrochemical control during fiber approach curves using the optical fiber is not possible because of the absence of UME tip. For this reason, the fiber was positioned by physical contact with the substrate and then, retracted 150  $\mu m$  in Z axis. The optical fiber was approached towards the substrate by the position controller until a slight bending on the fiber indicated its contact with the substrate, which means distance  $OF_{-}subs = 0$ . Then the optical fiber was withdrawn 150  $\mu m$  from the FTO surface and maintained at a constant height during the scan. The fiber-substrate distance effect was already evaluated by previous PhD students and no significant decrease in photocurrent was reported for fiber-substrate distance  $\leq 200 \mu m$ . For this reason, this distance  $OF_{-}subs$  guarantees a constant and local photons flow without touching the semiconductor spots. However, when large samples are scanned, the tilt of the substrate must be corrected as much as possible. Thus, to ensure a horizontally placed substrate, 3 different approach are performed with the fiber at 3 points



above the substrate to evaluate the tilt, then, this is corrected by the leveling screws on the substrate platform until the height difference ( $\Delta z$ ) between each pair of points is smaller than 25  $\mu\text{m}$ .

An additional long pass filter (8 mm diameter and 2 mm thickness), which only transmits higher wavelengths than 400 nm, was inserted within an in-line filter holder between the lamp and the optical fiber in order to remove UV contribution and perform visible light illumination experiments. A light power meter was set vertically under the OF at distance of 150  $\mu\text{m}$  to measure the light power coming out of the fiber, but only visible light was in the range of the instrument 15.84  $\mu\text{mol m}^{-2}\text{s}^{-1}$  ( $\approx 0.34 \text{ mW/cm}^2$ ). Unit transfer was according to  $1 \text{ W/m}^2 \approx 0.46 \mu\text{mol m}^{-2}\text{s}^{-1}$ .

All SPECM images in chapter 3 are presented simultaneously in 2D and 3D projection in order to present a clearer representation of the photocurrent calculated as a function of fiber position. It is important to highlight that 3D image does not correspond to topography of the spot.

Figure 2.4c shows the schematic representation of SPECM for its application in the detection of PEC  $\text{CO}_2\text{RR}$  products with a dual tip OF-UME. The OF allows the light to locally illuminate p-type semiconductor materials on the biased substrate electrode (WE2). By moving the OF in the X-Y direction, a dual mapping of photocurrent and electrochemical detection was obtained. Simultaneously, the biased Pt UME (WE1) can detect and distinguish the photoelectrochemically generated products ( $\text{H}_2$ , CO and  $\text{HCOOH}$ ) by electrochemical oxidation.

#### 2.4.2.2. Chronoamperometric Photoactivity Quantification by SPECM

SPECM current quantification was carried by chronoamperometry (CH Instrument 920D) on individual  $\text{CuCo}_2\text{O}_4$  spots. First of all, a SPECM image was obtained for identifying the position and the shape of the  $\text{CuCo}_2\text{O}_4$  spots in the form of photocurrent, then the optical fiber was placed at 150  $\mu\text{m}$  above (X, Y coordinates known from the SPECM image) a  $\text{CuCo}_2\text{O}_4$  spot and it was kept still during chronoamperometry measurements. Initially, the substrate electrode is held at a constant potential while the light source is turned off. When a steady-state background substrate current is recorded ( $I_{\text{photo}}^{\text{OFF}}$ ), the light source was turned on and a constant photon flux facing the  $\text{CuCo}_2\text{O}_4$  spot is maintained for 50 s. Then, the corresponding

photocurrent response was recorded. Finally, the light source was turned off again. Then, the photocurrent average value ( $I_{photo}^{ON}$ ) was compared with ( $I_{photo}^{OFF}$ ) to quantitatively evaluate the photocatalyst  $CuCo_2O_4$  performance ( $\Delta I$ ) at different potentials and in different electrolyte solutions as is described in Equation 2-1. All SPECM photocurrent quantification data presented in this work correspond to the average value obtained after between 2 and 4 identical and independent experiments.

$$\Delta I = I_{photo}^{on} - I_{photo}^{Off} \quad 2-1$$

### 2.4.3. Fabrication of Agar Bridge

The salt bridge has been widely used in electroanalytic chemistry, because it can minimize ion exchange, liquid-junction potential (a few tens millivolts at most), Ohmic drop (IR drop), which is of vital importance for the electrochemical measurements [9]. IR drop is defined as the overpotential caused by the electrons flowing through the electrolyte solution with resistance between the RE and WE. This overpotential can induce the difference between the theoretical and practical applied potential. For this reason, it is convenient to use a salt bridge to lower the distance between the RE and WE and also to minimize the interaction of ions within the RE solution and that of the bulk electrolyte solution. In this work, 0.5 M  $KHCO_3$  agar bridge was fabricated and used for the SPECM experiment, particularly in the case of aqueous solution of 0.1 M  $KHCO_3$  and 0.1 M  $Na_2SO_4$  and the binary RTILs /water mixture solution. To fabricate the agar bridge, 1.0 g agar was dissolved in 50 ml of 80 °C distilled water, then the suspension solution was heated and magnetically stirred until reaching the boiling point to obtain a transparent agar solution. Then, 2.503 g  $KHCO_3$  was added into the agar solution. Once the  $KHCO_3$  salt was totally dissolved and a homogeneous suspension was obtained, the mixture was transferred into glass capillary which has a long and thin part with a small opening. It is important not to leave any air bubbles in the glass capillary to ensure the proper ionic continuity within the agar gel. The final step was cooling down the mixture for the formation of agar gel. Then, seal the two ends of the agar bridge with Parafilm to avoid the direct contact of the gel with the air, otherwise it would be dry and will not work anymore.

However, in the experiments of detecting PEC  $CO_2RR$  products by a dual tip OF-UME, instead of 0.5 M  $KHCO_3$  agar bridge, the Luggin capillary (a commercial capillary made of glass) was filled with the same solution used for products detection. This will be discussed in

detail in chapter 4.2. Furthermore, 0.1 M  $\text{KHCO}_3$  solution was filled in the Luggin capillary to connect the reference electrode with the electrochemical cell in chapter 5.

## 2.5. Fabrication and Characterization of Dual Tip OF-UME

### 2.5.1. Introduction of P-2000 Laser-Based Micropipette Puller

The fabrication of dual tip OF-UME was carried out with P-2000 micropipette puller from Sutter Instrument Co. (abbreviated as P-2000). P-2000 is designed for fabrication of micropipettes and fibers with the advantage of using  $\text{CO}_2$  laser as heat source. Compared to the conventional electric resistance wire heat source, P-2000 is capable of heating and pulling quartz glass, which has higher melting point than the conventional glasses, as well as precisely control the uniform temperature distribution on the micropipette. It can heat and pull borosilicate and aluminosilicate glass capillaries various size from 1.2 to 0.125 mm, as well as quartz and optical fibers [10].

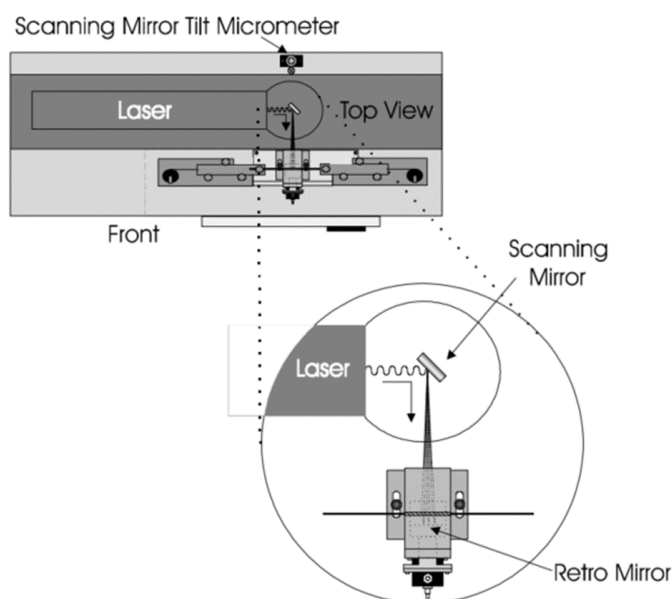


Figure 2.6 The diagram of the assembly and operation panel of the P-2000 micropipette puller.

The diagram of the assembly and operation panel of the P-2000 micropipette puller is shown Figure 2.6. The name and the function of each assembly unit are listed as follows:

1. Clamp knob, location where glass is placed and fixed by tightening down the clamping knob.
2. V-groove, confines the glass in horizontal position.

3. Puller bar, works together with bumper to fix and move the glass and prevent the impact forces from breaking glass.
4. Spring stop, prevents pipette tip collision by catching the puller bars as they rebound off.
5. Pull cable, conducts the pulling force of the solenoid to the puller bars.
6. Retro mirror assembly, a reflective concave mirror, which can collect and reflect the beam crossing the glass to redirect the divergent laser radiation onto the front side of the glass and thereby provides relatively uniform heating around the circumference of the glass. (See the optical pathway in Figure 2.7)
7. Finger bar, controls puller bar manually.
8. Liquid crystal display (LCD), displays program parameters.
9. Keyboard, programs parameter values and execute programs.



*Figure 2.7 Optical pathway (top view without laser housing). Reprinted from ref [10].*

Figure 2.7 shows the optical pathway of P-2000. The most important part is the CO<sub>2</sub> laser providing the heat source, whose output power is controlled by the HEAT value in the program. (see below in details). The laser beam is projected to the glass by a rotating scanning mirror, which can provide controllable scanning area by the value of FILAMENT parameter. In addition, a retro concave mirror can reflect the laser beam onto the front side of the glass, which ensures a uniform heating distribution around the circumference of the glass.

P-2000 has 100 separated programs with 5 adjustable parameters to control the micropipette tip geometry and size, namely HEAT, FILAMENT, VELOCITY, DELAY and PULL. A complete understanding of these parameters is necessary for achieving high reproducibility and success rate in fabricating micropipette with the same size.

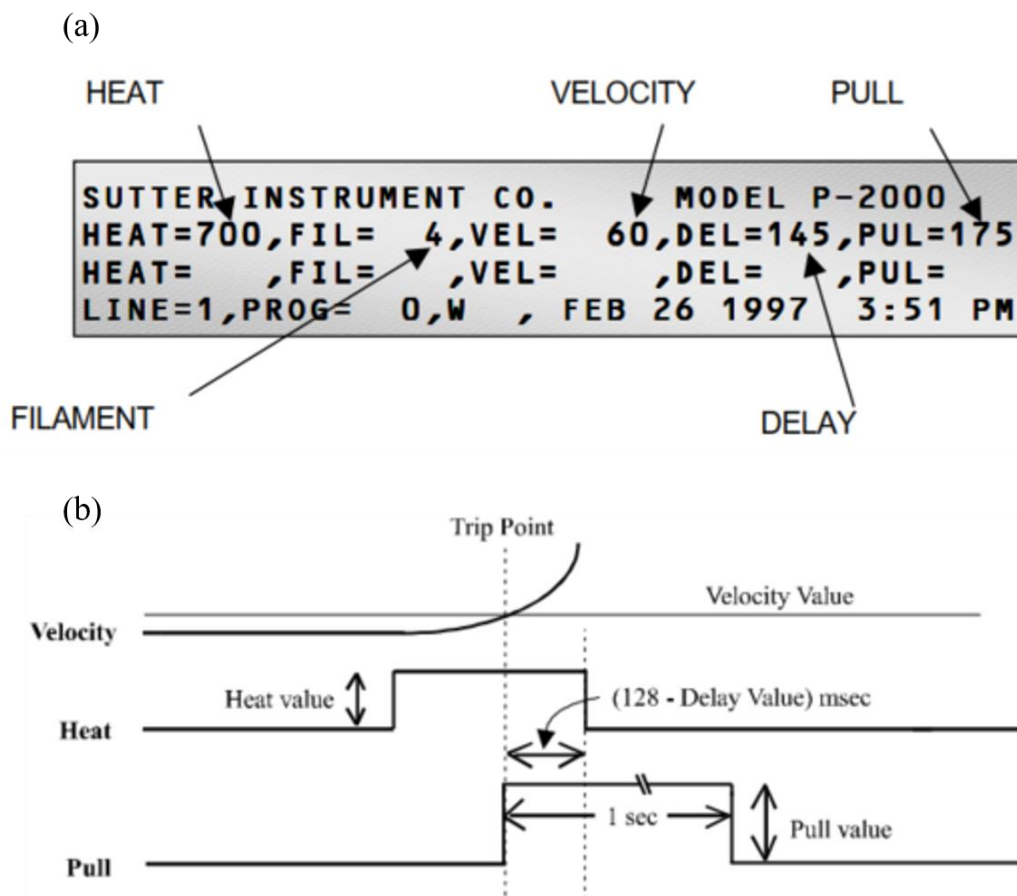


Figure 2.8 (a) LCD display with the program parameters. (b) Pull cycle when PULL is greater than 0 and DELAY is less than 128.

The LCD display in Figure 2.8a shows the program information and 5 parameters.

**HEAT:** Value range from 0 to 999. HEAT determines the output power of the laser and the micropipette tip length and size. In general, higher HEAT value means shorter melting time and longer and thinner tip. Increasing the HEAT value is necessary if the glass hasn't melted in less than 15 seconds.

**FILAMENT:** Value range from 0 to 15. FILAMENT determines the scanning pattern and velocity of the laser beam, together with HEAT, it can also control the fabrication time. The

higher the FILAMENT value is, the less power per unit length of the glass will get. A narrower FILAMENT is suggested if the melting time is too long.

**PULL:** Value range from 0 to 255. PULL determines the strength of the hard PULL. The higher value means the smaller of the tip size.

**VELOCITY:** Value range from 0 to 255. VELOCITY reflects the speed at which the two carrier bars are moving forced by a weak pull of the pull cable before the hard PULL. This VELOCITY is affected by the viscosity of the glass. The higher the value, the faster the puller bars moving and the smaller of the size of the tip.

**DELAY:** Value range from 0 to 255. DELAY determines the time to start the hard PULL. The longer the DELAY, the cooler the glass will be when the hard PULL starts. When the value of PULL is 0 or a very small value, the DELAY value has relative slight influence on the capillary tip size.

Figure 2.8b shows the flow diagram of P-2000 to execute one pull cycle when PULL is greater than 0. The steps are as follows:

2. The laser beam starts according to the set HEAT and FILAMENT values.
3. The glass is heated and pull weakly until the VELOCITY value (trip point).
4. If DELAY = 128, HEAT stops and hard PULL starts;  
If DELAY > 128, HEAT stops and hard PULL starts after (DELAY-128) ms;  
If DELAY < 128, hard PULL starts and HEAT stops after (128-DELAY) ms.

Overall, each parameter has effect on the fabrication process and the morphology of the capillaries or micropipettes. Then, suitable parameters should be precisely adjusted to obtain reproducible micropipettes.

### **2.5.2. Fabrication Procedure of Dual Tip OF-UME**

The dual tip OF-UME consists of 3 most important elements: noble metal wires (Pt or Au) as the UME, optical fiber (diameter of 50  $\mu\text{m}$  in our case) and the outer surround glass capillary. The metal wire should be embedded in the glass, which is heated to reach the softening point. Therefore, it is necessary to choose glass capillary materials with a matched softening point and expansion coefficient with the metal wires to taper the glass meanwhile no deformation is induced [11].

Table 2.5 Melting/softening points and thermal expansion coefficients of Pt, Au, borosilicate glass and quartz.

Material	Melting /softening point (°C)	Expansion coefficient, (25 °C) ( $\times 10^6 \text{ K}^{-1}$ )
Pt [11]	1769	9
Au [11]	1064	14
Borosilicate glass [12]	785	5.5
Quartz [13]	1670	0.55

In order to seal the metal wire in the glass, the sealing temperature should be higher than the softening point of the glass and lower than the melting point of the metal to avoid deformation. Thus, the softening point of the glass should be lower than the melting point of the metal wire. In addition, a higher thermal expansion coefficient of glass than that of metal is expected for a good fabrication. Table 2.5 listed melting/softening points and thermal expansion coefficients of Pt, Au, borosilicate glass and quartz. The melting point of Pt (1769 °C) is much higher than the softening point of the borosilicate glass (785 °C), which indicates that borosilicate glass is a good candidate for fabrication. However, the Au has a distinct higher expansion coefficient compared to the glass and the melting point is only ~ 300 °C higher, which makes it harder to be fabricated because of the low melting point. Compared to quartz which has been widely used to fabricate Pt UME, borosilicate glass has lower softening point and higher expansion coefficient, which are suitable properties for fabricating Pt and Au OF-UME.

The dual tip OF-UME fabrication process includes the following 5 steps:

1. Cleaning the Pt/Au wire (25  $\mu\text{m}$  in diameter) with ethanol and ultrapure water successively, each for 3 min.
2. Thinning of the borosilicate glass capillary (Figure 2.9). By placing the unprocessed borosilicate glass capillary (Figure 2.11a) in the V-groove and fixing it by the clam knobs in the puller bar of P-2000. Setup the suitable parameters in the program to start the fabrication process. The glass is heated to reach the softening point and is extended from both ends under a weak pull force until an hourglass shape is formed in the middle of the capillary. By adjusting

the values of HEAT, FILAMENT and VELOCITY, the size and morphology of the hourglass shape part is controlled. In order to avoid breaking down the capillary, no hard pull is applied in the program ( $PULL = 0$ ), which causes a short taper part of the capillary. Because of the final polishing process, a longer taper part is necessary to ensure a sharp tip with suitable length. Therefore, based on Program A in Table 2.6, firstly, the glass is heated for 20 s. Secondly, the capillary is moved right by 1.2 mm manually and the program A is repeated for another 12 s. Finally, the capillary is moved right for 0.5 mm more and repeat the same program for 8 s. In this way, a thin capillary was thinned with a long taper part is ready for the following steps (Figure 2.11b).

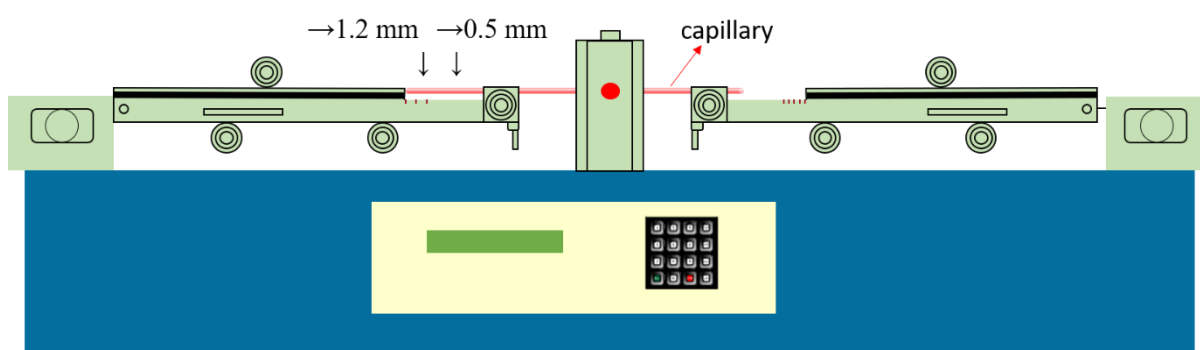


Figure 2.9 The sketch of the fabrication of dual tip (OF-UME) - thinning the capillary in the middle (step 2).

3. Sealing the metal wire and the optical fiber in the capillary (Figure 2.10). By putting the metal wire and the optical fiber together in the taper part of the capillary. Place and fix the capillary in the v-groove, meanwhile, two stoppers (O-rubber ring) are used to fix the puller bar in order to avoid the weak pulling force that could further thin and break the capillary. For sealing the capillary according to Program B for OF-UME (Pt) and Program C for OF-UME (Au) (see Table 2.6), start the heating for 15 s and move the capillary right for 0.5 mm repeating the same program for another 15 s. Given this, the same position of the capillary should be reached in the thinning and sealing process. As the melting point of Au is lower than that of Pt, program designed for Au (program C) is different from Program B for Pt, which includes a lower HEAT value in order to lower the heating temperature of the glass and avoid the melting of the Au. After this step, the sealed UME and OF in the capillaries shown in Figure 2.11c (with Pt wire) and d (with Au wire) are ready for the following steps.



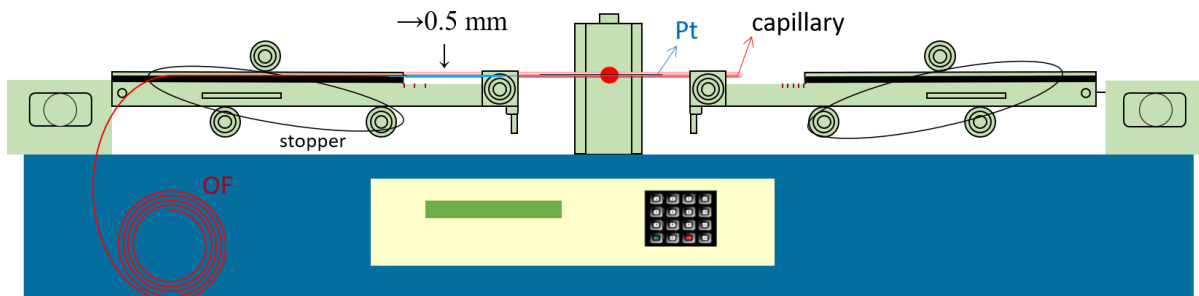


Figure 2.10 The sketch of the fabrication of dual tip (OF-UME) - sealing the capillary with metal wire (Pt or Au) and optical fiber with stopper to avoid the weak pulling (step 3).

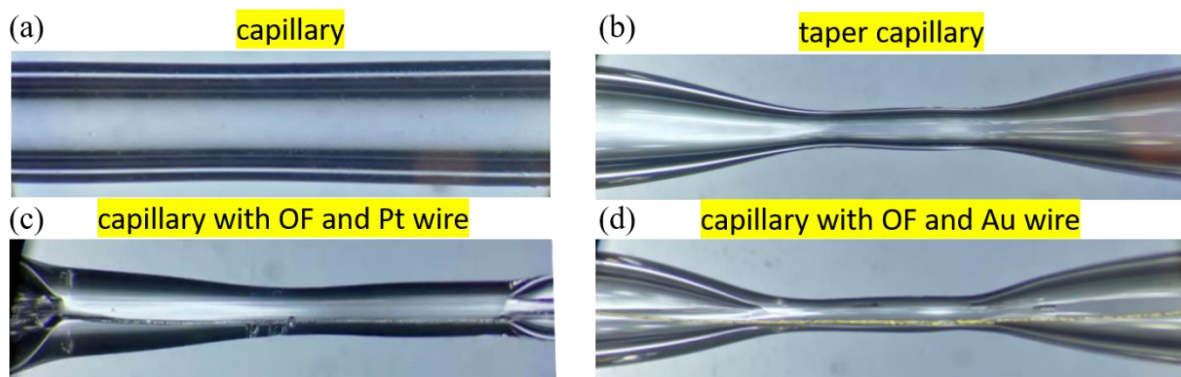


Figure 2.11 The optical micrographs of each step for fabricating dual tip: (a) unprocessed capillary. (b) capillary thinning. (c) Pt wire and optical fiber sealed in the capillary. (d) Au wire and optical fiber sealed in the capillary.

Table 2.6 Different P-2000 programs with suitable parameters used in the fabrication of OF-UME.

Program	Application	Parameters
A	Capillary thinning	HEAT = 380 FILAMENT = 4 VELOCITY = 15 DELAY = 120 PULL = 0
B	OF-UME (Pt) sealing	HEAT = 500 FILAMENT = 4 VELOCITY = 30 DELAY = 0 PULL = 0
C	OF-UME (Au) sealing	HEAT = 350 FILAMENT = 4 VELOCITY = 15 DELAY = 0 PULL = 0

4. Electrochemical connection of the OF-UME. The capillary in Figure 2.11c and d are cut in the right end of the taper capillary, which gives as a result the OF-UME tip. Conductive silver paint is injected into the compartment of the capillary to electrochemically connect the

Pt (or Au) wire with copper tinned wire. The other end of the capillary is sealed with epoxy resin to prevent solution entering (Figure 2.12a).

5. Polishing of the OF-UME. The end of the OF-UME tip is polished by sand paper and alumina suspension (0.3 and 0.05  $\mu\text{m}$ ) to get a flat surface.

The as-prepared dual tip OF-UME (Pt) is shown in Figure 2.12b and c for the side view and bottom view, which show the tip composed of an 50  $\mu\text{m}$  diameter optical fiber and 25  $\mu\text{m}$  diameter UME sealed next to each other (the gap between the centers of both is *ca.* 75  $\mu\text{m}$ ). In addition, the tip is  $\sim 0.2$  cm length and symmetrical about the center located OF. It can be further used for the detection of the photoelectrochemically generated products in SPECM configuration.

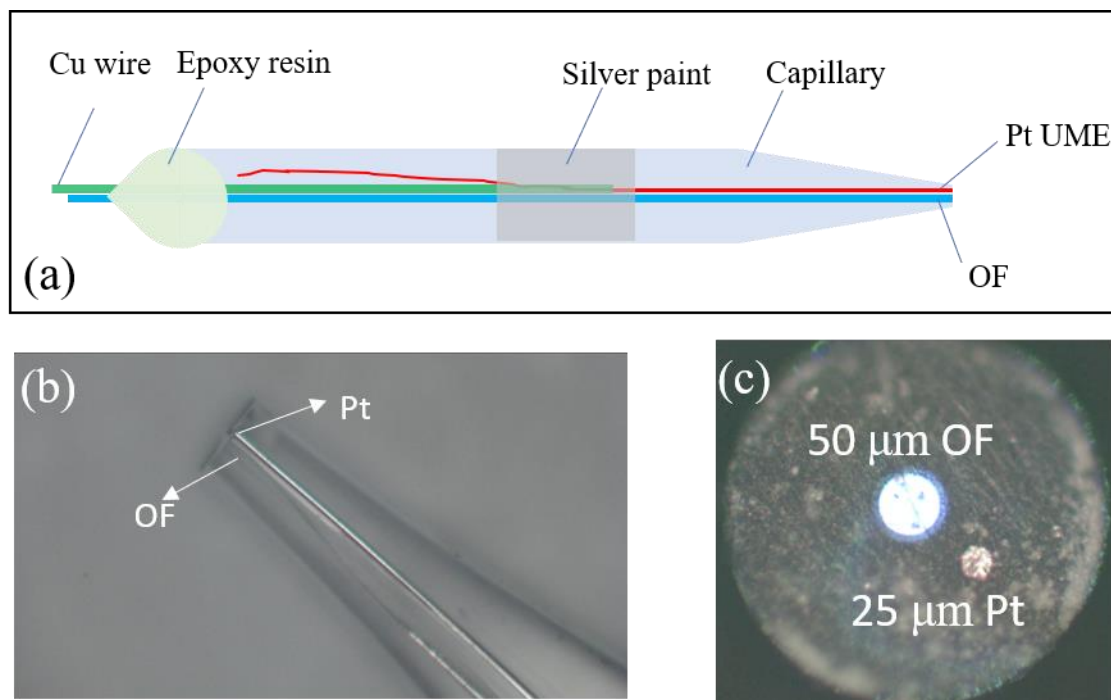


Figure 2.12 (a) Schematic representation of a whole fabricated dual tip OF-UME. Optical images of (b) side view and (c) bottom view of the OF-UME.

In general, cyclic voltammetry of reversible redox mediator species in solution such as ferrocenemethanol has been widely used for the characterization of the electrochemical properties, surface morphology and size of metallic microdisk UME, according to the steady-state diffusion current shown as Equation 1-2 in chapter 1.

Figure 2.13a and b show the steady-state cyclic voltammograms obtained by OF-UME (Pt) and (b) OF-UME (Au), respectively in solution of 1 mM ferrocenemethanol and 0.05 M KCl

as supporting electrolyte. A steady-state current response is reached in OF-UME (Pt) CVs showing the classic S-shape plot at low scan rate, this CV also shows a relatively small double layer charge-discharge current. From the steady state current reached at 0.4 V, knowing the diffusion coefficient of ferrocenemethanol  $7 \times 10^{-6} \text{ cm}^2/\text{s}$  and according to the Equation 1-2, the radius  $a$  of the Pt disk UME can be calculated. the theoretical radius of Pt disk UME is  $12.5 \text{ }\mu\text{m}$ , but the calculated value is larger ( $18.5 \text{ }\mu\text{m}$ ), this is because the surface of the Pt was not polished enough, since the tip is broken down easily during the mechanical polishing process, or because the Pt wire underwent some deformation during the sealing process. The CV obtained for the OF-UME (Au), doesn't reach a clear steady-state current. Moreover, the capacitive current displayed in the CV is much larger than that of Pt, indicating the existence of some resistance in the system probably caused by a poor electrical connection of the Au and the copper tinned wire. Overall, the CVs proved that combining the OF and UME we were able to fabricate dual tip OF-UMEs useful for the further application in our study.

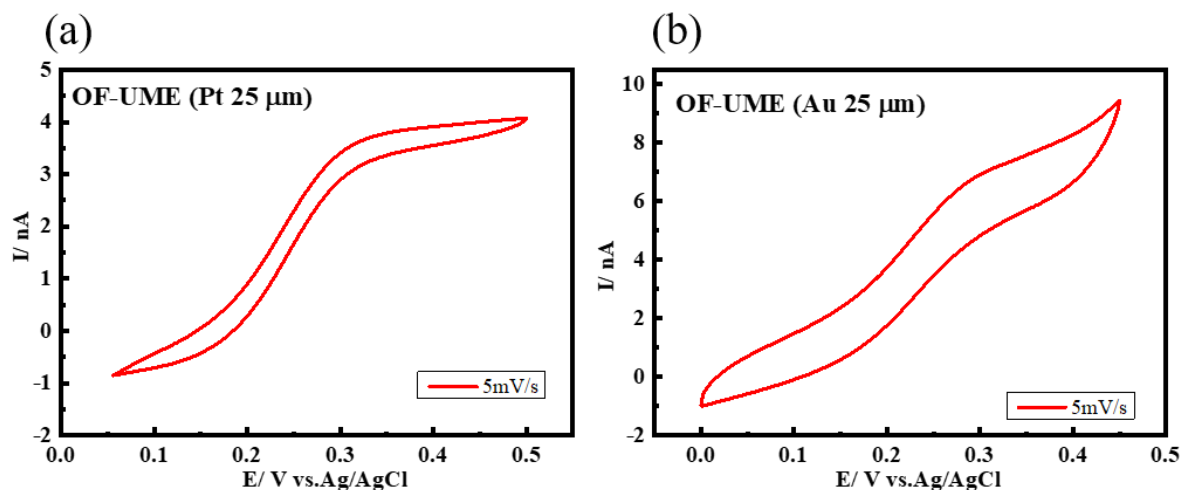


Figure 2.13 Steady-state cyclic voltammograms obtained at (a) OF-UME (Pt) and (b) OF-UME (Au) (both with diameter of  $25 \text{ }\mu\text{m}$ ) in solution of  $1 \text{ mM}$  ferrocenemethanol and  $0.05 \text{ M}$  KCl as supporting electrolyte. The potential limits were  $0.05$  to  $0.5 \text{ V}$  vs. Ag/AgCl initiated from  $0.05 \text{ V}$ . The scan rate was  $5 \text{ mV/s}$ .

## 2.6. Rotating Disk Electrode (RDE)

The Rotating Disk Electrode (RDE) is a hydrodynamic working electrode used in a three-electrode system. It is one of the few convective electrode systems in which the hydrodynamic equations and the convective-diffusion equation have been solved rigorously for the steady state [14]. RDE provides good reproducibility and stable polarization curve because the

diffusion layer thickness is controlled by the rotation speed. Moreover, the reactions (such as ORR) can reach the steady state profile very fast thanks to the electrode rotation. As a result, it is widely used in many electrochemical fields [15,16].

RDE (Figure 2.14) is composed of a disk electrode (glassy carbon in our case) embedded in an insulator rod (Teflon). The electrode is attached to a motor unit controlling its rotation speed. The rotation of the electrode produces a well-defined liquid flow pattern in laminar regime. In the diffusion layer the mass transfer is defined by diffusion, and out of the diffusion layer it is defined by convection [17]. For this reason, several kinetic parameters such as diffusion coefficient, the thickness of diffusion layer and the electron transfer number can be calculated, by which the mechanism of the reaction can be deduced.

The *Levich equation* is widely used to analyze steady-state voltammograms at the RDE, which is depended on both the rotation rate and the diffusion coefficient, and the rotation rate is varied to adjust the mass transfer coefficient:

$$i_{l,c} = 0.62nFAD_o^{2/3}\omega^{1/2}\nu^{-1/6}C_o^* \quad 2-2$$

where  $n$  is the number of electrons transferred in electrochemical reaction;  $F$  is Faraday constant, 96500 C/mol;  $A$  is the electrode area;  $D_o$  is diffusion coefficient ( $\text{m}^2/\text{s}$ );  $\nu$  is the kinematic viscosity ( $\text{m}^2/\text{s}$ );  $\omega$  is the rotation speed of RDE (rad/s);  $C_o^*$  is the bulk concentration of electroactive species ( $\text{mol}/\text{m}^3$ ).

In this thesis, the rotating disk electrode was used for evaluating the performance of different M–N–C catalysts for electrochemical  $\text{CO}_2\text{RR}$ . As shown in Figure 2.14b, the experiment configuration contains a 5-neck cell filled with 100 mL 0.1 M  $\text{KHCO}_3$ ; the working electrode (AFE5T050GC, Pine research) has a 5 mm OD glassy carbon disk electrode cladding with a 15 mm OD Teflon shroud; the counter electrode is graphite rod (PINE research, AFCTR3B); the reference electrode is Ag/AgCl which is immersed in a Luggin capillary full of 0.1 M  $\text{KHCO}_3$  solution. Cyclic voltammetry and Linear sweep voltammetry experiments were carried out to compare the performance of different M–N–Cs on  $\text{CO}_2\text{RR}$ . All experiments were carried out at room temperature.

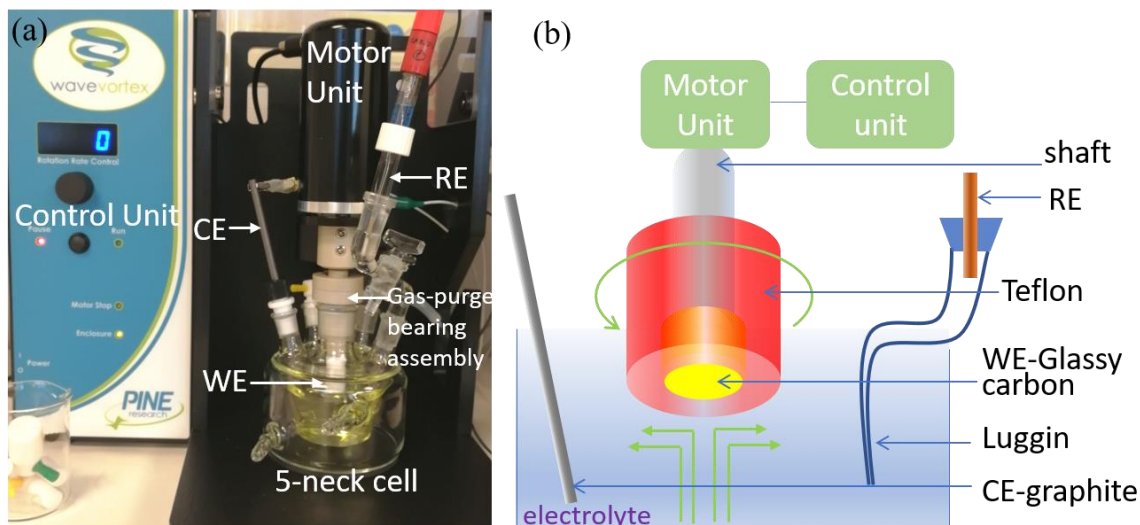


Figure 2.14 (a) Picture of the commercial RDE instrument. (b) Schematic representation of RDE.

## 2.7. Electrochemical CO<sub>2</sub>RR on Synthesized M–N–Cs

### 2.7.1. Synthesis and Characterization of Different M–N–Cs

To evaluate the electrocatalytic behavior of M–N–C materials for CO<sub>2</sub>RR, different M–N–C catalysts were prepared following the same methodology, and denoted as (1) 50%Co–N–C, (2) 50%Fe–N–C, (3) 50%Cu–N–C, (4) 25%Fe25%Co–N–C, (5) 25%Fe25%Cu–N–C, (6) 25%Co25%Mn–N–C and (7) 25%Cu25%Co–N–C, together with metal free–N–C. In all the samples, the percentage corresponds to the metal mass percentage relative to the initial amount of chitosan (Figure 2.15a). The general procedure to obtain these compounds is explained in base of the 25%Cu25%Co–N–C sample, as follows: 2 g of chitosan, 0.5 g Fe (3.6071 g Fe(NO<sub>3</sub>)<sub>2</sub>·9H<sub>2</sub>O) and 0.5 g Co (2.4692 g Co(NO<sub>3</sub>)<sub>2</sub>·6H<sub>2</sub>O) were added into 250 mL H<sub>2</sub>O and stirred during 24 h at room temperature to form a precipitate. Then, the precipitate was washed and stirred for 24 h in 250 mL H<sub>2</sub>O at room temperature, and dried in oven at 80 °C for 12 h. 4.0% KOH solution (4 g KOH/100 g H<sub>2</sub>O) was prepared and mixed with the precipitate to increase the surface area of M–N–C catalysts (25 mL KOH solution per 1 g of precipitate). In this step, it is better to grind the precipitate using an agate mortar for a better dispersion in KOH solution. Then, the mixture was stirred in 2 consecutive steps: 5 h at room temperature and 1 h at 50 °C. Afterwards, the mixture was totally dried at 100 °C for 5 h and ground to powder. Finally, the compound was pyrolyzed at 600 °C for 2 h with a heating ramp of 10 °C/min under N<sub>2</sub> atmosphere (Figure 2.15b) followed by a natural cooling down of the

furnace. Sequentially, the pyrolyzed compound was grinded for 20 min in an agate mortar. As a result, the transition metal–N doped–carbon catalyst of 25%Fe25%Co–N–C was prepared in a form of black powder (Figure 2.15c). The final ratio of the M: N: C in the catalyst has not been quantified yet. The structure of M–N–C can be represented as a 2D graphene-like structure with N and metal atoms embedded in the carbon matrix (Figure 2.15d).

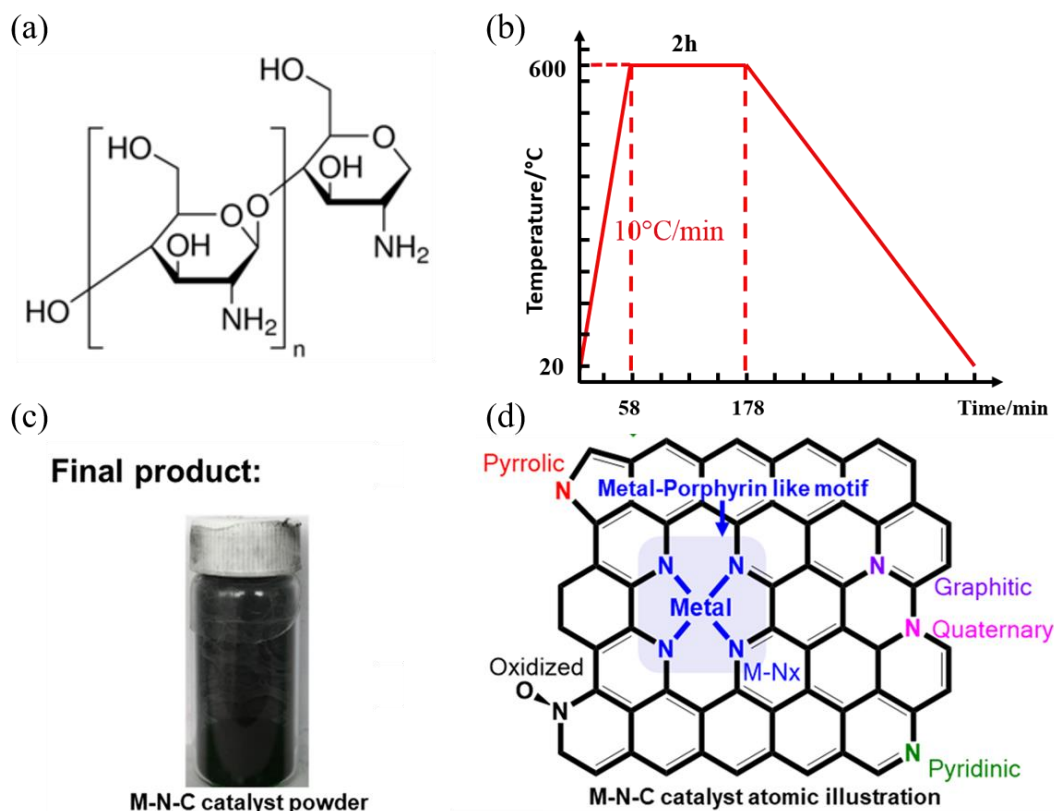


Figure 2.15 (a) Chemical structure of chitosan molecular. (b) Temperature program in pyrolysis process. (c) Appearance of the final product of M–N–C catalyst. (d) Model structure of M–N–C catalyst [18].

### 2.7.2. Electrode Preparation and Electrochemical Characterization

All electrochemical measurements were performed in a conventional electrochemical cell using a glassy carbon electrode (GC, active surface area: 0.126 cm<sup>2</sup>) as a working electrode, a Ag/AgCl (3 M KCl) electrode as a reference immersed in a Luggin capillary, filled with 0.1 M KHCO<sub>3</sub>, and a graphite rod as the counter electrode. All the potentials were converted to RHE considering the corresponding pH value.

To modify the GC surface, the electrode was polished with an alumina suspension (0.05 μm) for 3 min and sonicated in methanol and ultrapure water for 3 min sequentially. The

catalytic inks were prepared as follows: 6 mg of the catalyst dispersed in 0.5 mL DMF (N,N-dimethylformamide) were ultrasonicated for 15 min. Then, Nafion (7  $\mu$ L, 5wt% in alcohols, Sigma-Aldrich) was added into the suspension and it was ultrasonicated for another 30 minutes. The GC electrode was modified by spin coating: 7  $\mu$ L of the catalytic ink was dropped on the surface of GC electrode, following solvent evaporating while the electrode rotated at a speed of 300 rpm under a flow of N<sub>2</sub> to form a catalyst film on the GC electrode surface. The total amount of catalysts in the electrode was the same for all the samples and correspond to 0.67 mg/cm<sup>2</sup> (mass loading).

### 2.7.3. Evaluation Methods of Electrochemical CO<sub>2</sub>RR Performance on Different M–N–C catalyst by RDE

The Cyclic Voltammograms (CVs) and Linear Sweep Voltammograms (LSVs) experiments were carried out with a CH Instrument 760E potentiostat coupled to a WaveVortex 10 rotator (Pine research). All the scan rates in LSVs were 5 mV/s in CO<sub>2</sub> saturated solution (electrolyte: 0.1 M KHCO<sub>3</sub>). A flow of N<sub>2</sub> or CO<sub>2</sub> was kept as a blanket on top of the solution during the experiment in order to maintain a saturated atmosphere in the electrolyte. The catalytic activity was evaluated by the determination of the onset potential (calculated as the potential when the current density increases one order of magnitude from the capacitive current) and the current density at constant potential at -0.9V vs. RHE.

## 2.8. Bulk Electrolysis under Illumination

Bulk Electrolysis under illumination were performed at room temperature (25 °C) in a 25 vol.% [C<sub>2</sub>mim][BF<sub>4</sub>]/H<sub>2</sub>O (pH = 3.5). Before each experiment, the cell was degassed with CO<sub>2</sub> for 30 minutes and then sealed. Both compartments (cathode and anode) were gas-tight and were separated by a low-porosity glass frit. The counter electrode was a platinum mesh and the reference electrode was Ag/AgCl (3 M KCl) connected to the cell through a 0.5 M KHCO<sub>3</sub> agar bridge. The electrical contact between the working electrode (24 × 26 spots array of CuCo<sub>2</sub>O<sub>4</sub> on FTO substrate shown in Figure 2.16a, the gap between two spots center is 550  $\mu$ m) and the potentiostat was made by a copper tape. The array of CuCo<sub>2</sub>O<sub>4</sub> presents a total loading of 0.5 mg, the geometrical surface of WE immersed in solution is 1.54 cm<sup>2</sup>. The photoelectrochemical assembly is shown in Figure 2.16b. The cell has a lateral opening to which it is possible to attach the FTO substrate electrode, illuminate it from the front and



contact it with the solution from the front. Ohmic losses in the cell were minimized by placing the electrodes as close as possible to each other and stirring both solution compartments during the experiment. Moreover, 85% of the electrolyte resistance was compensated by the Ohmic drop compensation module of the potentiostat. Bulk electrolysis experiments were performed using a 280 W, high pressure Xe arc lamp (lamp power: 10 mW/cm<sup>2</sup>). The beam was passed through a water infrared filter and a collimating lens (Asahi Spectra). During irradiation, solutions were vigorously stirred and aliquots of gas and liquid were analyzed.

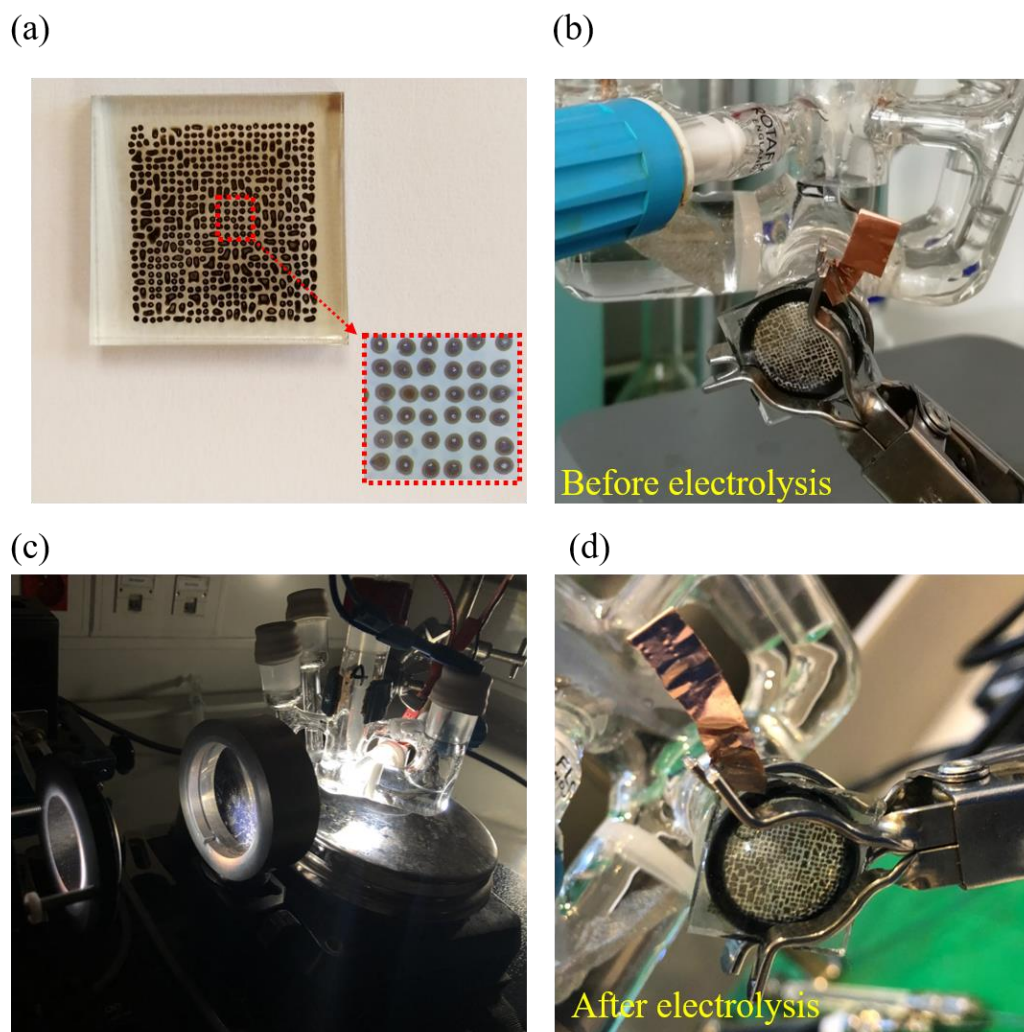


Figure 2.16 (a) CuCo<sub>2</sub>O<sub>4</sub> spots array with a pattern of 26×24 spots, inset is the magnification of a portion of the array. (b) Configuration of the electrolysis cell with CuCo<sub>2</sub>O<sub>4</sub> spots array immersed in the electrolyte (25 vol.% [C<sub>2</sub>mim][BF<sub>4</sub>]/H<sub>2</sub>O saturated with CO<sub>2</sub>), 11 mL in the cathode chamber and 6 mL in the anode chamber. the O-ring was used to seal and confine the surface area contacting the electrolyte with diameter 14 mm. (c) Configuration of the electrolysis process under illumination of



*Xenon-lamp, light illumination from the front side of the substrate electrode. (d) The morphology of  $\text{CuCo}_2\text{O}_4$  spots array after electrolysis under illumination for 2 h.*

## 2.9. Characterization Methods

### 2.9.1. Scanning Electron Microscopy (SEM)

For obtaining the morphology and structure of the p-type semiconductor materials and M–N–C materials, Field emission gun scanning electron microscopy (FEG-SEM) (Zeiss, Supra 55 microscope) was used.

### 2.9.2. Energy-Dispersive X-ray Spectroscopy (EDS)

The chemical composition of synthesized p-type semiconductor materials and M–N–C materials were quantified by energy dispersive X-ray spectroscopy (EDS) (Bruker QUANTAX).

### 2.9.3. Gas Chromatography (GC) and Ionic Chromatography (IC)

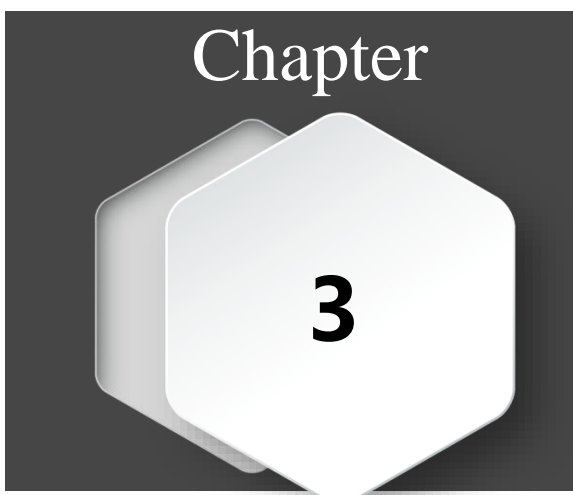
Electrolysis products yields are reported as Faradaic efficiency (FE), which is defined as the ratio between the charge consumed to form each reaction product and the total circulated charge. Gas products from the bulk electrolysis were quantified by gas chromatography (Model 8610C SRI Instruments) from 50  $\mu\text{L}$  aliquots of the headspace of both compartments.  $\text{H}_2$  and  $\text{CO}$  were detected by thermal conductivity detector (TCD) and flame ionization detector (FID), respectively. Products in the electrolyte solution were determined using a Metrohm 883 Basic IC plus ionic exchange chromatography instrument, equipped with a Metrosep A Supp 5 column and a conductivity detector. A typical measurement requires the sampling of 50  $\mu\text{L}$  of solution, followed by a 200 times dilution in ultrapure water and injection of 20  $\mu\text{L}$  into the IC chromatograph.

## 2.10. References

- [1] B.A. Rosen, A. Salehi-Khojin, M.R. Thorson, W. Zhu, D.T. Whipple, P.J.A. Kenis, R.I. Masel, Ionic liquid-mediated selective conversion of  $\text{CO}_2$  to  $\text{CO}$  at low overpotentials, *Science*. 334 (2011) 643–644. <https://doi.org/10.1126/science.1209786>.
- [2] Y. Wang, T. Hayashi, D. He, Y. Li, F. Jin, R. Nakamura, A reduced imidazolium cation layer serves as the active site for electrochemical carbon dioxide reduction, *Appl. Catal. B Environ.* 264 (2020) 118495. <https://doi.org/10.1016/j.apcatb.2019.118495>.

- [3] S.P. Berglund, H.C. Lee, P.D. Núñez, A.J. Bard, C.B. Mullins, Screening of transition and post-transition metals to incorporate into copper oxide and copper bismuth oxide for photoelectrochemical hydrogen evolution, *Phys. Chem. Chem. Phys.* 15 (2013) 4554–4565.
- [4] J.L. Fernández, D.A. Walsh, A.J. Bard, Thermodynamic guidelines for the design of bimetallic catalysts for oxygen electroreduction and rapid screening by scanning electrochemical microscopy. M-Co (M: Pd, Ag, Au), *J. Am. Chem. Soc.* 127 (2005) 357–365. <https://doi.org/10.1021/ja0449729>.
- [5] J.E. Katz, T.R. Gingrich, E.A. Santori, N.S. Lewis, Combinatorial synthesis and high-throughput photopotential and photocurrent screening of mixed-metal oxides for photoelectrochemical water splitting, *Energy Env. Sci.* 2 (2009) 103–112. <https://doi.org/10.1039/B812177J>.
- [6] J. Cheng, H. Yan, Y. Lu, K. Qiu, X. Hou, J. Xu, L. Han, X. Liu, J.-K. Kim, Y. Luo, Mesoporous  $\text{CuCo}_2\text{O}_4$  nanograsses as multi-functional electrodes for supercapacitors and electro-catalysts, *J. Mater. Chem. A* 3 (2015) 9769–9776.
- [7] Y. Sharma, N. Sharma, G.V.S. Rao, B.V.R. Chowdari, Lithium recycling behaviour of nano-phase- $\text{CuCo}_2\text{O}_4$  as anode for lithium-ion batteries, *J. Power Sources* 173 (2007) 495–501. <https://doi.org/10.1016/j.jpowsour.2007.06.022>.
- [8] A.J. Bard, M.V. Mirkin, *Scanning electrochemical microscopy*, CRC Press, 2012.
- [9] T. Kakiuchi, Salt bridge in electroanalytical chemistry: past, present, and future, *J. Solid State Electrochem.* 15 (2011) 1661–1671. <https://doi.org/10.1007/s10008-011-1373-0>.
- [10] P-2000 laser based micropipette puller system operation manual, Sutter Instrum. (2010) 86.
- [11] B. Zhang, J. Galusha, P.G. Shiozawa, G. Wang, A.J. Bergren, R.M. Jones, R.J. White, E.N. Ervin, C.C. Cauley, H.S. White, Bench-top method for fabricating glass-sealed nanodisk electrodes, glass nanopore electrodes, and glass nanopore membranes of controlled size, *Anal. Chem.* 79 (2007) 4778–4787. <https://doi.org/10.1021/ac070609j>.
- [12] WORLD PRECISION INSTRUMENTS, Physical properties of WPI glass capillaries, (n.d.).
- [13] Thermal properties of fused quartz, (n.d.). <https://www.momentive.com/en-us/categories/quartz/thermal-properties>.
- [14] A.J. Bard, L.R. Faulkner, J. Leddy, C.G. Zoski, *Electrochemical methods: fundamentals and applications*, Wiley New York, 1980.
- [15] S.-J. Lee, S.-I. Pyun, S.-K. Lee, S.-J.L. Kang, Fundamentals of rotating disc and ring-disc electrode techniques and their applications to study of the oxygen reduction mechanism at Pt/C electrode for fuel cells, *Isr. J. Chem.* 48 (2008) 215–228. <https://doi.org/10.1560/IJC.48.3-4.215>.
- [16] O.A. Baturina, Q. Lu, M.A. Padilla, L. Xin, W. Li, A. Serov, K. Artyushkova, P. Atanassov, F. Xu, A. Epshteyn, T. Brintlinger, M. Schuette, G.E. Collins,  $\text{CO}_2$  electroreduction to hydrocarbons on carbon-supported Cu nanoparticles, *ACS Catal.* 4 (2014) 3682–3695. <https://doi.org/10.1021/cs500537y>.
- [17] J. Nikolic, E. Expósito, J. Iniesta, V. Montiel, Theoretical concepts and applications of a rotating disk electrode, 77 (2000) 2–5.
- [18] A.S. Varela, W. Ju, A. Bagger, P. Franco, J. Rossmeisl, P. Strasser, Electrochemical reduction of  $\text{CO}_2$  on metal-nitrogen-doped carbon catalysts, *ACS Catal.* 9 (2019) 7270–7284. <https://doi.org/10.1021/acscatal.9b01405>.





# Photoelectrochemical Activity for CO<sub>2</sub>RR in Different RTILs-based Solvent Media Evaluated by SPECM

---



## Chapter 3 Photoelectrochemical Activity for CO<sub>2</sub>RR in Different RTILs-based Solvent Media Evaluated by SPECM

### 3.1. Introduction

The rapid development of the global economics relies on the consumption of fossil fuels such as coal and petroleum, which causes the emission of CO<sub>2</sub> and other greenhouse gases, leading to energy crisis and environmental problems [1]. Electrochemical CO<sub>2</sub> reduction reaction (CO<sub>2</sub>RR) is a promising method to convert CO<sub>2</sub> into different value-added products such as carbon monoxide (CO), formic acid (HCOOH), methanol (CH<sub>3</sub>OH) and methane (CH<sub>4</sub>). In particular, photoelectrochemical CO<sub>2</sub> reduction reaction (PEC CO<sub>2</sub>RR) on photoelectrocatalysts driven by ultraviolet (UV) or visible light fulfills a synergetic role of both photovoltage and electrical bias to promote CO<sub>2</sub> conversion process [2,3].

The activity and product selectivity in PEC CO<sub>2</sub> conversion are affected by many factors including the chemical composition of the electrochemical catalysts and the properties of the electrolytes used [4]. Considering the role of electrolytes, PEC CO<sub>2</sub>RR in aqueous solution is confined by two main drawbacks: *i*) CO<sub>2</sub> presents much lower solubility in aqueous solution than in nonaqueous solvents [5]; *ii*) Some competitive side reactions such as hydrogen evolution reaction (HER) from water reduction takes place at a similar thermodynamic potential than CO<sub>2</sub> conversion, which causes low selectivity and efficiency of the conversion process [6]. Conventional nonaqueous solvents such as acetonitrile or dimethylformamide show high toxicity and flammability and this represents a severe limitation as well. Room temperature ionic liquids (RTILs) have been proposed as suitable non-conventional solvents to perform CO<sub>2</sub> conversion and to overcome all those limitations [7]. They are widely used in different electrochemical applications due to their physicochemical advantages such as suitable ionic conductivity, low volatility, high thermal stability, wide electrochemical potential window [8]. Amongst RTILs, imidazolium based RTILs ([C<sub>n</sub>mim]<sup>+</sup>) show high conductivity and CO<sub>2</sub> solubility and they have been extensively studied for electrochemical CO<sub>2</sub>RR [9]. However, the use of pure RTILs as electrolyte requires a lot of precautions, since the amount of impurities (especially H<sub>2</sub>O) present in the RTIL significantly affect the electrochemical response [10,11]. Moreover, the maximum current achieved at the electrode surface is limited

by the high viscosity displayed by most of the RTILs, which slows down the diffusion of all electroactive species in solution [7]. For this reason, mixing RTILs with molecular solvents have been proposed as a suitable strategy to overcome those limitations. The seminal work of Rosen *et al.* [12] proved the relevant synergetic effect of mixing H<sub>2</sub>O and [C<sub>2</sub>mim][BF<sub>4</sub>] to increase CO<sub>2</sub> reduction on silver electrodes by lowering the energy barrier of this reaction. Most recent published works on this topic are devoted to explore binary and ternary mixtures such as RTIL/water, RTIL/acetonitrile and RTIL/acetonitrile/water, since it has been recently demonstrated the cocatalyst role played by the imidazolium cations in those mixtures by reaching remarkable results in electrochemical CO<sub>2</sub>RR on different metallic electrodes. Lau *et al.* [13] evaluated a series of imidazolium based RTILs as cocatalysts in acetonitrile containing 0.1 M [TBA][PF<sub>6</sub>] for electrochemical CO<sub>2</sub>RR on Ag electrode. By comparing the performance of the addition of a small quantity of water or imidazolium salts, they proved the increase of the current density should not be credited to the presence of water, but to the imidazolium cations, thus proving the cocatalyst role of imidazolium cations. In contrast, the anions have little effect on the CO<sub>2</sub>RR. Zhu *et al.* evaluated [BMIM][PF<sub>6</sub>]/AN/H<sub>2</sub>O ternary mixture and found that the addition of small amount water can greatly enhance the efficiency of CO<sub>2</sub> to HCOOH compared to binary mixture [BMIM][PF<sub>6</sub>]/AN and pure [BMIM][PF<sub>6</sub>] [14].

Furthermore, owing to the extremely stable symmetric CO<sub>2</sub> molecule, high energy of 750 kJ/mol is necessary to break the carbonyl bond. For this reason, the adoption of PEC catalysts with high catalytic activity and products selectivity, as well as long-term stability and capable of lowering the energy barrier is indispensable. Amongst numerous PEC catalysts, p-type semiconductor materials, especially metal oxide semiconductors, consisting of earth-abundant and cost-effective metallic materials present outstanding catalysis on PEC CO<sub>2</sub>RR with the ability of absorbing light and produce photogenerated electron-hole pairs as charge carriers. However, some p-type semiconductors suffer from low stability in aqueous solutions because the conduction band energy is more negative than the reduction potential of the metal ion in the lattice, thus resulting in a degradation of the semiconductor surface and then inactivating the photoelectrocatalytic efficiency. Furthermore, compared to single metal oxide semiconductor, multi-metal semiconductors can provide suitable band gap energies and increase the separation of electron-hole pairs by inhibiting their recombination through the

interaction of different elements [15]. Therefore, combination of binary or ternary metals oxide material have grasp tons of attention in the application of PEC catalysis.

SECM and SPECM represent electroanalytical local techniques widely used for screening sample arrays. In this work, SPECM was used for selecting the candidate semiconductor catalysts for PEC CO<sub>2</sub>RR based on activity evaluation, as well as qualitatively and quantitatively explored the role of imidazolium based RTILs as a solvent electrolyte and cocatalyst in the PEC CO<sub>2</sub>RR.

Nevertheless, as far as the author know, there is not one single publication devoted to explore PEC CO<sub>2</sub>RR using p-type semiconductors in imidazolium based RTIL/H<sub>2</sub>O mixtures taking advantage of light absorption properties of imidazolium cations. In particular, this chapter is focused on studying the role of imidazolium based RTILs acting as solvent supporting electrolyte and/or cocatalyst by comparing photocurrent production in different solvent media. For this reason, we prepared and screened different p-type semiconductors and choose CuCo<sub>2</sub>O<sub>4</sub> as a model material in order to selectively address the effect of imidazolium based RTILs in the interfacial charge transfer rate for PEC CO<sub>2</sub>RR, and thus, in the photocurrent production efficiency. All other effects such as band gap, light absorption efficiency, carrier mobility and carrier recombination rate are mainly controlled by the chemical composition and morphology of the semiconductor material and will be kept constant in this work.

### **3.2. Screening and Comparison of different p-type Metal Oxide Semiconductors**

All p-type semiconductors were in-situ synthesized and screened for PEC CO<sub>2</sub>RR by SPECM. This evaluation was only performed in aqueous solution. The eligible p-type semiconductor candidates should be chemically stable with a suitable band gap energy compared to CO<sub>2</sub> reduction potential and capable of absorbing light. Transition metals are commonly employed to synthesize metal-based catalysts such as Cu, Fe, Co, Ag, Ni, and Mn, etc. due to their catalytic activity and selectivity, low-cost and earth-abundance. Several p-type metal oxide semiconductors have been reported for their abilities in electrochemical or photoelectrochemical catalysis for CO<sub>2</sub>RR or HER including CuO<sub>x</sub> [16], CuCo<sub>2</sub>O<sub>4</sub> [17], AgCoO<sub>2</sub> [18], NiMn<sub>2</sub>O<sub>4</sub> [19], CuNiO [20]. We adopted and combined above mentioned metals



to form p-type metal oxide semiconductors as the catalysts to explore the role of RTILs in the performance of PEC CO<sub>2</sub>RR. It's worth noting that the metallic combinations should be miscible to make sure the intimate metallic contact.

The preparation process of various arrays of substrate electrodes containing different PEC catalysts of oxide-derived metal materials was presented in detail in chapter 2.2. The molar ratio of different precursor solutions is modified according to the stoichiometry of the target metal oxide. For example, to obtain CuCo<sub>2</sub>O<sub>4</sub>, one single precursor solution containing of 0.1 M Cu(NO<sub>3</sub>)<sub>2</sub> and 0.2 M Co(NO<sub>3</sub>)<sub>2</sub> in ethylene glycol were used, whereas 0.1 M AgNO<sub>3</sub> and 0.1 M Co(NO<sub>3</sub>)<sub>2</sub> solutions drove the synthesis of AgCoO<sub>2</sub>. After the thermal treatment in air, the as-prepared array substrate with metal oxides catalysts were screened by SPECM, which experimental procedure was also explained in chapter 2.4.2.

Figure 3.1 shows some initial array tests with of CuO<sub>x</sub> (upper row) and NiO<sub>x</sub> (lower row). In Figure 3.1a, 0.5 M Cu(NO<sub>3</sub>)<sub>2</sub> was used to synthesize CuO<sub>x</sub> spot array, which presents similar diameter size under same parameters and diminishes as the dispensing number of drops decreases from 30, 20, to 10 drops, which produced spots of 385 μm, 335 μm and 270 μm in diameter, respectively. The CuO<sub>x</sub> spots are composed of black microparticle clusters, which dispersed more intensively in the border and sparse in the middle of the spot. Figure 3.1b shows the corresponding SPECM image of the 3 spots in the first row of the CuO<sub>x</sub> array substrate under UV-vis light, the potential of the array substrate is held at -0.1 V vs. Ag/AgCl. The color map in the image represents the magnitude of the photocurrent generated on the array substrate, the bright yellow part in the SPECM images represents the photocurrent generated when the CuO<sub>x</sub> spots are illuminated and the green color represents the background current of the illuminated FTO substrate. A small oxidation current (10<sup>-10</sup> A) was collected on the SPECM image b and e, which probably corresponds to the oxidation of CuO<sub>x</sub> and NiO<sub>x</sub> at this potential. The low photocurrent detected provokes a poor contrast between background and catalysts regions, which gives as a result a poor definition of the spots. Scanning the array substrate at different potentials (-0.1 V, -0.2 V, -0.4 V, -0.5 V and -0.7 V vs. Ag/AgCl), the CuO<sub>x</sub> spots become less dense and some of the material lost (Figure 3.1c), proves that the CuO<sub>x</sub> has low stability and low catalytic efficiency.



the spots shows higher photocurrent compared with the border part, indicating different composition and activity of the inhomogeneous FeO<sub>x</sub> spot (Figure 3.3e). However, it should be mentioned that the advantage of CuFe<sub>2</sub>O<sub>x</sub> and FeO<sub>x</sub> are their relative stability, since no significant change is observed after the SPECM experiment (Figure 3.3c and f).

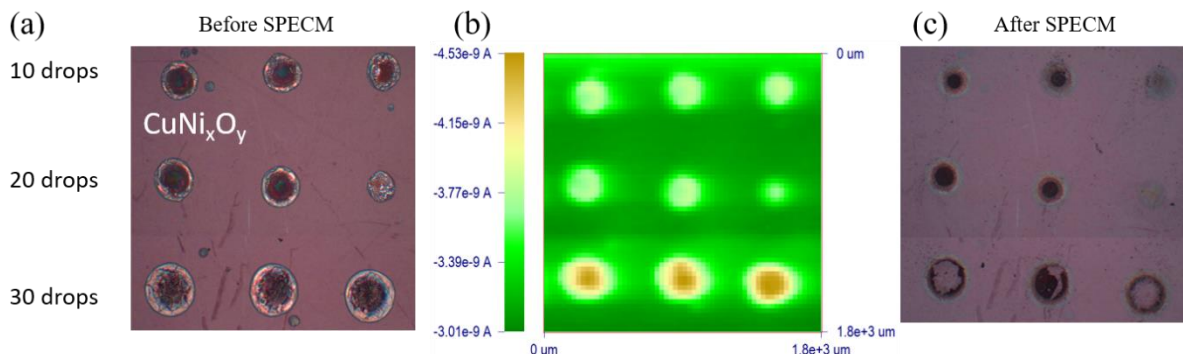


*Figure 3.2 Optical microscopy images of CuNi<sub>x</sub>O<sub>y</sub> array substrate electrode (a) before and (c) after SPECM imaging experiment. (b) The corresponding SPECM image of CuNi<sub>x</sub>O<sub>y</sub> array substrate of (a). Applied potential of -0.2 V vs. Ag/AgCl in 0.1 M Na<sub>2</sub>SO<sub>4</sub> solution saturated with CO<sub>2</sub> (pH = 4.3). UV-vis illumination.*

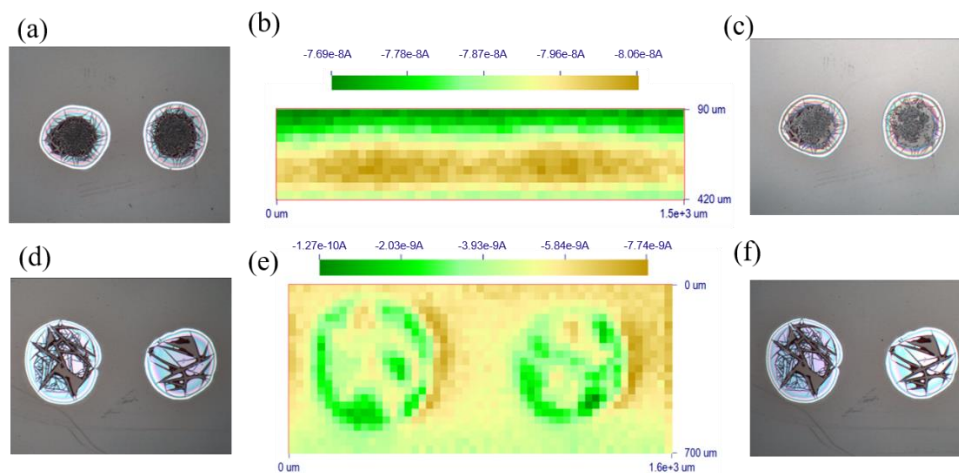


*Figure 3.3 Optical microscopy images of CuFe<sub>2</sub>O<sub>x</sub> array substrate electrode (a) before and (c) after SPECM imaging experiment. Optical microscopy images of FeO<sub>x</sub> array substrate electrode (d) before and (f) after SPECM imaging experiment. (b) and (e) are the corresponding SPECM images of array substrates (a) and (d), respectively. Applied potential of -0.1 V and -0.3 V vs. Ag/AgCl respectively in 0.1 M Na<sub>2</sub>SO<sub>4</sub> solution saturated with CO<sub>2</sub> (pH = 4.3). UV-vis illumination.*

Figure 3.4 shows the CoO<sub>x</sub> spot array substrate, similar to NiO<sub>x</sub> array substrate, CoO<sub>x</sub> displayed poor dispersion morphology and have no contribution to the reduction of CO<sub>2</sub>RR.

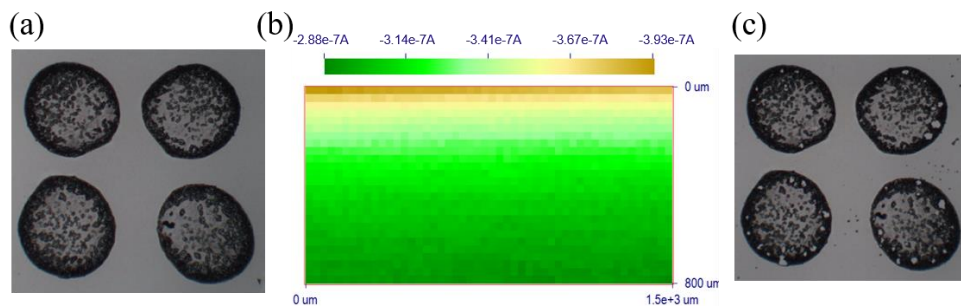


Figure 3.4 Optical microscopy images of CoO<sub>x</sub> array substrate electrode (a) before and (c) after SPECM imaging experiment (b) the corresponding SPECM images of array substrate (a). Applied potential of -0.2 V vs. Ag/AgCl respectively in 0.1 M Na<sub>2</sub>SO<sub>4</sub> solution saturated with CO<sub>2</sub> (pH = 4.3). UV-vis illumination.

Figure 3.5a shows optical image of CuCo<sub>2</sub>O<sub>4</sub> array substrate with 3 similar spots, prepared from precursor solution of 0.1 M Cu(NO<sub>3</sub>)<sub>2</sub> and 0.2 M Co(NO<sub>3</sub>)<sub>2</sub>. After the annealing process, a homogeneous, compact and regular-shaped binary metal oxide is formed with each spot presenting a diameter of about 400 μm. Figure 3.5b is the corresponding photocurrent-based image of CuCo<sub>2</sub>O<sub>4</sub> array substrate at a potential of 0 V vs. Ag/AgCl in CO<sub>2</sub> saturated 0.1 M Na<sub>2</sub>SO<sub>4</sub> solution. The 3 spots in yellow have higher photoreduction current compared to the background current under UV-vis light, which proves the good PEC performance of CuCo<sub>2</sub>O<sub>4</sub>. Furthermore, no relevant change in spot density or morphology were visually observed after the SPECM imaging experiments as shown in Figure 3.5c, proving its relatively good stability and catalytic efficiency over the experimental time scale.

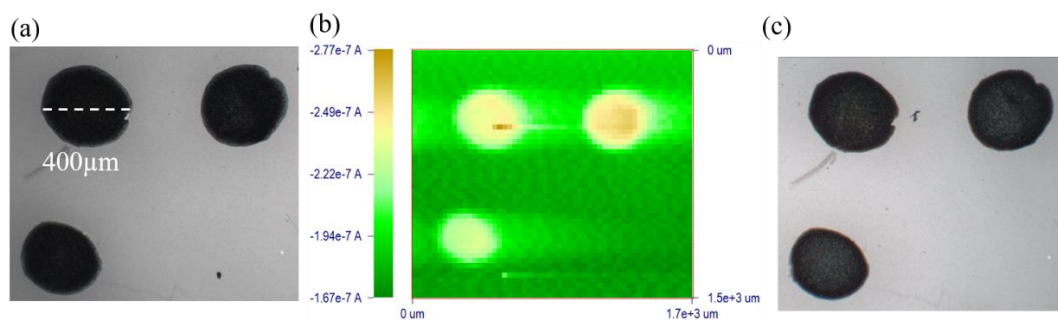


Figure 3.5 Optical microscopy images of CuCo<sub>2</sub>O<sub>4</sub> array substrate electrode (a) before and (c) after SPECM imaging experiment (b) the corresponding SPECM images of array substrate (a) Applied potential of 0 V vs. Ag/AgCl in 0.1 M Na<sub>2</sub>SO<sub>4</sub> solution saturated with CO<sub>2</sub> (pH = 4.2), under UV-vis light illumination. UV-vis illumination.

AgCoO<sub>x</sub> array was compared with CuCo<sub>2</sub>O<sub>4</sub>, results are shown in Figure 3.6. From Figure 3.6a, the AgCoO<sub>x</sub> exhibit high sample loading and homogeneous distribution the CuCo<sub>2</sub>O<sub>4</sub>, however, only CuCo<sub>2</sub>O<sub>4</sub> displays photocurrent for the same experimental conditions in the SPECM image, as shown in Figure 3.6b. The dark dash circles indicate the position of AgCoO<sub>x</sub> in the corresponding SPECM image. This image shows a good PEC catalytic efficiency of CuCo<sub>2</sub>O<sub>4</sub> as a candidate in the PEC CO<sub>2</sub>RR system. Several articles have already shown the photocatalytic ability of the spinel CuM<sub>2</sub>O<sub>4</sub> and have identified copper cobaltite CuCo<sub>2</sub>O<sub>4</sub> as an interesting catalytic material for HER or as a cocatalyst for CO<sub>2</sub>RR in tandem with Ru(bpy)<sub>3</sub><sup>2+</sup> [17,21]. It is reported that CuCo<sub>2</sub>O<sub>4</sub> has higher electrochemical activity and better conductivity (at least two orders of magnitude higher compared to the behavior of individual components of Cu<sub>x</sub>O and Co<sub>x</sub>O [22]). In conclusion, after the evaluation of several p-type semiconductor materials, we have selected CuCo<sub>2</sub>O<sub>4</sub> as the model PEC catalyst to study the role of RTILs in the PEC CO<sub>2</sub>RR system in this thesis.

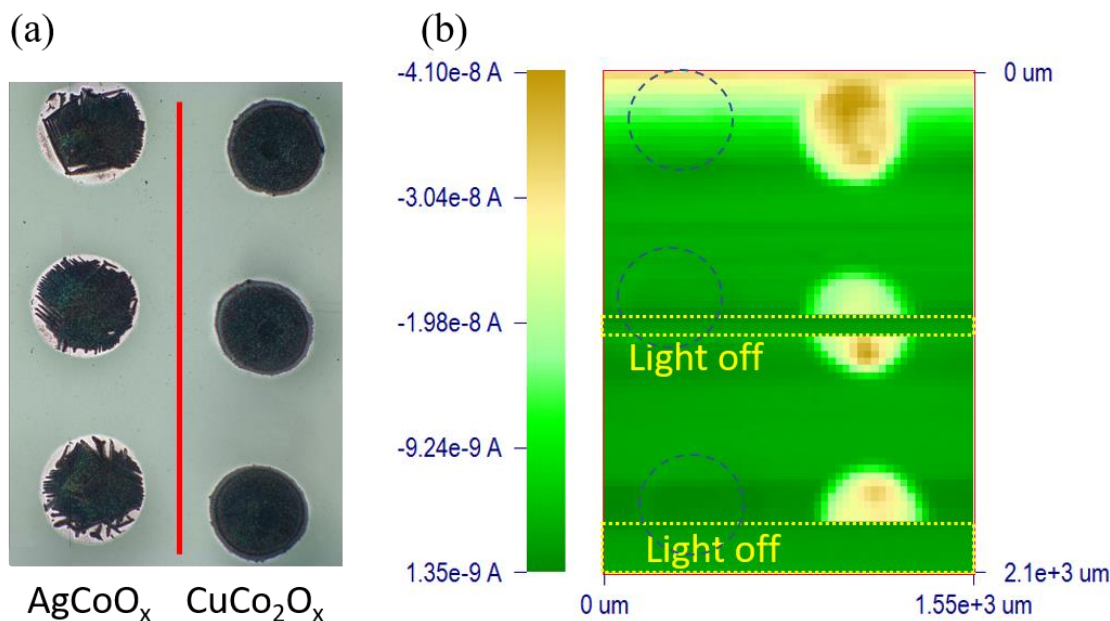


Figure 3.6 Optical microscopy images of (a) AgCoO<sub>x</sub> and CuCo<sub>2</sub>O<sub>4</sub> array substrate electrode and (b) the corresponding SPECM image of array substrates (a). Inside the yellow dash line are the area with light blocked during the middle of scan. Applied potential of 0.15 V vs. Ag/AgCl in 0.1 M KHCO<sub>3</sub> solution (pH = 6.9). UV-vis illumination.



### 3.3. Results and Discussion

#### 3.3.1. SEM and EDS Analysis of p-type Semiconductor CuCo<sub>2</sub>O<sub>4</sub>

In order to know the morphology and the composition of the synthesized compounds, SEM and EDS spectrum were measured on CuCo<sub>2</sub>O<sub>4</sub>. Figure 3.7a shows a representative SEM image of the prepared CuCo<sub>2</sub>O<sub>4</sub> microparticles in an individual spot synthesized on FTO glass. The spot exhibited rough morphology and was formed by semi-spherical shape microparticles with a diameter of *ca.* 2  $\mu$ m which were dispersed homogeneously without aggregation on FTO glass.

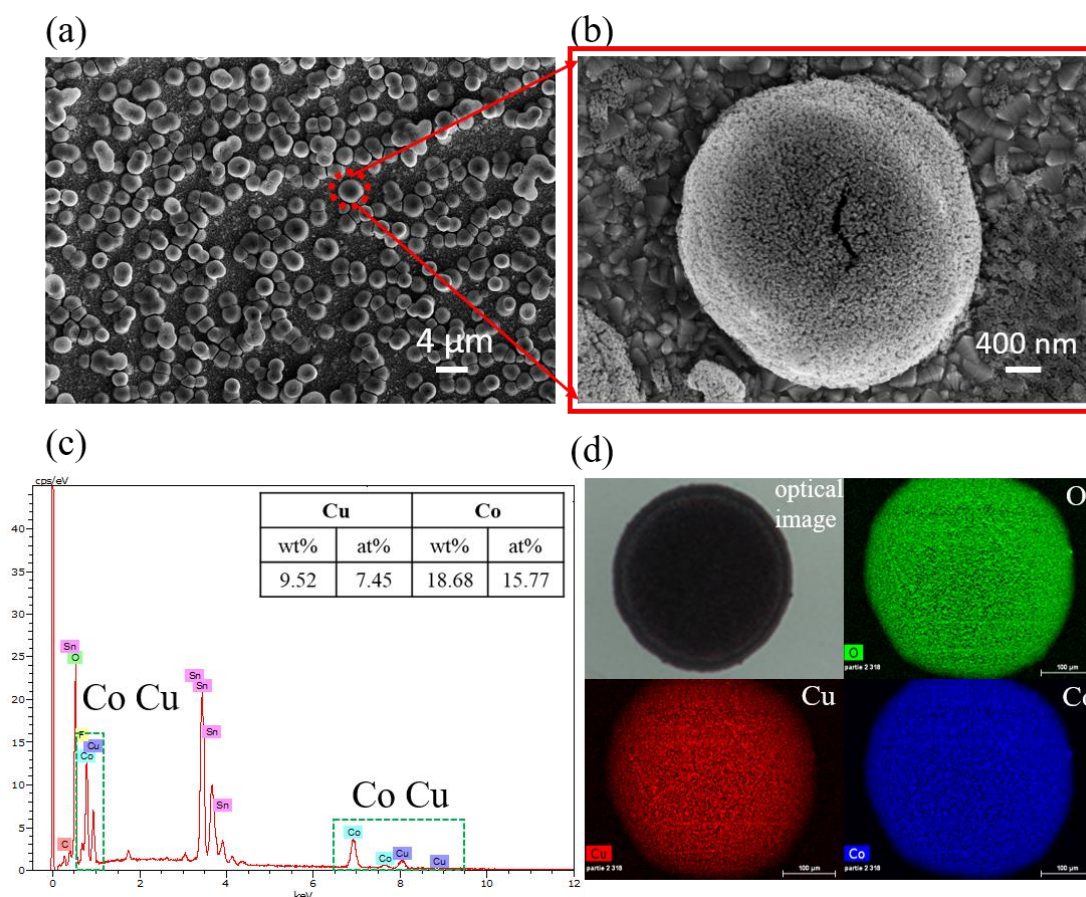


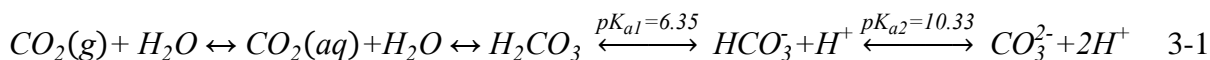
Figure 3.7 SEM images of CuCo<sub>2</sub>O<sub>4</sub> spot synthesized on FTO glass (a) center area on one spot (b) magnification of one CuCo<sub>2</sub>O<sub>4</sub> microparticle. (c) EDS spectrum analysis and (d) corresponding EDS-mapping images of the CuCo<sub>2</sub>O<sub>4</sub> spot.

Figure 3.7b shows the magnification of one of these microparticles appearing with numerous porous nanostructures and voids, resulting in high specific surface area which is beneficial for catalysis. Figure 3.7c is the corresponding EDS spectrum of the compound

showing the element atomic ratio of Cu to Co being about 1:2.1 (See all the elements content and atomic ratio in Table 3.3), which is in agreement with the expected ratio of the initial precursor solution (Co:Cu = 2:1). To gain insight in the elemental distribution of the CuCo<sub>2</sub>O<sub>4</sub> spots, EDS elemental mapping analysis was carried out and the corresponding images (Figure 3.7d) clearly elucidate homogeneous distribution of Cu, Co, and O elements in the whole spot. These observations further confirm the formation of CuCo<sub>2</sub>O<sub>4</sub>, in agreement with the literature, which reported that the coexistence of Co and Cu in the oxide favors the formation of CuCo<sub>2</sub>O<sub>4</sub> microparticles [22,23].

### 3.3.2. Effect of the Electrolyte Nature and Composition in CuCo<sub>2</sub>O<sub>4</sub> Photoactivity

In addition to the properties and the behavior of catalysts, the activity and selectivity performance of PEC CO<sub>2</sub>RR are also affected by the nature and the compositions of the electrolytes. Typically, electrochemical CO<sub>2</sub>RR mainly takes place in neutral or moderately acid or basic aqueous solutions such as Na<sub>2</sub>SO<sub>4</sub>, NaHCO<sub>3</sub>/KHCO<sub>3</sub> or phosphate buffers. Cheap and environmentally friendly 0.1 ~ 0.5 M bicarbonate solution is the most common electrolyte with a pH value about 7 after CO<sub>2</sub> saturated, since it can act as a buffer to maintain the pH value by the pathways shown in Equation 3-1. Besides, as the proton is indispensable in the PEC CO<sub>2</sub> conversion process to form various products through protonation, bicarbonate solution can also act as proton source. Furthermore, bicarbonate was reported to increase CO<sub>2</sub> concentration near the interface by building equilibrium with dissolved CO<sub>2</sub> [24], making it a good choice in the electrochemical CO<sub>2</sub>RR [25].



Moreover, imidazolium based RTILs were adopted to form binary mixture with water to work as electrolyte, namely 1-Butyl-3-methylimidazolium tetrafluoroborate ([C<sub>4</sub>mim][BF<sub>4</sub>] or [BMIM][BF<sub>4</sub>]) and 1-Ethyl-3-methylimidazolium tetrafluoroborate ([C<sub>2</sub>mim][BF<sub>4</sub>] or [EMIM][BF<sub>4</sub>]), whose structure and abbreviations are displayed in Figure 3.8. Three different electrolyte solutions were used: aqueous solution (0.1 M KHCO<sub>3</sub> or 0.1 M Na<sub>2</sub>SO<sub>4</sub>), binary RTIL/H<sub>2</sub>O mixtures (25 vol.% [C<sub>2</sub>mim][BF<sub>4</sub>] in H<sub>2</sub>O and 25 vol.% or 50 vol.% [C<sub>4</sub>mim][BF<sub>4</sub>] in H<sub>2</sub>O), pure RTILs ([C<sub>2</sub>mim][BF<sub>4</sub>] and [C<sub>4</sub>mim][BF<sub>4</sub>]; [C<sub>2</sub>mim][NTf<sub>2</sub>] and [C<sub>4</sub>mim][NTf<sub>2</sub>] – immiscible in water) as shown in Table 2.2, in all cases purged with either CO<sub>2</sub> or Ar gas for 30 min. All the electrolyte solutions were prepared and used in 2 ~ 3 h (except for the 25 vol.%

[C<sub>2</sub>mim][BF<sub>4</sub>]/H<sub>2</sub>O in bulk electrolysis experiments). Figure 3.9 displays the pH values evolution of a binary RTIL/H<sub>2</sub>O mixture as the CO<sub>2</sub> purging time is extended, proving that the aerated time of 30 min can guaranty a saturated CO<sub>2</sub> environment, which is also a common aerate duration in literature. After bubbling CO<sub>2</sub> for 45 min, the 25 vol.% [C<sub>2</sub>mim][BF<sub>4</sub>]/H<sub>2</sub>O solution is kept sealed and still. Then, its pH value changed by 9 % (from 3.67 to 3.34), which maybe because of the hydrolysis of [C<sub>2</sub>mim][BF<sub>4</sub>] to some hydroxyl ions such as [BF<sub>3</sub>OH]<sup>-</sup>, [BF<sub>2</sub>(OH)<sub>2</sub>]<sup>-</sup> and [BF(OH)<sub>3</sub>]<sup>-</sup>, which has been reported by Kumar *et al.* [26]. But it seems not to be related with HF formation indicated by the slight change of pH.

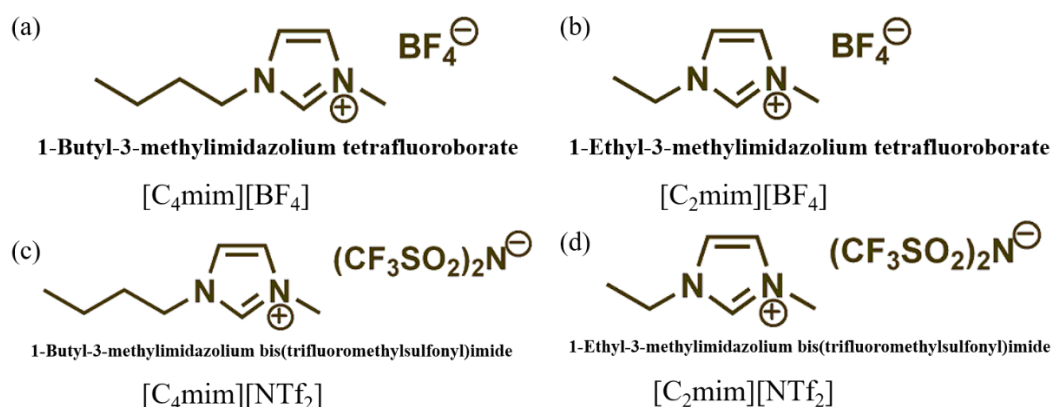


Figure 3.8 Chemical structure, name and the corresponding abbreviation of room-temperature ionic liquids used in this work.

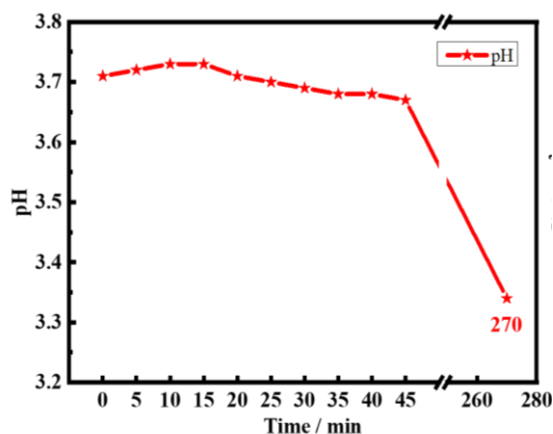


Figure 3.9 pH values evolution with CO<sub>2</sub> bubbling time (0 ~ 45 min) for 25 vol.% [C<sub>2</sub>mim][BF<sub>4</sub>]/H<sub>2</sub>O solution at 293 K; pH value at 270 min after bubbling CO<sub>2</sub> for 45 min, and keeping the solution sealed and still.



In general, mass transfer might be a relevant step in electrochemical reaction processes. Therefore, the physicochemical properties of the electrolyte solution have wide influence on the activity of the electrochemical reactions via controlling the diffusion coefficient and the concentration of the electroactive species. For instance, the Levich equation (Equation 2-2) used in rotating disk electrode reveals the relationship of the steady-state current with the diffusion coefficient and the concentration, as well as other factors. Table 3.1 shows some important parameters of imidazolium based RTILs used in this thesis compared with a standard aqueous solution such as conductivity, viscosity and CO<sub>2</sub> solubility, which strongly affect the maximum current density for the electrochemical CO<sub>2</sub>RR. A lower solvent viscosity value provides an easier mass transfer, a smaller diffusion layer thickness and a higher limiting current for the same electrochemical reaction. In particular, [C<sub>4</sub>mim][BF<sub>4</sub>] has a higher CO<sub>2</sub> solubility compared to aqueous solution, which means a higher concentration of electroactive species. However, it also exhibits high viscosity and low conductivity, which are unfavorable for the mass transfer. Overall, a relative lower current is expected in the pure RTILs than that in aqueous solutions. For this reason, mixing RTILs with a molecular solvent such as acetonitrile or water can be a good strategy to combine the advantages of both and elude the drawbacks, that is, to increase the dissolved CO<sub>2</sub> concentration and inhibiting HER, meanwhile keeping low viscosity and high diffusion coefficient. However, [C<sub>4</sub>mim][NTf<sub>2</sub>] and [C<sub>2</sub>mim][NTf<sub>2</sub>] are immiscible in water, therefore only 100% of these two RTILs were studied in this thesis. Table 3.2 displays the pH and conductivity values measured at 293 K of aqueous and binary RTIL/H<sub>2</sub>O solutions saturated with CO<sub>2</sub> or Ar used as solvent media in the PEC CO<sub>2</sub>RR. The water content in pure RTILs can affect the pH value and the viscosity.

*Table 3.1 Physicochemical properties of aqueous solution and imidazolium based RTILs as supporting electrolytes used in electrochemistry at temperature between 293 K and 298 K. Adapted from ref [7].*

Solvent supporting electrolyte system	Conductivity (mS/cm)	Viscosity (cP)	CO <sub>2</sub> Solubility (M)
0.5 M H <sub>2</sub> SO <sub>4</sub> in H <sub>2</sub> O	237	1	0.033
[C <sub>2</sub> mim][BF <sub>4</sub> ]	14	25.7	n.a.
[C <sub>4</sub> mim][BF <sub>4</sub> ]	3.5	180	0.096
[C <sub>4</sub> mim][NTf <sub>2</sub> ]	3.9	52	n.a.
[C <sub>2</sub> mim][NTf <sub>2</sub> ]	8.8	29	0.13

*Table 3.2 pH and conductivity values measured at 293 K of purely aqueous and binary RTIL /H<sub>2</sub>O solutions used as solvent media for PEC CO<sub>2</sub>RR in this thesis.*

	pH	Conductivity with CO <sub>2</sub> mS/cm	Conductivity without CO <sub>2</sub> mS/cm
0.1 M KHCO <sub>3</sub> /CO <sub>2</sub> <sup>sat</sup>	6.9	9.95	9.56
0.1 M KHCO <sub>3</sub> /Ar <sup>sat</sup>	9.4	n.a.	n.a.
0.1 M Na <sub>2</sub> SO <sub>4</sub> /CO <sub>2</sub> <sup>sat</sup>	4.3	n.a.	16.4
25 vol.% [C <sub>2</sub> mim][BF <sub>4</sub> ] in H <sub>2</sub> O/CO <sub>2</sub> <sup>sat</sup>	(3.8-4.1)	59.3	58.2
25 vol.% [C <sub>2</sub> mim][BF <sub>4</sub> ] in H <sub>2</sub> O/Ar <sup>sat</sup>	(3.8-4.1)	n.a.	n.a.
25 vol.% [C <sub>4</sub> mim][BF <sub>4</sub> ] in H <sub>2</sub> O/CO <sub>2</sub> <sup>sat</sup>	(3.8-4.1)	38.7	38.0
25 vol.% [C <sub>4</sub> mim][BF <sub>4</sub> ] in H <sub>2</sub> O/Ar <sup>sat</sup>	4.2	n.a.	n.a.
50 vol.% [C <sub>4</sub> mim][BF <sub>4</sub> ] in H <sub>2</sub> O/CO <sub>2</sub> <sup>sat</sup>	4.4	45.6	44.4

### 3.3.3. Photoelectrochemical Activity Evaluation by SPECM on CuCo<sub>2</sub>O<sub>4</sub> in Different Solvent Media

Figure 3.10a shows the schematic representation of SPECM experiments. The array of CuCo<sub>2</sub>O<sub>4</sub> spots acting as substrate electrode is immersed in an electrolyte solution purged with either CO<sub>2</sub> or Ar. The optical fiber is set up perpendicularly at 150 μm above the substrate, which allows a controlled and local illumination of each spot on the array. Applying on the substrate electrode a series of different potentials and scanning the optical fiber for introducing the UV-visible or visible light along the X-Y plane simultaneously, a SPECM image is built displaying the reduction photocurrent obtained as a function of optical fiber position.

P-type CuCo<sub>2</sub>O<sub>4</sub> semiconductor absorbs light in a wide range of wavelengths in both visible and UV regions, which indicates that CuCo<sub>2</sub>O<sub>4</sub> has capability in photocatalytic applications [27]. Moreover, imidazolium based RTILs also presents a wide absorption light band in UV region [28]. Figure 3.10b shows the principle and energy band diagram in PEC CO<sub>2</sub>RR system on p-type CuCo<sub>2</sub>O<sub>4</sub> photoelectrocatalyst. When CuCo<sub>2</sub>O<sub>4</sub> spot array photocathode is immersed in the electrolyte (KHCO<sub>3</sub> or RTIL/H<sub>2</sub>O), because of the different work functions (also the Fermi levels) of the two sides, electrons transfer at the interface tending to establish thermodynamic equilibrium. However, because of the large amount of the electroactive species in the electrolyte, the redox potential (E<sub>R</sub>) remains stable compared to the Fermi level (E<sub>F</sub>) of the CuCo<sub>2</sub>O<sub>4</sub>. Illuminated by incident light with larger energy than its band

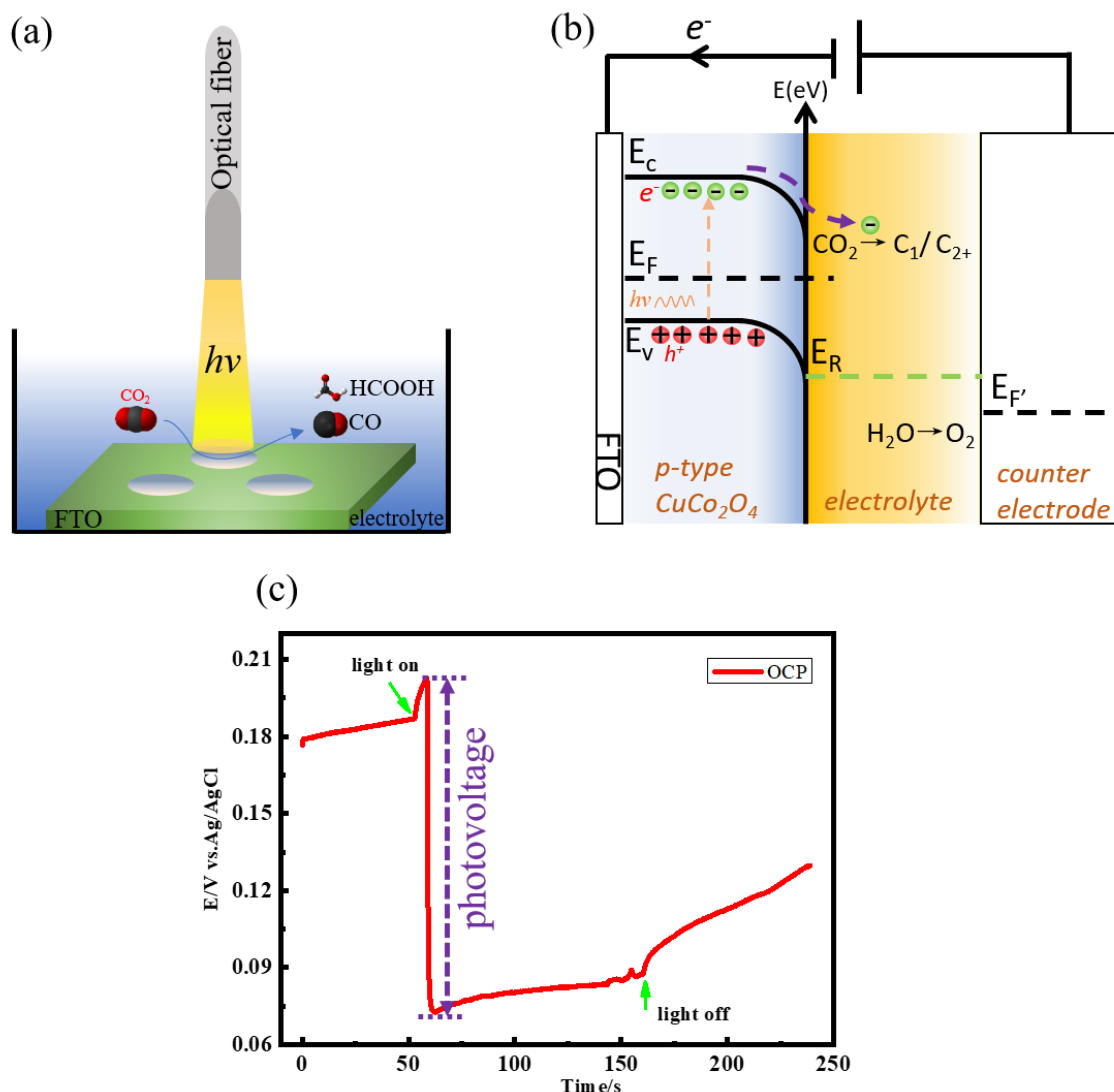


Figure 3.10 (a) Schematic representation of SPECM experiments of photoelectrocatalyst activity evaluation for PEC CO<sub>2</sub>RR illuminated by UV-vis or visible light. (b) Principle and energy band diagram in PEC CO<sub>2</sub>RR system on p-type CuCo<sub>2</sub>O<sub>4</sub> photoelectrocatalyst. (c) OCP evolution with or without the visible light illumination of the spot array substrate electrode (5×5 spots array; surface area of 0.07 cm<sup>2</sup> in 25 vol.% [C<sub>2</sub>mim][BF<sub>4</sub>]/H<sub>2</sub>O solution). Green arrows in the panel indicate when local illumination is on and off, and the purple dash arrow shows the photovoltage.

gap energy (1.45 eV [29] or 1.74 eV [27]) ( $h\nu > E_g$ ), CuCo<sub>2</sub>O<sub>4</sub> can absorb photons to excite electrons to the conduction band and leaving positive holes on the valence band, following the separation and diffusion of electrons and holes due to the light-induced photovoltage on the semiconductor electrode upon illumination as is shown in Figure 3.10c, (0.1 V ~ 0.4 V in our system depending on the light source and the electrolyte in solution) of a CuCo<sub>2</sub>O<sub>4</sub> spot immersed in solution and the electric field formed by the external negative electric bias.

Furthermore, the electric field induced by the potential bias also inhibits the recombination of the electron and positive holes. This combination of the illumination and external bias induce the band bending upward near the surface. Therefore, the photogenerated electrons at the interface move to the electrolyte and are captured and utilized by the CO<sub>2</sub> reduction reaction to generate value-added products. Whereas oxidation reaction happens at the counter electrode.

Figure 3.11a exhibits a typical SPECM image showing the substrate photocurrent (Z axis) plotted as a function of the optical fiber position (X-Y axis) when scanning the CuCo<sub>2</sub>O<sub>4</sub> array substrate with an applied potential more negative than the open circuit potential under the illumination of UV-vis light. The lower panel is a 2D projection image where the current is represented by a color map and the upper is an actual 3D representation of reduction photocurrent collected from the substrate as function of X-Y position. The green color represents the background current. The substrate photocurrent increases when the optical fiber passes over the CuCo<sub>2</sub>O<sub>4</sub> spots, defining the shape and the size of these catalyst spots (shown in the optical microscope image of Figure 3.11b) with high resolution and indicating their catalytic activity. An additional test was performed meanwhile the optical fiber was scanning over the middle of spot 2 and the end of spot 3, the UV-vis light source was blocked (zone inside the yellow dash lines), leading to a sharp decrease in photocurrent which became equal to the background current, and demonstrated the light driven reaction taking place on the CuCo<sub>2</sub>O<sub>4</sub> spots.

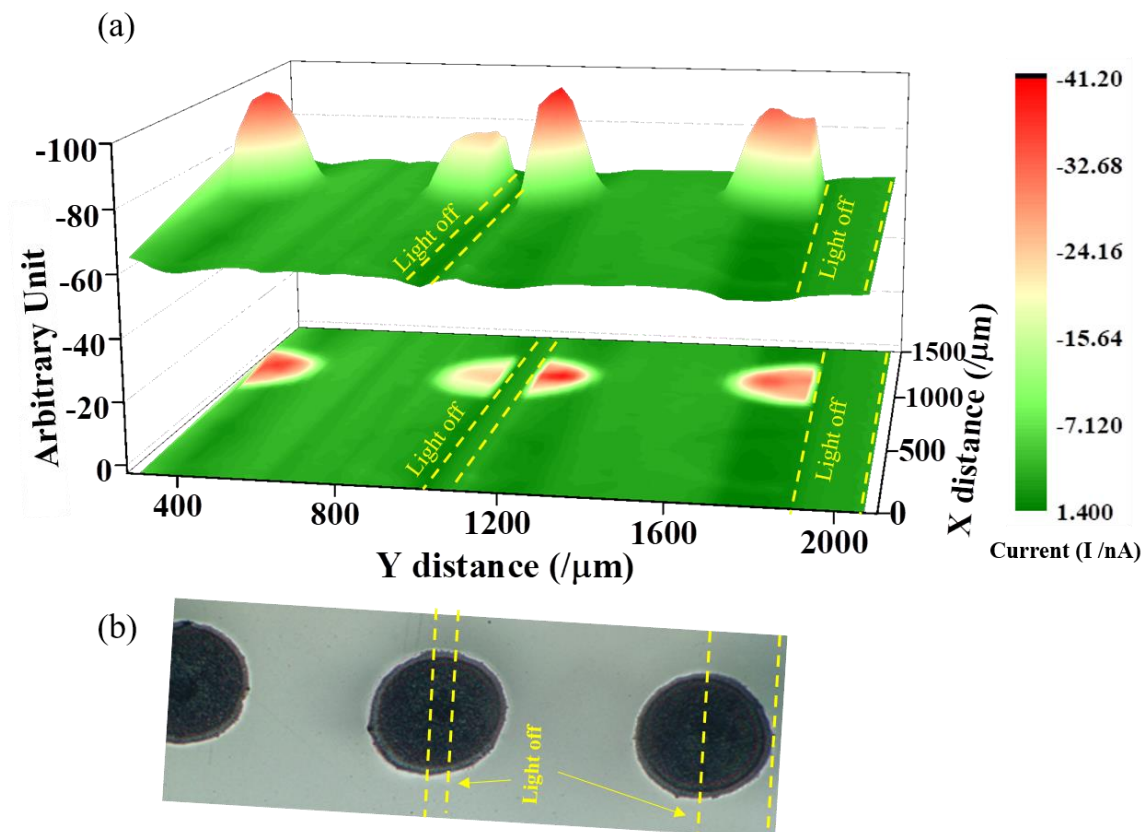


Figure 3.11 (a) SPECM image of CuCo<sub>2</sub>O<sub>4</sub> array substrate displaying the reduction photocurrent obtained (Z axis) as a function of optical fiber position (X-Y axis) with UV-vis light blocked in the middle and end of the scan (inside the yellow dash lines). Substrate potential held constant at 0.15 V vs. Ag/AgCl. Optical fiber-substrate distance = 150 μm. Tip scan rate = 200 μm/s, using increments of 30 μm each 0.15 s. 0.1 M KHCO<sub>3</sub> solution saturated with CO<sub>2</sub>. In the SPECM image, the lower figure is a 2D projection image where the current is represented by color map and the upper is an actual 3D representation of reduction photocurrent collected from the substrate as function of X-Y position. (b) The corresponding optical microscopy image of the array substrate scanned in (a).

The role of different RTILs dissolved in H<sub>2</sub>O acting as simultaneous supporting electrolyte and cocatalyst for photoelectrochemical CO<sub>2</sub> reduction is studied here by SPECM imaging. This approach allows to screen the effect of altering the photocatalyst environment by the presence of dissolved species in solution. Initially, Figure 3.12 shows the response of the model semiconductor electrode in aqueous solution of 0.1 M KHCO<sub>3</sub>/CO<sub>2</sub> (pH = 6.9) as a function of applied potential. This is the electrolyte of choice in most CO<sub>2</sub>RR studies reported in literature. This figure displays the SPECM image obtained when 2 individual and identical spots of CuCo<sub>2</sub>O<sub>4</sub> are scanned. The photocurrent collected at both spots is almost identical, which already points out the reproducibility of our measurements. Comparing the maximum

photoreduction current reached at the CuCo<sub>2</sub>O<sub>4</sub> spots with the background current displayed on FTO allows to calculate the net photocurrent generated in each SPECM images ( $\Delta I$ ). The corresponding  $\Delta I$ s are 21 nA (Figure 3.12a), 38.4 nA (Figure 3.12b) and 50.7 nA (Figure 3.12c), respectively. This illustrates that the photoreduction current increases as the potential goes towards more negative values. So far, the photoreduction current in the SPECM image cannot be attributed to a specific reduction reaction. Thus, the different possible reactions to be considered are: i) the CO<sub>2</sub>RR; ii) the HER and/or iii) the electroreduction of the catalyst CuCo<sub>2</sub>O<sub>4</sub>.

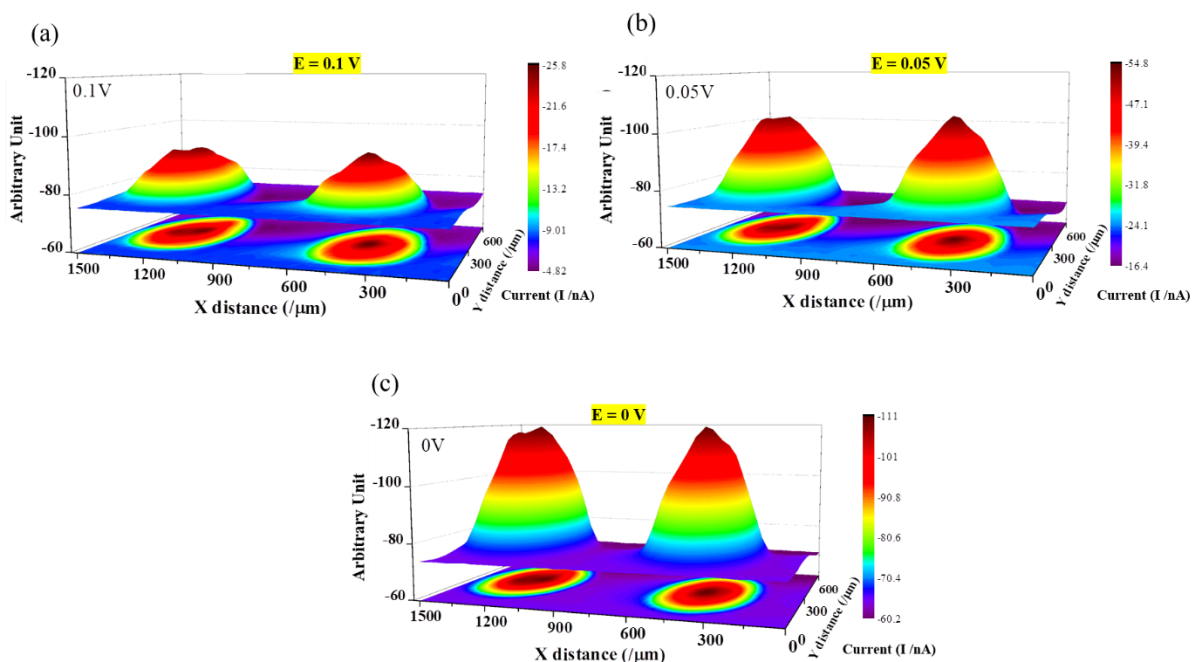


Figure 3.12 SPECM images of CuCo<sub>2</sub>O<sub>4</sub> array substrate under UV-visible light illumination in CO<sub>2</sub> saturated 0.1 M KHCO<sub>3</sub> aqueous solution (pH=6.9) at potentials of (a)  $E_{\text{subs}} = 0.1$ , (b) 0.05 and (c) 0 V vs. Ag/AgCl. Optical fiber-substrate distance = 150  $\mu\text{m}$ . Tip scan rate = 200  $\mu\text{m/s}$ , using increments of 30  $\mu\text{m}$  each 0.15 s.

It has been already shown in Table 3.2 that the natural pH reached when imidazolium based RTILs are dissolved in H<sub>2</sub>O is around 4. For this reason, Figure 3.13 shows the SPECM images of CuCo<sub>2</sub>O<sub>4</sub> array substrate under UV-visible light illumination in different CO<sub>2</sub> saturated solvent media at pH = 4. The corresponding  $\Delta I$  values are (a) 26.8 nA, (b) 14.8 nA, (c) 18.1 nA and (d) 13.9 nA, respectively. The most relevant fact comparing all 4 media is the highest photoreduction current displayed by 25 vol.% [C<sub>2</sub>mim][BF<sub>4</sub>]/H<sub>2</sub>O solution (Figure 3.13a), which seems to point out an enhanced performance in the PEC CO<sub>2</sub>RR system when

[C<sub>2</sub>mim][BF<sub>4</sub>] is present in solution. Interestingly, the 50 vol.% [C<sub>4</sub>mim][BF<sub>4</sub>]/H<sub>2</sub>O solution (Figure 3.13b) did not show any improvement in performance compared to the 25 vol.% [C<sub>4</sub>mim][BF<sub>4</sub>]/H<sub>2</sub>O solution (Figure 3.13c). However, both [C<sub>4</sub>mim][BF<sub>4</sub>]/H<sub>2</sub>O solutions (Figure 3.13b and c) provide a very fair improvement in photocatalytic activity compared with purely aqueous solution at constant pH (Figure 3.13d).

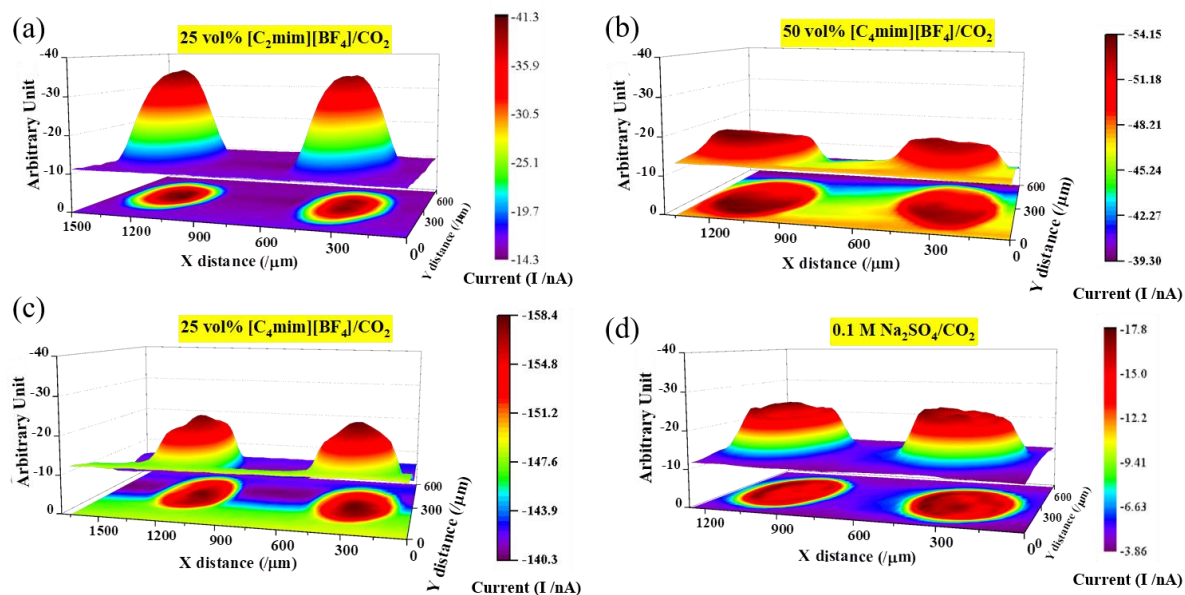


Figure 3.13 SPECM images of CuCo<sub>2</sub>O<sub>4</sub> array substrate under UV-visible light illumination in different CO<sub>2</sub> saturated solvent media at pH  $\approx$  4 of (a) 25 vol.% [C<sub>2</sub>mim][BF<sub>4</sub>]/H<sub>2</sub>O, (b) 50 vol.% [C<sub>4</sub>mim][BF<sub>4</sub>]/H<sub>2</sub>O, (c) 25 vol.% [C<sub>4</sub>mim][BF<sub>4</sub>]/H<sub>2</sub>O and (d) 0.1 M Na<sub>2</sub>SO<sub>4</sub>/CO<sub>2</sub> at potentials 0.1 V vs. Ag/AgCl. Optical fiber-substrate distance = 150  $\mu$ m. Tip scan rate = 200  $\mu$ m/s, using increments of 30  $\mu$ m each 0.15 s.

In spite of the fact that most pure RTILs exhibit high viscosity values, which represents an important drawback for electrochemical applications, pure RTILs working as solvent as well as supporting electrolyte were evaluated in the PEC CO<sub>2</sub>RR by SPECM imaging as well. Figure 3.14 shows the SPECM images of CuCo<sub>2</sub>O<sub>4</sub> array substrate under UV-visible light illumination in different CO<sub>2</sub> saturated 100% RTILs of (a) [C<sub>4</sub>mim][BF<sub>4</sub>], (b) [C<sub>2</sub>mim][BF<sub>4</sub>], (c) [C<sub>4</sub>mim][NTf<sub>2</sub>] and (d) [C<sub>2</sub>mim][NTf<sub>2</sub>] at similar potentials. The magnitude of  $\Delta I$  in all 4 pure RTILs (8.5 nA, 4.28 nA, 9.7 nA and 4.4 nA respectively) are significantly smaller than those obtained in aqueous solution and RTIL/H<sub>2</sub>O mixtures, which could be explained by the high viscosity and low conductivity of pure RTILs system, which hinders the mass transfer of the electroactive species in the electrolyte and then limits the maximum current achieved.



Nevertheless, other additional factors affect the photocurrent produced because comparing [C<sub>4</sub>mim][BF<sub>4</sub>] and [C<sub>2</sub>mim][BF<sub>4</sub>], photocurrent results do not correlate the viscosity values for those RTILs. Actually, [C<sub>2</sub>mim][BF<sub>4</sub>] presents a much lower viscosity and higher conductivity than [C<sub>4</sub>mim][BF<sub>4</sub>] (Table 3.1), which should offer a higher photocurrent. Thus, other factors besides viscosity may play a key role in the promotion of the reduction reactions in pure RTILs.

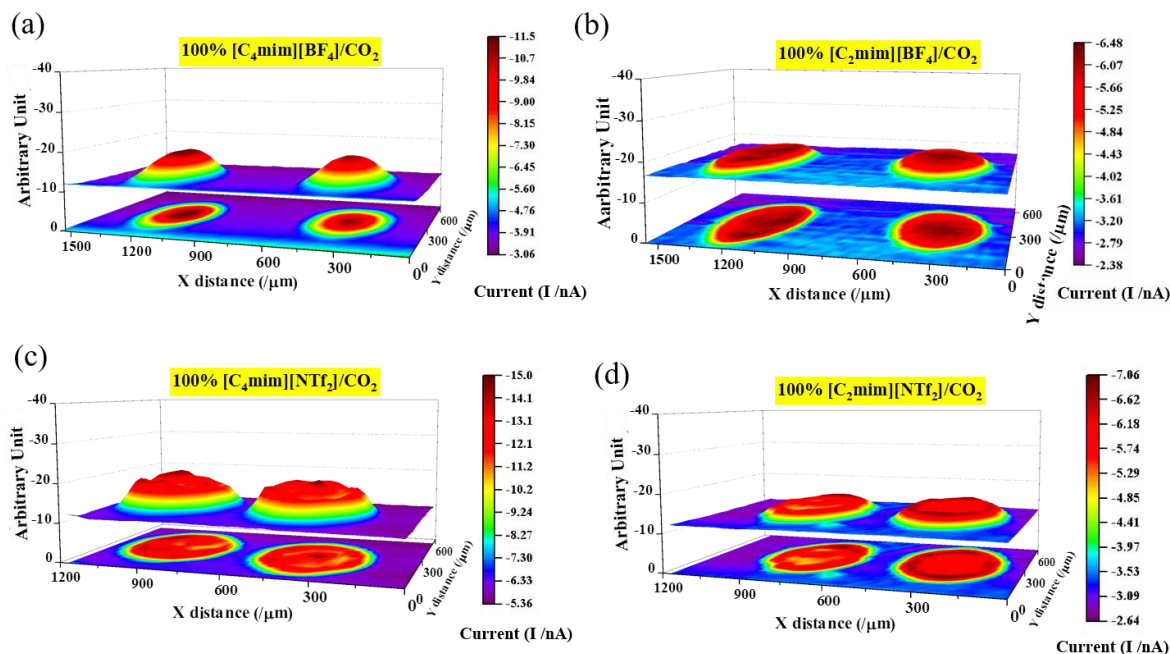


Figure 3.14 SPECM images of CuCo<sub>2</sub>O<sub>4</sub> array substrate under UV-visible light illumination in different CO<sub>2</sub> saturated 100% RTILs of (a) [C<sub>4</sub>mim][BF<sub>4</sub>], (b) [C<sub>2</sub>mim][BF<sub>4</sub>], (c) [C<sub>4</sub>mim][NTf<sub>2</sub>], (d) [C<sub>2</sub>mim][NTf<sub>2</sub>] at potentials of -0.61, -0.35, -0.50 and -0.65 V vs. Fc/Fc<sup>+</sup>. Optical fiber-substrate distance = 150 μm. Tip scan rate = 200 μm/s, using increments of 30 μm each 0.15 s.

As a general goal, photoelectrochemical CO<sub>2</sub> reduction reaction is expected to take place under solar light illumination, which is more easily available and cost effective. Furthermore, UV-vis light means a strong power input for the catalyst, which may cause photodegradation of semiconductor materials. Thus, photoactivity quantification experiments were also carried out under visible light illumination. Figure 3.15 shows SPECM images of CuCo<sub>2</sub>O<sub>4</sub> array substrate under visible light illumination in different CO<sub>2</sub> saturated solvent media of 100% [C<sub>2</sub>mim][BF<sub>4</sub>] (a), 25 vol.% [C<sub>4</sub>mim][BF<sub>4</sub>]/H<sub>2</sub>O (b) and 25 vol.% [C<sub>2</sub>mim][BF<sub>4</sub>]/H<sub>2</sub>O (c). Pure RTILs under visible illumination (Figure 3.15a) exhibits no significant photocurrent. In contrast, CuCo<sub>2</sub>O<sub>4</sub> spot in 25 vol.% [C<sub>2</sub>mim][BF<sub>4</sub>]/H<sub>2</sub>O solution exhibits more photocurrent than the other two electrolyte solutions, which is consistent with our previous results under



UV-vis irradiation shown in Figure 3.13. By comparing the photocurrent obtained under visible illumination with the corresponding photocurrent at the same potential but with the UV-vis illumination, the lower photocurrents obtained under visible light demonstrated that the photoactivity of CuCo<sub>2</sub>O<sub>4</sub> spot in solution rely on the light power and the number of photons. In spite of that fact, a significant photoactivity is displayed by the semiconductor in 25 vol.% [C<sub>2</sub>mim][BF<sub>4</sub>]/H<sub>2</sub>O solution by producing 11 nA, which correspond to approximately 1/3 of the photocurrent generated at the same potential under UV-vis illumination.

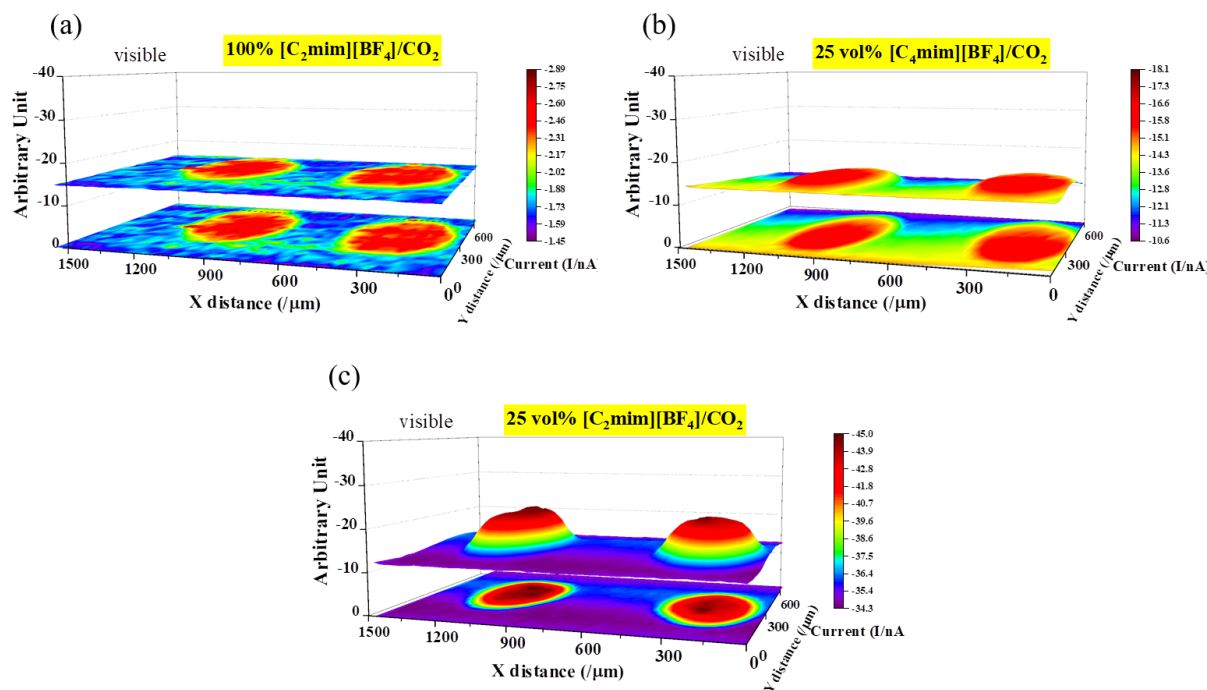


Figure 3.15 SPECM images of CuCo<sub>2</sub>O<sub>4</sub> array substrate under visible light illumination in different CO<sub>2</sub> saturated solvent media of (a) 100% [C<sub>2</sub>mim][BF<sub>4</sub>] at -0.65 V vs. Fc/Fc<sup>+</sup>; (b) 25 vol.% [C<sub>4</sub>mim][BF<sub>4</sub>]/H<sub>2</sub>O, (c) 25 vol.% [C<sub>2</sub>mim][BF<sub>4</sub>]/H<sub>2</sub>O at potentials 0.2 V and 0.1 V vs. Ag/AgCl, respectively. Optical fiber-substrate distance = 150 μm. Tip scan rate = 200 μm/s, using increments of 30 μm each 0.15 s.

### 3.3.4. Quantification of Photoelectrochemical Activity by SPECM

#### 3.3.4.1. Amperometry I-t Curves Analysis

SPECM photocurrent quantification was carried out by chronoamperometry on individual CuCo<sub>2</sub>O<sub>4</sub> spots. The experimental details are shown in chapter 2.4.2.2. Figure 3.16a shows an individual chronoresponse of the photocurrent obtained on one single spot belonging to the array substrate electrode when the optical fiber is held still at a constant tip-substrate distance

of 150  $\mu\text{m}$  on top of a p-type  $\text{CuCo}_2\text{O}_4$  spot. Red and green lines describe the current-time relationship acquired from amperometric experiment and the illumination condition, respectively. Starting from OCP, potential bias on the substrate was applied at which the photoelectrochemical reduction reaction can occur and meanwhile the substrate current of the system was registered. Without illumination from 0 ~ 25 s, the background current only corresponds to capacitive current of the electrode. At 25 s, illuminating the spot array using UV-vis light or visible light causes immediately a dramatic difference in the photoreduction current registered, the illumination time lasts for 50 s. Finally, by stopping the light source, the photocurrent signal goes back to the background current in the interval 75 ~ 100 s. Figure 3.16b shows the photocurrent time dependence if the optical fiber was held still above the individual  $\text{CuCo}_2\text{O}_4$  spot for a long time during chronoamperometries (8 cycles for a total time of 20 min). It shows the increment of photocurrent difference between the light on and off decreasing over time, from an initial photocurrent of  $\Delta I = 3.83$  nA to 1.46 nA after 20 min of “off-on” illumination cycles. This phenomenon is due to the photodegradation and inactivation of the catalyst.

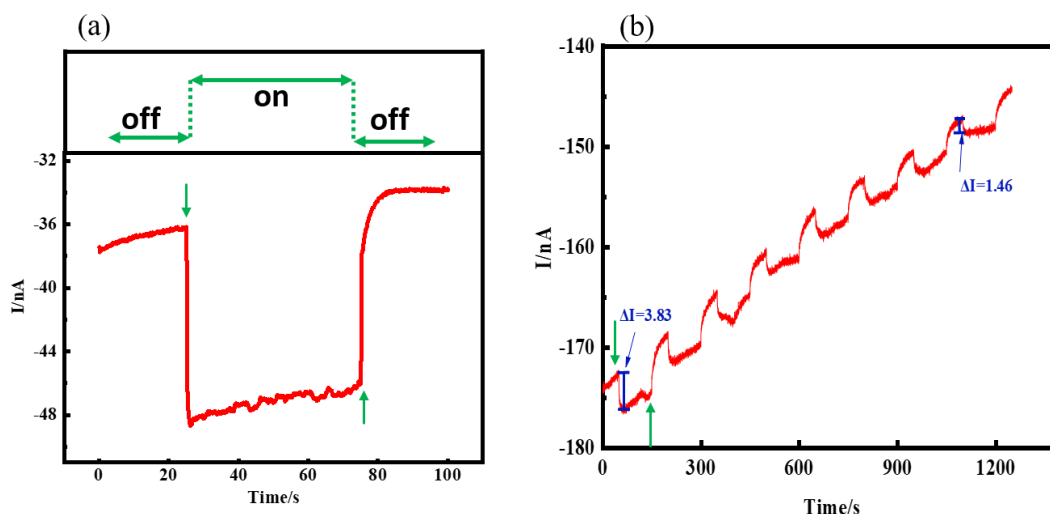


*Figure 3.16 (a) Typical chronoresponse of the photocurrent obtained at the array substrate electrode when the optical fiber is held still at a constant tip-substrate distance of 150  $\mu\text{m}$  on top of a p-type  $\text{CuCo}_2\text{O}_4$  spot. (b) Chronoresponse of the photocurrent of 8 “ON and OFF” consecutive cycles on a  $\text{CuCo}_2\text{O}_4$  spot. Green arrows in the panel indicate the different time intervals when local illumination is ON and OFF, the illumination duration is 50 s. The blue segments represent the photocurrent difference.*

### 3.3.4.2. Photodegradation of CuCo<sub>2</sub>O<sub>4</sub>

The semiconductor compound CuCo<sub>2</sub>O<sub>4</sub> has been reported very stable when working as supercapacitor, catalyst, and Li-ion batteries in literature. However, photodegradation of the CuCo<sub>2</sub>O<sub>4</sub> material occurs under the illumination when the substrate is biased and exposed to irradiation for several minutes. Figure 3.17 shows twice the same SPECM image of two CuCo<sub>2</sub>O<sub>4</sub> spots before (a) and after (b) performing the amperometric photoactivity quantification for 500 s, but only in one of the spots (marked with a red dash circle in the image). It is evident comparing both images that the photodegradation on the spot happened when the amperometric experiment was operated in a fixed point of the spot. The CuCo<sub>2</sub>O<sub>4</sub> spot where the photoactivity quantification was not performed presents almost identical photocurrent in Figures 3.17a and b. In contrast, the zone limited by a red circle on the other CuCo<sub>2</sub>O<sub>4</sub> spot only exhibits background photocurrent after performing the amperometric photoactivity quantification for 500 s. Moreover, other experiments not shown here proved that this photodegradation process is independent of the electrolyte solution used.

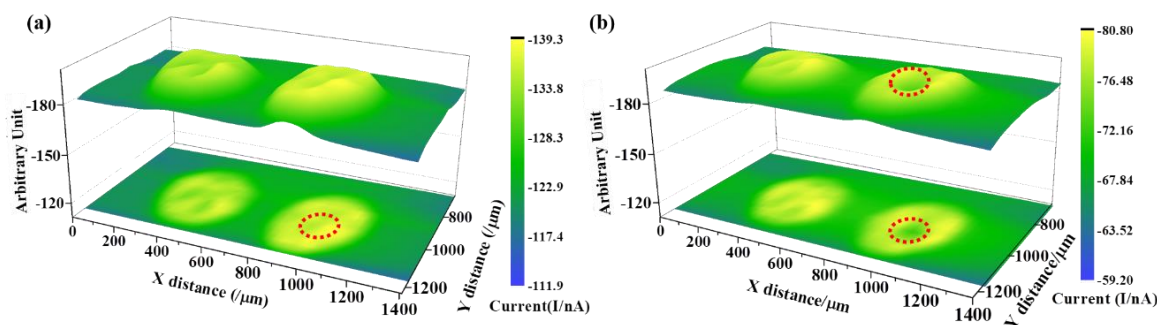
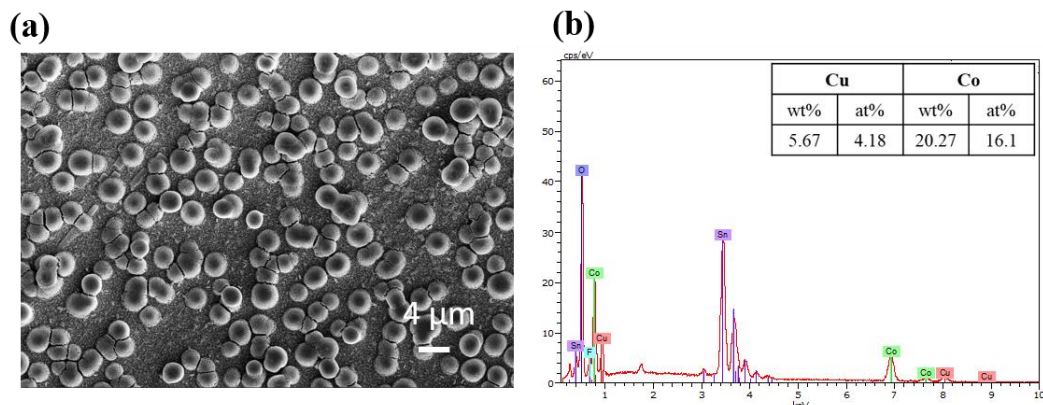


Figure 3.17 SPECM images of CuCo<sub>2</sub>O<sub>4</sub> spots under UV-visible light illumination in a CO<sub>2</sub> saturated 50 vol.% [C<sub>4</sub>mim][BF<sub>4</sub>]/H<sub>2</sub>O solution. Substrate potential held constant at 0 V vs. Ag/AgCl. Optical fiber-substrate distance = 150 μm. Tip scan rate = 200 μm/s, using in increments of 30 μm each 0.15 s. (a) First scan of the sample and (b) Second scan of the sample after keeping held the optical fiber locally illuminating one of the CuCo<sub>2</sub>O<sub>4</sub> spots for 500 s. That position is marked with a red dash circle in the image.

No variation can be virtually observed in the SEM image (Figure 3.18a) compared with the as-prepared array substrate (Figure 3.7a). However, after being immersed in solution, polarized and illuminated during the SPECM photoactivity quantification, the amount of Cu present in the semiconductor significantly decreases displaying a Co-rich ratio (Cu:Co atomic ratio of 1:3.9, Figure 3.18b). This seems to indicate a Cu leaching process taking place

under those conditions. Then, several new CuCo<sub>2</sub>O<sub>4</sub> samples with Cu:Co atomic ratio (1:2) were synthesized to study in more detail this degradation phenomenon.



*Figure 3.18 SEM images and EDS analysis of CuCo<sub>2</sub>O<sub>4</sub> spots under UV-vis light illumination for 500 s biased with different potentials (0.1 V, 0.05 V, 0 V, -0.05 V and -0.1 V) for photoactivity quantification. The optical fiber is held still at 150 μm above the array substrate, which was immersed in 0.1 M KHCO<sub>3</sub> saturated with CO<sub>2</sub>.*

Thus, it is necessary to figure out which effect plays the main role on inducing the photodegradation of the CuCo<sub>2</sub>O<sub>4</sub>. Illumination, polarization or the synergetic effect of both the photo illumination and the external bias. Given this, some additional experiments were performed to detect whether or not the illumination by itself could produce any damage on the CuCo<sub>2</sub>O<sub>4</sub> spots. Figure 3.19 shows SEM images and EDS analysis of 4 CuCo<sub>2</sub>O<sub>4</sub> spots on the same FTO sample under UV-vis light illumination for 0 s, 100 s, 300 s, 500 s, respectively. All 4 spots form a square shape and are located at the 4 vertexes with a center to center distance of 8 mm. Such a large distance avoids any interference from other illuminated spots.

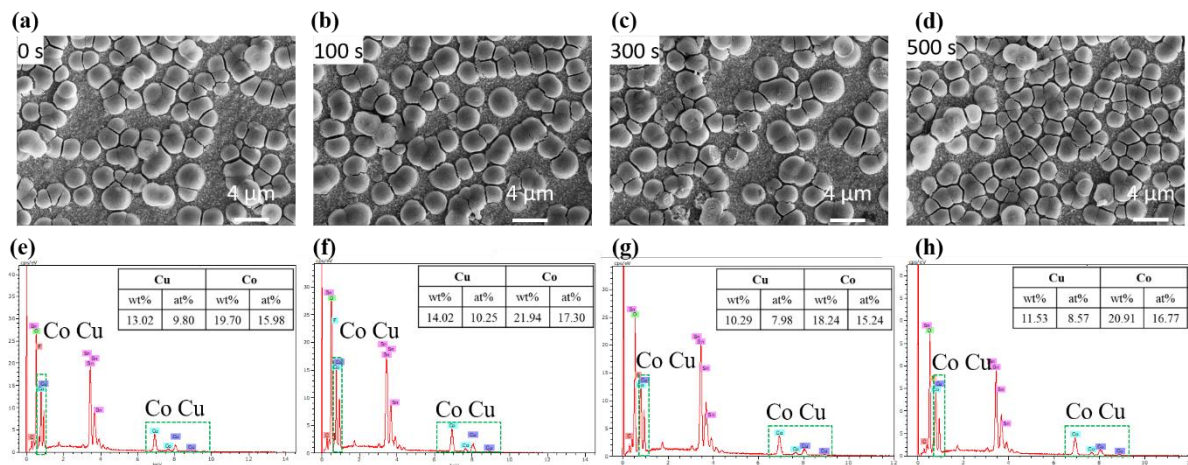


Figure 3.19 SEM images (upper row) and EDS analysis (lower row) of 4 CuCo<sub>2</sub>O<sub>4</sub> spots at open circuit potential under UV-vis light illumination for (a) and (e) 0 s, (b) and (f) 100 s, (c) and (g) 300 s, (d) and (h) 500 s, respectively. The optical fiber is held still 150  $\mu$ m above the array substrate which was immersed in 0.1 M KHCO<sub>3</sub> saturated with CO<sub>2</sub>.

Table 3.3 Cu and Co elements content from EDS spectra analysis and the corresponding atomic ratio in CuCo<sub>2</sub>O<sub>4</sub> spots as a function of applied potential and light irradiation exposure.

Illumination time (s)		Cu		Co		Cu : Co (at%)	
		wt%	at%	wt%	at%		
0		9.52	7.45	18.68	15.77	1:2.1	Figure 3.7
biased	500	5.67	4.18	20.27	16.10	1:3.9	Figure 3.18
unbiased	0	13.02	9.80	19.70	15.98	1:1.6	Figure 3.19
	100	14.02	10.25	21.94	17.30	1:1.7	
	300	10.29	7.98	18.24	15.24	1:1.9	
	500	11.53	8.57	20.91	16.77	1:2.0	

The CuCo<sub>2</sub>O<sub>4</sub> array substrate was immersed in 0.1 M KHCO<sub>3</sub> saturated with CO<sub>2</sub> and at open circuit potential (without any electric bias), which eliminated the electrical effect on the semiconductor degradation. The light irradiation came from an optical fiber held still at 150  $\mu$ m above the CuCo<sub>2</sub>O<sub>4</sub> spot. All the SEM images in Figure 3.19a-d show no evident morphology variation. Moreover, the EDS analysis results shown in Table 3.3 for all 4 spots with different illumination times exhibit no Cu content diminution (Cu:Co atomic ratio between 1:1.6 and 1:2.0). Interestingly, the atomic ratio of Cu and Co remains stable. In contrast with the Cu diminution displayed in Figure 3.19b, where the content of Cu decreased

by half whereas the Co content remained pretty constant (about 16 at%). The results indicate that the photodegradation is mainly caused by either the negative potential applied on the semiconductor material instead of the photo irradiation or the combination of both effects.

In fact, the effect of low stability of copper oxides as photocatalysts is well known in aqueous solution as photo-corrosion or photodegradation [30]. For instance, it was reported that this type of p-type semiconductor electrodes are somewhat unstable when acting as photocathodes for HER in aqueous solution. In most cases, this is because the conduction band potential is more negative than the reduction potential of the metal ion in the lattice, which induces the reduction of the semiconductor and inactivate the photocatalysis [15]. Even if CuCo<sub>2</sub>O<sub>4</sub> presents to a certain extent some photodegradation, it can still work as model photoelectrochemical catalyst in this thesis due to its good photoactivity compared to other evaluated semiconductors. In order to minimize photocatalyst degradation during amperometric photoactivity quantification experiments, five independent points within each studied CuCo<sub>2</sub>O<sub>4</sub> spot were chosen to record individual chronoamperometries as shown in Figure 3.20.

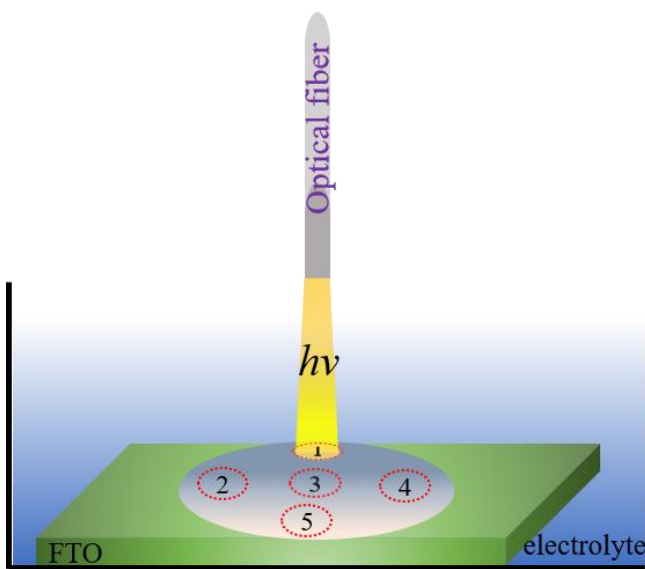


*Figure 3.20 Sequential sampling order within the same spot (from position 1 to 5) used for photocurrent quantification by SPECM*

This strategy allows to obtain reproducible results in the photoactivity quantification by SPECM. For this reason, we operated all the photoactivity quantification experiments



according to the sampling protocol described in Figure 3.20 in order to get a fresh point for each test.

The photocurrents collected under different bias potentials were compared for two different concentrations of RTILs in solution, 50 vol.% and 25 vol.% [C<sub>4</sub>mim][BF<sub>4</sub>]/H<sub>2</sub>O solution, respectively. In Figure 3.21, photoelectrochemical current in 50 vol.% [C<sub>4</sub>mim][BF<sub>4</sub>]/in H<sub>2</sub>O solution does not exhibit any enhancement with respect to 25 vol.% [C<sub>4</sub>mim][BF<sub>4</sub>]/H<sub>2</sub>O solution, which is in agreement with the SPECM imaging results already reported in Figure 3.13, which means that RTIL in 25 vol.% is already a good compromise for studying the cocatalyst role of imidazolium based RTILs. On the one hand, a too low percentage of RTILs in solution will not probably allow to profit the light absorption properties of imidazolium RTILs in this system. On the other hand, the viscosity of the solution increases when the percentage of RTILs is higher, which limits the current and increases the cost. For this reason, photocurrent quantification by SPECM is only performed in 25 vol.% RTILs in H<sub>2</sub>O binary solutions in this thesis.

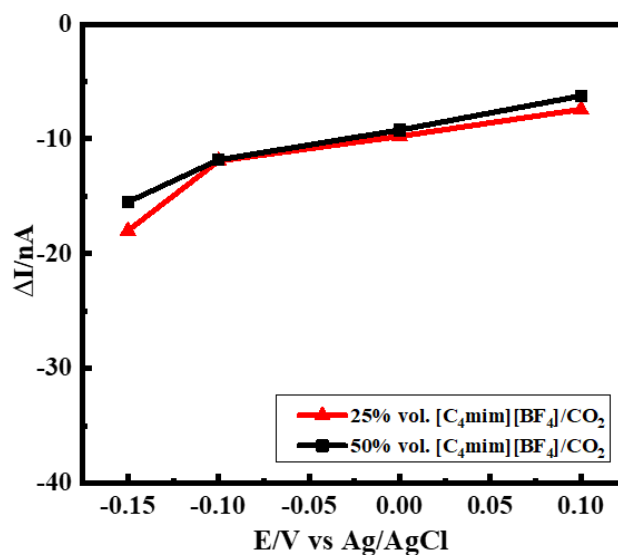


*Figure 3.21 Comparison of photocurrent collection on CuCo<sub>2</sub>O<sub>4</sub> in CO<sub>2</sub> saturated 25 vol.% and 50 vol.% [C<sub>4</sub>mim][BF<sub>4</sub>]/H<sub>2</sub>O solutions.*

This SPECM approach for evaluating photoactivity performance does not allow to separate CO<sub>2</sub>RR contribution in the total photocurrent from other reaction contributions. Nevertheless, it is possible to provide some information by comparing the photocatalytic activity in the presence and absence of CO<sub>2</sub> in solution. Figure 3.22 compares the photoreduction current

collected as a function of applied potential in different electrolyte solutions: (a) 0.1 M Na<sub>2</sub>SO<sub>4</sub> (b) 0.1 M KHCO<sub>3</sub>, (c) 25 vol.% [C<sub>4</sub>mim][BF<sub>4</sub>]/H<sub>2</sub>O and (d) 25 vol.% [C<sub>2</sub>mim][BF<sub>4</sub>]/H<sub>2</sub>O, which are previously purged either with Ar or CO<sub>2</sub> for 30 min. CuCo<sub>2</sub>O<sub>4</sub> spots are illuminated by UV-vis light in all cases.

The reactions to be considered as potential contributions to the total photoreduction current obtained in Figure 3.22 are: PEC CO<sub>2</sub>RR and/or HER and/or the reduction of the semiconductor CuCo<sub>2</sub>O<sub>4</sub>, and/or the RTIL cation reduction when it is present in solution. The only case where bubbling Ar does not ensure the absence of CO<sub>2</sub> in solution is when KHCO<sub>3</sub> is acting as electrolyte, because bicarbonate anion might become a source of CO<sub>2</sub> in solution. It has been reported that CO product was detected in Ar-saturated KHCO<sub>3</sub> solution, which was produced from the CO<sub>2</sub> molecules originated from the equilibrium with bicarbonate anions in the solution [31]. However, more photocurrent was collected in CO<sub>2</sub>-saturated KHCO<sub>3</sub> than that with Ar in the entire potential window investigated, but at different pH (Figure 3.22b). The same case for the photocurrent in 0.1 M Na<sub>2</sub>SO<sub>4</sub> with the presence of CO<sub>2</sub>, which surpassed that with Ar (Figure 3.22a), indicating that a portion of the photoreduction current could be related to CO<sub>2</sub>RR. In the case of 25 vol.% [C<sub>4</sub>mim][BF<sub>4</sub>]/H<sub>2</sub>O solution (Figure 3.22c), there is not a significant difference whether the solution is CO<sub>2</sub> saturated or not. This fact seems to indicate a poor contribution of CO<sub>2</sub>RR in the collected photocurrent. The most relevant results are obtained in the case of 25 vol.% [C<sub>2</sub>mim][BF<sub>4</sub>]/H<sub>2</sub>O solution (Figure 3.22d), where a clear improvement in photocurrent is observed compared with both aqueous solutions. However, no significant difference is observed whether the solution is CO<sub>2</sub> saturated or not, which mimics the 25 vol.% [C<sub>4</sub>mim][BF<sub>4</sub>]/H<sub>2</sub>O results, but displaying 5 times more photocurrent at -0.05 V. This relevant enhancement in photocurrent might be attributed either to the activation of HER or the reduction reaction of [C<sub>2</sub>mim]<sup>+</sup>. As the potentials change to more and more negative values, the collected photoreduction current increases in all solvent media studied, but reaching a too negative potential provokes degradation and deactivation of the semiconductor.

Proper comparison of any semiconductor performance must be done at constant pH. However, solution pH changes as a function of CO<sub>2</sub> presence in same aqueous solutions. For this reason, we have used two different aqueous solutions (0.1 M KHCO<sub>3</sub> and 0.1 M Na<sub>2</sub>SO<sub>4</sub>) in order to compare the photocurrent produced in the binary RTIL/H<sub>2</sub>O mixtures under the same pH conditions than in aqueous solution (see Table 3.2).



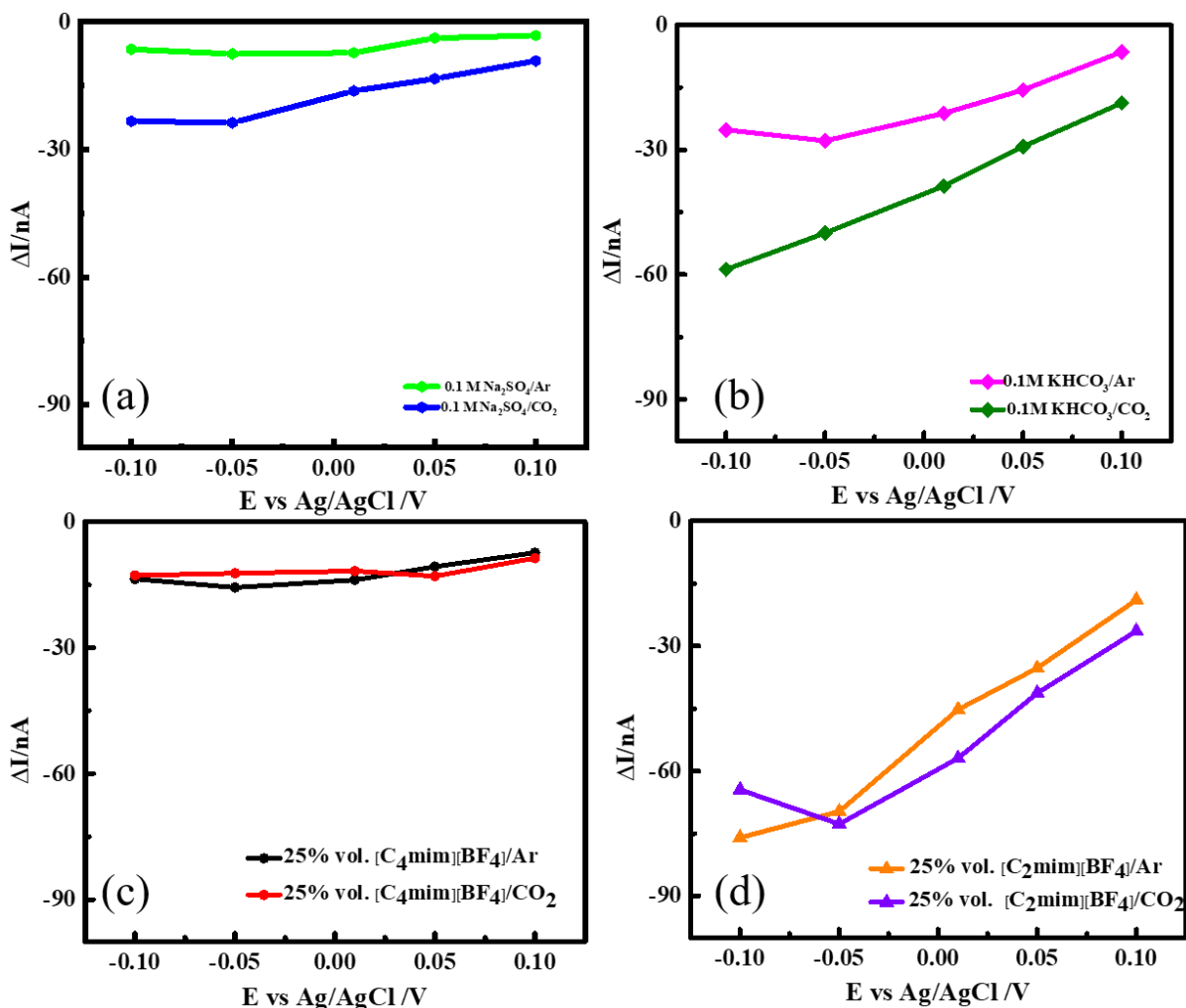


Figure 3.22 Comparison of photocurrent collection on CuCo<sub>2</sub>O<sub>4</sub> under UV-visible illumination as a function of applied potential in (a) 0.1 M Na<sub>2</sub>SO<sub>4</sub> and (b) 0.1 M KHCO<sub>3</sub> aqueous solutions (pH = 6.9); (c) 25 vol.% [C<sub>4</sub>mim][BF<sub>4</sub>]/H<sub>2</sub>O and (d) 25 vol.% [C<sub>2</sub>mim][BF<sub>4</sub>]/H<sub>2</sub>O solutions. Each solution is saturated either with CO<sub>2</sub> or Ar.

Each set of data shown in Figure 3.22 comes from the average of 2 or 3 independent experiments. As example, Figure 3.23 shows chronoresponses of the photocurrent collected at potentials of 0.1 V, 0.05 V, 0.01 V and -0.05 V vs. Ag/AgCl under UV-vis illumination in 25 vol.% [C<sub>2</sub>mim][BF<sub>4</sub>]/H<sub>2</sub>O CO<sub>2</sub> saturated solution (Figure 3.22d).

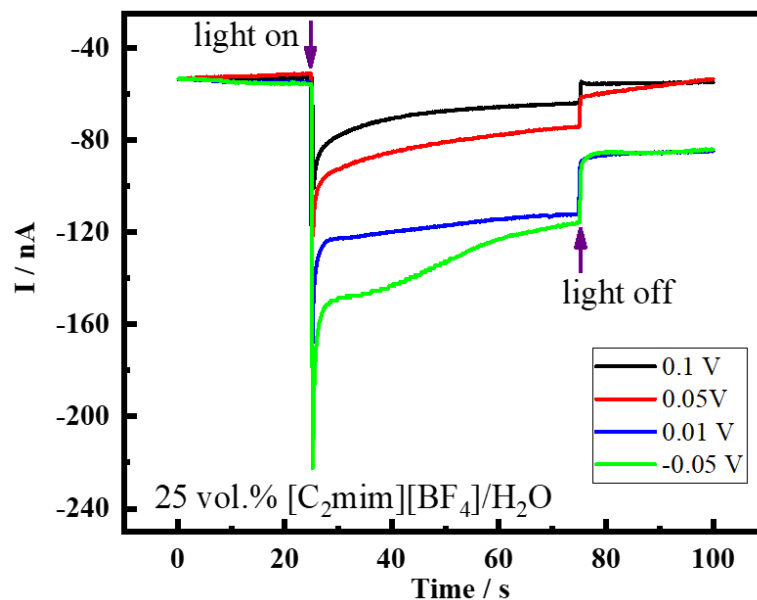


Figure 3.23 Chronoresponses of the photocurrent collected on a CuCo<sub>2</sub>O<sub>4</sub> spot in the array substrate electrode at potentials of 0.1 V, 0.05 V, 0.01 V and -0.05 V vs. Ag/AgCl under UV-vis illumination in CO<sub>2</sub> saturated 25 vol.% [C<sub>2</sub>mim][BF<sub>4</sub>]/H<sub>2</sub>O CO<sub>2</sub> saturated solution. The optical fiber is held still at a constant tip-substrate distance of 150  $\mu$ m on top of a CuCo<sub>2</sub>O<sub>4</sub> spot.

Sunlight wavelength spectrum includes 3 main components in a different ratio, 4% of ultraviolet (UV) rays (< 400 nm), 53% of visible light (400 ~ 800 nm) and 43% of infrared rays (> 800 nm). Thus, it is necessary to harvest, at least, a part of visible light for driving photoelectrochemical reactions by sunlight, since the presence of UV rays in sunlight is too limited. For this reason, Figure 3.24 summarizes the photoactivity of CuCo<sub>2</sub>O<sub>4</sub> at constant pH in the presence of different RTIL/H<sub>2</sub>O compared with aqueous solution and pure RTILs on the CO<sub>2</sub> photoreduction under the illumination of UV-vis light (Figure 3.24a). In addition to this, the photoactivity under visible light illumination is presented (Figure 3.24b). The photocurrent collected under visible light shows the same trend that the current recorded under UV-vis light. In all 4 electrolytes, it is obvious that the collected photocurrents under visible light are smaller than those under UV-vis light, whose stronger light power and broaden wavelength range strengthened the photogeneration of electron-holes pair and promoted their separation, diffusion and captured by a reduction reaction.

It is noteworthy that only 25 vol.% [C<sub>2</sub>mim][BF<sub>4</sub>]/H<sub>2</sub>O solution displays a significant enhanced photocurrent under visible light illumination. The other studied electrolyte solutions present almost null photoactivity ( $\Delta I = (1 \sim 4)$  nA). Overall, the CuCo<sub>2</sub>O<sub>4</sub> photoactivity as a

function of the electrolytes ranks as: 25 vol.% [C<sub>2</sub>mim][BF<sub>4</sub>]/H<sub>2</sub>O > 0.1 M KHCO<sub>3</sub> > 0.1 M Na<sub>2</sub>SO<sub>4</sub> > 25 vol.% [C<sub>4</sub>mim][BF<sub>4</sub>]/H<sub>2</sub>O > 100% [C<sub>2</sub>mim][BF<sub>4</sub>]/H<sub>2</sub>O. This is consistent with the result previously illustrated in SPECM imaging.

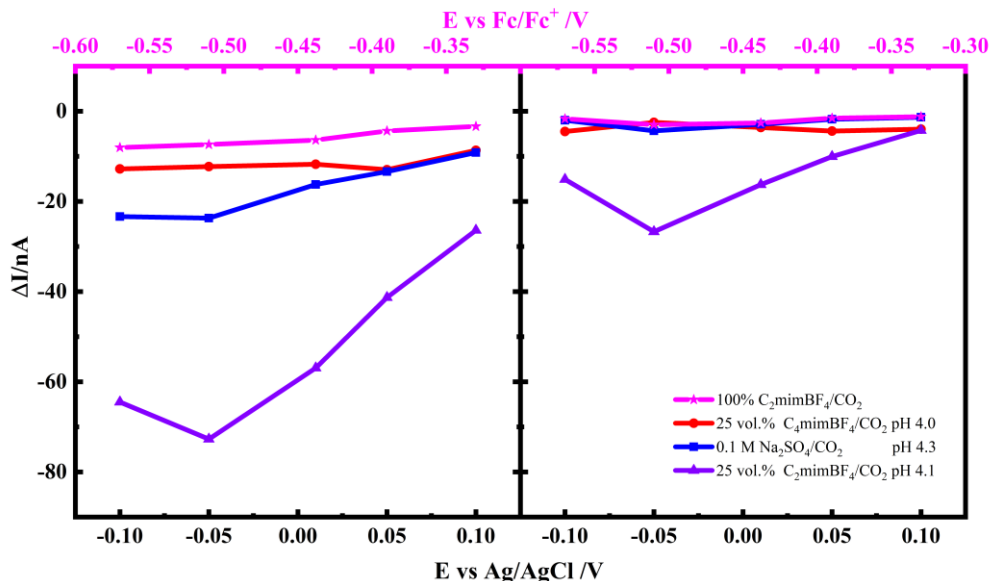


Figure 3.24 Photocurrent collection on CuCo<sub>2</sub>O<sub>4</sub> in different solutions saturated with CO<sub>2</sub> (a) under UV-visible light and (b) under visible light illumination. For 100% [C<sub>2</sub>mim][BF<sub>4</sub>], the potentials are reported versus Fc/Fc<sup>+</sup> (upper x axis scale) in pink color.

Thus, thanks to the fact of using a constant semiconductor material, the photocurrent production enhancement shown in Figure 3.24 can only be assigned to the presence of [C<sub>2</sub>mim][BF<sub>4</sub>] in solution and its effect on the semiconductor-electrolyte interface. However, no previous examples of this type of interaction are reported so far in the literature, only examples reporting enhancement of electrochemical CO<sub>2</sub>RR in the presence of [C<sub>2</sub>mim][BF<sub>4</sub>]/H<sub>2</sub>O solutions compared with conventional aqueous solution. Rosen *et al.* reported the positive effect of 18 mol% [EMIM][BF<sub>4</sub>] (or [C<sub>2</sub>mim][BF<sub>4</sub>]) in H<sub>2</sub>O on lowering the reduction overpotential of CO<sub>2</sub> to CO on silver electrode thanks to the formation of a complex (EMIM-CO<sub>2</sub>) [12]. Lau *et al.* also evaluated various imidazolium based RTILs as cocatalysts to facilitate electrochemical CO<sub>2</sub>RR, and demonstrated that the C4 and C5 protons on the imidazolium ring play a vital role on stabilizing the CO<sub>2</sub><sup>•-</sup> on the Ag electrode surface by hydrogen bonds [13].

Enhanced photoelectrochemical activity reported in this thesis is due to the presence of [C<sub>2</sub>mim][BF<sub>4</sub>] in solution and cannot be only accounted for the increased concentration of CO<sub>2</sub>

in solution. Furthermore, imidazolium cations present strong absorption peak among 200 ~ 400 nm wavelength because of the aromatic carbons in the imidazolium ring (see Figure 1.28 in chapter 1.3.3.3). The light absorption of the imidazolium cations can contribute to capture more light and then generate more photons on the semiconductor catalyst. However, the same strong light absorption band is present in [C<sub>4</sub>mim]<sup>+</sup> and the photocatalytic activity exhibited in the presence of this cation is much lower than in the case of [C<sub>2</sub>mim]<sup>+</sup> (Figure 3.24). Thus, some additional effect is provided when [C<sub>2</sub>mim]<sup>+</sup> is in solution. Mao *et al.* studied the electrochemical interfaces of imidazolium based RTILs on Au single crystal electrodes and illustrated that the interfacial structure of the imidazolium cations on Au were potential dependent. Imidazolium cation started to be adsorbed on the Au surface with a flat-lying structure, as the potentials became more and more negative, the cations tend to up-leaning and finally vertical-standing on the Au surface by HC4C5H side [32]. Taking into account this, [C<sub>4</sub>mim][BF<sub>4</sub>] contains a longer carbon chain compared to [C<sub>2</sub>mim][BF<sub>4</sub>], which may have a negative steric effect on the spatial arrangement of the imidazolium cation on the catalyst surface. This may cause the different catalytic performance when comparing [C<sub>2</sub>mim][BF<sub>4</sub>] and [C<sub>4</sub>mim][BF<sub>4</sub>].

The results shown in this chapter have already proved that the presence in solution of some particular imidazolium based ionic liquids plays a cocatalytic role by enhancing the photoelectrochemical activity of the studied semiconductor. However, it is not enough to illustrate its role for CO<sub>2</sub>RR. For this reason, chapter 4 in this thesis is devoted to identify the reaction products formed when [C<sub>2</sub>mim][BF<sub>4</sub>] is present in solution. The detection and analysis of those products was performed by SPECM using a dual tip optical fiber-UME and bulk electrolysis. Then, more details about products detection and some reasonable mechanism will be discussed in the following chapter.

### **3.4. Conclusions**

To sum up, several transition metals were adopted and combined to form different p-type metal oxide semiconductors as catalysts for photoelectrochemical CO<sub>2</sub> reduction reaction. Then, by comparing the stability and the catalytic activity of those different semiconductors, CuCo<sub>2</sub>O<sub>4</sub> was selected as the model catalyst to explore the role of RTILs in the performance of CO<sub>2</sub>RR evaluated by SPECM. The results shown in this chapter allow to quantify and

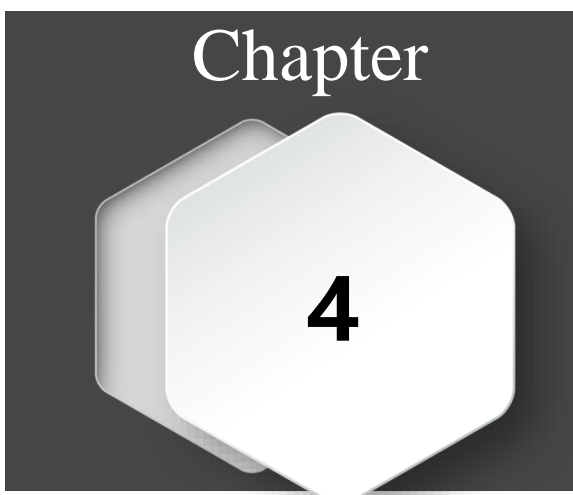
compare the photoelectrochemical activity of CuCo<sub>2</sub>O<sub>4</sub> in different media including pure RTILs, aqueous solution and binary RTIL/H<sub>2</sub>O mixtures. A relevant increase in photocurrent was exhibit in 25 vol.% [C<sub>2</sub>mim][BF<sub>4</sub>]/H<sub>2</sub>O solution either under UV-visible or visible illumination, whether the presence of CO<sub>2</sub> in solution or not. In contrast, changing the imidazolium cation from [C<sub>2</sub>mim]<sup>+</sup> to [C<sub>4</sub>mim]<sup>+</sup> does not enhance the photoelectrochemical activity, this fact might be due to some steric effects when [C<sub>4</sub>mim]<sup>+</sup> is adsorbed on the semiconductor surface.

### 3.5. References

- [1] M. Mikkelsen, M. Jørgensen, F.C. Krebs, The teraton challenge. A review of fixation and transformation of carbon dioxide, *Energy & Environmental Science*. 3 (2010) 43–81.
- [2] T. Inoue, A. Fujishima, S. Konishi, K. Honda, Photoelectrocatalytic reduction of carbon dioxide in aqueous suspensions of semiconductor powders, *Nature*. 277 (1979) 637–638. <https://doi.org/10.1038/277637a0>.
- [3] S. Sato, T. Morikawa, S. Saeki, T. Kajino, T. Motohiro, Visible-light-induced selective CO<sub>2</sub> reduction utilizing a ruthenium complex electrocatalyst linked to a p-type nitrogen-doped Ta<sub>2</sub>O<sub>5</sub> semiconductor, *Angewandte Chemie International Edition*. 49 (2010) 5101–5105. <https://doi.org/10.1002/anie.201000613>.
- [4] B. Kumar, M. Llorente, J. Froehlich, T. Dang, A. Sathrum, C.P. Kubiak, Photochemical and photoelectrochemical reduction of CO<sub>2</sub>, *Annual Review of Physical Chemistry*. 63 (2012) 541–569. <https://doi.org/10.1146/annurev-physchem-032511-143759>.
- [5] I. Taniguchi, B. Aurian-Blajeni, J.O. Bockris, The reduction of carbon dioxide at illuminated p-type semiconductor electrodes in nonaqueous media, *Electrochimica Acta*. 29 (1984) 923–932. [https://doi.org/10.1016/0013-4686\(84\)87137-6](https://doi.org/10.1016/0013-4686(84)87137-6).
- [6] C.M. Sánchez-Sánchez, J. Souza-Garcia, E. Herrero, A. Aldaz, Electrocatalytic reduction of carbon dioxide on platinum single crystal electrodes modified with adsorbed adatoms, *Journal of Electroanalytical Chemistry*. 668 (2012) 51–59.
- [7] C.M. Sánchez-Sánchez, Electrocatalytic reduction of CO<sub>2</sub> in imidazolium based ionic liquids, In: Wandelt, K., (Ed.) *Encyclopedia of Interfacial Chemistry: Surface Science and Electrochemistry*. 5 (2018) 539–551.
- [8] S. Pandey, Analytical applications of room-temperature ionic liquids: A review of recent efforts, *Analytica Chimica Acta*. 556 (2006) 38–45. <https://doi.org/10.1016/j.aca.2005.06.038>.
- [9] B.A. Rosen, W. Zhu, G. Kaul, A. Salehi-Khojin, R.I. Masel, Water enhancement of CO<sub>2</sub> conversion on silver in 1-ethyl-3-methylimidazolium tetrafluoroborate, *Journal of The Electrochemical Society*. 160 (2013) H138–H141.
- [10] M.A. Montiel, J. Solla-Gullón, C.M. Sanchez-Sanchez, Electrochemical reactivity and stability of platinum nanoparticles in imidazolium based ionic liquids, *Journal of Solid State Electrochemistry*. 20 (2016) 1043–1052.
- [11] M.A. Montiel, J. Solla-Gullón, V. Montiel, C.M. Sánchez-Sánchez, Electrocatalytic studies on imidazolium based ionic liquids: Defining experimental conditions, *Physical*

- Chemistry      Chemical      Physics.      20      (2018)      19160–19167.  
<https://doi.org/10.1039/c8cp02662a>.
- [12] B.A. Rosen, A. Salehi-Khojin, M.R. Thorson, W. Zhu, D.T. Whipple, P.J.A. Kenis, R.I. Masel, Ionic liquid-mediated selective conversion of CO<sub>2</sub> to CO at low overpotentials, *Science*. 334 (2011) 643–644. <https://doi.org/10.1126/science.1209786>.
- [13] G.P.S. Lau, M. Schreier, D. Vasilyev, R. Scopelliti, M. Grätzel, P.J. Dyson, New insights into the role of imidazolium based promoters for the electroreduction of CO<sub>2</sub> on a silver electrode, *Journal of the American Chemical Society*. 138 (2016) 7820–7823. <https://doi.org/10.1021/jacs.6b03366>.
- [14] Q. Zhu, J. Ma, X. Kang, X. Sun, H. Liu, J. Hu, Z. Liu, B. Han, Efficient reduction of CO<sub>2</sub> into formic acid on a lead or tin electrode using an ionic liquid catholyte mixture, *Angewandte Chemie International Edition*. 55 (2016) 9012–9016. <https://doi.org/10.1002/anie.201601974>.
- [15] K.M. Nam, H.S. Park, H.C. Lee, B.H. Meekins, K.C. Leonard, A.J. Bard, Compositional screening of the Pb-Bi-Mo-O system. Spontaneous formation of a composite of *p*-PbMoO<sub>4</sub> and *n*-Bi<sub>2</sub>O<sub>3</sub> with improved photoelectrochemical efficiency and stability, *Journal of Physical Chemistry Letters*. 4 (2013) 2707–2710. <https://doi.org/10.1021/jz401334k>.
- [16] X. Ba, L.-L. Yan, S. Huang, J. Yu, X.-J. Xia, Y. Yu, New way for CO<sub>2</sub> reduction under visible light by a combination of a Cu electrode and semiconductor thin film: Cu<sub>2</sub>O conduction type and morphology effect, *J. Phys. Chem. C*. 118 (2014) 24467–24478. <https://doi.org/10.1021/jp5063397>.
- [17] S. Saadi, A. Bouguelia, M. Trari, Photoassisted hydrogen evolution over spinel CuM<sub>2</sub>O<sub>4</sub> (M=Al, Cr, Mn, Fe and Co), *Renewable Energy*. 31 (2006) 2245–2256. <https://doi.org/10.1016/j.renene.2005.10.014>.
- [18] F. Saib, F. Özel, A. Sarılmaz, O. Mahroua, B. Bellal, M. Trari, Photo-electrochemical properties of p-type AgCoO<sub>2</sub> prepared by low temperature method, *Materials Science in Semiconductor Processing*. 91 (2019) 174–180. <https://doi.org/10.1016/j.mssp.2018.11.026>.
- [19] G. Rekhila, Y. Gabes, Y. Bessekhoud, M. Trari, Hydrogen production under visible illumination on the spinel NiMn<sub>2</sub>O<sub>4</sub> prepared by sol gel, *Solar Energy*. 166 (2018) 220–225. <https://doi.org/10.1016/j.solener.2018.02.064>.
- [20] E.Y. Frag, R.M. Abdel Hameed, Preparation, characterization and electrochemical application of CuNiO nanoparticles supported on graphite for potentiometric determination of copper ions in spiked water samples, *Microchemical Journal*. 144 (2019) 110–116. <https://doi.org/10.1016/j.microc.2018.08.060>.
- [21] M. Jiang, Y. Gao, Z. Wang, Z. Ding, Photocatalytic CO<sub>2</sub> reduction promoted by a CuCo<sub>2</sub>O<sub>4</sub> cocatalyst with homogeneous and heterogeneous light harvesters, *Applied Catalysis B: Environmental*. 198 (2016) 180–188. <https://doi.org/10.1016/j.apcatb.2016.05.055>.
- [22] J. Cheng, H. Yan, Y. Lu, K. Qiu, X. Hou, J. Xu, L. Han, X. Liu, J.-K. Kim, Y. Luo, Mesoporous CuCo<sub>2</sub>O<sub>4</sub> nanograsses as multi-functional electrodes for supercapacitors and electro-catalysts, *Journal of Materials Chemistry A*. 3 (2015) 9769–9776.
- [23] Y. Sharma, N. Sharma, G.V.S. Rao, B.V.R. Chowdari, Lithium recycling behaviour of nano-phase-CuCo<sub>2</sub>O<sub>4</sub> as anode for lithium-ion batteries, *Journal of Power Sources*. 173 (2007) 495–501. <https://doi.org/10.1016/j.jpowsour.2007.06.022>.

- [24] M. Dunwell, Q. Lu, J.M. Heyes, J. Rosen, J.G. Chen, Y. Yan, F. Jiao, B. Xu, The central role of bicarbonate in the electrochemical reduction of carbon dioxide on gold, *J. Am. Chem. Soc.* 139 (2017) 3774–3783. <https://doi.org/10.1021/jacs.6b13287>.
- [25] Q. Lu, F. Jiao, Electrochemical CO<sub>2</sub> reduction: Electrocatalyst, reaction mechanism, and process engineering, *Nano Energy*. 29 (2016) 439–456. <https://doi.org/10.1016/j.nanoen.2016.04.009>.
- [26] B. Kumar, M. Asadi, D. Pisasale, S. Sinha-Ray, B.A. Rosen, R. Haasch, J. Abiade, A.L. Yarin, A. Salehi-Khojin, Renewable and metal-free carbon nanofibre catalysts for carbon dioxide reduction, *Nature Communications*. 4 (2013) 1–8. <https://doi.org/10.1038/ncomms3819>.
- [27] R. Rahmatolahzadeh, M. Mousavi-Kamazani, S.A. Shobeiri, Facile co-precipitation-calcination synthesis of CuCo<sub>2</sub>O<sub>4</sub> nanostructures using novel precursors for degradation of azo dyes, *J Inorg Organomet Polym*. 27 (2017) 313–322. <https://doi.org/10.1007/s10904-016-0473-9>.
- [28] A. Paul, P.K. Mandal, A. Samanta, On the optical properties of the imidazolium ionic liquids, *J. Phys. Chem. B*. 109 (2005) 9148–9153. <https://doi.org/10.1021/jp0503967>.
- [29] M.H. Habibi, Z. Rezvani, Photocatalytic degradation of an azo textile dye (C.I. Reactive Red 195 (3BF)) in aqueous solution over copper cobaltite nanocomposite coated on glass by Doctor Blade method, *Spectrochimica Acta Part A: Molecular and Biomolecular Spectroscopy*. 147 (2015) 173–177. <https://doi.org/10.1016/j.saa.2015.03.077>.
- [30] S.P. Berglund, H.C. Lee, P.D. Núñez, A.J. Bard, C.B. Mullins, Screening of transition and post-transition metals to incorporate into copper oxide and copper bismuth oxide for photoelectrochemical hydrogen evolution, *Physical Chemistry Chemical Physics*. 15 (2013) 4554–4565.
- [31] S. Zhu, B. Jiang, W.-B. Cai, M. Shao, Direct observation on reaction intermediates and the role of bicarbonate anions in CO<sub>2</sub> electrochemical reduction reaction on Cu surfaces, *J. Am. Chem. Soc.* 139 (2017) 15664–15667. <https://doi.org/10.1021/jacs.7b10462>.
- [32] M. Zhang, L.-J. Yu, Y.-F. Huang, J.-W. Yan, G.-K. Liu, D.-Y. Wu, Z.-Q. Tian, B.-W. Mao, Extending the shell-isolated nanoparticle-enhanced Raman spectroscopy approach to interfacial ionic liquids at single crystal electrode surfaces, *Chem. Commun.* 50 (2014) 14740–14743. <https://doi.org/10.1039/C4CC06269H>.



# Detection and Identification of Photoelectrochemically Generated Products by SPECM and Chromatography

---





## Chapter 4 Detection and Identification of Photoelectrochemically Generated Products by SPECM and Chromatography

### 4.1. Introduction

So far, in this thesis, we have adopted SPECM to compare photoelectrochemical reduction performance in different media including pure RTILs, aqueous solution and binary RTIL/H<sub>2</sub>O mixtures. A relevant increase in photocurrent in 25 vol.% [C<sub>2</sub>mim][BF<sub>4</sub>]/H<sub>2</sub>O solution was obtained in comparison with all other media tested under both UV-visible and visible illumination, whether the presence of CO<sub>2</sub> in solution or not. In order to explore deeply this promising performance and discover the story and the reason behind, the detection of the photoelectrochemical products generated is imperative and necessary. Actually, as it was already mentioned in chapter 3, several reactions could be responsible of producing this enhanced photocurrent on CuCo<sub>2</sub>O<sub>4</sub>: *i*) PEC CO<sub>2</sub>RR and/or *ii*) HER and/or *iii*) reduction of semiconductor and/or *iv*) [C<sub>2</sub>mim]<sup>+</sup> reduction.

Initially, a combined optical fiber-ultramicroelectrode (OF-UME) dual tip in a SPECM configuration is proposed for in-situ products detection. In fact, the principle of combining an optical fiber for triggering the photoelectrochemical reaction and a UME for detecting the products generated has been proposed and developed for several years. An Au ring coated OF core sealed in an insulating sheath (electrophoretic paint or glass) has been successfully employed for SPECM applications such as imaging interdigitated array electrode [1] or water splitting reaction [2]. However, this protocol requires metal coating, which is high-cost and needs precise control of the coated metal layer. Another alternative couples an OF at the end of the UME in a glass sheath, which can guide the light to locally illuminate the sample. This approach has been also developed to explore water splitting on n-type semiconductor-based photoanodes [3], despite UV light can be weakened by the refraction on the glass sheath. Finally, Zigah *et al.* [4] proposed a dual tip configuration where an optical fiber and a gold UME (OF-UME) are combined for acting simultaneously as a light source and a sensor for photoelectrochemically generated O<sub>2</sub>.

In this thesis, a dual tip OF-UME based on Zigah *et al.* methodology was fabricated for studying the photoelectrochemically generated products in SPECM. The OF allows the light

to locally illuminate the p-type semiconductor material under study. Simultaneously, the biased UME (Pt or Au) can detect the electrochemically active generated products ( $\text{H}_2$ , CO and/or  $\text{HCOOH}$ ) by electrochemical oxidation at the UME and distinguish among them depending on the oxidation potential required. Thus, the SG-TC operation mode of SPECM was employed. The dual OF-UME tip serves simultaneously as a light source for locally illuminate the p-type semiconductor under study, on the other side, as an electrochemical probe for the detection of the products collected on the biased UME tip. All results reported in this chapter were done using dual tips fabricated by my own. Experimental details in home-made fabrication of dual tips OF-UME are provided in chapter 2. Finally, some bulk electrolysis under illumination were carried out in addition to the in-situ detection experiments performed with the dual tip OF-UME in SPECM configuration. Actually, bulk electrolysis allowed to accumulate significant amount of photoelectrochemically generated products for being quantified by gas and/or ionic chromatography.

## **4.2. Detection of Photoelectrochemically Generated Products by OF-UME**

The dual tip OF-UME was employed in the configuration of SPECM capable of triggering PEC reactions and simultaneously detecting the photoelectrochemically generated reduction products from either  $\text{CO}_2\text{RR}$  or HER. The schematic illustration of the principle of the application of dual tip OF-UME for PEC  $\text{CO}_2\text{RR}$  on  $\text{CuCo}_2\text{O}_4$  spots is shown in Figure 4.1. The conventional 4-electrode electrochemical cell presented is filled with the electrolyte saturated with  $\text{CO}_2$ . The Pt probe acts as the working electrode 1 (WE1) and the semiconductor  $\text{CuCo}_2\text{O}_4$  supported on FTO as working electrode 2 (WE2), Pt wire (500  $\mu\text{m}$ ) and  $\text{Ag}/\text{AgCl}$  (3 M) are counter and reference electrodes, respectively. The OF-UME was setup perpendicularly above the WE2 (Tip-substrate distance = 20  $\mu\text{m}$ ). The dual tip OF-UME was scanned along the X-Y plane and introduced UV-vis light locally on the WE2, which was usually biased, through the OF and this might convert  $\text{CO}_2$  into CO,  $\text{HCOOH}$  or other products on the photocatalyst surface. At the same time, the WE1 was biased at potentials at which the oxidation of the  $\text{CO}_2\text{RR}$  products occurs, hence, the oxidation current can be collected therein. As a result, two independent current signals could be plotted as a function of dual tip position in the (X-Y) plane. On the one hand, the photocurrent produced on the semiconductor and on the other hand, the oxidation current collected at the UME probe, which corresponded to the

electrochemical sensing of products. Therefore, the use of dual tip OF-UME required the SG-TC operation mode of SECM, which allowed both to trigger photocatalytic reactions and detect the corresponding generated products by electrochemical oxidation.

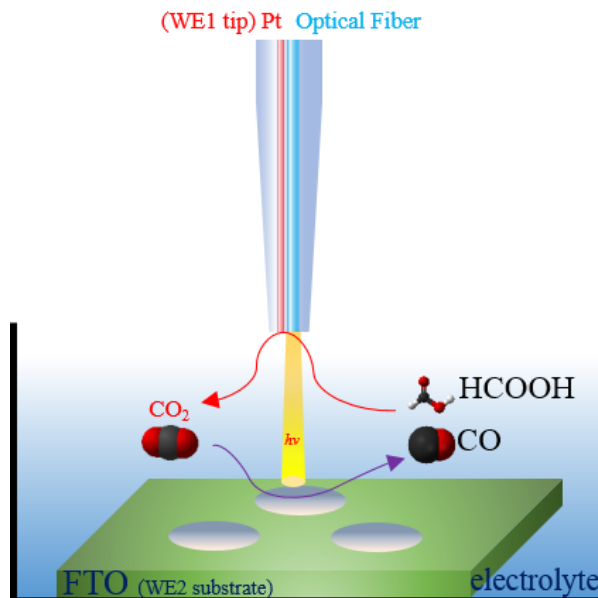


Figure 4.1 Schematic representation of the application of dual tip OF-UME application for simultaneously screening of  $\text{CuCo}_2\text{O}_4$  for PEC  $\text{CO}_2\text{RR}$  and simultaneous detection of products by oxidation reaction at the UME probe.

The dual tip OF-UME needed to be located within the diffusion layer of the products photoelectrochemically generated on the semiconductor surface. For this reason, the tip-substrate distance must be relatively small. Thus, the substrate electrode tilt must be reduced as much as possible in order to fulfill the condition of  $\Delta z / \Delta x$  (or  $\Delta y$ )  $< 1.5 \mu\text{m}/1 \text{ mm}$  [5]. Initially, the tip-substrate distance could be controlled by the ratio between the steady-state current and the final current collected by the Pt UME present in the dual tip. However, the control of this distance was not possible by conventional approach curves and the corresponding fitting curves due to the huge RG value of the OF-UME. Instead of that, the OF-UME was moved downwards to the substrate and stopped when the current at the Pt UME present in the dual tip reached the turning point indicating the contact of the surrounding glass with the substrate. Then the OF-UME was withdrawn for a given distance (20  $\mu\text{m}$  in most cases). This distance was within the diffusion layer of the products generated in spite of the fact that the UME part in OF-UME was not exactly above the illuminated area on the semiconductor, but it was inside the diffusion layer range, so the detection of the products was

available, making it a powerful and worthy detector in local electrochemistry. Moreover, the large RG value in the dual tip played a positive role for our products detection system because it confined the diffusion of the products in a narrow gap between tip and substrate. In contrast, this fact also provoked a decrease in the diffusion of reactants towards the semiconductor surface and then, in photocurrent. The sharp part of the OF-UME tip was so slender and fragile that it could not be polished properly to a mirror surface, leading to a rough surface. The same dual tip was used to obtain each set of data. For this reason, current instead of current density is used to illustrate the detection of the photoelectrochemically generated products.

### 4.3. SPECM Imaging by the Dual Tip OF-UME

The dual tip OF-UME was capable of triggering and mapping PEC reactions on semiconductors and simultaneously detecting and mapping the photoelectrochemically generated products. Our main goal was detecting products generated from the PEC CO<sub>2</sub>RR and HER, which must be electrochemically active. It means that it must be possible to oxidize them electrochemically on the Pt UME surface. Then, CO, HCOOH and H<sub>2</sub> were the only detectable products considered here and the most likely ones. First of all, the detection potential applied on the UME for electrochemically sensing those products needed to be selected. For this purpose, the corresponding CVs on OF-UME (Pt) of a standard solution containing different concentrations of NaCOOH is presented in Figure 4.2. Formic acid oxidation reaction (FAOR) on Pt electrode may follow two different reaction pathways: (1) Direct CO<sub>2</sub> formation by dehydrogenation, which is desired and (2) Indirect dehydration pathway, where firstly strongly adsorbed CO is formed, which blocks the Pt electrode surface, and secondly the completely oxidation of the CO<sub>ads</sub> is only achieved at more positive potentials [6]. Thus, Figure 4.2 shows the oxidation peaks corresponding to both pathways. On the one hand, the oxidation peak appeared in the positive-going scan at 0.15 V, which corresponds to the CO<sub>ads</sub> oxidation and on the other hand, the oxidation peak centered at 0 V in the backwards negative-going scan, which corresponds to the direct oxidation pathway. Thus,  $\geq 0.4$  V seemed to be a positive enough potential to perform the oxidation of all interesting products (CO, HCOOH and H<sub>2</sub>) on Pt under those conditions, since hydrogen oxidation reaction (HOR) on Pt takes place at more negative potential values because its low overvoltage ( $E^0_{H^+/H_2} = -0.6$  V vs. Ag/AgCl at pH = 6.9).

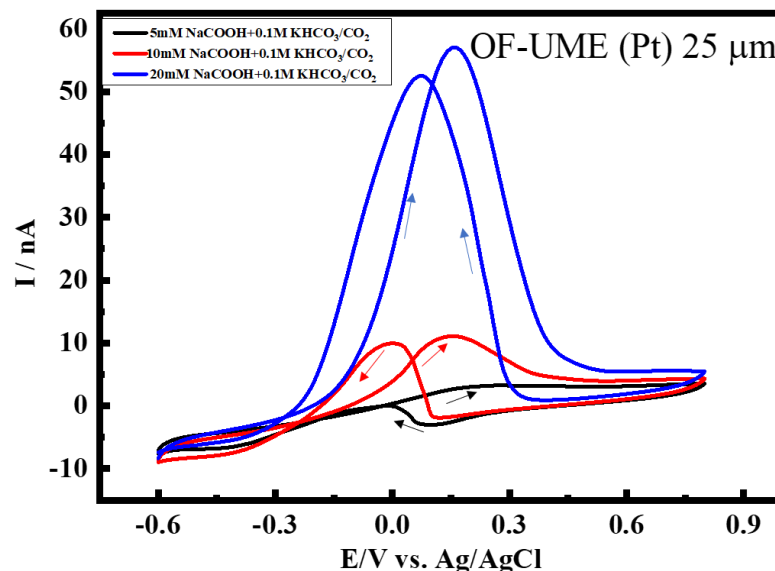


Figure 4.2 Cyclic voltammograms of the OF-UME (Pt) in  $\text{CO}_2$  saturated 0.1 M  $\text{KHCO}_3$  solution containing 5 mM (black line), 10 mM (red line) and 20 mM (blue line)  $\text{NaCOOH}$  at scan rate: 10 mV/s. The potential limits were -0.6 to 0.8 V vs. Ag/AgCl, initiated from -0.6 V; pH = 6.9.

Figure 4.3 shows two types of SPECM images obtained when the dual tip OF-UME scanned the semiconductor array. The products detection image from the UME tip (a and c), and the corresponding photocurrent image from the illuminated and biased semiconductor substrate (b and d). In this case, the dual tip was positioned above the substrate with a tip-substrate distance of 20  $\mu\text{m}$  and the UME was held at a constant potential for electrochemical sensing of generated products. Then, the OF-UME was scanned above the substrate along X-Y plane meanwhile the substrate was biased and illuminated by UV-vis light through the OF. Both pair of images (a-b) and (c-d) provided good spatial resolution and matching features. The photocurrent images (b) and (d), sequentially obtained under the same bias potential, exhibited the same current difference and spot morphology, indicating the high reproducibility of the PEC reaction under study. In contrast, the different applied potential on the Pt UME (0.4 V in Figure 4.3a and -0.35 V in Figure 4.3b) provided results completely different. A net oxidation current was collected when the UME was held at 0.4 V (Figure 4.3a). However, the current based spots position was neither exactly on the same place than in the photocurrent image nor showing a round shape. This was probably due to the tip scan direction effect and the physical separation in the dual tip between the OF and the UME, which provoked the distortion of the products diffusion layer on the spots before the products detection. In contrast,

no net oxidation current was collected when the UME was held at -0.35 V (Figure 4.3c), since the applied potential was not suitable for products detection. Only topographical information was achieved by applying this potential.

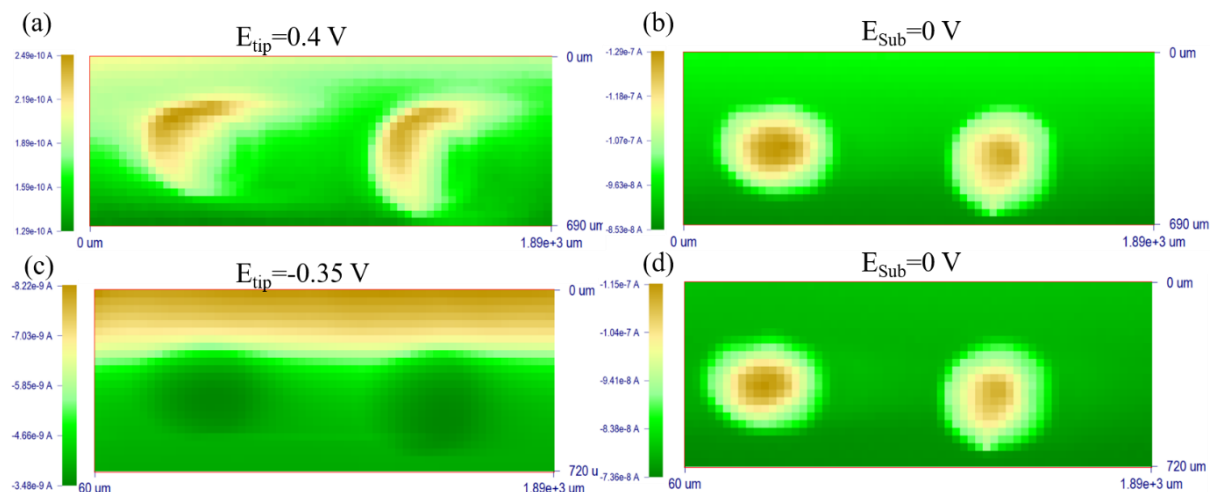


Figure 4.3 SPECM images of (a) and (c) the products oxidation current collected at the OF-UME tip at 0.4 V and -0.35 V, respectively. (b) and (d) The corresponding substrate photocurrent of (a) and (c), respectively and collected on the  $\text{CuCo}_2\text{O}_4$  spots array substrate at applied potential of 0 V and illuminated by UV-vis light. All potentials were reported versus Ag/AgCl. Electrolyte: 0.1 M  $\text{KHCO}_3$  saturated with  $\text{CO}_2$ , scan rate is 200  $\mu\text{m/s}$ .

Finally, if the semiconductor was not irradiated through the OF, negligible detection current was observed in the SPECM detection image at the OF-UME as shown in Figure 4.4c, in comparison with that of a biased and illuminated substrate (Figure 4.4a).

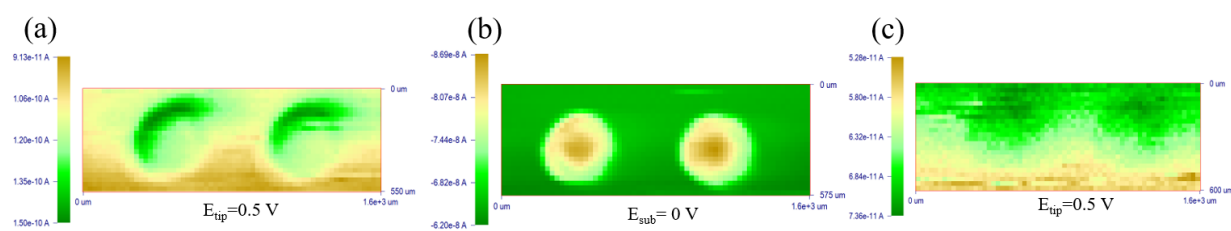


Figure 4.4 SPECM images of (a) the products oxidation current collected at the OF-UME tip at 0.5 V and (b) the corresponding photocurrent on the  $\text{CuCo}_2\text{O}_4$  spots array substrate biased at 0 V and illuminated by UV-vis light. (c) The products oxidation current collected at the OF-UME tip at 0.5 V when the substrate was at OCP and without illumination. All potentials were reported versus Ag/AgCl. Electrolyte: 0.1 M  $\text{KHCO}_3$  saturated with  $\text{CO}_2$ , scan rate is 200  $\mu\text{m/s}$ .

### 4.3.1. Constant Potential Products Detection by the Dual Tip OF-UME

In general, the imaging process is time consuming because of the large scanning surface area. In contrast, chronoamperometric experiments on individual semiconductor spots like the one presented in chapter 3 for quantification of photoelectrochemical activity, but operated by the dual tip OF-UME, could provide relevant information about the photoelectrochemically generated products in a shorter time. In this case, the dual tip acts as a simultaneous static light source and sensor. For this purpose, the OF-UME was positioned above the center of the catalyst spot within a tip-substrate distance of 20  $\mu\text{m}$ . Figure 4.5 shows the chronoresponse of the photocurrent collected on the semiconductor as a function of applied potential (Figure 4.5b) and the simultaneous oxidation current due to electrochemical products detection by holding the Pt UME present in the dual tip at constant potential of 0.5 V (Figure 4.5a). The semiconductor was only illuminated from 25 s to 50 s. Thus, as the applied potential of the substrate goes towards more negative values (from 0.05 V to -0.1 V), the photocurrent collected ( $\Delta I$ ) increase (Figure 4.5b), which was already described and properly discussed in chapter 3. Nevertheless, the same tendency was not exhibited by the products detection current (Figure 4.5a), since a clear oxidation current associated with the start and end of the semiconductor illumination time gap was only exhibited at 0.05 V of substrate potential and negligible products detection current was collected at -0.1 V of substrate potential. This fact might indicate deactivation or poisoning of the Pt UME during detection.

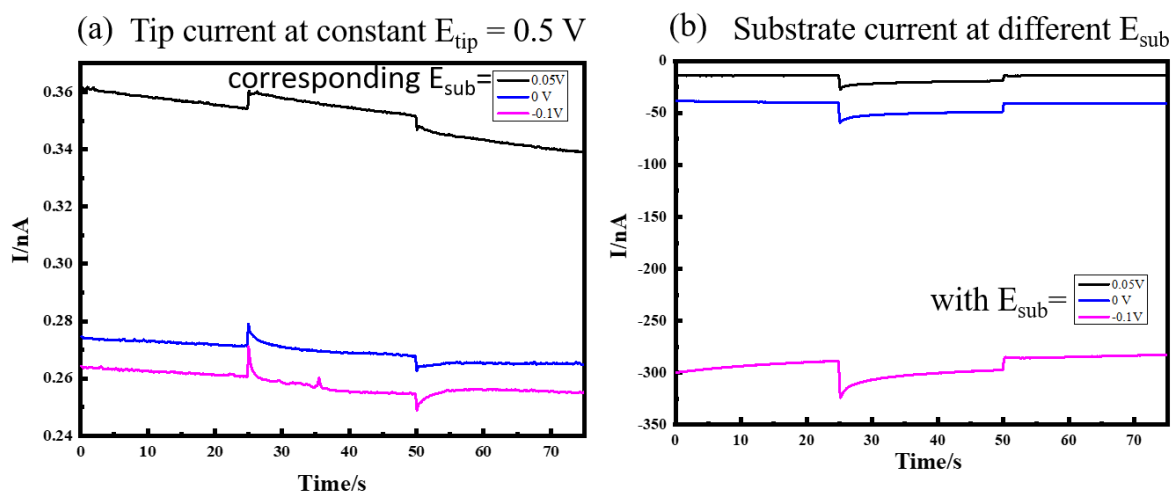


Figure 4.5 Chronoresponse of (a) the products oxidation currents collected at constant OF-UME tip potential ( $E_{\text{tip}} = 0.5 \text{ V}$ ). (b) The photocurrent collected on a  $\text{CuCo}_2\text{O}_4$  spot as a function of applied



*potential. CuCo<sub>2</sub>O<sub>4</sub> spot was illuminated by UV-vis light within the time gap between 25 s and 50 s. All potentials were reported versus Ag/AgCl. Electrolyte: 0.1 M KHCO<sub>3</sub> saturated with CO<sub>2</sub>.*

Using the dual tip for products detection by applying a constant potential to the Pt UME was the simplest approach, but it was a non-product selective approach, which meant that holding the Pt UME potential constant at 0.4 or 0.5 V did not allow to distinguish the different detectable products considered (CO, HCOOH and H<sub>2</sub>). For this reason, a different approach based on fast cyclic voltammetry was more deeply explored and it is described in the following section.

#### 4.3.2. Fast Cyclic Voltammetry Products Detection by the Dual Tip OF-UME

An alternative and interesting approach to distinguish the detectable products considered (CO, HCOOH and H<sub>2</sub>) by electrochemical means was to run a cyclic voltammogram on the UME Pt present in the dual tip, since an independent oxidation peak located at a different potential was associated with each considered product [7]. Moreover, detection by CV at fast scan rate (e.g. at 1 V/s) provided additional advantages. This approach has been recently proposed by E.L. Gyenge, *et al.*, (Communications Chemistry, 2020, doi.org/10.1038/s42004-020-00399-6) and it is specifically interesting for detecting adsorbed species because increasing the scan rate in CV enhances in a larger magnitude the peak current response associated with adsorbed species ( $I_{\text{peak}} \approx f(V)$ ) than associated with electroactive species in solution ( $I_{\text{peak}} \approx f(V^{1/2})$ ). Thus, detecting photoelectrochemically generated products, which could be adsorbed on Pt electrode like CO, by fast CV increases the sensitivity.

The results shown in chapter 3 proved a relevant increase in photocurrent only in the case of 25 vol.% [C<sub>2</sub>mim][BF<sub>4</sub>]/H<sub>2</sub>O solution either under UV-visible or visible illumination. For this reason, only products detection by the dual tip OF-UME using fast cyclic voltammetry was performed on this medium. For this purpose, the OF-UME was positioned above the center of the catalyst spot within a tip-substrate distance of 20  $\mu\text{m}$  following the same procedure previously described for constant potential products detection. Moreover, fast tip CVs (at 1 V/s) starting from -0.8 V and anodically sweeping to 1.2 V vs. Ag/AgCl were operated on the dual tip to prevent the inactivation over time reported on the Pt UME when a constant potential was used for products detection (Figure 4.5). First of all, the corresponding CV on OF-UME (Pt) of a standard solution containing NaCOOH in CO<sub>2</sub> saturated 25 vol.% [C<sub>2</sub>mim][BF<sub>4</sub>]/H<sub>2</sub>O solution at 1 V/s was registered (Figure 4.6). Typical voltammetric features associated with

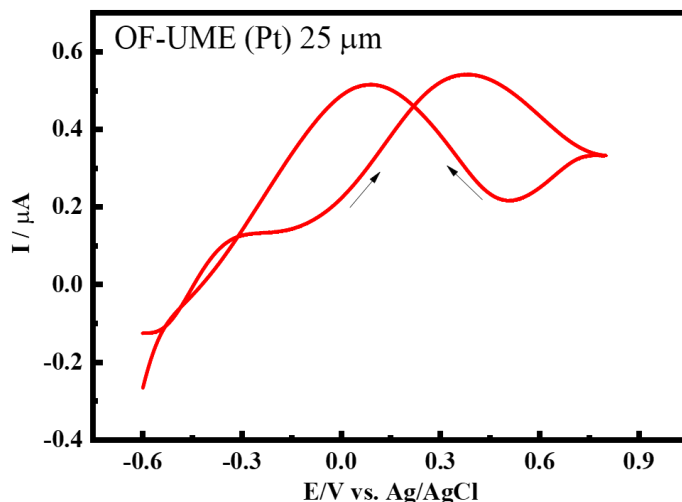


Figure 4.6 Cyclic voltammogram of the OF-UME (Pt) in  $\text{CO}_2$  saturated 25 vol.%  $[\text{C}_2\text{mim}][\text{BF}_4]/\text{H}_2\text{O}$  solution with the addition of NaCOOH salt at scan rate of 1 V/s. The potential limits were -0.6 to 0.8 V vs. Ag/AgCl, initiated from -0.6 V.

FAOR on Pt were displayed. In particular, a peak centered at 0.4 V in the positive-going scan, which was associated to  $\text{CO}_{\text{ads}}$  oxidation and another peak centered at 0.1 V in the negative-going scan, which was associated to the direct oxidation of formic acid to  $\text{CO}_2$ . Furthermore, both peak currents were almost identical. This particular voltammetric feature of FAOR on Pt in this medium could help distinguish between CO formed during FAOR and PEC produced CO, since no significant oxidation peak could be expected in the negative-going scan in the latest case, as is shown in Figure 4.7 [8].

PEC products detection by the dual tip OF-UME located in close proximity of the substrate (20  $\mu\text{m}$ ) and using fast cyclic voltammetry was successfully performed in  $\text{CO}_2$  saturated 25 vol.%  $[\text{C}_2\text{mim}][\text{BF}_4]/\text{H}_2\text{O}$  solution. Figure 4.8 shows fast CVs collected by the Pt UME present in the dual tip when the  $\text{CuCO}_2\text{O}_4$  semiconductor was unbiased in the dark (Figure 4.8a) and biased at -0.05 V vs. Ag/AgCl under UV-vis illumination (Figure 4.8b). No oxidation peak was observed in the positive-going of 2 consecutive scans in the dark (Figure 4.8a). In contrast, a sharp anodic peak centered at 0.4 V vs. Ag/AgCl (0.8 V vs. RHE at pH = 4), which fitted  $\text{CO}_{\text{ads}}$  oxidation peak shown in Figure 4.7, was clearly observed in the first positive-going scan shown in Figure 4.8b. This sharp oxidation peak resembled the conventional well-known CO-oxidation on Pt surface. The possibility of detecting CO formed as byproduct from FAOR (Figure 4.6) was totally ruled out, because no peak centered at 0.1 V in the negative-going scan associated with direct oxidation of formic acid to  $\text{CO}_2$  was registered in Figure 4.8b. In addition

to this, Phani *et al.* has already reported in the literature cyclic voltammetry on Pt UME for detection of CO generated from CO<sub>2</sub>RR on Pt electrode at a similar tip potential (0.4 V ~ 0.6 V vs. Ag/AgCl) [7]. Thus, a clear oxidation peak centered at 0.4 V only appeared under illumination and it was assigned to the CO<sub>ads</sub> stripping oxidation. Figure 4.8c exhibited an increasing CO<sub>ads</sub> oxidation peak current collected by fast CV when the CuCo<sub>2</sub>O<sub>4</sub> semiconductor was held biased at -0.05 V under UV-vis illumination for different time gaps: 0 s (black plot), 45 s (blue plot) and 3 min (red plot). The linear relationship between biased semiconductor illumination time and peak current for CO detection at  $\approx 0.4$  V shown in the inset of Figure 4.8c demonstrated that CO was continuously generated and accumulated in the gap between the dual tip and the substrate, as long as simultaneous bias potential and illumination were applied to CuCo<sub>2</sub>O<sub>4</sub>. In conclusion, CO was the main detectable photoelectrochemically generated product. This clearly demonstrated that CO<sub>2</sub>RR was taking place to form CO when a CuCo<sub>2</sub>O<sub>4</sub> spot was illuminated under UV-vis light and biased at -0.05 V. Finally, comparing the two consecutive scans shown in Figure 4.8d (3 min of CO accumulation), it is evident that collection time and resting potential of Pt UME tip were key parameters to reach CO detection.

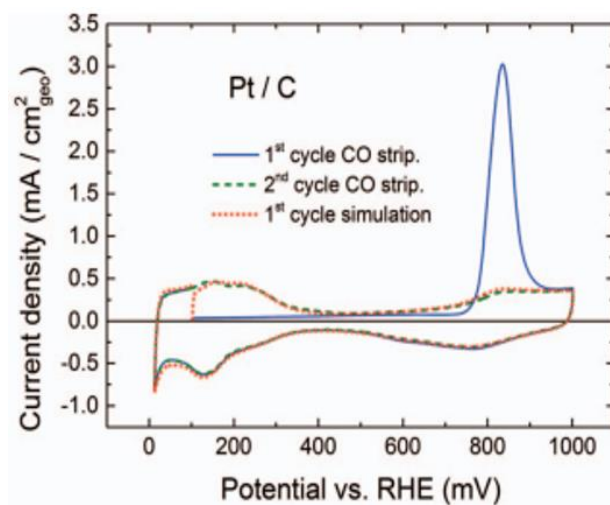


Figure 4.7 CO stripping CV and CO stripping simulation-CV of the Pt/C catalyst in 0.1 M HClO<sub>4</sub> at 20 mV/s. The CO stripping simulation-CV is performed after holding the potential at 0.1 V vs. RHE for 40 min in N<sub>2</sub> purged electrolyte [8]. Scan rate 20 mV/s.

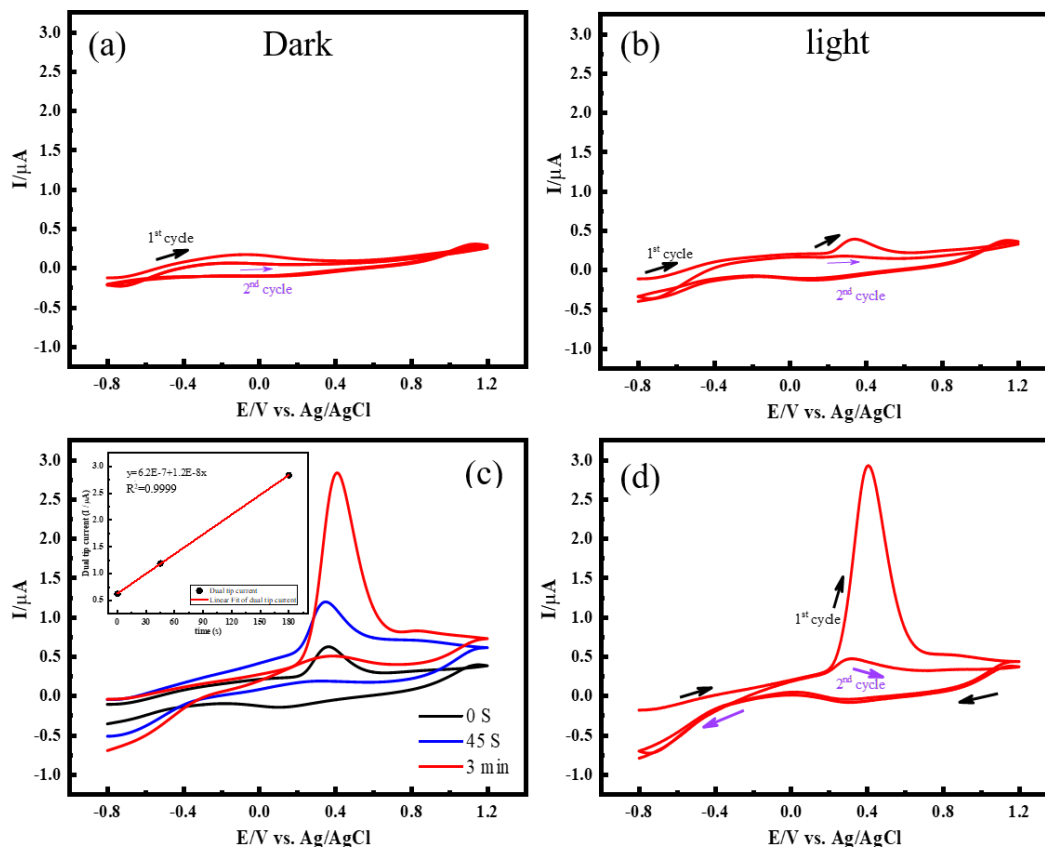


Figure 4.8 Cyclic voltammograms of the OF-UME (Pt) for detection of products generated from PEC  $\text{CO}_2\text{RR}$  in 25 vol.%  $[\text{C}_2\text{mim}][\text{BF}_4]/\text{H}_2\text{O}$  saturated with  $\text{CO}_2$ , pH = 4: (a) Two consecutive CVs on the tip in dark,  $E_{\text{sub}} = \text{OCP}$ ; (b) Two consecutive CVs on the tip, meanwhile  $\text{CuCo}_2\text{O}_4$  was held biased at  $-0.05 \text{ V vs. Ag/AgCl}$  under UV-vis illumination ( $I_{\text{photo}} = -1.3 \times 10^{-5} \sim -0.9 \times 10^{-5} \text{ A}$ ), (c) Independent CVs on the tip, meanwhile  $\text{CuCo}_2\text{O}_4$  was held biased at  $-0.05 \text{ V vs. Ag/AgCl}$  under UV-vis illumination for different time gaps (0 s, 45 s and 3 min) ( $I_{\text{photo}} = -1.1 \times 10^{-5} \sim -0.6 \times 10^{-5} \text{ A}$ ). Inset corresponds to the linear relationship between oxidation peak current at  $\approx 0.4 \text{ V}$  and biased  $\text{CuCo}_2\text{O}_4$  illumination time, (d) Two consecutive CVs on the tip after  $\text{CuCo}_2\text{O}_4$  was held biased at  $-0.05 \text{ V vs. Ag/AgCl}$  under UV-vis illumination for 3 min ( $I_{\text{photo}} = -0.7 \times 10^{-5} \sim -0.6 \times 10^{-5} \text{ A}$ ). All CVs were at a scan rate:  $1 \text{ V/s}$ . The potential limits were  $-0.8$  to  $1.2 \text{ V vs. Ag/AgCl}$ , initiated from  $-0.8 \text{ V}$ ; tip-substrate distance =  $20 \mu\text{m}$ .

Figure 4.9 demonstrated that the CO produced from PEC  $\text{CO}_2\text{RR}$  could remain within the dual tip-substrate gap for a significant period of time. A series of 9 consecutive, but independent 2 scans cyclic voltammograms on the OF-UME (Pt) tip located at  $20 \mu\text{m}$  above the substrate in  $\text{CO}_2$  saturated 25 vol.%  $[\text{C}_2\text{mim}][\text{BF}_4]/\text{H}_2\text{O}$  was registered. Only the first scan of each voltammogram was represented in Figure 4.9 for comparing the evolution of CO oxidation peak current at  $\approx 0.4 \text{ V}$ . Thus, CO oxidation peak current increased continuously

when  $\text{CuCo}_2\text{O}_4$  semiconductor was biased and under UV-vis illumination, Figure 4.9a (blue plots in scans 1, 3, 5, 7 and 9). However, CO oxidation peak current did not show a sharp decay in scan 11 of Figure 4.9b (red plot), in spite of the fact that no illumination was provided to the semiconductor at that moment. In contrast, scans 13, 15 and 17 in Figure 4.9b (red plots) exhibited a clear diminution and finally negligible CO oxidation current. This demonstrated that the narrow gap formed between the dual tip and the substrate electrode blocked products diffusion and then CO remained in the gap until total depletion during dark voltammograms.

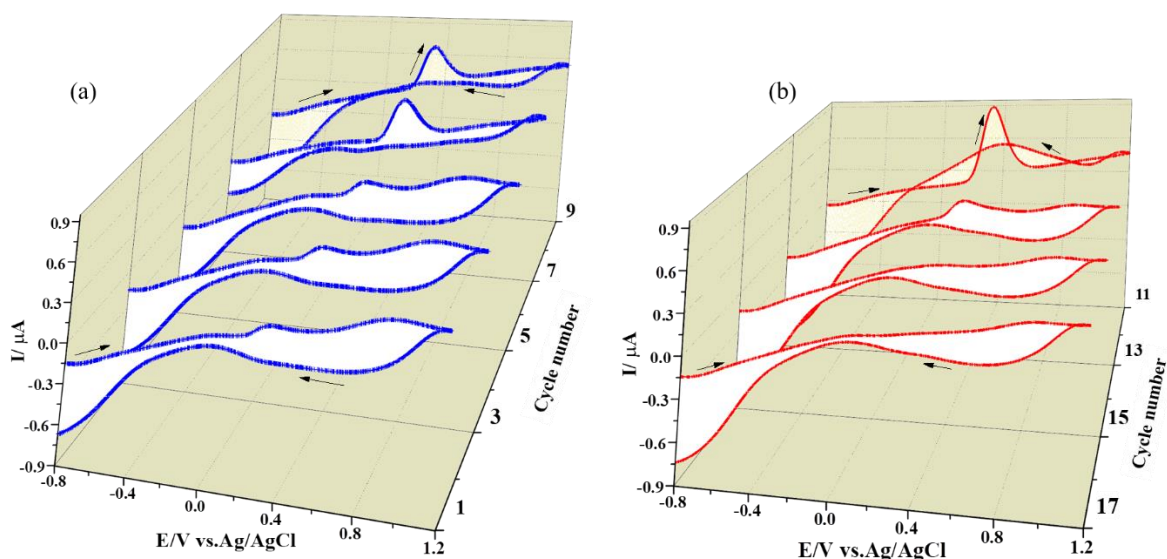


Figure 4.9 Only the first scan of a series of consecutive, but independent 2 scans cyclic voltammograms (scan number 1, 3, 5, 7, 9, 11, 13, 15 and 17) of the OF-UME (Pt) in  $\text{CO}_2$  saturated 25 vol.%  $[\text{C}_2\text{mim}][\text{BF}_4]/\text{H}_2\text{O}$  is presented here. (a, blue plot) illuminated under UV-vis light,  $E_{\text{sub}} = -0.05 \text{ V}$  ( $I_{\text{photo}} = -0.7 \times 10^{-5} - -0.5 \times 10^{-5} \text{ A}$ ); (b, red plot) dark,  $E_{\text{sub}} = \text{OCP}$ . All CVs were at a scan rate:  $1 \text{ V/s}$ . The potential limits were  $-0.8$  to  $1.2 \text{ V vs. Ag/AgCl}$ , initiated from  $-0.8 \text{ V}$ . Tip-substrate distance =  $20 \mu\text{m}$ .

#### 4.3.3. Bulk Electrolysis and Products Analysis by Chromatography

CO detection was further supported by bulk electrolysis. For that purpose, several bulk electrolysis under illumination were carried out to analyze the reaction products from the photocurrent generated on  $\text{CuCo}_2\text{O}_4$  spots in the presence of  $\text{CO}_2$  and 25 vol.%  $[\text{C}_2\text{mim}][\text{BF}_4]/\text{H}_2\text{O}$  solution as solvent-supporting electrolyte system. The experimental configuration and the operating steps were described in chapter 2.8.

The bulk electrolysis under illumination were carried out under different conditions: at OCP and different applied potentials. Some of the photocurrent results obtained as a function

of electrolysis duration were shown in Figure 4.10, the corresponding parameters including Faradaic efficiencies (FE) for various products and the comparison of a similar case reported in literature were listed in Table 4.2.

In Figure 4.10a, the currents obtained in bulk electrolysis with and without illumination at  $-0.35$  V vs. Ag/AgCl were compared, the electrolysis duration were 2 h (light) and 5 min (dark), respectively. The current generated after 5 min without illumination ( $-10.6$   $\mu$ A) is half of that produced when semiconductor illumination was taking place for 5 min ( $-20.9$   $\mu$ A), which confirmed the presence of a photocatalytic process.

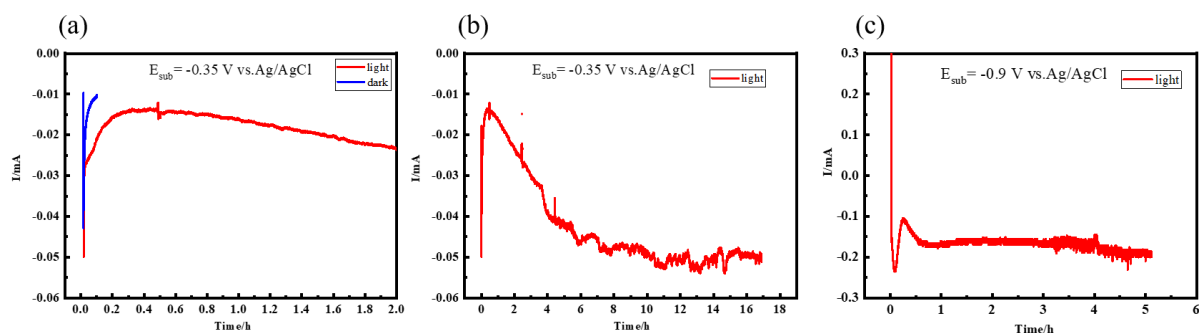


*Figure 4.10 (a) Comparison of photocurrent during electrolysis entry 2 without illumination for 5 min (blue) and with illumination for 2 h;  $E_{sub} = -0.35$  V vs. Ag/AgCl; (b) Photocurrent evolution during electrolysis entry 2 for 17 h,  $E_{sub} = -0.35$  V vs. Ag/AgCl, illuminated; (c) Photocurrent evolution during electrolysis entry 4 for 5 h,  $E_{sub} = -0.9$  V vs. Ag/AgCl, illuminated.*

The results of bulk electrolysis performed on high-density arrays of  $\text{CuCo}_2\text{O}_4$  spots were shown in Table 4.2. In particular, CO production was confirmed by gas chromatography in several electrolysis. For instance, under UV-vis illumination for 17 h at photovoltage (0 V, entry 1) and biased potential at  $-0.35$  V vs. Ag/AgCl (entry 2). However, only 25% of the CO quantified in entry 2 was detected in entry 1. This fact confirmed that PEC  $\text{CO}_2\text{RR}$  could be UV light driven, but the CO production was significantly increased when an external potential bias was imposed to the semiconductor. In addition to this,  $\text{H}_2$  production from HER was only detected under biased conditions (entries 2 (3.2%), 3 (19.6%) and 4 (31.6%)) and those electrolysis results demonstrated that applying more negative potentials generated larger photocurrents (Figure 4.10 and Table 4.1), but provoked activation of HER and deactivation of CO production from  $\text{CO}_2\text{RR}$ . The maximum FE achieved for CO production was 2.5% at  $-0.6$  V vs. Ag/AgCl, where almost no overpotential was applied (40 mV, see Table 4.2)). This FE value was close to the value reported in the literature (entry 5, Table 4.2) for CO production

on FeS<sub>2</sub> under UV-vis illumination, but in our case only applying 40 mV instead of 400 mV of overpotential.

Comparison of different photocurrent density achieved in bulk electrolysis under different potentials was reported in Table 4.1. Geometrical surface area of WE in solution: 1.54 cm<sup>2</sup>, CuCo<sub>2</sub>O<sub>4</sub> weight on each high-density array supported on FTO: 0.5 mg.

*Table 4.1 Comparison of different current density in bulk electrolysis under different potentials. Geometrical surface area of WE in solution: 1.54 cm<sup>2</sup>, semiconductor spots weight: 0.5 mg.*

	E <sub>sub</sub> = -0.35 V	E <sub>sub</sub> = -0.6 V	E <sub>sub</sub> = -0.9 V
Current density	-33 μA/cm <sup>2</sup>	-39 μA/cm <sup>2</sup>	-120 μA/cm <sup>2</sup>
	-102 μA/mg <sub>semiconductor</sub>	-120 μA/mg <sub>semiconductor</sub>	-372 μA/mg <sub>semiconductor</sub>

*Table 4.2 Comparison of our electrolysis results for CO<sub>2</sub>RR and similar case reported in the literature.*

Entry	Photo-cathode	pH	RTIL	[IL] (M)	E <sub>cat</sub> (V) vs Ag/AgCl	Over-potential (V) <sup>c</sup>	Light (mW/cm <sup>2</sup> )	Q (C)	Time (h)	FE <sub>CO</sub> (%)	FE <sub>HCOOH</sub> (%)	FE <sub>H<sub>2</sub></sub> (%)	Ref
1	CuCo <sub>2</sub> O <sub>4</sub>	4	[C <sub>2</sub> mim][BF <sub>4</sub> ]	1.6	OCP (0)	-0.56	ON 10	-	17	(25% of entry 2)	-	-	This work
2	CuCo <sub>2</sub> O <sub>4</sub>	4	[C <sub>2</sub> mim][BF <sub>4</sub> ]	1.6	-0.35	-0.21	ON 10	2.58	17	1.3	-	3.2	This work
3	CuCo <sub>2</sub> O <sub>4</sub>	4	[C <sub>2</sub> mim][BF <sub>4</sub> ]	1.6	-0.6	+0.04	ON 10	0.33	2	2.5	-	19.6	This work
4	CuCo <sub>2</sub> O <sub>4</sub>	4	[C <sub>2</sub> mim][BF <sub>4</sub> ]	1.6	-0.9	+0.34	ON 10	3.08	5	0.4	-	31.6	This work
5	FeS <sub>2</sub>	5.7	Imidazole	0.01 <sup>a</sup>	-1.1 <sup>b</sup>	+0.40	ON 890	-	-	2.4	4.9	Detected but not quantified	[9]

<sup>a</sup> 0.5 M KCl is used as additional supporting electrolyte.

<sup>b</sup> Applied potential versus SCE.

<sup>c</sup> Overpotential calculated for CO<sub>2</sub> reduction to CO.

All electrolysis experiments were performed in a three-compartment porous glass frit divided cell.

The thermodynamic potentials for HER (Equation 4-1), CO formation (Equation 4-2) and HCOOH formation (Equation 4-3) at pH = 4 (pH in 25 vol.% [C<sub>2</sub>mim][BF<sub>4</sub>] solution) are shown in Table 4.3. The electrolysis results at OCP and -0.35 V vs Ag/AgCl shown in Table 4.2 (entries 1 and 2) exhibited the formation CO at potentials more positive than the thermodynamic value (0.56 V and 0.21 V more positive than thermodynamic potential for CO production, respectively), which clearly pointed out that direct CO<sub>2</sub> reduction on the electrode surface was not the mechanism taking place and that CO was underpotential

photoelectrochemically produced [10]. Thus, we proposed a possible reaction scheme for the PEC CO<sub>2</sub>RR mediated by [C<sub>2</sub>mim]<sup>+</sup>.

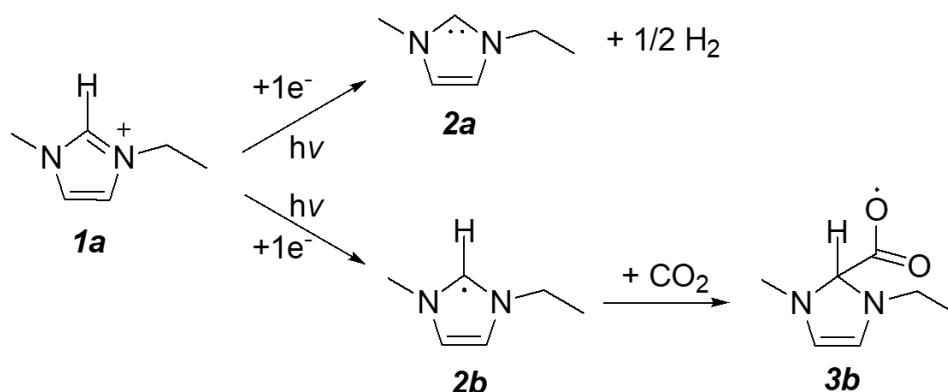
*Table 4.3 Thermodynamic potentials for direct electrochemical reduction of CO<sub>2</sub> and hydrogen evolution reaction (HER) in 25 vol.% [C<sub>2</sub>mim][BF<sub>4</sub>] solution in H<sub>2</sub>O (pH = 4).*

	E <sup>0</sup> (H <sup>+</sup> /H <sub>2</sub> )	E <sup>0</sup> (CO <sub>2</sub> /CO)	E <sup>0</sup> (CO <sub>2</sub> /HCOOH)
pH = 0	0.00 V vs. RHE	-0.12 V vs. RHE	-0.20 V vs. RHE
pH = 4	-0.24 V vs. RHE	-0.36 V vs. RHE	-0.44 V vs. RHE
pH = 4	-0.44 V vs. Ag/AgCl	-0.56 V vs. Ag/AgCl	-0.64 V vs. Ag/AgCl

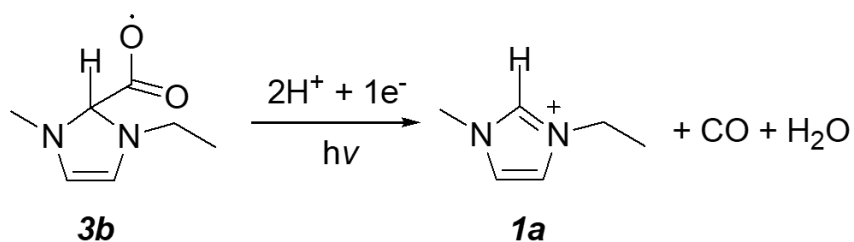


The electrochemical reduction of [C<sub>2</sub>mim]<sup>+</sup> have been already demonstrated on Pt single crystals [11,12]. Two possible pathways have been proposed (Figure 4.11): Either the formation of the imidazolium carbene (**2a**) when a very negative potential is applied, which allows electrochemical reduction and simultaneous hydrogen abstraction from the imidazolium molecule, or the formation of the imidazolium radical (**2b**) at moderate cathodic potentials. Our results show CO<sub>2</sub> photoelectrochemical reduction taking place near open circuit potential and for this reason, we preferentially consider the reaction of CO<sub>2</sub> with the imidazolium radical (**2b**) to form an imidazolium carboxylate radical as the activated CO<sub>2</sub> intermediate (**3b**), which was initially proposed from DFT calculations [13] and have been recently detected by Raman spectroscopy on Cu electrodes [14]. Then, the imidazolium carboxylate radical is further reduced to yield CO and to regenerate the initial 1,3-dialkylimidazolium cation (**1a**) [13]. Nevertheless, some controversy is still going on regarding the exact nature of the activated CO<sub>2</sub> intermediate, since some other reports in the literature suggested the formation of imidazolium carboxylate (**3a**) formed between the carbene (**2a**) and CO<sub>2</sub> as a key intermediate for imidazolium mediated CO<sub>2</sub> reduction [9,15]. We support the formation of activated CO<sub>2</sub> intermediate (**3b**) because imidazolium carboxylate (**3a**) is not an electroactive species under those conditions [11,16].

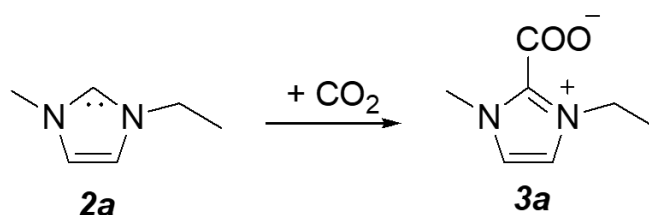




Scheme 1



Scheme 2



Scheme 3

Figure 4.11 Photoelectrochemical imidazolium mediated  $CO_2$  reduction pathway in aqueous solutions.

UV-vis light irradiation of the p-type semiconductor electrode surface plays a major role on achieving effective underpotential  $CO_2RR$  [17]. Actually, entry 1 in Table 4.2 exhibits  $CO$  formation only using the light-induced photovoltage (0 V vs. Ag/AgCl), which is established on the semiconductor electrode upon illumination. In contrast, entries 2, 3 and 4 also include an external cathodic bias to drive faster the  $CO_2RR$ . It is well-known that all imidazolium based RTILs are characterized by significant light absorption in the entire UV region and a long absorption tail that extends into the visible region [18]. These absorption characteristics are attributed to the imidazolium moiety and might be responsible for the formation of imidazolium radical (**2b**) as is described by Shkrob *et al.* [19]. In addition to this, photolysis of

a similar imidazolium carboxylate to **3a** and **3b** for producing CO has been recently reported in the literature [20].

Finally, surface-adsorbed electrogenerated CO from CO<sub>2</sub>RR has been recently detected at very low overpotential by in situ sum-frequency generation (SFG) spectroscopy on Pt electrodes using [C<sub>2</sub>mim][BF<sub>4</sub>] and 1.5 M H<sub>2</sub>O as solvent [15]. A strong dependence of the CO intensity on the applied potential is also reported. Actually, the CO band decreases by increasing the cathodic potential applied due to the competing HER, which perfectly fits the behavior reported in our electrolysis (Table 4.2). In contrast, no CO was detected when using either [C<sub>4</sub>mim][BF<sub>4</sub>] or [C<sub>8</sub>mim][BF<sub>4</sub>] with 1.5 M H<sub>2</sub>O as a solvent. This is probably due to the higher hydrophobicity of [C<sub>4</sub>mim]<sup>+</sup> and [C<sub>8</sub>mim]<sup>+</sup> cations with respect to [C<sub>2</sub>mim]<sup>+</sup>, which does not allow H<sub>2</sub>O accumulation at the electrode interface. This fact fits also well with our results shown in chapter 3, where much lower photocurrent was collected on CuCo<sub>2</sub>O<sub>4</sub> by SPECM when [C<sub>4</sub>mim][BF<sub>4</sub>] was used in solution instead of [C<sub>2</sub>mim][BF<sub>4</sub>] (see Figure 3.24).

#### 4.4. Conclusions

In conclusion, CO was the main detectable photoelectrochemically generated product. CO production was electrochemically detected by the home-made dual tip OF-UME in SPECM configuration. The dual tip was located in close proximity of the CuCo<sub>2</sub>O<sub>4</sub> semiconductor (20 μm) and detection was done by fast cyclic voltammetry in CO<sub>2</sub> saturated 25 vol.% [C<sub>2</sub>mim][BF<sub>4</sub>]/H<sub>2</sub>O solution under UV-vis illumination. The linear relationship reported between biased semiconductor illumination time and peak current for CO detection at ≈ 0.4 V demonstrated that CO was continuously generated and accumulated in the gap between the dual tip and the substrate, as long as simultaneous bias potential and illumination were applied to CuCo<sub>2</sub>O<sub>4</sub>. Thus, a clear oxidation peak centered at 0.4 V only appeared under illumination and it was assigned to the CO<sub>ads</sub> stripping oxidation.

Additionally, CO detection was further supported by bulk electrolysis. The results of bulk electrolysis, performed on high density arrays of CuCo<sub>2</sub>O<sub>4</sub> spots, confirmed CO production by gas chromatography in several electrolysis including biased and unbiased semiconductor under UV-vis illumination. Those results also demonstrated that applying more negative potentials generated larger photocurrents, but provoked activation of HER and deactivation of CO production from CO<sub>2</sub>RR. The maximum FE achieved for CO production was 2.5% at -0.6 V

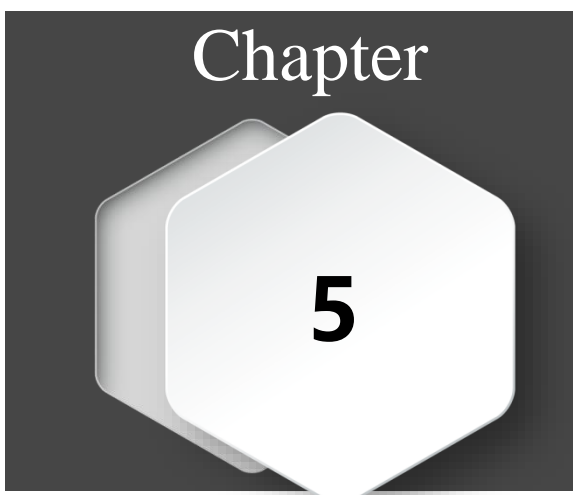
vs. Ag/AgCl. In particular, the electrolysis results at OCP and -0.35 V vs Ag/AgCl exhibited the formation CO at potentials more positive than the thermodynamic value, which clearly pointed out that direct CO<sub>2</sub> reduction on the electrode surface was not the mechanism taking place and that CO was underpotential photoelectrochemically produced. Thus, we proposed a possible reaction scheme for the PEC CO<sub>2</sub>RR mediated by [C<sub>2</sub>mim]<sup>+</sup>.

## 4.5. References

- [1] Y. Lee, Z. Ding, A.J. Bard, Combined scanning electrochemical/optical microscopy with shear force and current feedback, *Anal. Chem.* 74 (2002) 3634–3643. <https://doi.org/10.1021/ac015713u>.
- [2] S.K. Cho, H.S. Park, H.C. Lee, K.M. Nam, A.J. Bard, Metal doping of BiVO<sub>4</sub> by composite electrodeposition with improved photoelectrochemical water oxidation, *J. Phys. Chem. C.* 117 (2013) 23048–23056. <https://doi.org/10.1021/jp408619u>.
- [3] F. Conzuelo, K. Sliozberg, R. Gutkowski, S. Grützke, M. Nebel, W. Schuhmann, High-resolution analysis of photoanodes for water splitting by means of scanning photoelectrochemical microscopy, *Analytical Chemistry*. 89 (2017) 1222–1228. <https://doi.org/10.1021/acs.analchem.6b03706>.
- [4] V. Badets, G. Loget, P. Garrigue, N. Sojic, D. Zigah, Combined local anodization of titanium and scanning photoelectrochemical mapping of TiO<sub>2</sub> spot arrays, *Electrochimica Acta*. 222 (2016) 84–91. <https://doi.org/10.1016/j.electacta.2016.10.151>.
- [5] J.V. Perales-Rondón, E. Herrero, J. Solla-Gullón, C.M. Sánchez-Sánchez, V. Vivier, Oxygen crossover effect on palladium and platinum based electrocatalysts during formic acid oxidation studied by scanning electrochemical microscopy, *Journal of Electroanalytical Chemistry*. 793 (2017) 218–225. <https://doi.org/10.1016/j.jelechem.2016.12.049>.
- [6] G.A. El-Nagar, A.M. Mohammad, M.S. El-Deab, B.E. El-Anadouli, Novel fuel blends facilitating the electro-oxidation of formic acid at a nano-Pt/GC electrode, *RSC Adv.* 6 (2016) 29099–29105. <https://doi.org/10.1039/C6RA00118A>.
- [7] N. Sreekanth, K.L. Phani, Selective reduction of CO<sub>2</sub> to formate through bicarbonate reduction on metal electrodes: new insights gained from SG/TC mode of SECM, *Chem. Commun.* 50 (2014) 11143–11146. <https://doi.org/10.1039/C4CC03099K>.
- [8] T. Binninger, E. Fabbri, R. Kötz, T.J. Schmidt, Determination of the electrochemically active surface area of metal-oxide supported platinum catalyst, *J. Electrochem. Soc.* 161 (2014) H121–H128. <https://doi.org/10.1149/2.055403jes>.
- [9] A.B. Bocarsly, Q.D. Gibson, A.J. Morris, R.P. L’Esperance, Z.M. Detweiler, P.S. Lakkaraju, E.L. Zeitler, T.W. Shaw, Comparative study of imidazole and pyridine catalyzed reduction of carbon dioxide at illuminated iron pyrite electrodes, *ACS Catal.* 2 (2012) 1684–1692. <https://doi.org/10.1021/cs300267y>.
- [10] E.E. Barton, D.M. Rampulla, A.B. Bocarsly, Selective solar-driven reduction of CO<sub>2</sub> to methanol using a catalyzed p-GaP based photoelectrochemical cell, *J. Am. Chem. Soc.* 130 (2008) 6342–6344. <https://doi.org/10.1021/ja0776327>.
- [11] F.A. Hanc-Scherer, M.A. Montiel, V. Montiel, E. Herrero, C.M. Sánchez-Sánchez, Surface structured platinum electrodes for the electrochemical reduction of carbon dioxide

- in imidazolium based ionic liquids, *Physical Chemistry Chemical Physics*. 17 (2015) 23909–23916. <https://doi.org/10.1039/c5cp02361k>.
- [12] A.M. Navarro-Suárez, J.C. Hidalgo-Acosta, L. Fadini, J.M. Feliu, M.F. Suárez-Herrera, Electrochemical oxidation of hydrogen on basal plane platinum electrodes in imidazolium ionic liquids, *The Journal of Physical Chemistry C*. 115 (2011) 11147–11155. <https://doi.org/10.1021/jp201886m>.
- [13] Y. Wang, M. Hatakeyama, K. Ogata, M. Wakabayashi, F. Jin, S. Nakamura, Activation of CO<sub>2</sub> by ionic liquid EMIM-BF<sub>4</sub> in the electrochemical system: a theoretical study, *Phys. Chem. Chem. Phys.* 17 (2015) 23521–23531. <https://doi.org/10.1039/C5CP02008E>.
- [14] Y. Wang, T. Hayashi, D. He, Y. Li, F. Jin, R. Nakamura, A reduced imidazolium cation layer serves as the active site for electrochemical carbon dioxide reduction, *Applied Catalysis B: Environmental*. 264 (2020) 118495. <https://doi.org/10.1016/j.apcatb.2019.118495>.
- [15] B. Ratschmeier, A. Kemna, B. Braunschweig, Role of H<sub>2</sub>O for CO<sub>2</sub> reduction reactions at platinum/electrolyte interfaces in imidazolium room-temperature ionic liquids, *ChemElectroChem*. 7 (2020) 1765–1774. <https://doi.org/10.1002/celec.202000316>.
- [16] S.-F. Zhao, M. Horne, A.M. Bond, J. Zhang, Is the imidazolium cation a unique promoter for electrocatalytic reduction of carbon dioxide?, *J. Phys. Chem. C*. 120 (2016) 23989–24001. <https://doi.org/10.1021/acs.jpcc.6b08182>.
- [17] J.L. White, M.F. Baruch, J.E. Pander, Y. Hu, I.C. Fortmeyer, J.E. Park, T. Zhang, K. Liao, J. Gu, Y. Yan, T.W. Shaw, E. Abelev, A.B. Bocarsly, Light-driven heterogeneous reduction of carbon dioxide: photocatalysts and photoelectrodes, *Chem. Rev.* 115 (2015) 12888–12935. <https://doi.org/10.1021/acs.chemrev.5b00370>.
- [18] A. Paul, P.K. Mandal, A. Samanta, On the optical properties of the imidazolium ionic liquids, *J. Phys. Chem. B*. 109 (2005) 9148–9153. <https://doi.org/10.1021/jp0503967>.
- [19] I.A. Shkrob, T.W. Marin, S.D. Chemerisov, J.F. Wishart, Radiation induced redox reactions and fragmentation of constituent ions in ionic liquids. 1. anions, *J. Phys. Chem. B*. 115 (2011) 3872–3888. <https://doi.org/10.1021/jp2003062>.
- [20] M.I. Qadir, M. Zanatta, E.S. Gil, H.K. Stassen, P. Gonçalves, B.A.D. Neto, P.E.N. de Souza, J. Dupont, Photocatalytic reverse semi-combustion driven by ionic liquids, *ChemSusChem*. 12 (2019) 1011–1016. <https://doi.org/10.1002/cssc.201802974>.





## Electrochemical CO<sub>2</sub>RR on Synthesized M–N–Cs Evaluated by RDE

---



## Chapter 5 Electrochemical CO<sub>2</sub>RR on Synthesized M–N–Cs Evaluated by RDE

### 5.1. Introduction

One of the alternatives to mitigate CO<sub>2</sub> accumulation is the electrochemical CO<sub>2</sub>RR, which can convert CO<sub>2</sub> into useful molecules. Many researches focused on studying catalysts for electrochemical CO<sub>2</sub>RR such as metallic, non-metallic and molecular catalysts [1,2]. Nonetheless, there are still many challenges to be addressed to reduce the energy barrier or overpotential of CO<sub>2</sub>RR. In addition, multiple electrons, protons and pathways are involved in the process of CO<sub>2</sub>RR, leading to various and mixing products, which increase the difficulty in controlling the selectivity of CO<sub>2</sub>RR on present electrocatalysts [3]. Efficient electrocatalytic materials with high catalytic efficiency, strong stability and high product selectivity must be further exploited with the purpose of lowering the high overpotential of CO<sub>2</sub>RR, avoiding also the effect of the competitive HER, which negatively affect the selectivity of the reaction toward the target product [4]. Molecular catalysts such as transition metal–nitrogen–carbon complexes (M–N–Cs) exhibit high selectivity, stability and activity, huge catalytic surface area and low-cost for HER or CO<sub>2</sub>RR to C<sub>1</sub> compounds (CO) production. Here M can be monometal (Fe, Cu, Co, Mn, Ni) [5] or bimetallic combination (Mo–Ni–N–C, Fe–Co–N–C) [6,7]. In M–N–Cs materials, metal atoms are coordinated to nitrogen (pyridinic or pyrrolic) forming M–N<sub>x</sub> active sites, which act as catalytic site for CO<sub>2</sub>RR, by either reducing the overpotential or promoting CO formation and reaction rates [8].

Chitosan is a product from partial deacetylation of chitin, the most abundant biopolymer after cellulose [9]. Thanks to the presence of amine groups, it is reported that chitosan can be used as a carbon-nitrogen precursor via pyrolysis and prefer to form N–doped carbon based 2D graphene-like materials in literature [10]. Owing to high specific surface area, chitosan has been adopted to form complexes with metals ions and dope with hybrid atoms such as nitrogen and sulfur [11]. The basicity of the surface improves capacitive behavior and catalytic activity [12]. The addition of metal salts into the N–doped carbon materials leads to the metal aggregation impeded in the structure, which are promising alternatives to metallic catalysts on electrochemical CO<sub>2</sub>RR. It has been widely accepted that the primary active sites are the M–



N<sub>x</sub> moieties since the presence of metal dramatically increases the catalytic activity of CO<sub>2</sub>RR. However, the N–C moieties were also proved to be active on CO<sub>2</sub> conversion to CO and HCOOH etc. [13]. Furthermore, the carbon structure also has effect on the catalytic activity, for example, porous structure can minimize the mass transport limitations of electroactive species [14]. Hence, acquisition of desirable carbon structure by tuning the starting precursor and the synthesis conditions is of vital importance.

Rotating disk electrode (RDE), working as a hydrodynamic working electrode, is one of the few convective electrode systems for which the hydrodynamic equations and the convective-diffusion equation have been solved rigorously for the steady state [15]. RDE provides good reproducibility and stable polarization curve because the diffusion layer thickness is controlled by the rotation speed. What's more, the RDE system can reach the steady state very fast thanks to the electrode rotation. As a result, it is widely used in different electrochemical fields [16,17].

In this thesis, chitosan was adopted as a nitrogen-carbon precursor via pyrolysis to synthesize N-doped-carbon materials, which has numerous nitrogen-doped groups. With the addition of metal salts precursors (Fe, Co, Cu, Mn), different M–N–Cs were synthesized including monometal doped materials: Cu–N–C, Co–N–C, Fe–N–C; bimetal doped materials: Fe–Co–N–C, Fe–Cu–N–C, Co–Cu–N–C and Co–Mn–N–C; and metal free–N–C material. These M–N–Cs were evaluated about their performance for electrochemical CO<sub>2</sub>RR with RDE. In addition, NaSCN was used as a probe agent by poisoning the Fe-related moieties to understand the role of active sites in the CO<sub>2</sub>RR.

## 5.2. Results and Discussion

### 5.2.1. Structure Morphology and Composition of M–N–Cs

Figure 5.1 and Figure 5.2 show SEM images, EDS spectra and analysis of M–N–Cs of (a) 25%Fe25%Co–N–C, (b) 50%Fe–N–C and (c) 50%Co–N–C and (d) metal free–N–C, respectively. The primary bulk structure of all the M–N–Cs are constituted of carbon skeleton with huge amount of N and K atoms which were originated from the added KOH during synthesis in order to increase the surface area of the catalysts, reflected by the high peaks and atom percentages (at%) in most of the EDS spectra and element analysis. 25%Fe25%Co–N–C shows sponge structure with numerous microcubes with an average side length of 200 nm

uniformly distributed and well-dispersed (Figure 5.1a), in which Fe content is much higher compared to that of the bulk structure (Figure 5.2b and Figure 5.2a). The similar sponge-like morphology is found in 50%Fe–N–C (Figure 5.1b) yet no microcube is present therein. Furthermore, the Fe content in 50%Fe–N–C (Figure 5.2c) is less than the bimetallic combination 25%Fe25%Co–N–C. The pores of micrometric dimension maybe caused by the decomposition of the organic precursor [18] and the addition of the KOH. In comparison, the morphology of 50%Co–N–C shows stacked cluster with rough surface (Figure 5.1c) whereas the metal free–N–C displays entangled flakes formed microporous morphology (Figure 5.1d). In addition, the Co content (Figure 5.2d) is even less than that of both 25%Fe25%Co–N–C and 50%Fe–N–C. The reason for the low content of Co in any kind of M–N–Cs is that the high solubility of Co salt precursor led to a high concentration in the liquid supernatant which was discarded in the synthesis process.

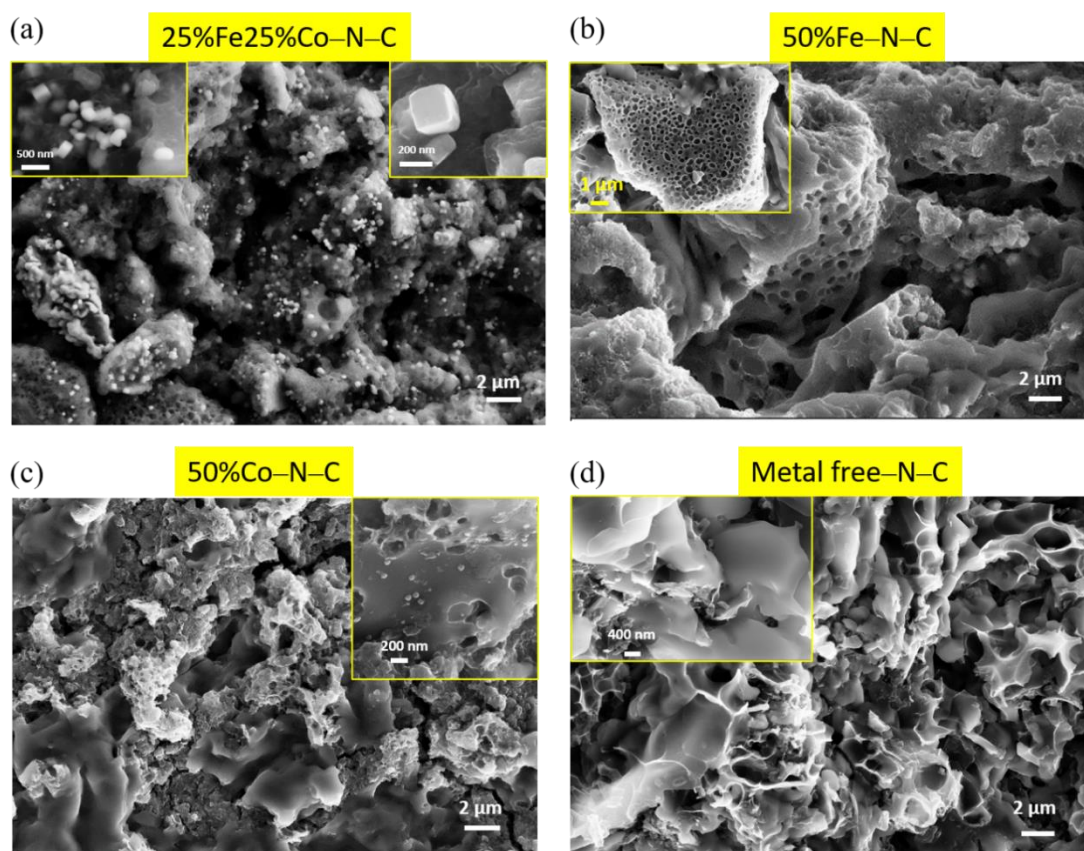


Figure 5.1 SEM images of different M–N–C catalysts: (a) 25%Fe25%Co–N–C, (b) 50%Fe–N–C and (c) 50%Co–N–C and (d) metal free–N–C. The inset images are the magnification of the corresponding SEM image.

The sponge-like and porous nature with of the M–N–Cs is favorable for the transport of CO<sub>2</sub> to and gas products out of the active sites, in particularly in the reactions where the rate determine step is the CO<sub>2</sub> diffusion form bulk electrolyte towards the active sites. It was reported that carbon nanotubes grew in the fiber surface with the presence of Fe and Co, while no obvious growth of carbon nanotubes were observed over individual Fe or Co metal particles catalysts, strongly suggesting the synergetic effect between Fe and Co components [7]. In our system, the presence of Co provided synergic effect for the generation of these microcubes, which acted as active sites in electrochemical CO<sub>2</sub>RR and illustrate the better performance for the bimetal doped carbon materials. The different morphology of M–N–Cs implied the different catalysis performance of CO<sub>2</sub>RR.

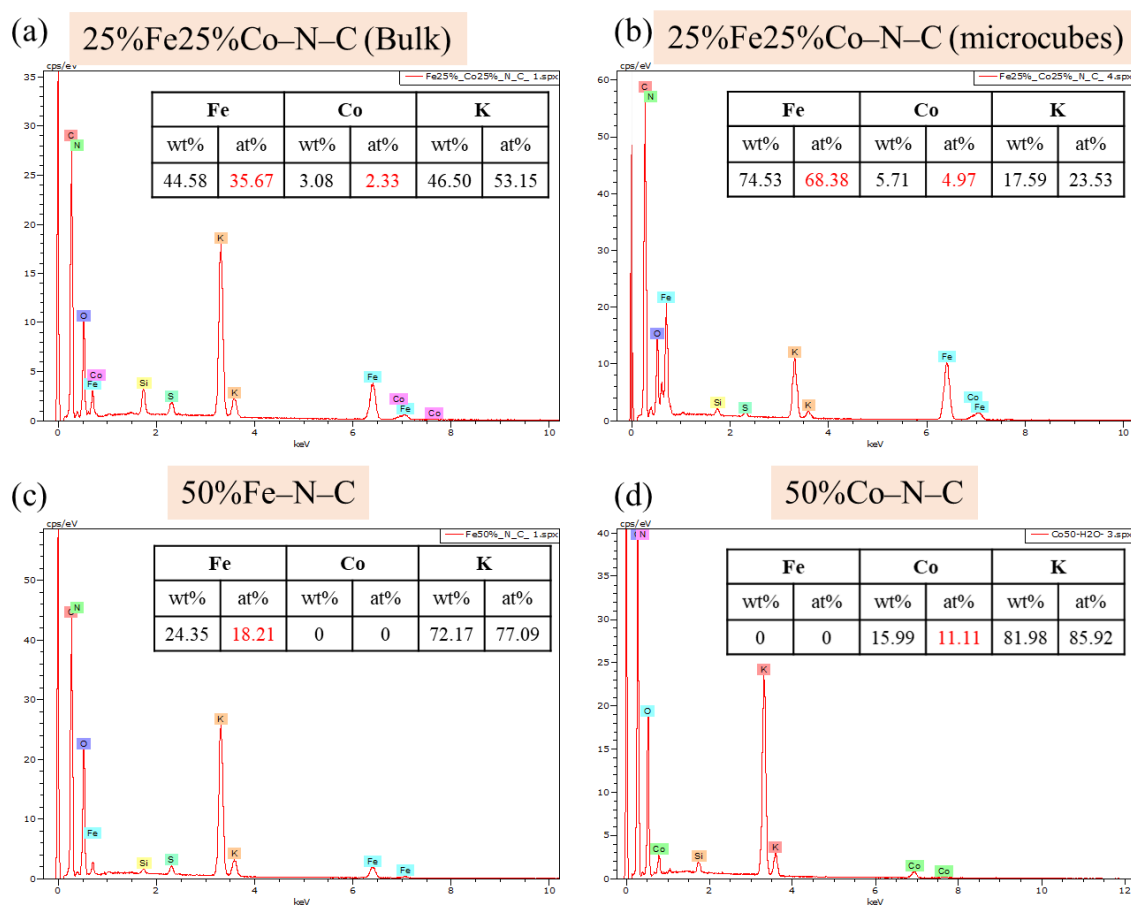


Figure 5.2 EDS spectrum and metal content analysis of the bulk M–N–Cs: (a) and (b) were obtained in the bulk and the microcubes of 25%Fe25%Co–N–C, respectively. (c) 50%Fe–N–C and (d) 50%Co–N–C.

### 5.2.2. Comparison of M–N–Cs on Electrochemical CO<sub>2</sub>RR Performance

The combination of Cu and Co was introduced in chapter 3 in the form of p-type semiconductor material CuCo<sub>2</sub>O<sub>4</sub>, which was illustrated to be a good PEC catalyst for PEC CO<sub>2</sub>RR evaluated by SPECM. The bimetallic 25%Cu25%Co–N–C was synthesized to study its catalytic activity towards electrochemical CO<sub>2</sub>RR. First of all, CVs were performed to evaluate its electrochemical properties. Figure 5.3 shows the comparison of CVs of (a) 25%Cu25%Co–N–C, (b) 50%Cu–N–C and (c) 50%Co–N–C in 0.1 M NaHCO<sub>3</sub> saturated with N<sub>2</sub>. In Figure 5.3a, two anodic faradaic processes are shown at 0.68 V and 1.12 V vs. RHE, and the two cathodic processes at 0.59 V and 0.09 V vs. RHE, respectively. The voltammograms recorded for 50%Cu–N–C (Figure 5.3c), shows similar faradaic anodic and cathodic process at the same potentials. Nevertheless, 50%Co–N–C doesn't exhibit these characteristic peaks (Figure 5.3b), indicating that the two well defined faradaic process are attributed to the presence of Cu in the catalysts. In Figure 5.3a, the potentials of the second oxidation peak become more positive when the scan rate increases, which means the oxidation process is irreversible. In Figure 5.3d, the relationship between the Faradic current at 0.68 V and the square root of scan rate is mainly linear indicating a diffusion-controlled process.

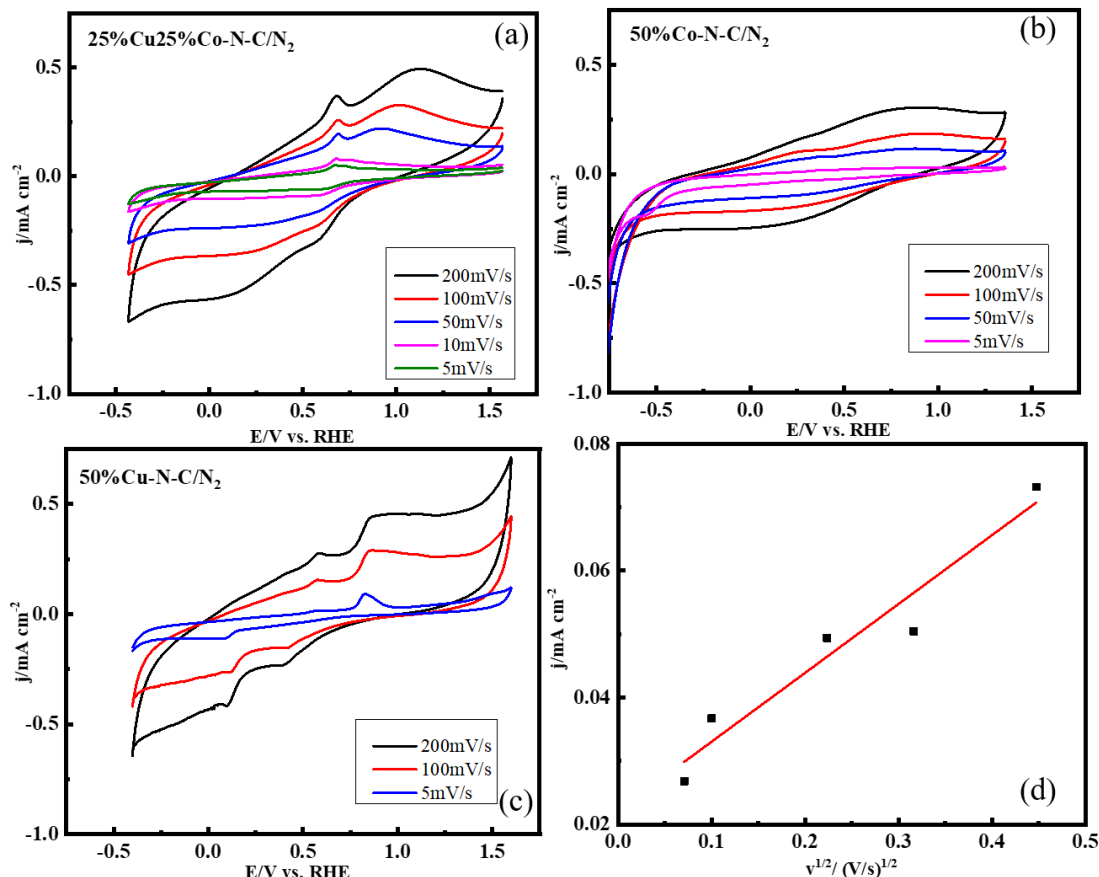


Figure 5.3 Cyclic voltammograms in 0.1 M NaHCO<sub>3</sub> saturated with N<sub>2</sub> under different scan rate with catalyst of (a) 25%Cu25%Co–N–C, (b) 50%Co–N–C and (c) 50%Cu–N–C and (d) plot showing the linear relationship between the oxidation current at 0.68 V vs. RHE and scan rate for 25%Cu25%Co–N–C.

The CO<sub>2</sub>RR catalytic performance of different M–N–Cs was evaluated by LSV with the RDE. As shown in Figure 5.4a, except 25%Cu25%Co–N–C, the catalytic activities of all the other studied M–N–C are remarkably higher than that of the metal free–N–C, as deduced by more positive onset potential and higher current densities (Table 5.1), demonstrating the dramatical activity enhancement by the presence of metal atoms, which is in accordance with the research of Daasbjerg *et al.* [19]. Among all the catalysts, the bimetallic 25%Fe25%Co–N–C and 25%Fe25%Cu–N–C are the most active materials for the electrochemical CO<sub>2</sub>RR with similar catalytic activity and the most positive onset potentials, close to -0.48 V vs. RHE (0.37 mV overpotential for CO<sub>2</sub>/CO) for 25%Fe25%Co–N–C. The shapes of polarization curves for both catalysts are different from the typical sigmoidal shape for the CO<sub>2</sub>RR, since these catalysts present a diffusion-controlled region. After the initial current increase, a short

plateau appears at the potential range of -0.88 ~ -1.03 V and -0.95 ~ -1.02 V for 25%Fe25%Cu–N–C and 25%Fe25%Co–N–C, respectively. These plateau currents are associated with the electrochemical CO<sub>2</sub>RR as can be proposed previously by Baturina *et al.* [20]. After the plateau current, the currents increase monotonically due to the HER. The catalyst 25%Fe25%Co–N–C was regarded with the highest catalytic activity because of higher CO<sub>2</sub> reduction current density at the potential range of -0.42 ~ -1.02 V compared to the others, which will be singled out and explained later in Figure 5.4c. In addition, the catalysts 50%Co–N–C and 50%Fe–N–C and bimetallic 25%Co25%Mn–N–C catalysts present a typical behavior for the CO<sub>2</sub>RR coupled by HER due to the high overpotentials applied, as can be observed previously by Huan's group [21], they proved that this behavior mainly ascribed to proton reduction, which is promising for exploiting materials for generating syngas (H<sub>2</sub>/CO).

In addition, Figure 5.4c shows of the electrochemical CO<sub>2</sub>RR performance of metal free–N–C, Co–N–C, Fe–N–C and bimetal doped 25%Fe25%Co–N–C materials, displaying that the presence bimetallic Fe and Co present more positive onset potential and provides more CO<sub>2</sub> reduction current compared to the others (Table 5.1). This could be associated with the presence of Co, which provided synergic effect for the generation of distributed microcubes in the structure of 25%Fe25%Co–N–C. These nanostructures will act as the active sites in electrochemical CO<sub>2</sub>RR and illustrated better performance for the bimetal doped M–N–C.

In addition, the comparison of the behavior of 25%Fe25%Co–N–C with other N doped carbon materials reported in literature was shown in Table 5.1. For example, Fe–NS–C [22] exhibited a more positive onset potential together with a higher CO<sub>2</sub> reduction current, which represented a better catalytic efficiency than 25%Fe25%Co–N–C. In contrast, the Fe–N–C [22] and Ni–N–C [23] shown a poorer CO<sub>2</sub> reduction performance compared with 25%Fe25%Co–N–C because of more negative onset potentials and lower current, illustrating that 25%Fe25%Co–N–C ranks as a relatively good catalyst among the studied catalyst.

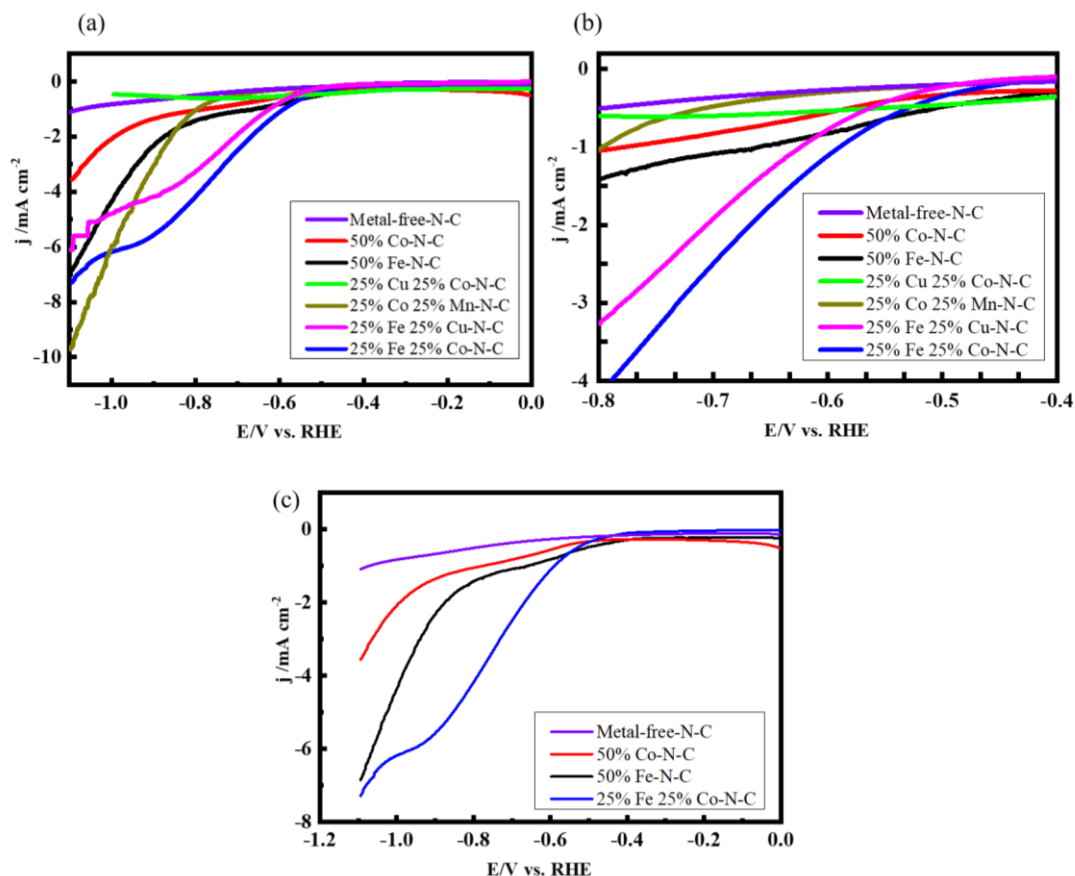


Figure 5.4 (a) Linear scanning voltammograms for different metal containing M–N–Cs in 0.1 M  $\text{KHCO}_3$  saturated with  $\text{CO}_2$ : 50%Fe–N–C, 50%Co–N–C, 25%Fe25%Co–N–C, 25%Co25%Mn–N–C, 25%Fe25%Cu–N–C, 25%Fe25%Cu–N–C and metal free–N–C. (b) is the magnification of LSVs in the potential range of -0.3 V to -0.8 V vs. RHE. (c) Comparison of 50%Fe–N–C, 50%Co–N–C, 25%Fe25%Co–N–C and metal free–N–C in 0.1 M  $\text{KHCO}_3$  saturated with  $\text{CO}_2$ . All the measurements were at 5 mV/s with a rotating speed of 1600 rpm.

Table 5.1 Comparison of onset potential and current density at -0.9 V vs. RHE of different M–N–Cs catalysts used in this thesis (1 ~ 8) and in literature.

	M–N–C	$E_{\text{onset}}$ /V vs. RHE	$j/\text{mA}/\text{cm}^2$ at -0.9V vs. RHE
1	50%Co–N–C	-1.08	-1.4
2	50%Fe–N–C	-0.88	-2.3
3	50%Cu–N–C	n.a.	n.a.
4	25%Fe25%Co–N–C	-0.48	-5.6
5	25%Fe25%Cu–N–C	-0.54	-4.2
6	25%Co25%Mn–N–C	-0.77	-3.1

7	25%Cu25%Co–N–C	inactive	-0.5
8	Metal free–N–C	-1.07	-0.7
[22]	Fe–NS–C	-0.38	-18.5
	Fe–N–C	-0.55	-5.5
[23]	Ni–N–C	-0.72	-1.6

In order to identify the active sites of 25%Fe25%Co–N–C for CO<sub>2</sub>RR, sodium thiocyanate (NaSCN) was used as a poisoning agent to understand the role of Fe, since SCN<sup>−</sup> has high affinity and selectivity with Fe, it can form a complex with Fe and block the Fe–N<sub>x</sub> moieties (act as active sites and play a vital role on the catalytic efficiency) and the iron based nanoparticles, which decreased the catalytic performance of the Fe doped catalyst [24]. We adopted this property of SCN<sup>−</sup> to detect the role of Fe in 25%Fe25%Co–N–C catalyst. The results in Figure 5.5 shown a displacement of the onset potential to negative values and a clear decrease of the reduction current with the presence of NaSCN in the electrolyte, but almost no change was found with the metal free–N–C with or without the presence of the NaSCN, indicating that the Fe and/or the surrounding atoms play the role of the active sites.

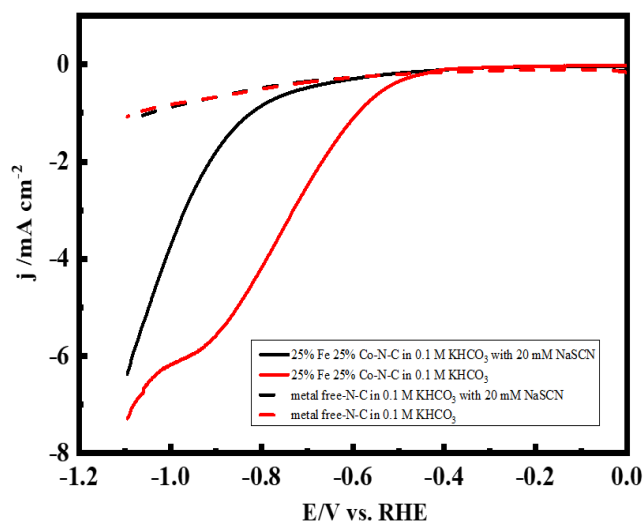


Figure 5.5 Linear scanning voltammograms for 25%Fe25%Co–N–C and metal free–N–C in 0.1 M KHCO<sub>3</sub> saturated with CO<sub>2</sub> with and without the presence of NaSCN. All the measurements were at 5 mV/s with a rotating speed of 1600 rpm.



### 5.3. Conclusions

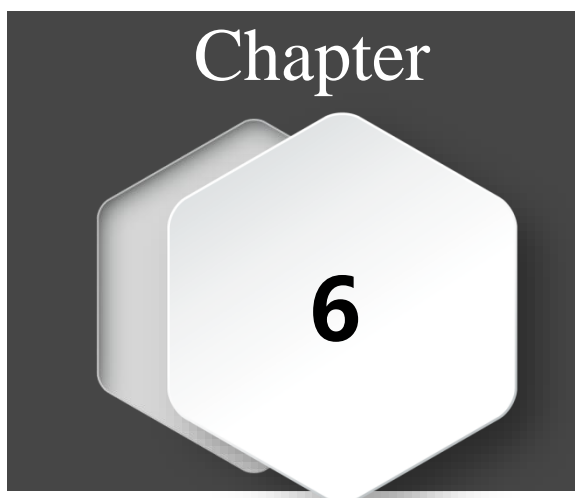
In this thesis, chitosan with the presence of amine groups was adopted as a nitrogen-carbon precursor via pyrolysis to form transition metal–N–carbon materials. With the addition of metal salts precursors (Fe, Co, Cu, Mn), different M–N–Cs were synthesized including Cu–N–C, Co–N–C, Fe–N–C, and bimetal doped 25%Fe25%Co–N–C, 25%Co25%Mn–N–C, 25%Fe25%Cu–N–C, 25%Cu25%Co–N–C and metal free–N–C. LSVs with RDE were used to evaluate the catalytic performance of all M–N–Cs. Except 25%Cu25%Co–N–C, the catalytic activities of all the other studied M–N–Cs are remarkably higher than that of the metal free–N–C, displaying that the presence of metal provoked more positive onset potential and provides more CO<sub>2</sub> reduction current compared to metal free–N–C. Among all the compared M–N–Cs (and metal free–N–Cs), bimetal doped 25%Fe25%Co–N–C exhibited the highest catalytic activity because of more positive onset potential and higher reduction current density. In addition, comparison of the electrochemical CO<sub>2</sub>RR performance of metal free–N–C, Co–N–C, Fe–N–C and bimetal doped 25%Fe25%Co–N–C materials was studied, together with the poisoning of Fe containing moieties by NaSCN, indicating that the Co provided synergic effect for the generation of distributed Fe-rich microcubes only in the structure of 25%Fe25%Co–N–C, which acted as the active sites in electrochemical CO<sub>2</sub>RR and illustrated better performance for the bimetal doped carbon materials.

### 5.4. References

- [1] R.J. Lim, M. Xie, M.A. Sk, J.M. Lee, A. Fisher, X. Wang, K.H. Lim, A review on the electrochemical reduction of CO<sub>2</sub> in fuel cells, metal electrodes and molecular catalysts, *Catalysis Today*. 233 (2014) 169–180. <https://doi.org/10.1016/j.cattod.2013.11.037>.
- [2] Q. Lu, F. Jiao, Electrochemical CO<sub>2</sub> reduction: Electrocatalyst, reaction mechanism, and process engineering, *Nano Energy*. 29 (2016) 439–456. <https://doi.org/10.1016/j.nanoen.2016.04.009>.
- [3] R. Kortlever, J. Shen, K.J.P. Schouten, F. Calle-Vallejo, M.T.M. Koper, Catalysts and reaction pathways for the electrochemical reduction of carbon dioxide, *J. Phys. Chem. Lett.* 6 (2015) 4073–4082. <https://doi.org/10.1021/acs.jpcclett.5b01559>.
- [4] L. Zhang, I. Merino-Garcia, J. Albo, C.M. Sánchez-Sánchez, Electrochemical CO<sub>2</sub> reduction reaction on cost-effective oxide-derived copper and transition metal–nitrogen–carbon catalysts, *Current Opinion in Electrochemistry*. 23 (2020) 65–73. <https://doi.org/10.1016/j.coelec.2020.04.005>.
- [5] F. Pan, W. Deng, C. Justiniano, Y. Li, Identification of champion transition metals centers in metal and nitrogen-codoped carbon catalysts for CO<sub>2</sub> reduction, *Applied Catalysis B: Environmental*. 226 (2018) 463–472. <https://doi.org/10.1016/j.apcatb.2018.01.001>.

- [6] F. Wang, Y. Sun, Y. He, L. Liu, J. Xu, X. Zhao, G. Yin, L. Zhang, S. Li, Q. Mao, Y. Huang, T. Zhang, B. Liu, Highly efficient and durable MoNiNC catalyst for hydrogen evolution reaction, *Nano Energy*. 37 (2017) 1–6. <https://doi.org/10.1016/J.NANOEN.2017.04.050>.
- [7] Q. Liu, S. Cao, Y. Qiu, L. Zhao, Bimetallic Fe-Co promoting one-step growth of hierarchical nitrogen-doped carbon nanotubes/nanofibers for highly efficient oxygen reduction reaction, *Materials Science and Engineering: B*. 223 (2017) 159–166. <https://doi.org/10.1016/j.mseb.2017.06.012>.
- [8] A.S. Varela, N. Ranjbar Sahraie, J. Steinberg, W. Ju, H.-S. Oh, P. Strasser, Metal-doped nitrogenated carbon as an efficient catalyst for direct CO<sub>2</sub> electroreduction to CO and hydrocarbons, *Angewandte Chemie International Edition*. 54 (2015) 10758–10762. <https://doi.org/10.1002/anie.201502099>.
- [9] A. Olejniczak, M. Lezanska, J. Wloch, A. Kucinska, J.P. Lukaszewicz, Novel nitrogen-containing mesoporous carbons prepared from chitosan, *Journal of Materials Chemistry A*. 1 (2013) 8961–8967. <https://doi.org/10.1039/c3ta11337j>.
- [10] A. Primo, P. Atienzar, E. Sanchez, J. María Delgado, H. García, From biomass wastes to large-area, high-quality, N-doped graphene: catalyst-free carbonization of chitosan coatings on arbitrary substrates, *Chemical Communications*. 48 (2012) 9254–9256. <https://doi.org/10.1039/C2CC34978G>.
- [11] S. Basumallick, S. Santra, Chitosan coated copper-oxide nano particles: A novel electro-catalyst for CO<sub>2</sub> reduction, *RSC Advances*. 4 (2014) 63685–63690. <https://doi.org/10.1039/c4ra12696c>.
- [12] D. Lee, M. Jin, D. Oh, S. Lee, J. Park, Straightforward synthesis of hierarchically porous nitrogen-doped carbon via pyrolysis of chitosan/urea/KOH mixtures and its application as a support for formic acid dehydrogenation catalysts, (2017). <https://doi.org/10.1021/acssuschemeng.7b01888>.
- [13] J. Wu, M. Liu, P.P. Sharma, R.M. Yadav, L. Ma, Y. Yang, X. Zou, X.-D. Zhou, R. Vajtai, B.I. Yakobson, J. Lou, P.M. Ajayan, Incorporation of nitrogen defects for efficient reduction of CO<sub>2</sub> via two-electron pathway on three-dimensional graphene foam, *Nano Lett.* 16 (2016) 466–470. <https://doi.org/10.1021/acs.nanolett.5b04123>.
- [14] A.S. Varela, W. Ju, A. Bagger, P. Franco, J. Rossmeisl, P. Strasser, Electrochemical reduction of CO<sub>2</sub> on metal-nitrogen-doped carbon catalysts, *ACS Catalysis*. 9 (2019) 7270–7284. <https://doi.org/10.1021/acscatal.9b01405>.
- [15] A.J. Bard, L.R. Faulkner, J. Leddy, C.G. Zoski, *Electrochemical methods: fundamentals and applications*, Wiley New York, 1980.
- [16] J. Masa, C. Batchelor-McAuley, W. Schuhmann, R.G. Compton, Koutecky-Levich analysis applied to nanoparticle modified rotating disk electrodes: Electrocatalysis or misinterpretation, *Nano Res.* 7 (2014) 71–78. <https://doi.org/10.1007/s12274-013-0372-0>.
- [17] U.A. Paulus, T.J. Schmidt, H.A. Gasteiger, R.J. Behm, Oxygen reduction on a high-surface area Pt/Vulcan carbon catalyst: a thin-film rotating ring-disk electrode study, *Journal of Electroanalytical Chemistry*. 495 (2001) 134–145. [https://doi.org/10.1016/S0022-0728\(00\)00407-1](https://doi.org/10.1016/S0022-0728(00)00407-1).
- [18] A. Roy, D. Hursán, K. Artyushkova, P. Atanassov, C. Janáky, A. Serov, Nanostructured metal-N-C electrocatalysts for CO<sub>2</sub> reduction and hydrogen evolution reactions, *Applied Catalysis B: Environmental*. 232 (2018) 512–520. <https://doi.org/10.1016/j.apcatb.2018.03.093>.

- [19] X.-M. Hu, H.H. Hval, E.T. Bjerglund, K.J. Dalgaard, M.R. Madsen, M.-M. Pohl, E. Welter, P. Lamagni, K.B. Buhl, M. Bremholm, M. Beller, S.U. Pedersen, T. Skrydstrup, K. Daasbjerg, Selective CO<sub>2</sub> reduction to CO in water using earth-abundant metal and nitrogen-doped carbon electrocatalysts, *ACS Catal.* 8 (2018) 6255–6264. <https://doi.org/10.1021/acscatal.8b01022>.
- [20] O.A. Baturina, Q. Lu, M.A. Padilla, L. Xin, W. Li, A. Serov, K. Artyushkova, P. Atanassov, F. Xu, A. Epshteyn, T. Brintlinger, M. Schuette, G.E. Collins, CO<sub>2</sub> electroreduction to hydrocarbons on carbon-supported Cu nanoparticles, *ACS Catal.* 4 (2014) 3682–3695. <https://doi.org/10.1021/cs500537y>.
- [21] T.N. Huan, N. Ranjbar, G. Rousse, M. Sougrati, A. Zitolo, V. Mougel, F. Jaouen, M. Fontecave, Electrochemical reduction of CO<sub>2</sub> catalyzed by Fe–N–C materials: a structure-selectivity study, *ACS Catal.* 7 (2017) 1520–1525. <https://doi.org/10.1021/acscatal.6b03353>.
- [22] F. Pan, B. Li, E. Sarnello, S. Hwang, Y. Gang, X. Feng, X. Xiang, N.M. Adli, T. Li, D. Su, G. Wu, G. Wang, Y. Li, Boosting CO<sub>2</sub> reduction on Fe–N–C with sulfur incorporation: synergistic electronic and structural engineering, *Nano Energy.* 68 (2020) 104384. <https://doi.org/10.1016/j.nanoen.2019.104384>.
- [23] Q. Fan, P. Hou, C. Choi, T.-S. Wu, S. Hong, F. Li, Y.-L. Soo, P. Kang, Y. Jung, Z. Sun, Activation of Ni particles into single Ni–N atoms for efficient electrochemical reduction of CO<sub>2</sub>, *Advanced Energy Materials.* (2019) 1903068. <https://doi.org/10.1002/aenm.201903068>.
- [24] Y. Chen, L. Zou, H. Liu, C. Chen, Q. Wang, M. Gu, B. Yang, Z. Zou, J. Fang, H. Yang, Fe and N co-doped porous carbon nanospheres with high density of active sites for efficient CO<sub>2</sub> electroreduction, *J. Phys. Chem. C.* 123 (2019) 16651–16659. <https://doi.org/10.1021/acs.jpcc.9b02195>.



## General Conclusions and Outlook





## Chapter 6 General Conclusions and Outlook

### 6.1. General Conclusions

This thesis studies photoelectrocatalytic CO<sub>2</sub> conversion on p-type semiconductor materials (CuCo<sub>2</sub>O<sub>4</sub>) in different solvent-supporting electrolyte media by scanning photoelectrochemical microscopy (SPECM). In particular, a lot of attention has been devoted to study the effect on CuCo<sub>2</sub>O<sub>4</sub> photocatalytic performance of altering the solution environment by the presence of imidazolium based room temperature ionic liquids (RTILs) acting as simultaneous supporting electrolyte and cocatalyst. Moreover, most imidazolium based RTILs strongly absorb photons from ultraviolet (UV) light irradiation. Nevertheless, almost no examples can be found in the literature addressing the cocatalytic role of imidazolium RTILs in photoelectrochemical (PEC) CO<sub>2</sub> reduction reaction (CO<sub>2</sub>RR) using semiconductor materials. This highlights the novelty (and difficulty) of the topic addressed in this thesis.

CO production from PEC CO<sub>2</sub>RR in the presence of [C<sub>2</sub>mim][BF<sub>4</sub>] in solution was electrochemically detected by the home made dual tip in SPECM configuration at potentials more positive than the thermodynamic value. Additionally, CO detection was further supported by PEC CO<sub>2</sub>RR bulk electrolysis. The analysis of bulk electrolysis products by gas chromatography confirmed CO production. Thus, it was demonstrated that direct CO<sub>2</sub>RR on the electrode surface was not the mechanism taking place and that CO was underpotential photoelectrochemically produced. Finally, an original and never described before mechanism for indirect PEC CO<sub>2</sub>RR mediated by [C<sub>2</sub>mim]<sup>+</sup> acting as cocatalyst is proposed.

As a part of my thesis, I had the opportunity to participate in the bilateral project of scientific cooperation between France and Chile called ECOS-Sud-Chile (2017-2020), which was headed by my supervisor (Dr. C. M. Sánchez-Sánchez) and Dr. F.J. Recio from Pontificia Universidad Católica de Chile. This project gave me the opportunity to spend two months in 2019 as a visiting researcher at Recio's group of research in Chile. Then, I had the opportunity to synthesize and study some transition metal–nitrogen–carbon (M–N–C) materials for catalyzing the electrochemical CO<sub>2</sub>RR. Those results are also included as a part of this thesis.

Individual conclusions of each part of the thesis have been included in the corresponding chapter, general conclusions are highlighted as follows:

Firstly, in chapter 1, an overview with regards to the research background of this thesis was introduced in detail. It includes a brief description of the state of the art and the major achievements in electrochemical and PEC CO<sub>2</sub>RR, the principle and applications of SPECM, the fundamentals and advantages of RTILs and a review about the application of cost-effective oxide-derived Cu and M–N–C electrocatalysts on CO<sub>2</sub> conversion.

In chapter 2, chemical reagents, electrode materials, equipment and instruments used in this thesis were introduced. Furthermore, synthesis processes and experimental procedures were also described, including the synthesis of different p-type semiconductors on fluorine doped tin oxide (FTO) coated glass in the form of an array of spots, which then worked as substrate working electrode in SPECM; the configuration of SPECM to evaluate the photoactivity of those p-type semiconductors and to detect in-situ the products formed by a homemade dual tip, which fabrication was also described in detail; as well as, catalysts evaluation by rotating disk electrode (RDE) and bulk electrolysis. Furthermore, the physical characterization methods and techniques employed in this thesis were introduced including the corresponding description of the instrument type and configuration.

In chapter 3, several transition metals were adopted and combined to form different p-type metal oxide semiconductors as candidate catalysts for PEC CO<sub>2</sub>RR. CuCo<sub>2</sub>O<sub>4</sub> was selected as the model catalyst to explore the role of RTILs in the performance of CO<sub>2</sub>RR evaluated by SPECM. PEC activity of CuCo<sub>2</sub>O<sub>4</sub> was quantified and compared in different media including pure RTILs, aqueous solution and binary RTIL/H<sub>2</sub>O mixtures. A relevant increase in photocurrent was only exhibited in 25 vol.% [C<sub>2</sub>mim][BF<sub>4</sub>]/H<sub>2</sub>O solution either under UV-visible or visible illumination, whether the presence of CO<sub>2</sub> in solution or not. In contrast, changing the imidazolium cation from [C<sub>2</sub>mim]<sup>+</sup> to [C<sub>4</sub>mim]<sup>+</sup> did not enhance the PEC activity.

In chapter 4, a homemade dual tip combining optical fiber and ultramicroelectrode (OF-UME) was fabricated for studying the photoelectrochemically generated products on CuCo<sub>2</sub>O<sub>4</sub> in SPECM configuration. This dual tip acted simultaneously as a light source and electrochemical sensor. CO production from PEC CO<sub>2</sub>RR, at potentials more positive than the thermodynamic value, was electrochemically detected by the dual tip in CO<sub>2</sub> saturated 25 vol.% [C<sub>2</sub>mim][BF<sub>4</sub>]/H<sub>2</sub>O solution under UV-vis illumination. The dual tip was located in close proximity of the CuCo<sub>2</sub>O<sub>4</sub> semiconductor (20 μm) and detection was done by fast cyclic voltammetry. Additionally, CO detection, at potentials more positive than the thermodynamic

value, was further supported by bulk electrolysis on high density arrays of  $\text{CuCo}_2\text{O}_4$  spots. Bulk electrolysis also demonstrated that applying more negative potentials on the semiconductor generated larger photocurrents, but provoked activation of HER and deactivation of CO production from  $\text{CO}_2\text{RR}$ . The maximum faradaic efficiency (FE) achieved for CO production was 2.5% at -0.6 V vs. Ag/AgCl (pH = 4). Thus, based on dual tip and bulk electrolysis results, which demonstrated PEC CO production at underpotential  $\text{CO}_2\text{RR}$ , a possible reaction scheme for the PEC  $\text{CO}_2\text{RR}$  mediated by  $[\text{C}_2\text{mim}]^+$  is proposed, where the reduction of  $[\text{C}_2\text{mim}^+]$  was considered the first PEC reaction step.

In chapter 5, chitosan was adopted as a nitrogen-carbon precursor via pyrolysis to synthesize different transition metal-N-carbon materials. 3 monometallic (Cu-N-C, Co-N-C, Fe-N-C) and 4 bimetallic (25%Fe25%Co-N-C, 25%Co25%Mn-N-C, 25%Fe25%Cu-N-C, 25%Cu25%Co-N-C) catalysts besides the metal free-N-C. Electrochemical  $\text{CO}_2\text{RR}$  performance of those materials was evaluated by RDE in aqueous bicarbonate solution. Among all 8 materials compared, bimetal doped 25%Fe25%Co-N-C exhibited the highest catalytic activity. Further electrochemical studies in the presence of  $\text{SCN}^-$  and chemical composition quantification by SEM-EDS demonstrated that Co role in the bimetallic catalyst was controlling the growth of Fe by the generation of well-distributed Fe-rich microcubes, which acted as the active site in electrochemical  $\text{CO}_2\text{RR}$ .

## 6.2. Outlook

Electrochemical and PEC  $\text{CO}_2\text{RR}$  represent promising methods to solve the environmental problem due to  $\text{CO}_2$  accumulation in the atmosphere. Tremendous efforts are still necessary to completely understand each factor involved in  $\text{CO}_2$  conversion process. More importantly, researches cannot be confined in the laboratory and need to address the industrial scale, which means upgrade in every aspect and more challenges.

A novel pathway for PEC  $\text{CO}_2$  conversion is presented here working at underpotential thanks to the cocatalytic role of  $[\text{C}_2\text{mim}]^+$  in solution, which enhances photocurrent generation and controls CO production. It is demonstrated that  $[\text{C}_2\text{mim}^+]$  reduction triggers an indirect pathway for CO production from  $\text{CO}_2\text{RR}$ , which is not optimized, but opens a novel approach in  $\text{CO}_2$  mitigation. I think the design of new RTILs for optimizing their cocatalytic role in  $\text{CO}_2\text{RR}$  should be considerate. For example, the RTILs conductivity and viscosity, the



interaction of the RTIL cation and anion with  $\text{CO}_2$ , the solubility of  $\text{CO}_2$  should all be taken into consideration. Furthermore, RTILs are relatively more expensive compared to other kinds of electrolytes or solvents, which compromises their large-scale or industrial application. Thus, exploration and synthesis of cheap and tunable cation and anion combinations with suitable properties is the next challenge.

The model photocatalyst studied ( $\text{CuCo}_2\text{O}_4$ ) presents both advantages and disadvantages. Ideally, we should be able to keep the advantages and mitigate the drawbacks in future works. Although  $\text{CuCo}_2\text{O}_4$  exhibited promising PEC catalysis ability, its degradation under simultaneous potential bias and high light power illumination ruled out any potential large-scale application. Thus, enhancing the long-term stability of photocatalysts is imperative. Alternatively, p-type  $\text{CuBi}_2\text{O}_4$  has been reported in the literature to present a suitable band gap of 1.5 eV and could be adopted as photoelectrocatalyst. The synthesized  $\text{CuBi}_2\text{O}_4$  spots array substrate was already evaluated by SPECM and compared with  $\text{CuCo}_2\text{O}_4$ . It showed better stability and catalytic activity under visible light illumination, deserving deeper investigation in the future applications of PEC  $\text{CO}_2\text{RR}$  (Figure 6.1).

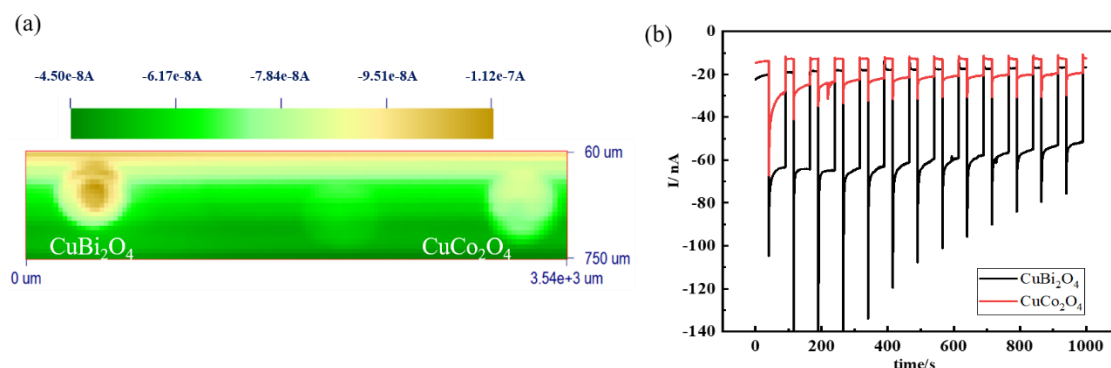


Figure 6.1 (a) SPECM image of p-type  $\text{CuBi}_2\text{O}_4$  and  $\text{CuCo}_2\text{O}_4$  array substrate displaying the reduction photocurrent as a function of optical fiber position (X-Y axis) illuminated with UV-vis light in 0.1 M  $\text{KHCO}_3$  solution saturated with  $\text{CO}_2$ . Substrate potential was held constant at 0.2 V vs. Ag/AgCl. Optical fiber-substrate distance = 150  $\mu\text{m}$ . Tip scan rate = 200  $\mu\text{m/s}$ , using increments of 30  $\mu\text{m}$  each 0.15 s. (b) Chronoresponse of the photocurrent by chopping the light off and on in segments. This photocurrent was obtained at the array substrate electrode when the optical fiber was held still at a constant tip-substrate distance of 150  $\mu\text{m}$  on top of a p-type  $\text{CuCo}_2\text{O}_4$  (red line) and  $\text{CuBi}_2\text{O}_4$  (black line) spot. Each segment had illumination duration of 50 s.

In addition, the photocorrosion of the p-type semiconductor catalysts inhibit their application, to avoid the photocorrosion, five typical strategies were introduced by Chen's

group [1] to suppress photocorrosion and increase the long-term stability of photoelectrochemical catalysts: introduction of sacrificial agents, deposition of cocatalysts, incorporation of nanocarbons, formation of heterojunctions and preparation of protective overlayers, which are expected to significantly improve the stability of p-type semiconductors.

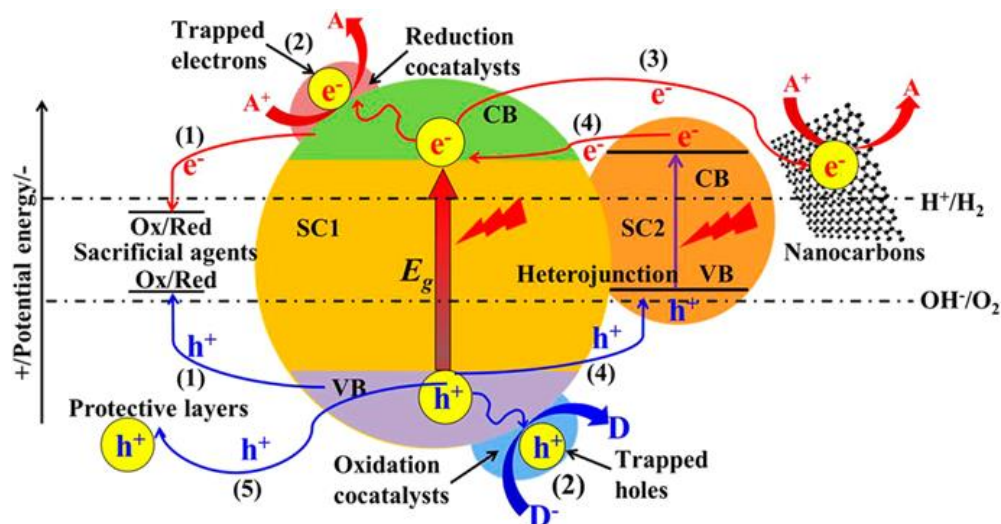


Figure 6.2 Strategies for inhibiting photocorrosion of unstable semiconductors: (1) use of sacrificial agents, (2) deposition of cocatalysts, (3) incorporation of nanocarbons, (4) formation of heterojunctions, and (5) preparation of protective overlayers [1].

Furthermore, the long-term stability of M–N–C materials is still an issue, because relevant leaching of the metal center is usually produced under reaction conditions during CO<sub>2</sub>RR. For this reason, the future research in that field should be also concentrate on improving stability. Many methods can be adopted to fulfill this goal, for example, synthesizing homogenous M–N–C catalysts with exclusive M–N<sub>4</sub> active sites but without inactive and soluble metal aggregates or engineering local coordination structures to strengthen M–N bond [2].

### 6.3. References

- [1] X. Li, J. Yu, M. Jaroniec, X. Chen, Cocatalysts for selective photoreduction of CO<sub>2</sub> into solar fuels, *Chem. Rev.* 119 (2019) 3962–4179. <https://doi.org/10.1021/acs.chemrev.8b00400>.
- [2] Y. He, S. Liu, C. Priest, Q. Shi, G. Wu, Atomically dispersed metal–nitrogen–carbon catalysts for fuel cells: advances in catalyst design, electrode performance, and durability improvement, *Chem. Soc. Rev.* 49 (2020) 3484–3524. <https://doi.org/10.1039/C9CS00903E>.



## Résumé de la Thèse en Français

Les réactions électrochimiques et photoélectrochimiques (PEC) de réduction du  $\text{CO}_2$  ( $\text{CO}_2\text{RR}$ ) pour former des produits à valeur ajoutée tels que le monoxyde de carbone ( $\text{CO}$ ), l'acide formique ( $\text{HCOOH}$ ), le méthane ( $\text{CH}_4$ ), le méthanol ( $\text{CH}_3\text{OH}$ ), l'éthanol ( $\text{CH}_3\text{CH}_2\text{OH}$ ), l'éthylène ( $\text{C}_2\text{H}_4$ ) et l'acétone ( $(\text{CH}_3)_2\text{CO}$ ), etc. constituent une approche efficace et prometteuse pour atténuer l'augmentation de la concentration de  $\text{CO}_2$  dans l'atmosphère et promouvoir le stockage de l'énergie. Bien qu'une grande variété de catalyseurs électrochimiques et PEC  $\text{CO}_2\text{RR}$  aient été largement explorés et évalués, plusieurs limitations telles que la faible efficacité d'absorption des photons et la stabilité sur le long terme de ces catalyseurs due à l'environnement à pH extrême restent des défis ouverts et doivent encore être abordés [1,2].

Tous les facteurs doivent être pris en compte et optimisés pour réussir la conversion du  $\text{CO}_2$ , dont l'un des éléments les plus impératifs est un catalyseur économique et abondant, doté d'une haute performance catalytique, d'une stabilité à long terme et d'une grande sélectivité des produits [3]. Parmi les catalyseurs électrochimiques et PEC  $\text{CO}_2\text{RR}$  déjà décrits dans la littérature, les catalyseurs économiques à base de cuivre dérivé d'un oxyde (OD-Cu) pour la génération de produits  $\text{C}_{2+}$  (hydrocarbures et alcools) à partir du  $\text{CO}_2\text{RR}$  électrochimique [4] et les matériaux electrocatalytiques à base de carbone dopé à l'azote par un métal de transition (M-N-C) pour la production de composés  $\text{C}_1$  ( $\text{CO}$ ) [5] ont été largement étudiés et se sont révélés prometteurs, ouvrant la voie à la conception et au développement futurs d'electrocatalyseurs pour la réduction électrochimique et photoélectrochimique du  $\text{CO}_2$ .

Les systèmes d'électrolyte à base de solvants utilisant des liquides ioniques à température ambiante (RTIL) à base d'imidazolium ( $[\text{C}_n\text{mim}]^+$ ) présentent plusieurs avantages par rapport aux solutions aqueuses. En particulier, parmi les propriétés physico-chimiques des RTIL, il faut souligner leur conductivité ionique appropriée, leur faible volatilité, leur stabilité thermique élevée, leur pression de vapeur négligeable, leur large fenêtre de potentiel électrochimique et leur capacité à dissoudre davantage de  $\text{CO}_2$  et à inhiber la réaction compétitive d'évolution de l'hydrogène. En revanche, la plupart des RTIL présentent une viscosité élevée et un faible taux de transfert de masse. Pour cette raison, les RTIL purs jouant simultanément le rôle de solvant et d'électrolyte support sont limités dans leurs applications.

C'est pourquoi des mélanges binaires et ternaires de RTIL avec un solvant moléculaire (eau ou acétonitrile) ont été explorés et ont fait l'objet d'une attention particulière pour différentes applications électrochimiques [6].

D'un point de vue catalytique, Rosen *et al.* [7] ont démontré en 2011 l'effet synergique pertinent du mélange de H<sub>2</sub>O et de [C<sub>2</sub>mim][BF<sub>4</sub>] pour augmenter la réduction de CO<sub>2</sub> sur l'électrode d'argent en abaissant la barrière énergétique de cette réaction. Depuis la publication de ce travail fondamental, de nombreux chercheurs ont étudié le rôle de cocatalyseur des cations imidazolium pour le CO<sub>2</sub>RR. Ainsi, différents RTIL à base d'imidazolium ont montré qu'ils jouaient un rôle actif de cocatalyseur dans le CO<sub>2</sub>RR électrochimique [8–10]. Néanmoins, on ne trouve pratiquement aucun exemple dans la littérature traitant du rôle cocatalytique des RTIL à base d'imidazolium dans le CO<sub>2</sub>RR photoélectrochimique utilisant des matériaux semi-conducteurs. Malgré le fait que la plupart des RTIL à base d'imidazolium absorbent fortement les photons de l'irradiation de la lumière ultraviolette (UV) en raison de la présence d'un cycle aromatique [11], cela souligne la nouveauté (et la difficulté) du sujet abordé dans cette thèse.

La microscopie électrochimique à balayage (SECM) utilise une ultramicroélectrode (UME) à laquelle on applique un potentiel approprié et on recueille la réponse du signal électrochimique correspondant sous forme de courant, ce qui permet d'explorer les propriétés électrocatalytiques de différents matériaux. Sur cette base, la microscopie photoélectrochimique à balayage (SPECM) a été développée en remplaçant l'UME par une fibre optique, qui est connectée à une source de lumière Xénon et introduit une lumière UV-visible ou visible pour éclairer localement les catalyseurs candidats pour l'évaluation de l'activité photoélectrochimique

Compte tenu de ce qui précède, les principaux objectifs de cette thèse sont décrits comme suit :

- (1) Synthétiser des échantillons miniaturisés de différents semi-conducteurs de type p déjà décrit dans la littérature, présentant une forte activité catalytique pour les réactions photoélectrochimiques et sélectionner parmi eux, un semi-conducteur modèle par SPECM.
- (2) Étudier par SPECM l'effet de la modification de l'environnement du photocatalyseur par la présence de RTIL à base d'imidazolium pur et de ceux dissous dans H<sub>2</sub>O agissant

simultanément comme électrolyte de support et cocatalyseur dans la PEC CO<sub>2</sub>RR sur des échantillons modèles de CuCo<sub>2</sub>O<sub>4</sub> de type p.

- (3) Détecter in situ les produits formés lors des réactions de PEC sur des échantillons modèles de CuCo<sub>2</sub>O<sub>4</sub> de type p par une double sonde développée au laboratoire (fibre optique - UME) utilisée dans le SPECM. En outre, analyser les produits générés par photocatalyse à partir de l'électrolyse en masse sous illumination par chromatographie.
- (4) Synthétiser et caractériser des matériaux de métaux transition–azote–carbone (M–N–Cs) pour le CO<sub>2</sub>RR électrochimique en solution aqueuse que l'on évaluera avec une électrode à disque tournant (RDE).

## Chapitre 1

Dans le chapitre 1, une vue d'ensemble concernant le contexte de recherche nécessaire à la réalisation de cette thèse a été présentée en détail. Il comprend une brève description de l'état de l'art et des principales réalisations dans le domaine de l'électrochimie et de la PEC CO<sub>2</sub>RR, le principe et les applications de la microscopie (photo)électrochimique à balayage, les principes fondamentaux et les avantages des RTIL et un examen des électrocatalyseurs de faible coût à base d'oxydes de cuivre et de métaux de transition–azote–carbone.

## Chapitre 2

Dans le chapitre 2, les réactifs chimiques, les matériaux des électrodes, l'équipement et les instruments utilisés dans cette thèse sont présentés. En outre, les procédés de synthèse et les procédures expérimentales sont également décrits, y compris la synthèse de 9 types de différents semi-conducteurs de type p de métaux de transition dérivés d'oxydes, déposés sur de l'oxyde d'étain dopé au fluor (FTO) sous la forme d'un réseau de spots (**Figure 1**) ; la configuration du SPECM pour évaluer le photocourant généré par ces semi-conducteurs de type p (**Figure 2b**) et la détection in situ des produits générés par photoélectrochimie (**Figure 2c**). À cette fin, la combinaison d'une fibre optique et d'une UME (OF-UME) agissant simultanément comme source de lumière et capteur pour les réactions de PEC a été jugée pratique et applicable [12]. Le même type de sonde double OF-UME « fait-maison » (**Figure 3**) a été construit dans cette thèse pour étudier les produits des réactions photocatalytiques par SPECM. Enfin, les méthodes et techniques de caractérisation physique employées ont été introduites, y compris la description correspondante du type et de la configuration de l'instrument.

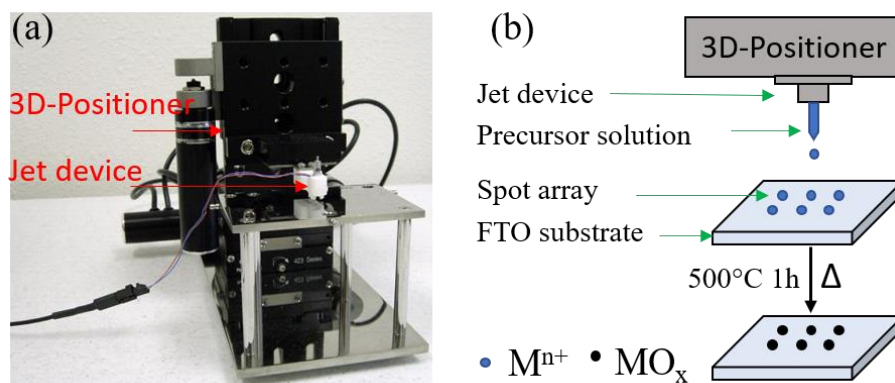


Figure 1. (a) Distributeur de solutions CHI 1550A. (b) Représentation schématique de la synthèse des électrodes de substrat à réseau miniaturisé.

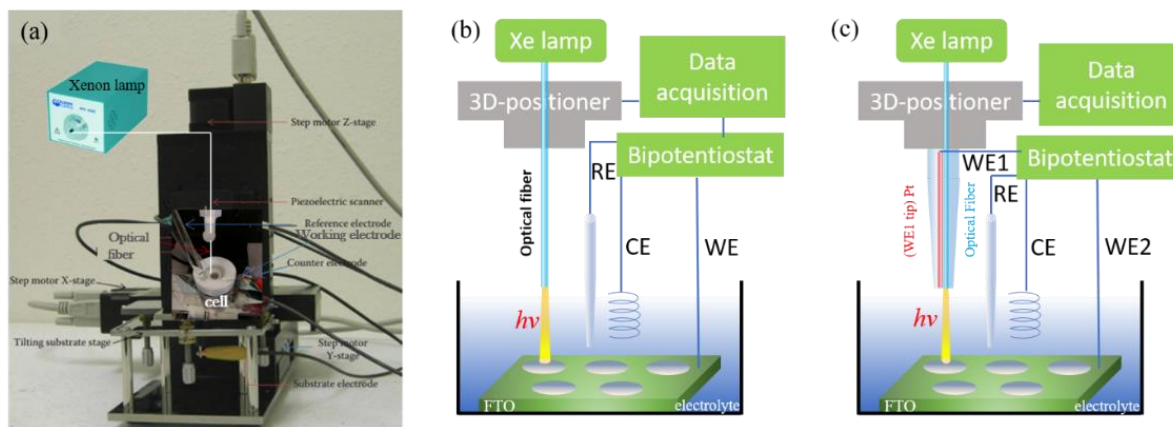


Figure 2. (a) Photo de l'instrument SPECM. (b) Croquis du SPECM pour l'évaluation de l'activité PEC. (c) Croquis du SPECM pour le déclenchement des réactions PEC et la détection simultanée des produits générés.

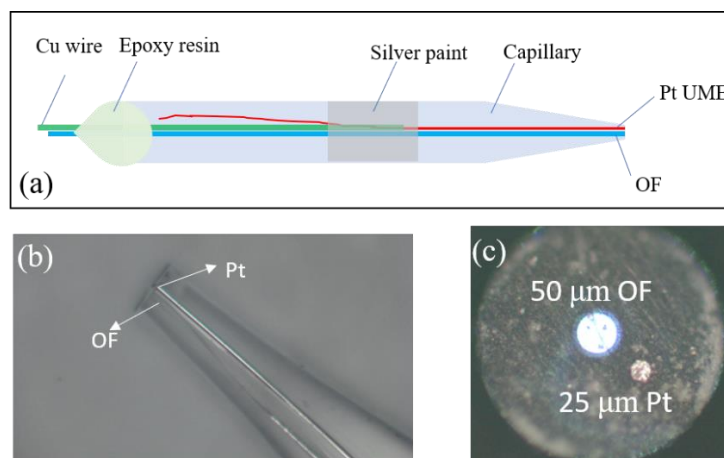


Figure 3. (a) Représentation schématique d'un double embout OF-UME fait maison. Images optiques de (b) vue de côté et (c) vue de dessous de la double sonde OF-UME faite maison.

## Chapitre 3

Ce chapitre décrit comment plusieurs métaux de transition ont été adoptés et combinés pour former différents semi-conducteurs d'oxyde métallique de type p comme catalyseurs pour le CO<sub>2</sub>RR PEC. Le modèle de semi-conducteur de type p sélectionné, le CuCo<sub>2</sub>O<sub>4</sub>, a été immergé dans différents électrolytes supports, notamment une solution aqueuse (0,1 M KHCO<sub>3</sub> et 0,1 M Na<sub>2</sub>SO<sub>4</sub>), une solution de mélange binaire (25 vol.% [C<sub>2</sub>mim][BF<sub>4</sub>]/H<sub>2</sub>O et 25 vol.% [C<sub>4</sub>mim][BF<sub>4</sub>]/H<sub>2</sub>O) et RTIL purs ([C<sub>2</sub>mim][BF<sub>4</sub>], [C<sub>4</sub>mim][BF<sub>4</sub>], [C<sub>4</sub>mim][NTf<sub>2</sub>] et [C<sub>2</sub>mim][NTf<sub>2</sub>]) pour explorer par SPECM le rôle des RTIL dans le modèle de performance de la PEC des semi-conducteurs. La représentation schématique du SPECM mis en place pour évaluer les performances de la PEC est présentée **Figure 4a**.

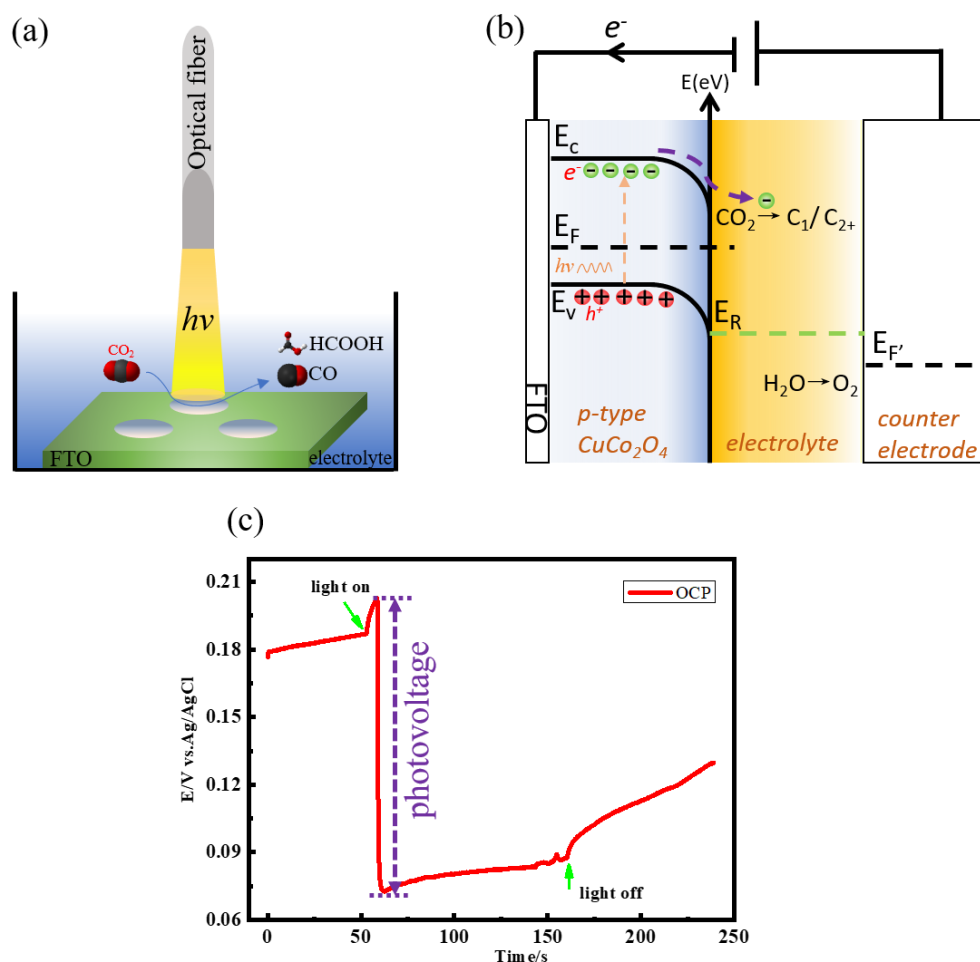


Figure 4. (a) Représentation schématique des expériences SPECM évaluation de l'activité du photoélectrocatalyseur pour PEC CO<sub>2</sub>RR éclairé par l'UV-vis ou la lumière visible. (b) Principe et diagramme des bandes d'énergie dans le système PEC CO<sub>2</sub>RR sur photoélectrocatalyseur CuCo<sub>2</sub>O<sub>4</sub> de type p. (c) Photovoltage induit par l'illumination en lumière visible de l'électrode substrat du



*réseau de spots (réseau de spots 5×5 ; surface de 0,07 cm<sup>2</sup> dans une solution à 25 vol.% [C<sub>2</sub>mim][BF<sub>4</sub>]/H<sub>2</sub>O). Les flèches vertes dans le panneau indiquent quand l'éclairage local est allumé et éteint, et la flèche violette du tableau de bord indique la tension photoélectrique.*

La fibre optique focalise la lumière UV-vis ou visible localement sur l'électrode du réseau de semi-conducteurs, qui est généralement polarisée dans différents solvants saturés soit en CO<sub>2</sub> soit en Ar. Ensuite, on enregistre une image SPECM du photocourant de réduction qui est mesuré en fonction de la position de la fibre optique dans le plan X-Y. La **Figure 4b** illustre le principe selon lequel la combinaison de l'illumination et de la polarisation externe induit l'excitation des électrons, la séparation de la paire électron-trou et la flexion de la bande vers le haut près de la surface du semi-conducteur. Par conséquent, les électrons photogénérés à l'interface se déplacent dans l'électrolyte où ils sont capturés et utilisés par le CO<sub>2</sub>RR pour former des produits à valeur ajoutée. La **Figure 4c** montre le photopotential induit par la lumière, qui s'établit sur l'électrode semi-conductrice lors de l'illumination.

La réponse de l'électrode semi-conductrice modèle en solution aqueuse de 0,1 M KHCO<sub>3</sub>/CO<sub>2</sub> (pH = 6,9) en fonction du potentiel appliqué illustre que le courant de photoréduction augmente lorsque le potentiel va vers des valeurs plus négatives (**Figure 5**). La **Figure 6** montre des images SPECM d'un réseau de CuCo<sub>2</sub>O<sub>4</sub> sous illumination de lumière UV-visible dans différents solvants saturés en CO<sub>2</sub> à pH constant (≈ 4). Ces résultats montrent l'effet sur le photocourant généré de différents électrolytes en solution, le courant de photoréduction le plus élevé étant obtenu dans une solution à 25 vol.% [C<sub>2</sub>mim][BF<sub>4</sub>]/H<sub>2</sub>O, ce qui semble indiquer une performance accrue dans le PEC CO<sub>2</sub>RR lorsque [C<sub>2</sub>mim][BF<sub>4</sub>] est présent en solution. Le même comportement est obtenu à partir de la quantification de l'activité de la PEC par SPECM (**Figure 7**). Cependant, aucune différence significative n'est observée que la solution soit saturée en CO<sub>2</sub> ou non, ce qui indique que la présence en solution de certains liquides ioniques particuliers à base d'imidazolium joue un rôle cocatalytique en augmentant l'activité photoélectrochimique du semi-conducteur étudié. De plus, cette augmentation significative du courant photoélectrique a été mise en évidence dans une solution à 25 vol.% [C<sub>2</sub>mim][BF<sub>4</sub>]/H<sub>2</sub>O, soit sous éclairage UV-visible, soit sous éclairage visible (**Figure 8**).

Enfin, l'amélioration de la production de photocourant ne peut être attribuée qu'à la présence de [C<sub>2</sub>mim][BF<sub>4</sub>] en solution et à son effet sur l'interface semi-conducteur/électrolyte. Cependant, aucun exemple précédent de ce type d'interaction n'a été rapporté jusqu'à présent dans la littérature.

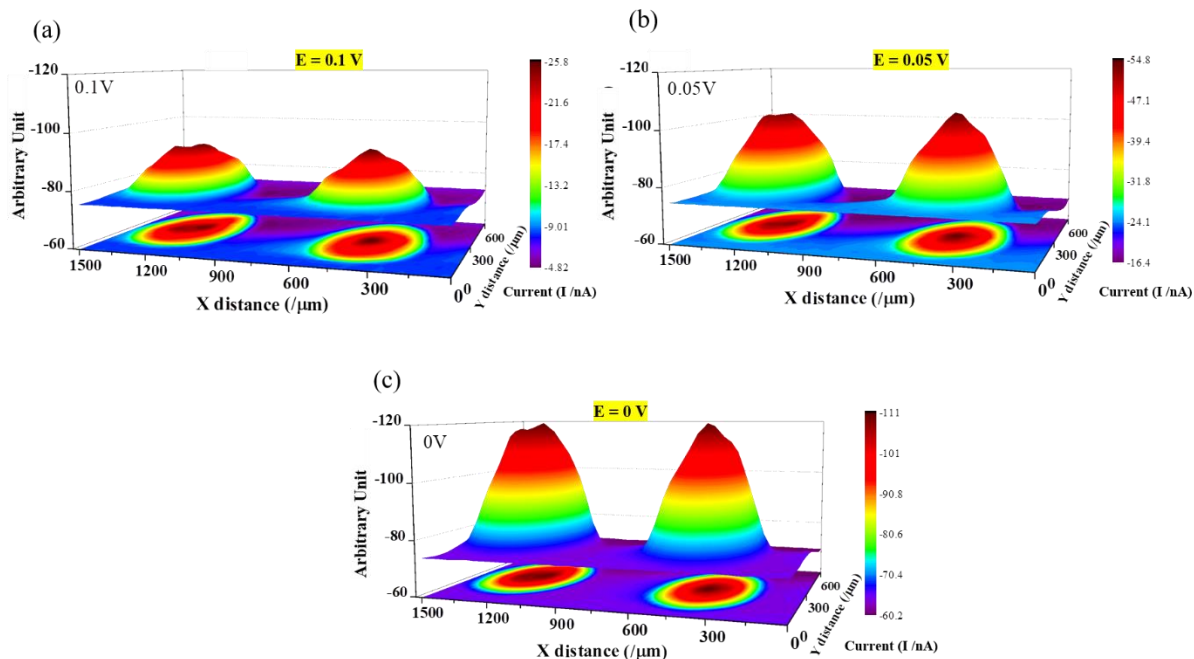


Figure 5. Images SPCM du réseau  $\text{CuCo}_2\text{O}_4$  sous illumination de lumière UV-visible dans une solution aqueuse de  $\text{KHCO}_3$  0,1 M saturée en  $\text{CO}_2$  (pH = 6,9) à des potentiels de (a)  $E_{\text{sub}} = 0,1$ , (b) 0,05 et (c) 0 V / Ag/AgCl. Distance fibre optique/substrat = 150  $\mu\text{m}$ . Vitesse de balayage de la sonde = 200  $\mu\text{m/s}$ , par incréments de 30  $\mu\text{m}$  toutes les 0,15 s.

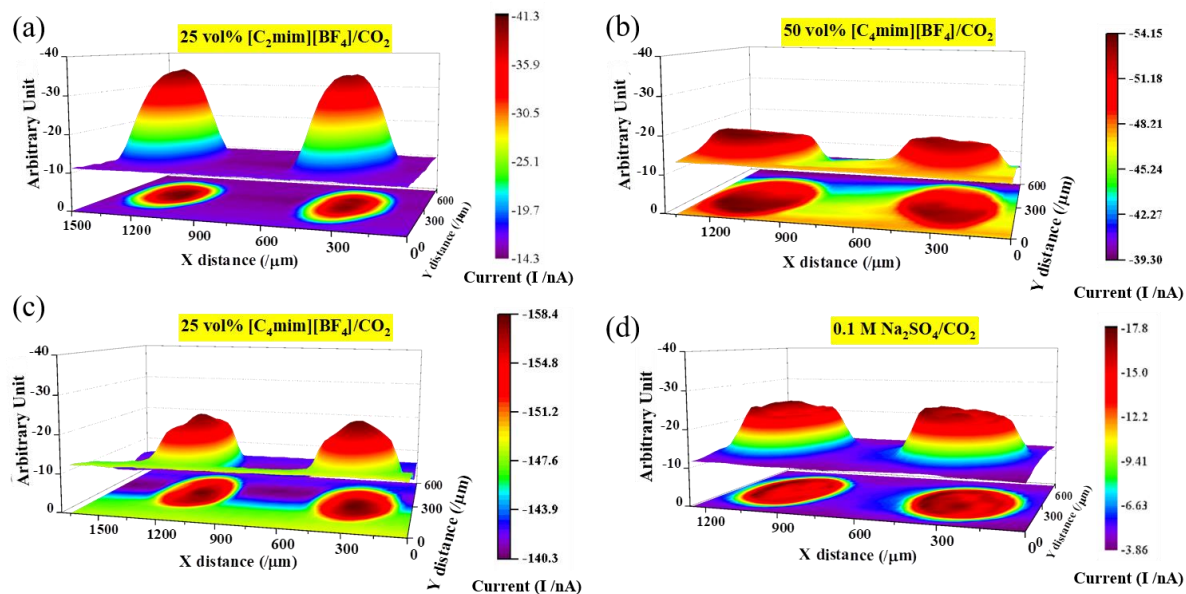


Figure 6. Images SPCM du réseau  $\text{CuCo}_2\text{O}_4$  sous illumination de lumière UV-visible dans différents milieux de solvants saturés en  $\text{CO}_2$  à pH  $\approx 4$  de (a) 25 vol.%  $[\text{C}_2\text{mim}][\text{BF}_4]/\text{H}_2\text{O}$ , (b) 50 vol.%  $[\text{C}_4\text{mim}][\text{BF}_4]/\text{H}_2\text{O}$ , (c) 25 vol.%  $[\text{C}_4\text{mim}][\text{BF}_4]/\text{H}_2\text{O}$  et (d) 0,1 M  $\text{Na}_2\text{SO}_4$  à des potentiels de 0,1 V /

Ag/AgCl. Distance fibre optique/substrat = 150  $\mu\text{m}$ . Vitesse de balayage de la sonde = 200  $\mu\text{m/s}$ , par incréments de 30  $\mu\text{m}$  toutes les 0,15 s.

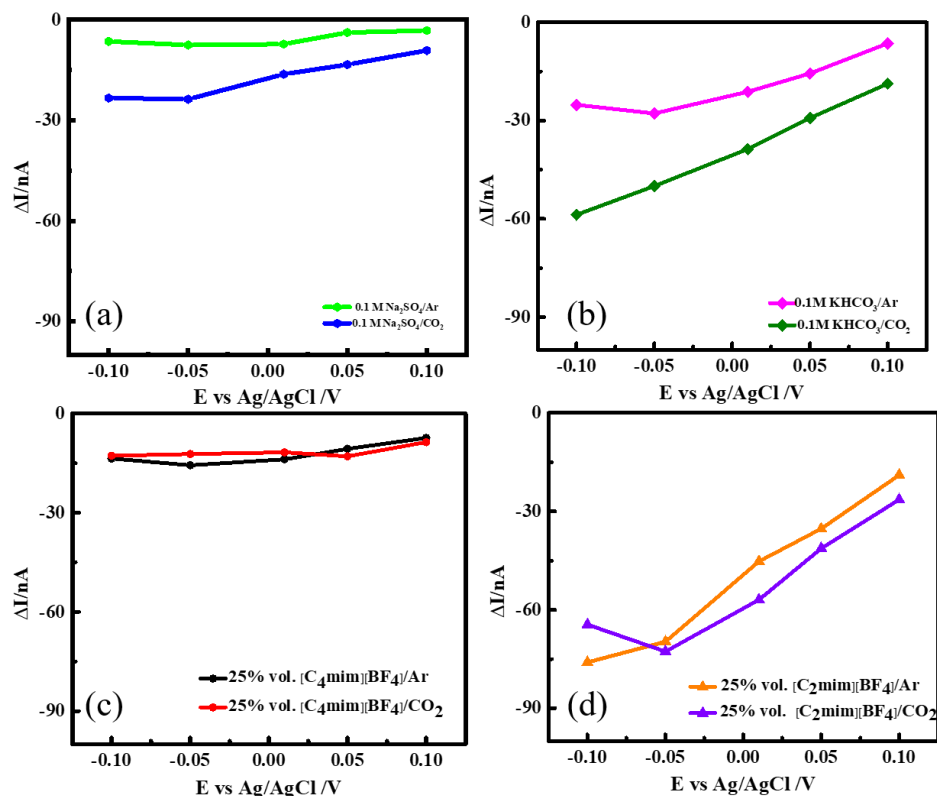


Figure 7. Comparaison du photocourant sur  $\text{CuCo}_2\text{O}_4$  sous éclairage UV-visible dans (a) une solution de 0,1 M  $\text{Na}_2\text{SO}_4$ , (b) une solution de 0,1 M  $\text{KHCO}_3$  (c) une solution à 25 vol.%  $[\text{C}_4\text{mim}][\text{BF}_4]/\text{H}_2\text{O}$  et (d) une solution à 25 vol.%  $[\text{C}_2\text{mim}][\text{BF}_4]/\text{H}_2\text{O}$ . Chaque solution est saturée soit en  $\text{CO}_2$ , soit en Ar.

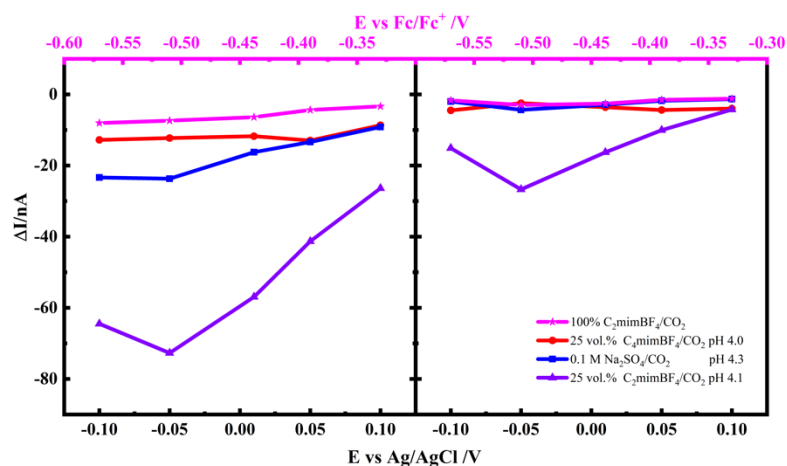
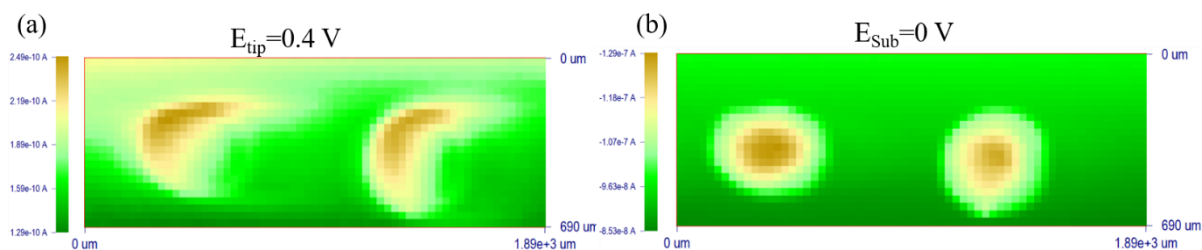


Figure 8. Comparaison du photocourant sur  $\text{CuCo}_2\text{O}_4$  dans différentes solutions saturées en  $\text{CO}_2$  (a) sous éclairage local en lumière UV-visible et (b) sous éclairage local en lumière visible.

Dans cette thèse, nous avons observé que la présence en solution de  $[\text{C}_2\text{mim}][\text{BF}_4]$  a non seulement augmenté la solubilité en  $\text{CO}_2$  dans la solution par rapport à la solution aqueuse,  $[\text{C}_2\text{mim}]^+$  peut également interagir avec le  $\text{CO}_2$  dissous pour former des intermédiaires présentant une barrière énergétique inférieure pour activer la conversion du  $\text{CO}_2$ . En outre, la propriété d'absorption de la lumière des cations imidazolium peut contribuer à capturer plus de lumière et générer ensuite plus de photons sur le catalyseur semi-conducteur, ainsi qu'accélérer la réaction de réduction suivante. En revanche, aucune amélioration significative du photocourant n'a été constatée dans un mélange de 25 vol.%  $[\text{C}_4\text{mim}][\text{BF}_4]/\text{H}_2\text{O}$ . Cela peut être lié à la chaîne de carbone plus longue présente dans le  $[\text{C}_4\text{mim}][\text{BF}_4]$  par rapport au  $[\text{C}_2\text{mim}][\text{BF}_4]$ , qui peut présenter un effet négatif stérique sur la disposition spatiale des cations imidazolium à la surface du catalyseur et peut entraîner des performances catalytiques différentes par rapport au mélange  $[\text{C}_2\text{mim}][\text{BF}_4]/\text{H}_2\text{O}$ .

## Chapitre 4

Dans le chapitre 4, la double sonde OF-UME a été utilisée dans la configuration du SPECM capable de déclencher des réactions de PEC et de détecter simultanément les produits de réduction générés par voie photoélectrochimique. La configuration est illustrée sur la **Figure 2c**. L'OF permet à la lumière d'illuminer localement le matériau semi-conducteur de type p  $\text{CuCo}_2\text{O}_4$  et simultanément, l'UME polarisée détecte les produits générés par photoélectrochimie par oxydation électrochimique. En balayant la double sonde à hauteur constante dans le plan X-Y, on a obtenu l'image SPECM de détection des produits à l'UME (**Figure 9a**), et l'image SPECM de photocourant correspondante du substrat semi-conducteur illuminé et polarisé (**Figures 9b**).



*Figure 9. Images SPECM (a) du courant d'oxydation des produits collectés à la sonde OF-UME à 0,4 V. (b) le photocourant correspondant du substrat de (a) sur le réseau de spots  $\text{CuCo}_2\text{O}_4$  au potentiel de 0 V et éclairé par la lumière UV-visible. Tous les potentiels sont rapportés par rapport à  $\text{Ag}/\text{AgCl}$ . Électrolyte : 0,1 M  $\text{KHCO}_3$  saturé de  $\text{CO}_2$ , la vitesse de balayage est de 200  $\mu\text{m/s}$ .*

Des expériences chronoampérométriques sur des spots semi-conducteurs individuels actionnés par la double sonde OF-UME située à proximité immédiate (20  $\mu\text{m}$ ) ont fourni des informations pertinentes sur les produits générés par voie photoélectrochimique. La détection des produits par voltampérométrie cyclique rapide (1 V/s) représente une approche intéressante pour distinguer les produits détectables considérés ( $\text{CO}$ ,  $\text{HCOOH}$  et  $\text{H}_2$ ), puisqu'un pic d'oxydation indépendant situé à un potentiel différent est associé à chaque produit considéré en CV. La détection des produits de PEC par la double sonde d'UME en utilisant la voltampérométrie cyclique rapide a été réalisée avec succès dans une solution saturée en  $\text{CO}_2$  à 25 vol.%  $[\text{C}_2\text{mim}][\text{BF}_4]/\text{H}_2\text{O}$ . La **Figure 10** montre le voltampérogramme rapide recueilli par l'UME de Pt lorsque le semi-conducteur  $\text{CuCo}_2\text{O}_4$  est dans l'obscurité (**Figure 10a**) et sous éclairage UV-vis (**Figure 10b**). Un pic d'oxydation clair centré à 0,4 V n'apparaissait que sous illumination et il a été attribué à l'oxydation du  $\text{CO}_{\text{ads}}$ .

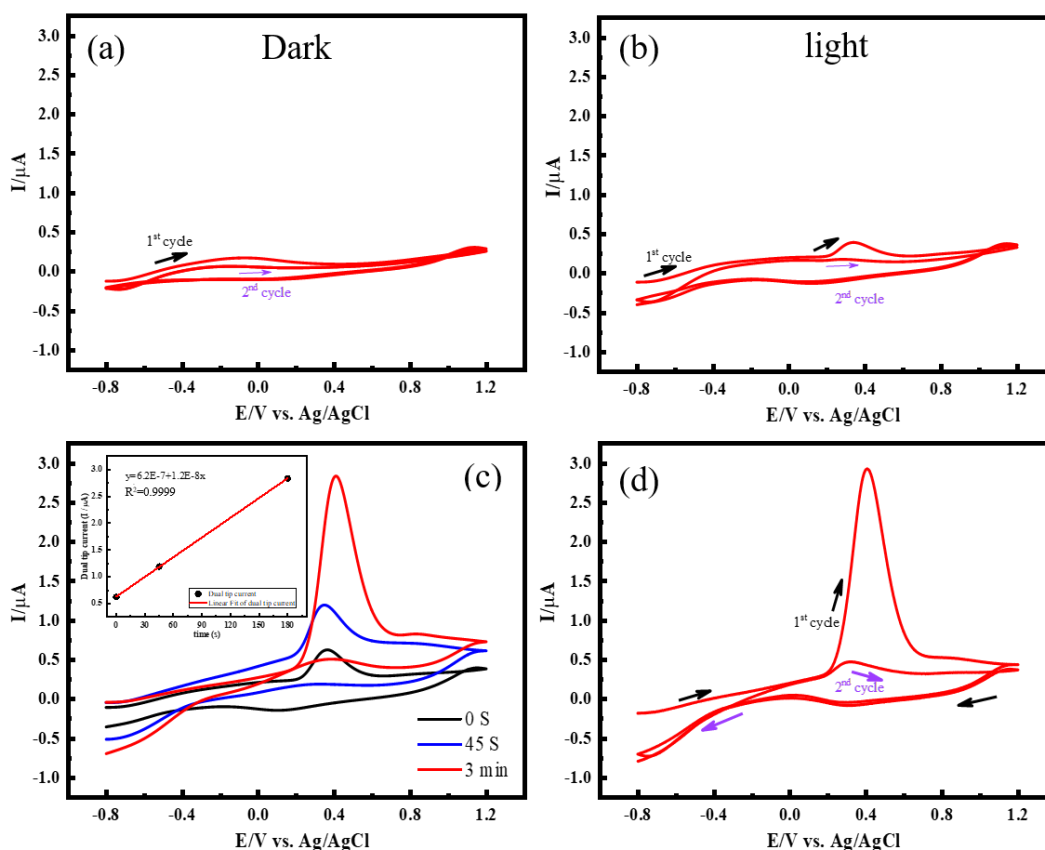
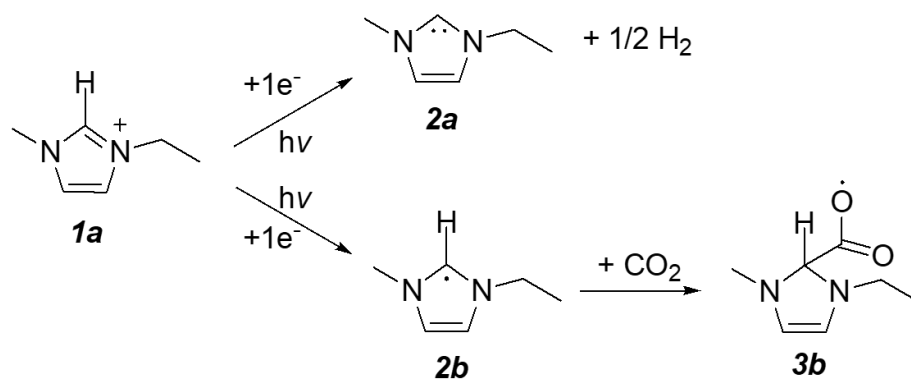


Figure 10. Voltammogrammes cycliques de l'OF-UME (Pt) pour la détection des produits générés par la PEC  $\text{CO}_2\text{RR}$  dans 25 vol.%  $[\text{C}_2\text{mim}][\text{BF}_4]/\text{H}_2\text{O}$  saturés en  $\text{CO}_2$ ,  $\text{pH} = 4$  : (a) Deux CVs consécutifs sur la sonde dans l'obscurité,  $E_{\text{sub}} = \text{OCP}$  ; (b) Deux CVs consécutifs sur la sonde, alors que le  $\text{CuCo}_2\text{O}_4$  est maintenu polarisé à -0,05 V/Ag/AgCl sous éclairage UV ( $I_{\text{photo}} = -1,3 \times 10^{-5}$  -0,9

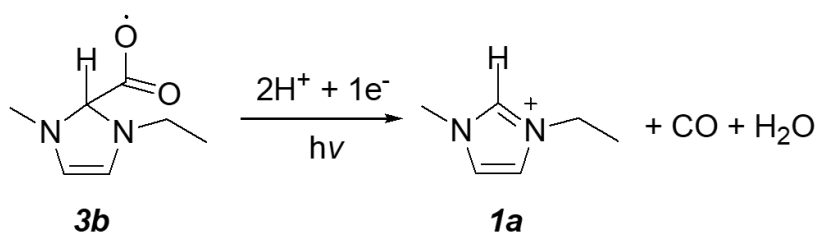
$\times 10^{-5}$  A), (c) CV indépendants sur la sonde, tandis que  $\text{CuCo}_2\text{O}_4$  était maintenu polarisé à  $-0,05$  V / Ag/AgCl sous éclairage UV pour différents intervalles de temps (0 s, 45 s et 3 min) ( $I_{\text{photo}} = -1,1 \times 10^{-5}$  -  $-0,6 \times 10^{-5}$  A). L'encadré correspond à la relation linéaire entre le pic de courant d'oxydation à  $0,4$  V et le temps d'illumination du  $\text{CuCo}_2\text{O}_4$  polarisé, (d) Deux CVs consécutifs sur la sonde après que le  $\text{CuCo}_2\text{O}_4$  ait été maintenu polarisé à  $-0,05$  V / Ag/AgCl sous illumination UV-vis pendant 3 min ( $I_{\text{photo}} = -0,7 \times 10^{-5}$  -  $-0,6 \times 10^{-5}$  A). Toutes les CVs sont obtenues pour une vitesse de balayage de  $1$  V/s. Distance sonde-substrat =  $20 \mu\text{m}$ .

De plus, un courant de crête d'oxydation croissant du  $\text{CO}_{\text{ads}}$  a été collecté par voltammetrie rapide lorsque le semi-conducteur  $\text{CuCo}_2\text{O}_4$  a été maintenu polarisé à  $-0,05$  V sous illumination pour différents intervalles de temps (0 s, 45 s et 3 min, **Figure 10c**). Cela indique que le CO est continuellement généré et accumulé dans l'espace entre la double sonde et le substrat. En outre, le deuxième balayage consécutif en CV après l'oxydation par stripping du CO ne montre pas de  $\text{CO}_{\text{ads}}$  significatif en raison du potentiel transitoire appliqué sur l'UME Pt et du court temps écoulé entre le premier et le deuxième balayage (**Figure 10d**). Cela a clairement démontré que le  $\text{CO}_2\text{RR}$  se mettait à former du CO lorsqu'un spot de  $\text{CuCo}_2\text{O}_4$  était éclairé sous une lumière UV-vis et polarisé à  $-0,05$  V.

En outre, des électrolyses préparatives sous éclairage UV-vis ont été effectuées pour analyser les produits générés. La formation de CO à des potentiels plus positifs que la valeur thermodynamique a clairement montré que la réduction directe du  $\text{CO}_2$  à la surface de l'électrode n'est pas le mécanisme qui se produit et que le CO est produit photoélectrochimiquement à un potentiel inférieur. Nous avons proposé un schéma réactionnel possible pour la PEC  $\text{CO}_2\text{RR}$  par l'intermédiaire de  $[\text{C}_2\text{mim}]^+$  (**Figure 11**). En particulier, le photocourant est consommé en réduisant le cation imidazolium et ensuite, le  $\text{CO}_2$  est combiné avec le radical imidazolium (**2b**) pour former un radical carboxylate d'imidazolium comme intermédiaire  $\text{CO}_2$  activé (**3b**), qui a été initialement proposé à partir des calculs DFT et a été récemment détecté par spectroscopie Raman sur des électrodes en cuivre. Ensuite, le radical carboxylate d'imidazolium est encore réduit pour produire du CO et régénérer le cation 1,3-dialkylimidazolium initial (**1a**). Dans l'ensemble, la détection in situ des produits générés à la sonde ou lors de l'électrolyse préparative a montré le même produit (CO), ce qui prouve le rôle cocatalytique des RTIL à base d'imidazolium pour la PEC  $\text{CO}_2\text{RR}$ .



Scheme 1



Scheme 2

Figure 11. Voie photoélectrochimique de réduction du  $\text{CO}_2$  par l'imidazolium dans les solutions aqueuses.

## Chapitre 5

Dans le chapitre 5, le chitosane (biopolymère abondant) a été adopté comme précurseur d'azote-carbone par pyrolyse pour former des matériaux carbonés dopés à l'azote, qui présentent une grande surface spécifique et la présence de groupes amines. Avec l'ajout de précurseurs de sels métalliques (Fe, Co, Cu, Mn), différents M–N–Cs ont été synthétisés, dont Cu–N–C, Co–N–C, Fe–N–C, des bimétalliques dopés à 25%Fe25%Co–N–C, 25%Co25%Mn–N–C, 25%Fe25%Cu–N–C, 25%Cu25%Co–N–C et sans métal –N–C. Ces M–N–C ont été évalués pour leurs performances électrochimiques pour le  $\text{CO}_2\text{RR}$  électrochimique avec une électrode à disque tournant (RDE) (**Figure 12a**), qui offre une bonne reproductibilité et une courbe de polarisation stable car l'épaisseur de la couche de diffusion est contrôlée par la vitesse de rotation. Parmi tous les M–N–C étudiés (et sans métal –N–C), le 25%Fe25%Co–N–C bimétallique présente l'activité catalytique la plus élevée en raison d'un potentiel d'amorçage plus positif et d'un courant de réduction plus élevé. En outre, une comparaison des performances électrochimiques du  $\text{CO}_2\text{RR}$  des matériaux sans métal–N–C, de Co–N–C, de Fe–N–C et de 25%Fe25%Co–N–C bimétallique a été effectuée, montrant que la présence de

métal provoque un potentiel d'attaque plus positif et fournit un courant de réduction du  $\text{CO}_2$  plus important que celui du N-C sans métal. Afin d'identifier les sites actifs de 25%Fe25%Co-N-C, du NaSCN a été ajouté en solution et utilisé comme agent d'empoisonnement, car le  $\text{SCN}^-$  a une grande affinité pour le Fe et peut bloquer les fractions Fe-N<sub>x</sub> et les nanoparticules à base de fer, mais il n'affecte pas les sites N-C (**Figure 12b**). Les résultats ont montré une diminution du courant de réduction après l'ajout de NaSCN dans l'électrolyte, ce qui indique que le Fe et/ou les atomes environnants jouent le rôle important de site actif. Sur l'image obtenue au MEB, seul le 25%Fe25%Co-N-C a montré de nombreux microcubes distribués, dans lesquels la teneur en Fe était majoritaire (**Figure 13**). Les résultats indiquent que la présence de Co a un effet synergique pour la génération de microcubes distribués riches en Fe dans la structure 25%Fe25%Co-N-C, qui jouent le rôle de sites actifs dans le  $\text{CO}_2\text{RR}$  électrochimique.

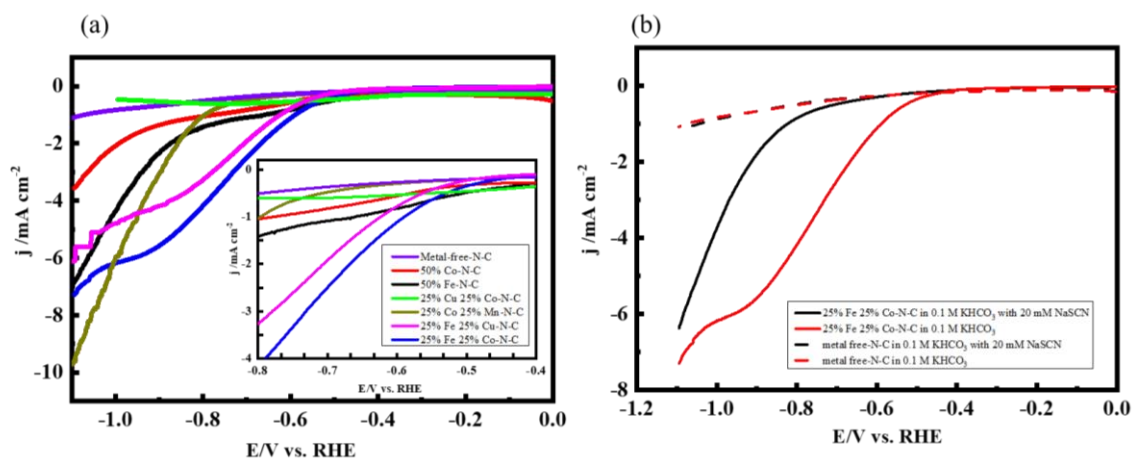


Figure 12. (a) Voltammogrammes en RDE pour différents M-N-Cs dans  $0,1 \text{ M KHCO}_3$  saturés en  $\text{CO}_2$  : 50%Fe-N-C, 50%Co-N-C, 25%Fe25%Co-N-C, 25%Co25%Mn-N-C, 25%Fe25%Cu-N-C, 25%Cu25%Co-N-C et sans métal-N-C. b) Voltammogrammes en RDE pour 25%Fe25%Co-N-C et sans métal-N-C dans  $0,1 \text{ M KHCO}_3$  saturé de  $\text{CO}_2$  avec et sans présence de NaSCN. Vitesse de balayage  $5 \text{ mV/s}$  avec une vitesse de rotation de  $1600 \text{ rpm}$ .



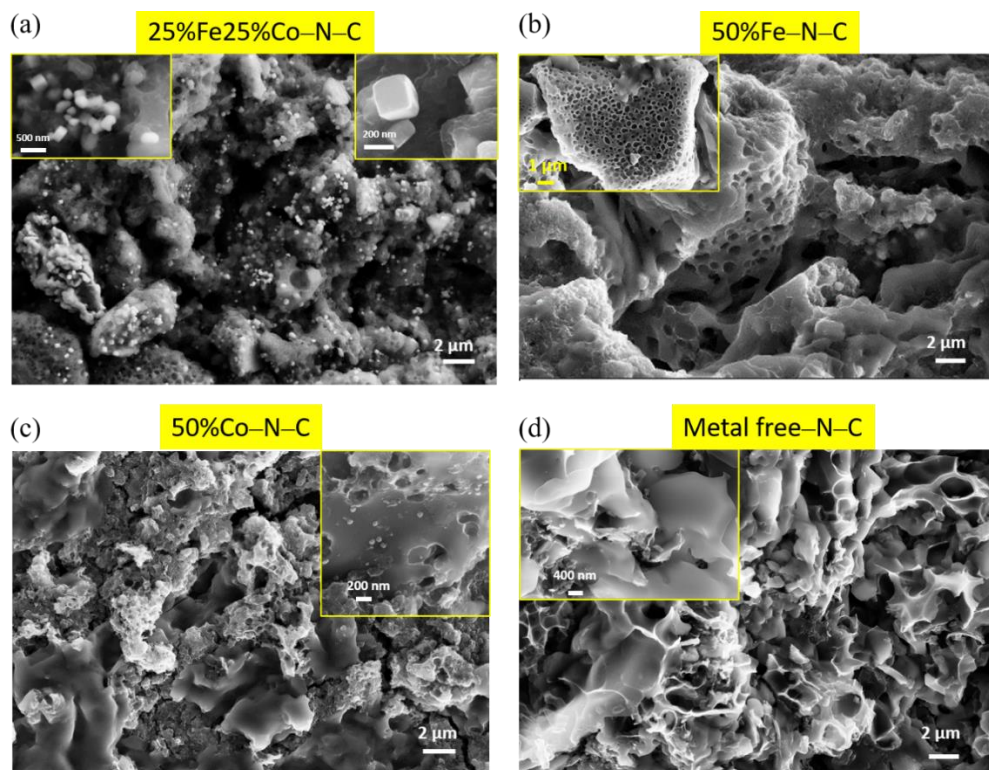


Figure 13. Images MEB de différents catalyseurs  $M-N-C$  : (a)  $25\%Fe25\%Co-N-C$ , (b)  $50\%Fe-N-C$ , (c)  $50\%Co-N-C$  et (d) sans métal- $N-C$ . Les images en médaillon sont le grossissement de l'image MEB correspondante.

## Chapitre 6

Dans le chapitre 6, les principales conclusions générales des travaux présentés dans cette thèse sont résumées et les perspectives sont présentées. Bien que le  $CuCo_2O_4$  ait montré une capacité catalytique PEC prometteuse, sa dégradation à des potentiels d'électroréduction et une puissance lumineuse élevée ont empêché son utilisation à grande échelle. Il est donc impératif de développer des méthodes synergétiques pour améliorer la stabilité sur le long terme des photocatalyseurs. Par ailleurs, un substrat de réseau de spots en  $CuBi_2O_4$  a été évalué et comparé à d'autres semi-conducteurs de type p à base d'oxydes de métaux de transition et a montré une meilleure stabilité et une meilleure activité catalytique sous la lumière UV-visible, ce qui mérite d'être étudié plus en profondeur dans de futures applications (**Figure 14**).

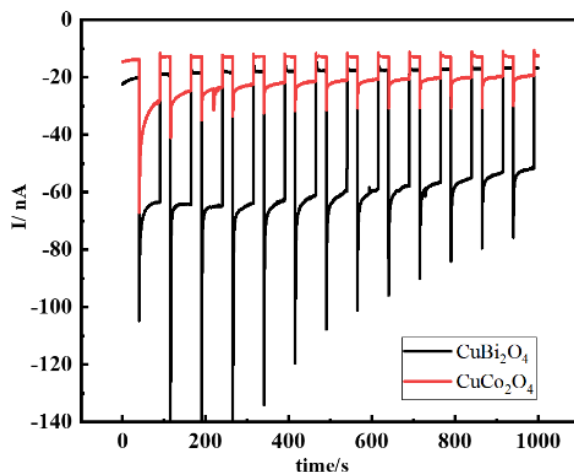


Figure 14. Chronoréaction du photocourant en coupant et en allumant la lumière par segments. Ce photocourant est obtenu au niveau de l'électrode de substrat du réseau lorsque la fibre optique est maintenue immobile à une distance constante de 150  $\mu\text{m}$  entre la sonde et le substrat, au-dessus de  $\text{CuCo}_2\text{O}_4$  (ligne rouge) et  $\text{CuBi}_2\text{O}_4$  (ligne noire). Chaque segment correspond à une durée d'illumination de 50 s.

Enfin, un mécanisme original et jamais décrit auparavant est proposé pour la PEC  $\text{CO}_2\text{RR}$  indirecte par l'intermédiaire de RTIL à base d'imidazolium agissant comme cocatalyseur. Ce mécanisme est basé sur les résultats de la photoactivité et de la détection des produits obtenus dans cette thèse. Les développements futurs dans ce domaine devraient se concentrer sur l'étude de l'interaction du  $\text{CO}_2$  et de la surface du catalyseur PEC en présence de RTIL ; sur l'exploitation des propriétés physico-chimiques et électrochimiques des RTIL tout en augmentant leur stabilité et leur activité à long terme ; ainsi que sur l'exploration d'autres types de RTIL.

## Bibliographie

- [1] J. Qiao, Y. Liu, F. Hong, J. Zhang, A review of catalysts for the electroreduction of carbon dioxide to produce low-carbon fuels, *Chem. Soc. Rev.* 43 (2014) 631–675. <https://doi.org/10.1039/C3CS60323G>.
- [2] J.L. White, M.F. Baruch, J.E. Pander, Y. Hu, I.C. Fortmeyer, J.E. Park, T. Zhang, K. Liao, J. Gu, Y. Yan, T.W. Shaw, E. Abelev, A.B. Bocarsly, Light-driven heterogeneous reduction of carbon dioxide: photocatalysts and photoelectrodes, *Chem. Rev.* 115 (2015) 12888–12935. <https://doi.org/10.1021/acs.chemrev.5b00370>.
- [3] Q. Lu, F. Jiao, Electrochemical  $\text{CO}_2$  reduction: Electrocatalyst, reaction mechanism, and process engineering, *Nano Energy*. 29 (2016) 439–456. <https://doi.org/10.1016/j.nanoen.2016.04.009>.
- [4] K. Rajeshwar, M.K. Hossain, R.T. Macaluso, C. Janáky, A. Varga, P.J. Kulesza, Review-copper oxide-based ternary and quaternary oxides: where solid-state chemistry meets

- photoelectrochemistry, *J. Electrochem. Soc.* 165 (2018) H3192–H3206. <https://doi.org/10.1149/2.0271804jes>.
- [5] A.S. Varela, W. Ju, A. Bagger, P. Franco, J. Rossmeisl, P. Strasser, Electrochemical reduction of CO<sub>2</sub> on metal-nitrogen-doped carbon catalysts, *ACS Catalysis*. 9 (2019) 7270–7284. <https://doi.org/10.1021/acscatal.9b01405>.
- [6] B.A. Rosen, W. Zhu, G. Kaul, A. Salehi-Khojin, R.I. Masel, Water enhancement of CO<sub>2</sub> conversion on silver in 1-ethyl-3-methylimidazolium tetrafluoroborate, *Journal of The Electrochemical Society*. 160 (2013) H138–H141.
- [7] B.A. Rosen, A. Salehi-Khojin, M.R. Thorson, W. Zhu, D.T. Whipple, P.J.A. Kenis, R.I. Masel, Ionic liquid-mediated selective conversion of CO<sub>2</sub> to CO at low overpotentials, *Science*. 334 (2011) 643–644. <https://doi.org/10.1126/science.1209786>.
- [8] G.P.S. Lau, M. Schreier, D. Vasilyev, R. Scopelliti, M. Grätzel, P.J. Dyson, New insights into the role of imidazolium based promoters for the electroreduction of CO<sub>2</sub> on a silver electrode, *Journal of the American Chemical Society*. 138 (2016) 7820–7823. <https://doi.org/10.1021/jacs.6b03366>.
- [9] Y. Wang, T. Hayashi, D. He, Y. Li, F. Jin, R. Nakamura, A reduced imidazolium cation layer serves as the active site for electrochemical carbon dioxide reduction, *Applied Catalysis B: Environmental*. 264 (2020) 118495. <https://doi.org/10.1016/j.apcatb.2019.118495>.
- [10] M. Zhang, L.-J. Yu, Y.-F. Huang, J.-W. Yan, G.-K. Liu, D.-Y. Wu, Z.-Q. Tian, B.-W. Mao, Extending the shell-isolated nanoparticle-enhanced Raman spectroscopy approach to interfacial ionic liquids at single crystal electrode surfaces, *Chem. Commun.* 50 (2014) 14740–14743. <https://doi.org/10.1039/C4CC06269H>.
- [11] A. Paul, P.K. Mandal, A. Samanta, On the optical properties of the imidazolium ionic liquids, *J. Phys. Chem. B*. 109 (2005) 9148–9153. <https://doi.org/10.1021/jp0503967>.
- [12] V. Badets, G. Loget, P. Garrigue, N. Sojic, D. Zigah, Combined local anodization of titanium and scanning photoelectrochemical mapping of TiO<sub>2</sub> spot arrays, *Electrochimica Acta*. 222 (2016) 84–91. <https://doi.org/10.1016/j.electacta.2016.10.151>.

## List of publications, trainings and conferences

### *Publications*

- [1] **L. Zhang**, I. Merino-Garcia, J. Albo, C M. Sánchez-Sánchez. Electrochemical CO<sub>2</sub> reduction reaction on cost-effective oxide-derived copper and transition metal-nitrogen-carbon catalysts. *Current Opinion in Electrochemistry*, 23 (2020) 65-73
- [2] C. Guo, **L. Zhang**, Z.-W. Tian, Z.-Q. Tian, D. Zhan, Photoelectric Effect Accelerated Electrochemical Corrosion and Nanoimprint Processes on Gallium Arsenide Wafer. *Chemical Science*, 10 (2019) 5893-5897. **(Co-first author)**
- [3] **L. Zhang**, J. Zhang, D. Yuan, L. Han, J.-Z. Zhou, Z.-W. Tian, Z.-Q. Tian, D. Zhan, Electrochemical nanoimprint lithography directly on n-type crystalline silicon (111) wafer. *Electrochemistry Communications*, 75 (2017) 1-4.
- [4] **L. Zhang**, B. Puga, V. Vivier, C. M. Sánchez-Sánchez, Photoelectrochemical activity for CO<sub>2</sub> reduction in different solvent media evaluated by scanning electrochemical microscopy, (2020). (to be submitted)

### *National and International Conferences*

- 2020.08 International Society of Electrochemistry (Online meeting)/Poster, Belgrade, Serbia
- 2019.12 L' IMPC Meeting/Oral presentation, Paris, France
- 2019.10 10<sup>th</sup> International Workshop on SECM and Related Techniques/Poster, Paris, France
- 2018.09 Workshop on Redox Films for Energy Conversion-bioelectrochemical and molecular systems, Marseille, France
- 2018.06 3<sup>rd</sup> conference of GDR Solar Fuels/Poster, Paris, France

### *Trainings*

- 2019.10 Training in fabricating dual tip in Université de Bordeaux for one week, Bordeaux, France
- 2019.03-05 2 months' stage at Pontificia Católica de Chile University, program ECOS SUD-Conicyt (code C17E10), work of thesis, Santiago, Chile



## Acknowledgements

Looking back on the three years' PhD study, my heart is full of mixed emotions.

My PhD study is inseparable from the inspiring and critical guidance of my supervisors and teachers, help from my colleagues and friends; care and support from my family. Here, I want to express my deepest and sincere gratitude to them.

Firstly, I want to express my sincere gratitude to my supervisor, Dr. Carlos M. SANCHEZ-SANCHEZ, with benevolent heart and creative mind, he gave me a lot of inspiring guidance, constructive suggestions and timely feedback. He acts as a role model for me not only in scientific research but also in life. It is his strict and optimistic attitude to scientific research that has a positive influence on my attitude to the research as well as to my life. With the help of Dr. SANCHEZ-SANCHEZ, I have participated in many academic conferences and scientific training in other labs. All these supports and helps are invaluable and irreplaceable for my PhD study.

Secondly, I want to show my gratitude to my co-supervisor, Dr. Vincent VIVIER, who has extensive theoretical and scientific knowledge, critical-thinking and works diligently and seriously. As the leader of the whole scientific team, he can always give me immediate answers and positive feedback no matter how busy he is. I express respect, admire and sincere appreciate to both of my supervisors for helping me to grow and make progress.

I also want to thank the jury committee members: Dr. Conchi ANIA, Prof. Enrique HERRERO and Dr. David PORTEHAULT for their efforts and time devoted to read and revise my PhD thesis.

I really want to thank Dr. Maria GOMEZ-MINGOT in Collège de France for her help and patience for the electrolysis measurements of my thesis work. My sincere thanks to Dr. Francisco Javier RECIO CORTES in Pontificia Universidad Católica de Chile, who taught me to do experiment and gave me tremendous helps in life during my two months' stay in Chile. The same thanks to Dr. Dodzi ZIGHA in Université de Bordeaux for his training of fabricating dual tips. Furthermore, I would like to thank Dr. Ivan MERINO-GARCIA in Universidade NOVA de Lisboa and Dr. Jonathan ALBO in University of Cantabria for the collaboration in the published paper. In addition, I owe the deep appreciate to my master's thesis supervisor, Prof. Dongping ZHAN, who trained and guided me a lot and provided

me the opportunity of pursuing PhD degree in France, without whose encourage and support I cannot be so brave like today.

My heartfelt thanks to all the support from the director of lab, Dr. Hubert PERROT; Mme. Françoise PILLIER and Stéphanie DELBREL for FEG-SEM and EDS measurements; Dr. Mireille TURMINE for providing experimental equipment; Dr. Alain PAILLERET for providing me some reagents; M. Damien BRICAULT for designing the equipment program; M. Axel DESNOYERS DE MARBAIX for machining work of the experimental pieces and Mme Isabelle LEFEBVRE and Martine CHADUC and Florence BILLON for their help.

I thank the funding of China Scholarship Council - Sorbonne Universite program (2017) and Labex Matisse program (ASDB/2017-12) for my PhD fellowship, as well as the ECOS Sud-Chile CONICYT program (Project C17E10).

My sincere appreciation to all the lab members for a harmonious and friendly social environment. I am grateful to make friends and acquire helps from them in my life. Thanks to Sophie, Gabriel, Elli, Dantong, Huiru, Zakaria, Alice, Aja, Ines, Antonin, Rafik, Adnane, Youssef, Sophia and my previous colleagues Wanli, David, Guillaume and Thomas. Great thanks to Dr. Ricardo VENEGAS, Dr. Christian CANDIA-ONFRAY, Dr. Karina MUNOZ-BECERRA in Chile and Dr. Eliana D. FARIAS in Bordeaux.

All my friends accompany and help me to conquer all the difficulties in life during these 3 years. I would say thanks to my dear friends: Baohuan, Pengfei, Xinlei, Bingbing, Yinan, Binghua, Kankan, Zhonghang, Hongyi, Guanzheng.

In the end, I want to thank my dear boyfriend, Yao ZHENG, who is also pursuing PhD degree in Sorbonne Université. He offers his sincere love and patience taking care of me, supports and encourages me when I am anxious and sad. He creates a comfortable environment and atmosphere for me to concentrate on my work. There is too much goodness to say but only a little can be expressed. I want to dedicate this thesis to my parents: Famin ZHANG and Changyu Xing. As parents, they gave me all they have and support me to realize my dream in another side of the earth, although they suffered from missing and worrying about me day and night. I hope I can be the proud of my parents. The same thanks to my other family members: my sister, aunts, uncles and grandparents for loving me all the time. Furthermore, great thanks to my dear motherland.